

**STUDIES ON THE MODIFICATION OF
NATURAL BIO-POLYMER FOR THE
ADSORPTIVE SEPARATION OF CATIONIC AND
ANIONIC POLLUTANTS FROM AQUEOUS
SOLUTIONS**



A THESIS SUBMITTED TO THE
CENTRAL DEPARTMENT OF CHEMISTRY
INSTITUTE OF SCIENCE AND TECHNOLOGY
TRIBHUVAN UNIVERSITY
NEPAL

FOR THE AWARD OF
DOCTOR OF PHILOSOPHY
IN CHEMISTRY

BY
RAM LOCHAN ARYAL
DECEMBER 2022

**STUDIES ON THE MODIFICATION OF
NATURAL BIO-POLYMER FOR THE
ADSORPTIVE SEPARATION OF CATIONIC AND
ANIONIC POLLUTANTS FROM AQUEOUS
SOLUTIONS**



A THESIS SUBMITTED TO THE
CENTRAL DEPARTMENT OF CHEMISTRY
INSTITUTE OF SCIENCE AND TECHNOLOGY
TRIBHUVAN UNIVERSITY
NEPAL

FOR THE AWARD OF
DOCTOR OF PHILOSOPHY
IN CHEMISTRY

BY
RAM LOCHAN ARYAL
DECEMBER 2022

DECLARATION

Thesis entitled “**Studies on the Modification of Natural Bio-polymer for the Adsorptive Separation of Cationic and Anionic Pollutants from Aqueous Solutions**” which is being submitted to the Central Department of Chemistry, Institute of Science and Technology (IoST), Tribhuvan University, Nepal for the award of the degree of Doctor of Philosophy (Ph.D.), is a research work carried out by me under the supervision of Prof. Dr. Kedar Nath Ghimire, of Central Department of Chemistry, Tribhuvan University and co-supervised by Asst. Prof. Dr. Hari Paudyal of Central Department of Chemistry, Tribhuvan University.

This research is original and has not been submitted earlier in part or full in this or any other form to any university or institute, here or elsewhere, for the award of any degree.

Ram Lochan Aryal

RECOMMENDATION

This is to recommend that **Mr. Ram Lochan Aryal** has carried out research entitled “**Studies on the Modification of Natural Bio-polymer for the Adsorptive Separation of Cationic and Anionic Pollutants from Aqueous Solutions**” for the award of Doctor of Philosophy (Ph.D.) in **Chemistry** under our supervision. To our knowledge this work has not been submitted for any other degree.

He has fulfilled all the requirements laid down by the Institute of Science and Technology (IoST), Tribhuvan University, Kathmandu, Nepal for the submission of the thesis for the award of Ph.D. degree.

.....

Prof. Dr. Kedar Nath Ghimire

Supervisor

(Professor)

Central Department of Chemistry

Tribhuvan University

Kirtipur, Kathmandu, Nepal

.....

Dr. Hari Paudyal

Co-supervisor

(Assistant Professor)

Central Department of Chemistry

Tribhuvan University

Kirtipur, Kathmandu, Nepal

DECEMBER 2022

LETTER OF APPROVAL

Date: 9, January 2023

On the recommendation of **Prof. Dr. Kedar Nath Ghimire** and **Dr. Hari Paudyal**, this Ph.D. thesis submitted by **Mr. Ram Lochan Aryal**, entitled “**Studies on the Modification of Natural Bio-polymer for the Adsorptive Separation of Cationic and Anionic Pollutants from Aqueous Solutions**” is forwarded by Central Department Research Committee (CDRC) to the Dean, IoST, T.U..

Dr. Jagadeesh Bhattarai

Professor

Head

Central Department of Chemistry

Tribhuvan University

Kirtipur, Kathmandu

Nepal

ACKNOWLEDGEMENTS

It is indeed a pleasure to acknowledge my gratitude to all those who have directly and indirectly helped me to complete this research work successfully.

With a deep sense of gratitude, I express my indebtedness and reverence to my Principal Supervisor, Prof. Dr. Kedar Nath Ghimire, Central Department of Chemistry, Tribhuvan University, Kirtipur, Kathmandu, Nepal, for his effort, guidance, and open-handed cooperation throughout the span of my Ph.D. research work. I also would like to thank my Co-Supervisor, Dr. Hari Paudyal for his regular monitoring of research details, invaluable guidance, and remarkable support throughout this research.

I would also like to express my sincerest thanks to Prof. Dr. Jagadeesh Bhattarai, Head of the Central Department of Chemistry, and Prof. Dr. Ram Chandra Basnyat, former Head of Central Department of Chemistry, T.U. for providing me with the space, and all the laboratory facilities to accomplish my research work. I am highly thankful to Prof. Dr. Megh Raj Pokhrel and Assoc. Prof. Dr. Surendra Kumar Gautam for their insightful suggestions and moral support.

I also express my abounding feelings of gratitude to Principal Scientist, Dr. Satyakam Patnaik, CSIR-Indian Institute of Toxicology Research (CSIR-IITR) for providing me an opportunity to conduct this research work and characterize the biosorbents (FE-SEM/EDX, XRD, TGA & zeta potential measurements) partly in Lucknow, India. I am extremely privileged to thank Dr. Markandeya Tiwari for his support and encouragements in Lucknow, India. I am thankful to Indian National Science Academy (INSA), New Delhi, India, and the Department of Science and Technology (DST), Ministry of Science and Technology, Government of India for providing me with the India Science and Research Fellowship (ISRF).

I express my sincere thanks to Dr. Bipeen Dahal (Jeonbuk National University, Jeonju, South Korea) and Mr. Sitaram Bhattarai (Korea Center for Artificial

Photosynthesis, Department of Chemistry, Sogang University, Seoul, Korea) who helped me in sample characterization (FE-SEM/EDX, XRD & XPS) during their study period, Dr. Tista Prasai Joshi (Nepal Academy of Science and Technology, Khumaltar, Lalitpur) for zeta potential measurement and Mr. Dipak Kumar Hitan and Mr. Lekh Nath Khatiwada (Laboratory section, Ministry of Finance, Department of Customs, Tripureshwor Kathmandu) for FTIR analysis. I would like to thank Mr. Khem Prasad Bhurtel, Mr. Anil Thapa and all other laboratory members in CDC, T.U., and Lucknow, India. I wish to thank Kalpana Padaria and Satgur prasad of CSIR-IITR, Lucknow, India for ICP-MS and AAS measurements of the samples. I am thankful for all the academic, administrative, and laboratory staffs of the Central Department of Chemistry, T.U., Kirtipur, Amrit Campus, Department of Chemistry, Kathmandu, and CSIR-IITR, Lucknow, India. I appreciate the Research Committee of CDC, and Dean's Office, Institute of Science and Technology (IoST), Tribhuvan University (T.U.), Nepal for enrolling me in Ph.D. programme in CDC, T.U., Nepal and grateful for the study leave granted during my Ph.D. research work.

I also extend my thanks to Mr. Bhoj Raj Poudel, a Ph.D. colleague, who motivates and encourages me in the research for the accomplishment of Ph.D. degree.

Simple words of gratitude will never be adequate to express my gratitude to my family members who have always supported me and shown confidence and faith in all my endeavours. Memories to my father Mr. Prem Narayan Aryal whom, I lost during my Ph.D. journey. I am highly thankful to my loving mother Goma Devi Aryal for her moral support. My special thanks are also to my wife Paru Aryal, and my kids Adhish Aryal and Akshaj Aryal. Without their unstinted support and encouragement, the work would not have been the light of the day.

At the outset, thanks to the almighty God who has given to me spiritual support and courage to accomplish this research work.

.....

Ram Lochan Aryal

December, 2022

ABSTRACT

Cationic and anionic pollutants have adverse effects on water resources, ecosystem, and human health. Modified watermelon rind (WR) and banana peels (BP) has the potential for the removal of pollutants. The carboxyl groups were increased through lime water treatments onto methylated ester part of pectic acid present in WR and BP. The biosorption by the saponified pectic acid (SWR and SBP) occurred through cationic exchange between carboxyl functional groups and Hg(II) and Pb(II) by releasing hydrogen ions. Furthermore, higher valent metals such as [Zr(IV) and La(III)] were loaded onto saponified WR and BP to create ligand exchange sites for anionic pollutants like F⁻, PO₄³⁻, and As(III). The characterization of these biosorbents were done by FE-SEM, EDX, FTIR, XPS, XRD, TGA/DSC and Zeta potential measurements to know the structural changes, chemical composition, and thermal stability. The various experimental parameters such as solution pH, equilibration time, initial concentration, biosorbent dosages were examined for Hg(II), Pb(II), F⁻, PO₄³⁻, and As(III) biosorption from aqueous solution in batch mode for as-modified biosorbents [Zr(IV)-SWR, La(III)-SWR, Zr(IV)-SBP, SWR and SBP]. Based on the higher coefficient of determination (R²) and lower error function values, PSO model and Langmuir isotherm model described better the biosorption of investigated biosorbents.

The findings revealed that the maximum biosorption capacities of Zr(IV)-SWR for F⁻ and PO₄³⁻ was 28.98 and 27.65 mg/g whereas that of Zr(IV)-SBP for F⁻ was 36.02 mg/g and La(III)-SWR for As(III) was 37.73 mg/g, respectively. Similarly, the biosorption capacity of SWR and SBP for Hg(II) was 97.18 and 61.31 mg/g and Pb(II) was 253.16 and 230.94 mg/g, respectively. Thermodynamics parameters revealed that As(III) biosorption onto La(III)-SWR is spontaneous and endothermic in nature. The presence of higher concentration of co-existing ions such as HCO₃⁻, SO₄²⁻ and PO₄³⁻ markedly interfered while Cl⁻ and NO₃⁻ showed insignificant effect for the biosorption of F⁻ and As(III). Base solution (2M NaOH) was effective for the

desorption of anionic pollutants (F^- , and $As(III)$) however, 0.3M NaOH was effective for PO_4^{3-} ion desorption. Acidic solution (1M HNO_3) was effective for desorption of cationic ($Hg(II)$, $Pb(II)$) pollutants. The biosorption-desorption of anionic pollutants took place through ligand exchange mechanism while that for cationic pollutants through cation exchange mechanism. The regeneration of tested biosorbents were found effective up to 4-5 cycles. Finally, La(III)-SWR could effectively lowered $As(III)$ concentration present in natural water below the WHO and USEPA standard. Similarly, SBP could lowered $Pb(II)$ concentration present in industrial water below the WHO standard.

Thus, investigated biosorbents are expected to be the potential biosorbents which can be effective for the removal of trace concentration of cationic and anionic pollutants from aqueous solution.

LIST OF ACRONYMS AND ABBREVIATIONS

% R	:Biosorption Efficiency
ΔG°	:Standard Gibb's Free Energy Change
ΔH°	:Standard Enthalpy Change
ΔS°	:Standard Entropy Change
1/n	:Heterogeneity Factor Related to Biosorption Capacity
AAS	:Atomic Absorption Spectroscopy
AR	:Analytical Reagent
b	:Langmuir Equilibrium Constant
BP	:Banana Peel
C_r	:Residual Concentration
C_i	:Initial Concentration
D %	:Desorption Efficiency
DI	:Deionized Water
EDX	:Energy Dispersive X-ray Spectroscopy
FE-SEM	:Field Emission Scanning Electron Microscopy
FTIR	:Fourier Transform Infrared Spectroscopy
ICP-MS	:Inductively Coupled Plasma-Mass Spectroscopy
ICP-OES	:Inductively Coupled Plasma-Optical Emission Spectroscopy
k_1	:PFO Rate Constant
k_2	:PSO Rate Constant
K_C	:Thermodynamic Equilibrium Constant
K_D	:Distribution Coefficient
K_F	:Freundlich Constant

L	:Liter
La(III)-SWR	:Lanthanum(III)-Loaded Saponified Watermelon
MAE	:Mean Absolute Error
mg	:Milligrams
min	:Minutes
mL	:Milliliter
pH _{pzc}	:Point of Zero Charge
ppb	:Parts Per Billion
ppm	:Parts Per Million
q _e	:Amount Biosorbed at Equilibrium
q _{m, cal}	:Calculated Maximum Biosorption Capacity
q _{m, expt}	:Experimental Biosorption Capacity
q _t	:Quantity Biosorbed at Specified Time
RBP	:Raw Banana Peels
R _L	:Dimensionless Separation Factor
RMSE	:Root Mean Square Error
RWR	:Raw Watermelon Rind
SBP	:Saponified Banana Peels
SWR	:Saponified Watermelon Rind
TGA	:Thermogravimetric Analysis
WR	:Watermelon Rind
XPS	:X-ray Photoelectron Spectroscopy
XRD	:X-ray Diffraction
Zr(IV)-SBP	:Zirconium(IV)-Loaded Saponified Banana Peel
Zr(IV)-SWR	:Zirconium(IV)-Loaded Saponified Watermelon

LIST OF SYMBOLS

R^2	:Coefficient of Determination
χ^2	:Chi Square
λ	:Wavelength
K	:Kelvin Scale
$^{\circ}\text{C}$:Degree Celsius
R	:Universal Gas Constant
eV	:Electron Volt
μg	:Microgram
m	:Mass of Biosorbent
V	:Volume of Biosorbate Solution
h	:Hour

LIST OF TABLES

	Page No.
Table 1: Sources, hazardous effects, and permissible limit of cationic and anionic pollutants	4
Table 2: List of chemicals used throughout the experimental work	52
Table 3: List of instruments used for the characterization of biosorbents	54
Table 4: Kinetic parameters for biosorption of fluoride ion onto biosorbents	72
Table 5: Isotherm parameters for biosorption of fluoride ions onto biosorbents	73
Table 6: Error analysis on kinetic studies of fluoride ion biosorption onto biosorbents	75
Table 7: Error analysis on isotherm studies of fluoride biosorption onto biosorbents	75
Table 8: Comparison of defluoridation capacity of Zr(IV)-SWR and Zr(IV)-SBP with the other adsorbents	76
Table 9: Chemical composition of RWR, SWR and Zr(IV)-SWR	80
Table 10: Kinetics parameters for the biosorption of phosphate onto Zr(IV)-SWR	84
Table 11: Isotherm parameters for the biosorption of phosphate onto Zr(IV)-SWR	85
Table 12: Comparison of biosorption capacities of Zr(IV)-SWR with other bio/adsorbents	86
Table 13: Error analysis of biosorption of fluoride ion onto Zr(IV)-SWR	87
Table 14: Chemical compositions of SWR, La(III)-SWR, and arsenic biosorbed La(III)-SWR	91
Table 15: Kinetics parameters for As(III) biosorption onto La(III)-SWR	97

Table 16: Isotherm parameters for the biosorption of As(III) onto La(III)-SWR	99
Table 17: Comparison of As(III) biosorption onto La(III)-SWR with other adsorbents	100
Table 18: Thermodynamic parameters for the As(III) biosorption onto La(III)-SWR	101
Table 19: Kinetic parameters for biosorption of Hg(II) onto SWR and SBP biosorbents	114
Table 20: Biosorption isotherm parameters of Hg(II) onto SWR and SBP	117
Table 21: Comparison of Hg(II) removal capacities of SWR and SBP with other adsorbents	119
Table 22: Error function determination for kinetics studies for the biosorption of Hg(II)	120
Table 23: Error function determination for isotherms studies for the biosorption of Hg(II)	120
Table 24: Kinetic parameters for the Pb(II) biosorption onto biosorbents	130
Table 25: Biosorption isotherm parameters of Pb(II) biosorption onto biosorbents	132
Table 26: Comparative study of Pb(II) biosorption onto investigated biosorbents with other adsorbents	133
Table 27: Error analysis for kinetic studies of biosorption of Pb(II) onto biosorbents	134
Table 28: Error analysis for isotherm studies of biosorption of Pb(II) onto biosorbents	135

LIST OF FIGURES

	Page No.
Figure 1: Sources of heavy metals pollutants	3
Figure 2: Speciation diagram of various fluoride species at different pH	5
Figure 3: Speciation diagram of phosphorus species at different pH	7
Figure 4: Speciation diagram of arsenic species at different pH	8
Figure 5: Speciation diagram of mercury species at different pH	9
Figure 6: Speciation diagram of lead species at different pH	10
Figure 7: Adsorption process	15
Figure 8: Chemical structure of cellulose pectin	17
Figure 9: Photographs of watermelon fruit and dried watermelon rinds	17
Figure 10: Photograph of banana fruits and banana peels	18
Figure 11: Biosorption mechanism	19
Figure 12: Methodological framework for the study	51
Figure 13: Reaction scheme for the saponification of RWR and RBP	55
Figure 14: Reaction scheme for loading of metal onto SWR/SBP (M = Zr(IV) & La(III))	56
Figure 15: Reaction mechanism for the synthesis of M-SWR and M-SBP biosorbent (M = Zr(IV), La(III))	62
Figure 16: FE-SEM micrographs of (a) RWR (b) SWR (c) Zr(IV)-SWR (d) Zr(IV)-SBP (e) and (f) after biosorption of fluoride	63
Figure 17: EDX spectra and elemental mapping of SWR (a, d), Zr(IV)-SWR (b, e) and fluoride biosorption onto Zr(IV)-SWR (c, f)	65
Figure 18: FTIR spectra of (a) RWR, SWR and Zr(IV)-SWR (b) RBP, SBP and Zr(IV)-SBP in the range from 4000- 400 cm⁻¹	66
Figure 19: Thermogravimetric curves for RWR, SWR and Zr(IV)-SWR	66
Figure 20: XRD pattern of RBP and Zr(IV)-SBP	67

Figure 21:	Zeta potential analysis at different pH of (a) Zr(IV)-SWR and (b) Zr(IV)-SBP	68
Figure 22:	Effect of pH on the biosorption of fluoride onto (a) RWR and Zr(IV)-SWR and (b) RBP and Zr(IV)-RBP	69
Figure 23:	Biosorption kinetics of Zr(IV)-SWR (a) Non-linear plot of kinetic modelling with experimental data (b) PFO and (c) PSO model	70
Figure 24:	Biosorption of fluoride onto Zr(IV)-SBP (a) Non-linear kinetic modeling of PFO and PSO model (b) PFO and (c) PSO model	71
Figure 25:	Biosorption isotherms of fluoride ion onto Zr(IV)-SWR (a) Non-linear modeling of Langmuir and Freundlich isotherm with experimental data (b) Langmuir isotherm model (c) Freundlich isotherm model and (d) Variation of R_L with initial concentration	73
Figure 26:	Biosorption isotherm studies onto Zr(IV)-SBP (a) Non-linear plot of Langmuir and Freundlich isotherm model with experimental data (b) Langmuir isotherm model and (c) Freundlich isotherm model (d) variation of R_L with initial concentration	73
Figure 27:	Effect of biosorbent dosage of Zr(IV)-SWR and SBP onto fluoride ion biosorption	75
Figure 28:	Effect of co-existing ions for the fluoride biosorption onto (a) Zr(IV)-SWR and (b) Zr(IV)-SBP	77
Figure 29:	Desorption of fluoride from fluoride biosorbed (a) Zr(IV)-SWR and (b) Zr(IV)-SBP	77
Figure 30:	Variation of percentage biosorption of fluoride in 5 cycle's biosorption regeneration process of Zr(IV)-SWR and Zr(IV)-SBP	79
Figure 31:	SEM micrographs of surface morphology of a) Zr(IV)-SWR and b) Zr(IV)-SWR after phosphate biosorption	80

Figure 32:	Zeta potential of Zr(IV)-SWR at different pH	81
Figure 33:	Effect of pH on phosphate biosorption by Zr(IV) loaded SWR	82
Figure 34:	Phosphate biosorption mechanism in Zr(IV)-SWR	82
Figure 35:	Phosphate biosorption onto Zr(IV)-SWR (a) Non-linear plot of PFO and PSO model with experimental data (b) PFO model and (c) PSO kinetic model	83
Figure 36:	(a) Non-linear plot of Langmuir and Freundlich isotherm with experimental data (b) Langmuir isotherm model and (c) Freundlich isotherm for the biosorption of phosphate onto Zr(IV)-SWR	85
Figure 37:	Effect of biosorbent dose in the biosorption of phosphate onto Zr(IV)-SWR	87
Figure 38:	Effect of co-existing anions in the phosphate biosorption onto Zr(IV)-SWR	88
Figure 39:	Desorption of phosphate from phosphate biosorbed Zr(IV)-SWR at varied molar concentration of NaOH	89
Figure 40:	Plausible mechanism of desorption of phosphate biosorbed Zr(IV)-SWR	89
Figure 41:	SEM micrographs of (a) RWR (b) SWR (c) La(III)-SWR before biosorption (d) La(III)-SWR after As(III) biosorption	90
Figure 42:	EDX analysis of SWR, La(III)-SWR, and As-La(III)-SWR showing respective (a), (b), and (c) elemental mapping, (d), (e), and (f) EDX spectra	92
Figure 43:	FTIR analysis of RWR, SWR and La(III)-SWR	93
Figure 44:	Plot of zeta potential <i>versus</i> pH of La(III)-SWR	94
Figure 45:	As(III) biosorption onto La(III)-SWR (a) Effect of pH and (b) $\log(K_D)$ <i>versus</i> pH_e	95
Figure 46:	Biosorption kinetics of As(III) onto La(III)-SWR (a) Non-linear fitting of PFO and PSO model with experimental data (b) PFO and (b) PSO	96

Figure 47:	Isotherm of As(III) biosorption onto La(III)-SWR (a) Isotherm plot at varied temperatures (b) Non-linear modeling of Langmuir and Freundlich isotherm data with experimental data at 298K (c) Langmuir isotherm model and (d) Freundlich isotherm model	98
Figure 48:	Van't Hoff plot of $\ln k_c$ versus reciprocal of absolute temperature	101
Figure 49:	Effect of co-existing ions for the As(III) biosorption onto La(III)-SWR	102
Figure 50:	XPS analysis of La(III)-SWR after biosorption of As(III) (a) Survey spectrum (b) La 3d (c) As 3d (d) O 1s	103
Figure 51:	Desorption of As(III) from As(III) biosorbed La(III)-SWR with varied concentration of NaOH	104
Figure 52:	Inferred mechanism of As(III) biosorption-desorption onto La(III)-SWR	105
Figure 53:	FE- SEM micrographs of (a) RWR (b) SWR and (c) Hg(II) biosorbed SWR (d) RBP (e) SBP and (f) Hg(II) biosorbed SBP	106
Figure 54:	EDX spectra (a) SWR (b) after Hg(II) biosorption (c) EDX electron image layered images, and EDX color mapping images of all elements of SWR (d) EDX electron image, layered images, and EDX color mapping images of all elements of SWR after Hg(II) biosorption	108
Figure 55:	EDX spectra of (a) SBP (b) Hg(II) biosorbed SBP (c) EDX electron image, layered images and EDX color mapping images of all overlapping elements of SBP (d) EDX electron image, layered images and EDX color mapping images of all overlapping elements Hg(II) biosorbed SBP	110
Figure 56:	FTIR spectra of (a) RWR, SWR, Hg(II) biosorbed SWR and (b) RBP, SBP, Hg(II) biosorbed SBP	111

Figure 57: Zeta potential at different pH showing pHpzc of SWR and SBP	112
Figure 58: Effect of pH in the biosorption of Hg(II) onto (a) RWR, SWR and (b) RBP, SBP	113
Figure 59: Biosorption of Hg(II) onto SWR (a) Non-linear plot of PFO and PSO fittings with experimental data (b) PFO and (c) PSO model	114
Figure 60: Biosorption kinetic study of Hg(II) onto SBP (a) Non-linear kinetic modeling of PFO and PSO with experimental data (b) PFO model and (c) PSO model	115
Figure 61: Biosorption isotherm studies onto SWR (a) Non-linear plot of Langmuir and Freundlich isotherm model with experimental data (b) Langmuir isotherm model (c) Freundlich isotherm model and (d) Variation of R_L with initial concentration	116
Figure 62: Biosorption isotherm of SBP on Hg(II) biosorption (a) Non-linear Langmuir and Freundlich isotherm fittings with experimental data (b) Langmuir isotherm and (c) Freundlich isotherm model	117
Figure 63: Effect of SWR and SBP dosage on biosorption of Hg(II)	118
Figure 64: Effect on biosorption of Hg(II) with co-existing ions (a) SWR and (b) SBP	121
Figure 65: Desorption of Hg(II) from Hg(II) biosorbed (a) SWR and (b) SBP	122
Figure 66: Variation of biosorption capacity in successive biosorption desorption cycles of Hg(II) biosorption onto SWR, SBP	122
Figure 67: SEM images of (a) SWR (b) Pb(II) biosorbed SWR (c) SBP and (d) Pb(II) biosorbed SBP	123
Figure 68: EDX spectra of (a) SWR (b) Pb(II) biosorption (c) EDX electron image, layered images and EDX color mapping images of all overlapping elements of SWR (d) EDX electron	

	image, layered images and EDX color mapping images of all overlapping elements of Pb(II) loaded SWR	125
Figure 69:	EDX spectra of (a) SBP (b) Pb(II) biosorption; EDX electron image, layered images and EDX color mapping images of all overlapping elements of (c) SBP and (d) after Pb(II) loaded SBP	126
Figure 70:	FTIR spectra of (a) RWR, SWR, Pb(II) biosorbed SWR and (b) RBP, SBP and Pb(II) biosorbed SBP	127
Figure 71:	Effect of solution pH for biosorption of Pb(II) onto SWR and SBP	128
Figure 72:	Biosorption kinetics of Pb(II) onto SWR (a) Non-linear plot of PFO and PSO model with experimental data (b) PFO model and (c) PSO model	129
Figure 73:	Biosorption of Pb(II) onto SBP (a) Non-linear fitting of kinetics models with experimental data (b) PFO and (c) PSO model	130
Figure 74:	Biosorption of Pb(II) onto SWR (a) Non-linear plot of Langmuir and Freundlich modeling with experimental data (b) Langmuir and (c) Freundlich isotherm model	131
Figure 75:	Biosorption isotherm of Pb(II) onto SBP (a) Nonlinear plot of Langmuir and Freundlich modelling with experimental data (b) Langmuir isotherm model (c) Freundlich isotherm model and (d) Variation of R_L with initial concentration	132
Figure 76:	Effect of SWR dosage in the biosorption of Pb(II) ions	134
Figure 77:	Effect of co-existing ions on biosorption of Pb(II) onto (a) SWR and (b) SBP	135
Figure 78:	Biosorption mechanism of M(II) onto monomeric unit of SWR and SBP	136
Figure 79:	Desorption of Pb(II) using HNO_3 (a) biosorbed SWR and (b) biosorbed SBP	137

Figure 80: Variation of the % biosorption of Pb(II) in four- five cycle's biosorption-regeneration process of SWR and SBP	138
Figure 81: Application of investigated SBP for the removal of Pb(II) from polluted textile water	139
Figure 82: Application of La(III)-SWR for the dearsenification of contaminated groundwater	140

TABLE OF CONTENTS

	Page No.
Declaration	iii
Recommendation	iii
Letter of Approval	iv
Acknowledgements	v
Abstract	vii
List of Acronyms and Abbreviations	ix
List of Symbols	xi
List of Tables	xii
List of Figures	xiv
Table of Contents	xxi
CHAPTER 1	1
1. INTRODUCTION	1
1.1 Water- sources, status, and availability of drinking water	1
1.2 Sources, hazardous effects, and permissible limits of pollutants	2
1.2.1 Fluoride	5
1.2.2 Phosphates	5
1.2.3 Arsenic	7
1.2.4 Mercury	8
1.2.5 Lead	10
1.3 Conventional technologies for the separation of cationic and anionic pollutants	11
1.3.1 Chemical precipitation	11
1.3.2 Ion exchange	12

1.3.3	Electrowinning	12
1.3.4	Coagulation and flocculation	13
1.3.5	Membrane processes	13
1.3.6	Electrodialysis	14
1.3.7	Adsorption	14
1.4	Biosorption	16
1.5	Biosorbents: Watermelon rinds and Banana peels	16
1.6	Biosorption mechanism	18
1.7	Batch biosorption studies	19
1.8	Factors influencing biosorption	20
1.8.1	pH of solution	20
1.8.2	Contact times	21
1.8.3	Initial concentration of biosorbate	21
1.8.4	Biosorbent dosages	22
1.8.5	Effect of co-existing ions	22
1.9	Modeling of biosorption data	22
1.9.1	Modeling of kinetic data	22
1.9.1.1	Pseudo first order (PFO) model	23
1.9.1.2	Pseudo second order (PSO) kinetic model	23
1.10	Modeling of isotherm data	24
1.10.1	Langmuir isotherm model	24
1.10.2	Freundlich isotherm model	25
1.11	Thermodynamics studies	25
1.12	Determination of distribution coefficient	27
1.13	Desorption studies	27
1.14	Regeneration and reusability studies	27
1.15	Characterization of biosorbents	28
1.15.1	Fourier transform infrared (FTIR) spectroscopy	28
1.15.2	Scanning electron microscopic (FE-SEM) analysis	28
1.15.3	Energy dispersive X-ray (EDX) spectroscopy	29

1.15.4 X-ray diffraction (XRD) analysis	29
1.15.5 X-ray photoelectron spectroscopic (XPS) analysis	29
1.15.6 Zetapotential analysis	30
1.16 Rationale of the study	30
1.17 Objectives	31
1.17.1 General objectives	31
1.17.2 Specific objectives	31
CHAPTER 2	32
2. LITERATURE REVIEW	32
2.1 Fluoride biosorption	32
2.2 Phosphate biosorption	35
2.3 Arsenic biosorption	39
2.4 Lead biosorption	41
2.5 Research gap	49
CHAPTER 3	51
3. MATERIALS AND METHODS	51
3.1 Methodological framework	51
3.2 Chemical reagents	52
3.3 Preparation of reagents	53
3.3.1 Preparation of sodium fluoride solution	53
3.3.2 Preparation of phosphate solution	53
3.3.3 Preparation of arsenic solution	53
3.3.4 Preparation of Pb(II) solution	53
3.3.5 Preparation of Hg(II) solution	53
3.3.6 Preparation of HCl solution	53
3.3.7 Preparation of NaOH solution	53
3.3.8 Preparation of buffer solution	54
3.3.9 Preparation of CDTA solution	54

3.4	Instrumentation	54
3.5	Preparation of biosorbents	55
3.5.1	Raw watermelon rind and banana peel powder	55
3.5.2	Preparation of SWR and SBP powder	55
3.5.3	Preparation of metal loaded watermelon rind/banana peel	55
3.6	Characterization of biosorbents	56
3.7	Experimental procedure for batch studies	56
3.7.1	Biosorption solution pH studies	57
3.7.2	Biosorption kinetic studies	57
3.7.3	Biosorption isotherm studies	58
3.7.4	Biosorption biosorbent dosages studies	58
3.7.5	Biosorption co-existing ions studies	58
3.7.6	Desorption studies	59
3.7.7	Regeneration and reusability studies	60
3.7.8	Concentration analysis	60
3.7.9	Error function analysis	60
CHAPTER 4		62
4. RESULTS AND DISCUSSION		62
4.1	Chemical modification of watermelon rind and banana peels	62
4.2	Fluoride ion biosorption	62
4.2.1	Characterization of biosorbents	63
4.2.1.1	Surface morphology of biosorbents	63
4.2.1.2	EDX spectra with color mapping	63
4.2.1.3	Functional groups analysis	65
4.2.1.4	Thermogravimetric analysis	66
4.2.1.5	XRD analysis of biosorbent	67
4.2.1.6	Surface charge of Zr(IV)-loaded biosorbents	67
4.2.2	Batch biosorption studies	68
4.2.2.1	Effect of pH and fluoride biosorption mechanism	68

4.2.2.2	Effect of contact time	70
4.2.2.3	Biosorption isotherm of fluoride ion	72
4.2.2.4	Effect of biosorbent dosage	74
4.2.3	The error analysis	75
4.2.4	Effect of co-existing ions	76
4.2.5	Desorption studies	77
4.2.6	Regeneration and reusability of biosorbents	78
4.3	Biosorption of phosphate onto Zr(IV)-SWR	79
4.3.1	Characterization of biosorbents	79
4.3.1.1	Surface morphology of the biosorbents	79
4.3.1.2	Energy dispersive X-ray analysis (EDX)	80
4.3.1.4	Surface charge of the biosorbents	80
4.3.2	Batch biosorption studies	81
4.3.2.1	Effect of solution pH and phosphate biosorption mechanism	81
4.3.2.2	Effect of contact time	83
4.3.2.3	Effect of initial concentration	84
4.3.2.4	Effect of biosorbent dosage	86
4.3.2.5	Error function analysis	87
4.3.3	Effect of co-existing ions	88
4.3.4	Desorption studies	88
4.4	Biosorption of As(III) onto La(III)-SWR	89
4.4.1	Characterization of biosorbents	89
4.4.1.1	FE-SEM analysis of the biosorbents	89
4.4.1.2	EDX spectra analysis with color mapping	90
4.4.2	Functional group analysis by FTIR spectroscopy	93
4.4.3	Surface charge analysis of biosorbent	94
4.4.3.1	Effect of pH and mechanism of As(III) biosorption	94
4.4.3.2	Effect of contact time	96
4.4.3.3	Biosorption isotherm studies	97
4.4.4	Investigation of thermodynamic parameters	100

4.4.5	Effects of co-existing ions	101
4.4.6	XPS analysis of the biosorbent	102
4.4.7	Desorption studies	103
4.4.8	Mechanism of As(III) biosorption- desorption	104
4.5	Biosorption of Hg(II) onto biosorbents	105
4.5.1	Biosorbents characterization	105
4.5.1.1	FE-SEM analysis on the biosorbents	105
4.5.1.2	EDX spectra with elemental mapping	105
4.5.1.3	FTIR analysis	110
4.5.1.4	Surface charge of biosorbents	111
4.5.2	Batch studies	112
4.5.2.1	Effect of pH	112
4.5.2.2	Effect of contact time	113
4.5.2.3	Effect of initial concentration	115
4.5.2.4	Effect of biosorbent dosage	118
4.5.3	Error Analysis	119
4.5.4	Effect of co-existing ions	120
4.5.5	Desorption studies	121
4.5.6	Regeneration and reusability of biosorbent	122
4.6	Biosorption of Pb(II) onto biosorbents	123
4.6.1	Biosorbents characterization	123
4.6.1.1	Surface morphology of the biosorbents	123
4.6.1.2	EDX spectra with elemental mapping	124
4.6.1.3	FTIR spectroscopy analysis	127
4.6.2	Batch wise biosorption studies	128
4.6.2.1	Effect of solution pH and biosorption mechanism	128
4.6.2.2	Effect of contact time	128
4.6.2.3	Biosorption isotherm of Pb(II) ion	130
4.6.2.4	Effect of biosorbent dosages	133
4.6.3	Error Analysis	134

4.6.4	Effect of co-existing ions	135
4.6.5	Mechanism of biosorption of Hg(II) and Pb(II)	136
4.6.6	Desorption studies	136
4.7	Application of investigated biosorbents for the treatment of natural water sample	141
4.7.1	Application of investigated SBP for the treatment of Pb(II) polluted textile wastewater	141
4.7.2	Application of La(III)-SWR for the dearsenification of contaminated groundwater	139
	CHAPTER 5	141
	5. CONCLUSION AND RECOMMENDATION	141
5.1	Conclusion	141
5.2	Recommendations	142
	CHAPTER 6	144
	6. SUMMARY	144
	7. REFERENCES	148
	APPENDIX	

CHAPTER 1

INTRODUCTION

1.1 Water- sources, status, and availability of drinking water

Water is the primary requirement for the sustenance of life. It is an essential component of all living organisms. We require water in many ways such as cooking food, bathing, irrigation, generation of hydroelectricity and so on. Water covers 71% of the Earth's surface. According to estimates, 96.5% of the world's water is found in seas and oceans, 1.7% is found underground, and 1.7% frozen in glaciers and ice caps in the Arctic and Antarctic (Peters & Meybeck, 2000). A significant amount of water is found in water bodies, while a considerably smaller portion (0.001%) is suspended in the atmosphere as vapors, clouds, etc., which eventually turns into precipitation (Loucks, 2000). Thus, fresh water makes up only 2.5% of the planet's total water supply, and that of 98.8% is frozen in ice and stored in groundwater. Less than 0.3% of fresh water can be found in rivers, lakes, and the atmosphere, and even less (0.003%) can be found in biological structures and manufactured goods. Only a tiny fraction (0.01%) of this amount is usable by humans (Hinrichsen & Tacio, 2002). In the present context, the population growth, unplanned urbanization, agricultural run offs, manufacturing discharge, vehicles emissions, and unthoughtful race of industrial development degrade the ecological environment, especially water.

The effect of natural and human activities causes changes in the physicochemical and biological features, as well as in the quality, quantity, and availability of water resources (Peters & Meybeck, 2000). Metals, pesticides, pathogens, minerals, and salts that affect surface water are among the pollutants discharged by agricultural practices (Akhtar *et al.*, 2021). The effects of water pollution are significant in developing countries, because of which, individuals are deprived of clean drinking water systems. The World Health Organization (WHO) estimates that 844 million people lack access to a primary source of drinking water and that 230 million spend more than 30 minutes per day fetching water from an improved source, that may include protected wells and springs, boreholes, piped water, packaged/delivered water

rainwater, and so forth (Ward *et al.*, 2018). Water-related diseases are more likely to occur when people in developing nations do not consistently have access to a better source of drinking water. WHO approximates that 1.6 million people lose their lives each year from diseases related to water (Dadonaite *et al.*, 2018). The unavailability of safe and clean water is a global concern due to its adverse influence on human health and on ecosystem.

1.2 Sources, hazardous effects, and permissible limits of pollutants

Some inorganic compounds containing Zn, Fe, Cu, Ni, P, F etc., are necessary for the development of both plants and animals but are detrimental when their limits exceed the permitted levels. Most metals, however, are hazardous above certain threshold concentrations. Additionally, several heavy metals including Pb, Hg, Cd, and As are no longer required for the development of plants and animals. The existence of Pb, Hg, and As in trace level contaminate the quality of drinking water (Wimalawansa, 2020).

Heavy metals include metallic species whose specific gravity exceeds 5.0 g/cm^3 and falls in the d block of the periodic table. These heavy metals such as Hg (13.53 g/cm^3), Pb (11.34 g/cm^3), Ni (8.91 g/cm^3), Cd (8.65 g/cm^3), Cu (8.95 g/cm^3), Cr (7.14 g/cm^3), Co (8.90 g/cm^3) are hazardous to human health and the environment (Rai *et al.*, 2021). Despite being present in very small concentrations, a metalloid like As (5.73 g/cm^3) is hazardous (Jaishankar *et al.*, 2014). Industrial operations like mining, metallurgy, iron sheet cleaning, smelting, energy and fuel production, leather working, photography, automobile parts manufacturing, dyeing, textile, fertilizer, and petroleum production, release pollutants into environment (Joseph *et al.*, 2019). Corrosion, industrial waste, agricultural pesticides, and waste disposal are vulnerable sources of heavy metal pollutants in aqueous solution (**Figure 1**).

The prolonged existence of these pollutants even at trace concentration affect environment, animals, and human health (Ali & Khan, 2018). Due to their inability to biodegrade, heavy metals can accumulate in living tissues and result in several diseases and ailments. Consequently, the environment as well as living beings are prone to different damages and disorders like osteoporosis, infertility in women, brain damage, thyroid disorder, cardiovascular diseases, eutrophication, and so on (Desai *et*

al., 2016). They can transform from low-toxin species to highly toxic forms in certain environments. Food chain accumulation of heavy metals could damage the normal physiological function and threaten human life (Vaish *et al.*, 2020).



Figure 1: Sources of heavy metals pollutants (Adapted with permission from Nivetha *et al.*, 2021)

However, excess concentrations of anionic pollutants, such as fluorine in the form of fluoride and phosphorus in the form of phosphate, effect on human physiology, biological systems, water resources, and the environmental quality (Han *et al.*, 2021). The proliferation of anionic pollutants degrades the quality of drinking water. A long-time ingestion of high concentration of fluoride (>1.5 mg/L) causes many health problems such as dental and skeletal fluorosis, lower intelligence in children and bone cancer (Srivastava & Flora, 2020). Excessive inhalation of phosphate in human body leads to renal damage and osteoporosis (Nguyen *et al.*, 2015). Moreover, phosphorus discharged into stagnant water bodies causes algae growth (eutrophication), resulting in dissolved oxygen depletion in the water and affecting aquatic life. (Tiwari & Pal, 2022). The major sources, hazardous effects and permissible limit of F, P, As, Hg, and Pb are presented in **Table 1**.

Table 1: Sources, hazardous effects, and permissible limit of cationic and anionic pollutants

Pollutants	Major sources	Hazardous effects	Permissible limit (WHO)	References
Fluorine	Glass ceramics production, brick and iron works, semiconductor manufacturer, batteries industries, aluminium smelters, industrial effluents, agricultural wastes	Osteoporosis, arthritis, brittle bones, cancer, infertility in women, brain damage, alzheimer's syndrome, thyroid disorder, neurological damage	1.5 mg/L	(Paudyal, <i>et al.</i> , 2012; WHO, 2003)
Phosphorus	Industrial effluents, agricultural run-off, domestic wastes	Cardiovascular and cerebrovascular diseases, eutrophication problems, imbalance in ecosystem	5 mg/L	(Ajmal <i>et al.</i> , 2018; WHO, 2004)
Arsenic	Volcanic emissions, atmospheric deposition, non-ferrous smeltings, petroleum refinings, fossil fuel power plants, gold minings	Black foot disease, skin, liver, and lung cancer, genetic disorder	0.01mg/L	(Verma <i>et al.</i> , 2019; WHO, 2003)
Mercury	Batteries, paints, dyes, fluorescent lamps tubes, fertilizers pharmaceuticals, agricultural chemicals	Neurological disorders, paralysis, blindness, and chromosome breakage	0.006 mg/L	(Fabre <i>et al.</i> , 2020; WHO, 2014)
Lead	Automobile batteries, paints, printing processes, industrial effluents, pigments, fuels, matches, explosives	Mental retardation, kidney disease and anaemia, mental deficiency, insomnia, headache, sterility, stillbirths, neo-natal deaths	0.01mg/L	(Azizul-Rahman <i>et al.</i> , 2013; WHO, 2022)

1.2.1 Fluoride

Fluorine is abundant in the natural environment and can be accumulated in the human body *via* food and water in the form of fluorides. The fluoride content enters water resources due to natural sources like leaching of fluoride bearing rocks and minerals (Nizam *et al.*, 2022). A low concentration of fluoride in water (< 1 mg/L) is beneficial for preventing dental caries and tooth decay (Poza-Pascual *et al.*, 2021). WHO recommends the permissible limit of 1.5 mg/L fluoride in drinkable water (WHO, 2003). However, the fluoride concentration in the range of 0.5-1mg/L, is recommended (Ozsvath, 2006).

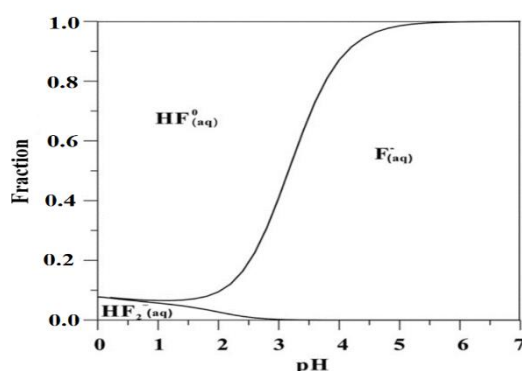


Figure 2: Speciation diagram of various fluoride species at different pH (Adapted with permission from Deng *et al.*, 2011).

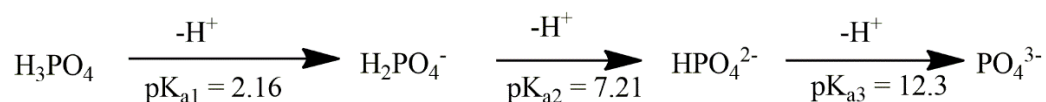
The variation of fluoride speciation with pH of aqueous solution is shown in **Figure 2**. It signifies that fluoride species at $\text{pH} < 3$, are protonated and fluoride ion (F^-) occurs predominantly as the weakly ionizable hydrofluoric acid with small fraction of hydrogen difluoride (HF_2^-) anion (Deng *et al.*, 2011). The fluoride anion (F^-) is ubiquitous at $\text{pH} > 3.0$. At low pH, the biosorption of fluoride ion onto positively charged surface of the biosorbent can occur through coulombic force of attraction. However, fluoride biosorption on the metal loaded biosorbents can take place at moderate pH through ligand exchange mechanism. At higher pH, fluoride ions can compete with hydroxyl ions in the solution for the same binding sites as a result biosorption of fluoride ions can be insignificant.

1.2.2 Phosphates

Phosphorus is one of the essential elements, required for the normal development of many living beings including crops and microorganisms. Its atomic weight, van der

Waal's radius and electronegativity are 30.97 g/mol, 1.95Å, and 2.19 (Pauling scale), respectively (Manna *et al.*, 2022). Phosphorus is commonly present in aqueous solution in the form of inorganic phosphate, organic phosphate, and polyphosphate (Biswas *et al.*, 2008a). Phosphate is the constituents of a component of DNA, RNA, ATP, and phospholipids. It takes part in performing various metabolic reactions (Du *et al.*, 2021). Human and animals waste, food processing effluents, commercial fertilizers, industrial wastewater, agricultural land runoffs, and household detergents discharged phosphates into aquatic environments such as lakes and rivers (Ahmed *et al.*, 2021). The overabundance of phosphates in water stimulate algal growth and other vegetation that consumes so much dissolved oxygen that inadequate amount remains for aquatic life, results eutrophication which is risk for the denizen of water and the whole ecosystem (Tiwari & Pal, 2022). Phosphates discharged into aquatic bodies causes harmful effects in aquatic life (Palansooriya *et al.*, 2021). The recommended phosphates concentration in drinking water is 5 mg/L (WHO, 2004) whereas the United State Environmental Protection Agency (USEPA) set the limit of phosphate as 3 mg/L.

The speciation of phosphate ions relies on the pH of aqueous solution. The existence of orthophosphates species at different pH is displayed in **Figure 3**. The figure showed that tri-protonated species (H_3PO_4) is common at pH below 2.12 whereas H_2PO_4^- and HPO_4^{2-} are common inbetween pH of 2.12 to 7.20 and 7.20 to 12.36, respectively. The de-protonated phosphate species (PO_4^{3-}) is common at pH greater than 12.36 (Chen *et al.*, 2021; Zhang *et al.*, 2021). The biosorption of phosphate species on the biosorbent can be favorable at lower pH due to electrostatic interaction and at moderate pH through ligand exchange mechanism. However, the biosorption of phosphate species at higher pH might be difficult (Wang *et al.*, 2015).



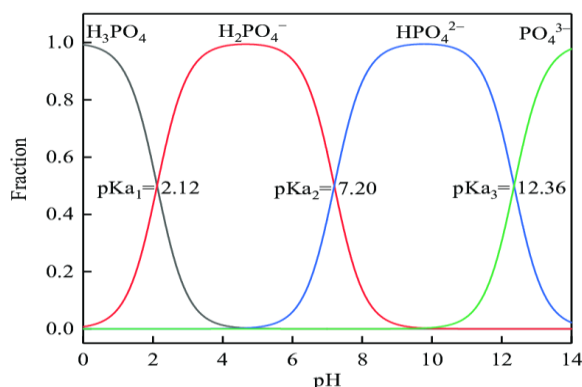


Figure 3: Speciation diagram of phosphorus species at different pH (Adapted with permission from Chen *et al.*, 2021).

1.2.3 Arsenic

In earth crust, arsenic the twentieth abundance element, fourteenth in sea water and twelfth in the human body, has myriad toxic effect in the environment (Alka *et al.*, 2021). Its atomic weight, van der Waal's radius and electronegativity are 74.9 g/mol, 1.81Å and 2.18 (Pauling scale), respectively (Pandey, 2021). Natural processes such as microbial activity, weathering of rocks, volcanic emissions and natural organic materials complexations and anthropogenic activities including metallurgical industries, industrial minings, combustion of fossil fuels, utilization of arsenic contaminated pesticides, and herbicides results arsenic contamination in ground water and surface water. Arsenite (AsO_3^{3-}) and arsenate (AsO_4^{3-}) are the frequently identified inorganic species detected in contaminated water (Navarathna *et al.*, 2020). The chemistry of arsenic depends on the redox potential and pH of the solution (Kumarathilaka *et al.*, 2018). It can exist in the -3, 0, +3 and +5 oxidation states. The +3 and +5 are the most common oxidation state of arsenic (Simon *et al.*, 1999). The trivalent arsenic is prevalent in anaerobic and moderately reducing conditions while pentavalent arsenic exists in aerobic and oxidizing conditions (Ghimire *et al.*, 2002). As(III) is about 60 times more hazardous than As(V) (Samal *et al.*, 2021). As(V) is common arsenic species available in oxygen-rich surface waters while As(III) is more common in ground water. International Agency for Research on Cancer (IARC) has declared Group 1 carcinogens for the compounds of arsenic (Samal *et al.*, 2021). The continuous exposure of arsenic leads to the multitudinous health problems ranging from skin lesions to cancer of liver, kidney, brain, respiratory tract, bladder, cardiovascular effects, pulmonary illnesses, neurological ailments, and reproductive

consequences (Alburaih *et al.*, 2022). Because of toxic nature of arsenic, the USEPA and WHO recommended the maximum contaminant level (MCL) of arsenic in drinking water as 0.01 mg/L (WHO, 2022; Basu *et al.*, 2014) while National drinking water quality standards and directives set out 0.05 mg/L arsenic as its drinking water standard (NDWQS, 2005). The speciation diagram of arsenic with pH of solution is shown in **Figure 4**. As(III) predominantly exists below pH 9.22 as neutral species (pK_{a1} of $H_3AsO_3 = 9.22$) while at pH around 12.13, significantly as anionic species, $H_2AsO_3^-$ and $HAsO_3^{2-}$ ($pK_{a2} = 12.3$) and prevalent at pH higher than 13.4 as AsO_3^{3-} (pK_{a3} of $AsO_3^{3-} = 13.4$) (Mohan & Pittman Jr, 2007; Wood *et al.*, 2002)).

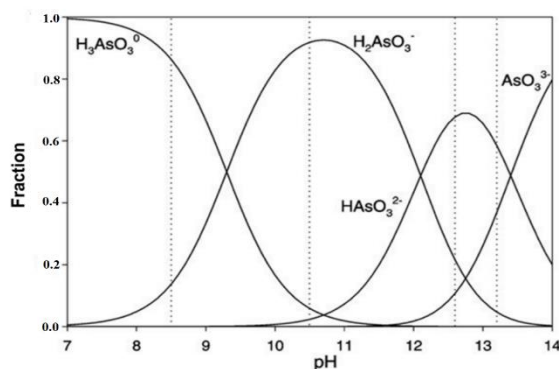
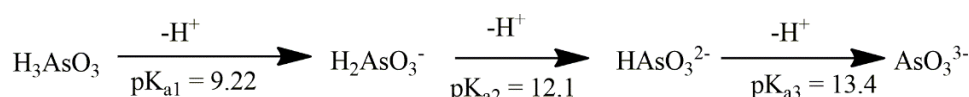


Figure 4: Speciation diagram of arsenic species at different pH (Adapted from Ghimire *et al.*, 2003).

1.2.4 Mercury

Mercury, even at low concentrations, is of specific concern due to its toxicity (Golzadeh *et al.*, 2020). Its atomic weight, van der Waal's radius and electronegativity are 200.6 g/mol, 1.55Å and 2.0, respectively. Mercury is released into the environment *via* natural processes (i.e., volcanic eruptions), anthropogenic activities (i.e., coal burning power plants), breakage or disposal of products that contain mercury (Chalkidis *et al.*, 2020; Pirrone *et al.*, 2010). It can be present in different forms. Organometallic mercury complexes, inorganic mercury salts, and elemental mercury metal all exhibit varying degrees of toxicity. It can have oxidation states +1 and +2. However, +2 is the common oxidation state of mercury.

Inorganic soluble mercury compounds are extremely poisonous. The hazardousness of mercury compounds depends on their solubilities. Hg(I) compounds are less soluble

than Hg(II) compounds. When Hg(II) levels are too high, it can lead to kidney failure, intestine corrosion, and eventually death. The lethal dose of HgCl₂ is 0.5 g while that of elemental mercury is 100 g (Langford *et al.*, 1999). By means of bacterial action involving methyl cobalamin (Vit B-12), less hazardous, insoluble metallic mercury is changed into extremely poisonous, soluble methyl mercury (CH₃Hg⁺) (Khoramzadeh *et al.*, 2013). Being lipophilic by nature, CH₃Hg⁺ enters the food chain and builds up in soft fatty tissues including the liver, kidneys, and central nervous system, where it damages the kidneys and causes blindness, and mental retardation. When mercury vapor is inhaled by the body, it mostly harms the central nervous system (Langford *et al.*, 1999). It readily pass from the bloodstream into the cerebellum and cortex, causing damage which is symphonized by numbness, awkwardness of gait, and blurred vision (Min, 2004). In recent years, Hg contamination has become a major seafood contamination and human health problem. One of the most popular cases of Hg contamination and accumulation in seafood was marked in Minamata Bay, Japan about 65 years ago, and it led severe deaths and illnesses to people who consumed contaminated fish and seafood (Sakamoto *et al.*, 2020). Around 90% of MeHg⁺ in ingested fish is absorbed through the gastro-intestinal tract and then enters to the central nervous system and placenta (Awad *et al.*, 2020). WHO recommends the permissible limit of Hg(II) as 0.006 mg/L (6 µg/L) in drinking water (WHO, 2014) whereas National drinking water quality standards and directives allows 0.001 mg/L of Hg(II) in drinking water (NDWQS, 2005).

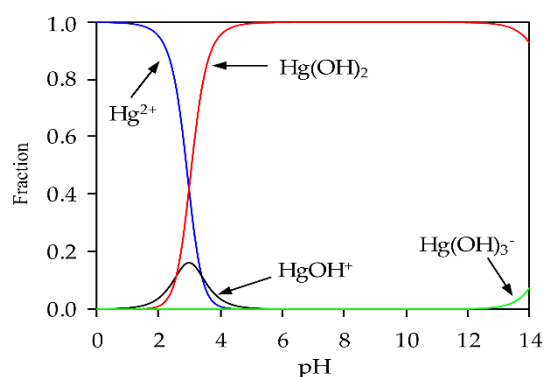


Figure 5: Speciation diagram of mercury species at different pH (Adapted with permission from Ugrina *et al.*, 2020).

The speciation of mercury varies with the solution pH as shown in **Figure 5**. It is evident from the diagram that Hg²⁺ predominantly exists at pH < 2.9 and HgOH⁺

species is prevalent in the pH range of 1.5 to 4.5 while $\text{Hg}(\text{OH})_3^-$ exists at $\text{pH} > 13.2$ (Ugrina *et al.*, 2020). The precipitation of $\text{Hg}(\text{II})$ starts at $\text{pH} = 2.4$ and proportion of $\text{Hg}(\text{OH})_2$ increases with increase in pH. $\text{Hg}(\text{II})$ exists completely in the form of $\text{Hg}(\text{OH})_2$ between pH 4.7 to 13.2. It revealed that biosorption of $\text{Hg}(\text{II})$ would take place in a narrow pH range excluding the effect of precipitation (Spyropoulou *et al.*, 2018).

1.2.5 Lead

Lead is one of the remarkable metals, among the potentially toxic heavy metals. Its atomic weight, van der Waal's radius and electronegativity are 207.2 g/mol, 2.02 and 2.33, respectively (Wang *et al.*, 2020). Mining, smelting, processing of lead generates $\text{Pb}(\text{II})$ in the environment. The incineration of lead containing wastes (industrial and households) and fossil fuels releases $\text{Pb}(\text{II})$ in the atmosphere (Xing *et al.*, 2018). Applications of $\text{Pb}(\text{II})$ compounds as plastics stabilizers, food-can solder, ceramic glazes, crystal glassware, lead-jacketed cables, paints, toys, and cosmetics generate $\text{Pb}(\text{II})$ contamination in the environment (Azizul-Rahman *et al.*, 2013). The prolonged exposure of $\text{Pb}(\text{II})$ even at low levels can also have detrimental consequences on people, aquatic fauna, and livestock (Rahman & Singh, 2019).

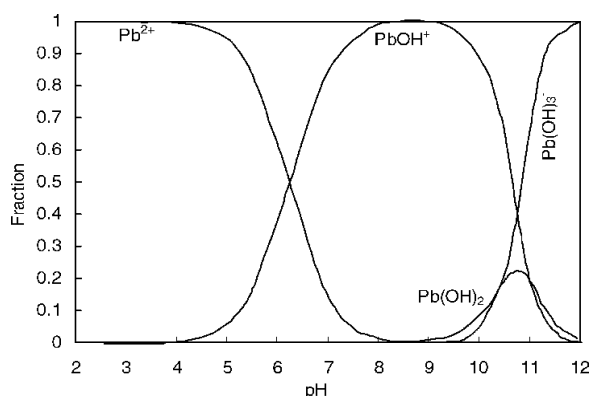


Figure 6: Speciation diagram of lead species at different pH (Adapted with permission from Liang *et al.*, 2007).

Mainly, it exists in divalent state in the aquatic environment. The effect of lead toxicity in humans include hypertension, anemia, brain damage, mental deficiency, cancer in children and behavioral problems in human leading to death in extreme cases (Boskabady *et al.*, 2018). According to WHO, the acceptable limit of $\text{Pb}(\text{II})$ in drinking water is 0.01 mg/L (WHO, 2003). The speciation of lead changes with pH of

aqueous solution as illustrated in **Figure 6**. It showed that lead exists only as Pb(II) species below pH 6. As pH increases, concentration of Pb(II) species significantly diminished whereas concentration of other hydrolytic species such as Pb(OH)^+ , Pb(OH)_2 (aq) and Pb(OH)_3^- are more common. The biosorption of Pb(II) becomes difficult above pH 6, due to increment in hydroxyl species of Pb(II) (Tang *et al.*, 2020; Beiyuan *et al.*, 2020).

1.3 Conventional technologies for the separation of cationic and anionic pollutants

The commonly employed technologies for the separation of F^- , PO_4^{3-} , As(III), Pb(II) and Hg(II) from aqueous solution are chemical precipitation, ion exchange, electro-winning, electro-coagulation, solvent extraction, evaporation, reverse osmosis and electrodialysis (Lau & Yong, 2021; Fatima & Kommalapati, 2021; Joo & Tansel, 2015). Low cost and easy operating technologies are attracting attention of researchers to remove F^- , PO_4^{3-} , As(III), Pb(II) and Hg(II). The brief introduction of the technologies and their complications in separation process is discussed below.

1.3.1 Chemical precipitation

The chemical precipitation is the effective technique to uptake ionic pollutants from aqueous solution (Guimaraes *et al.*, 2020). It is applicable to remove higher concentration of anionic pollutants like fluoride, cyanides and phosphates present in the solution. The suitable counter ions added in the solution reduce the solubility of the substance as a result precipitation takes place (Nikolenko *et al.*, 2020). Lime, aluminum sulphate and caustic soda are common precipitants used to precipitate pollutants in the form of hydroxides and sulphates (Saleh *et al.*, 2022). In this process, the heavy metals present in water are treated with the precipitants, to form insoluble precipitates. Fluoride can be precipitated using calcium and aluminium salts. However, the fluctuations in pH, hinders the separation of pollutants (Biswal *et al.*, 2018). Generally, heavy metals are precipitated in the form of hydroxides and sulfides (Zainuddin *et al.*, 2019). However, the process creates post-treatment and sludge management problem (Richards *et al.*, 2021).

1.3.2 Ion exchange

Ion exchange is a reversible process where substitution of ions takes place between the adsorbent and the solution. It takes place with the replacement of unwanted ions of solution with ions of solid material where the ions are sufficiently mobile (Dey *et al.*, 2021). The ion exchange process is affected by diffusional resistances of ions into and out of the solid particles as well as resistance to external surface diffusion. The concentration of the ions, solution pH and nature of exchangers play significant role in ion exchange process (Van der Bruggen, 2018). Inorganic three-dimensional matrix, new-generation hybrid materials, and synthetic organic resins are examples of matrices frequently utilized for ion-exchange materials. Natural and synthetic resins are broadly in practice as cationic and anionic exchangers for the treatment of wastewater. However, they are not appropriate to handle with concentrated metal solution which gets easily fouled from organic resins and other dissolved solids. The process is relatively costly, selective, incomplete and can even lower the pH of treated water. The existence of co-ions such as sulphate, chlorides, hydroxides, bicarbonates and phosphates in the wastewater results ionic competition that inhibit removal process (Jiang *et al.*, 2021).

1.3.3 Electrowinning

Electrochemistry, particularly electrochemical engineering plays a key role in the pollution abatement based on sustainability principles (He *et al.*, 2022). The electrochemical reactor can remove metal ions from effluents with a very low concentration of metal in the exit stream (Razzak *et al.*, 2022). Electrowinning is a process applicable to recover heavy metals such as Au(III), Ag(I), Zn(II), and Cu(II) from the solution due to applied electric potential in an electrolytic cell. When electric current is passed through the solution, addition of electron takes place so that metal ions convert into solid metal. The targeted metal ion can be electrodeposited from the aqueous solution (Barragan *et al.*, 2020). However, strongly acidic solutions can cause the cell to corrode, the process is risky, and appropriate cathode/anode electrodes should be kept for high current efficiency and metal deposition. It has high cost during installation and maintenance (Liu *et al.*, 2021).

1.3.4 Coagulation and flocculation

Coagulation is the process of adding chemicals such as $KAl(SO_4)_2 \cdot 12H_2O$, $MgCl_2$, polyaluminium chloride (PAC), and $Al(OH)_3/Al_2O_3$ into water (Abujazar *et al.*, 2022). These chemicals referred as coagulants, have positive/ negative charges (Sinha *et al.*, 2004). The positive/ negative charge of the coagulant neutralizes with the charge of dissolved and suspended particles into large aggregates. pH must be frequently controlled for the effective coagulation (Zamora-Ledezma *et al.*, 2021). However, coagulation is inefficient, produces high volumes of toxic sludge, low removal, readjustment of pH and required further treatment before disposal (Cai *et al.*, 2020).

Flocculation is a commonly applied technique to uptake heavy metals from contaminated water (Sun *et al.*, 2020). During the process, flocs bind the particles and forms the bridges in between flocculant and pollutant ions convert it into large agglomerates. Sodium dodecyl sulphate and polyferric sulphate are being used as flocculants in the treatment of wastewater (Shen *et al.*, 2015). However, flocculating agents produce large volumes of metallic floc, which must be disposed in a proper way. It added significant costs during disposal.

1.3.5 Membrane processes

The membranes practiced for the uptake of pollutants from aqueous solution are microfiltration (MF), ultrafiltration (UF), nanofiltration (NF), and reverse osmosis (RO) (Lau & Yong, 2021). MF has porous, symmetric, or asymmetric membrane can be applicable to retain bacteria, fat, oil, grease, colloids and microparticles (Fatima *et al.*, 2021). UF has microporous, asymmetric membrane applicable to retain proteins, pigments, oils, sugars, microplastics (Algieri *et al.*, 2021). NF has tight porous, asymmetric, thin film composite suitable to retain all contaminants including monovalent ions (Zheng *et al.*, 2022). Among the pressure driven membrane processes, RO is highly known for its efficiency in separating small particles including bacteria and monovalent ions like sodium ions and chloride ions up to 99.5%. Although, these processes have high removal efficiency, they require high investment for their establishment and operation. Researchers must develop alternate

methods for treating wastewater because membrane technologies are susceptible to membrane fouling and also requires high operating pressures (Tetteh *et al.*, 2019).

1.3.6 Electrodialysis

Electrodialysis (ED) and electro-dialysis reversal (EDR) are processes uses electricity and ion-permeable membranes to separate dissolved ions from water (Obotey Ezugbe & Rathilal, 2020). When electric current is passed through the system, ions from the dilute migrate into the concentrate ones through oppositely charged membranes *i.e.*, cations migrate to the cathode while anions migrate to the anode. The cations are retained by the positively charged anion exchange membrane (AEM). Likewise, anions are retained by the cation exchange membrane (CEM) (Mudau *et al.*, 2022). However, the process is costly, release of toxic wastewater and management of concentrated effluent is problematic.

1.3.7 Adsorption

Adsorption is the selective physio-chemical treatment processes for the sequestration of pollutants from aqueous solutions. In adsorption, a solid surface in contact with the solution has the capacity to accumulate solute molecules on the interface of the adsorbents (Zhou *et al.*, 2016). Adsorbent is the material where the adsorption occurs on, and adsorbate is the substance that is adsorbed. It is a mass transfer process used to remediate wastewater, moving mass from the wastewater's liquid phase to the adsorbent solid surface The process of adhering a single or a group of atoms, ions, or molecules to the surface of another solid or liquid is known as adsorption (Segura *et al.*, 2013). It is an economically viable alternative to conventional techniques for removing cationic and anionic pollutants from aqueous solution. It occurs commonly in industrial applications and can be found in several natural, physical, biological, and chemical systems. Adsorbents including activated carbon, activated zeolite, activated alumina, silica gel, various synthesized adsorbents, and different modified natural materials, such as chitosan, are often used during treatment of water (Yang *et al.*, 2022; Crini *et al.*, 2019; Zanella *et al.*, 2014). A widely used adsorbent to remove heavy metals is activated carbon. An activated carbon matrix is characterized by well-developed pores and a large internal surface area for adsorption. Any material with a high carbon content, such as agricultural wastes or industrial wastes, can be used to produce activated carbon. It has long been regarded as a superior method of treating

industrial pollutants due to its many benefits over conventional methods, particularly from an economic and environmental standpoint. These benefits include its low-cost, availability, profitability, ease of operation, and efficiency nevertheless, it is relatively non-selective and expensive (Lewoyehu, 2021). Based on the strength of the attraction between the adsorbent and adsorbate, the adsorption process is classified into physical adsorption and chemical adsorption.

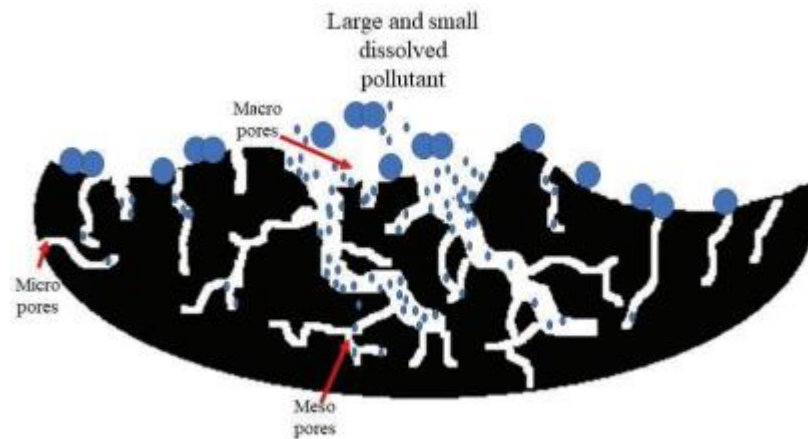


Figure 7: Adsorption process (Adapted with permission from Shamsudin & Ismail, 2019)

Physical adsorption, also referred as van der Waals' adsorption, takes place due to the van der Waals force of interaction. It is a reversible process. It takes place below or near the critical temperature of the material being adsorbed. The heat of physical adsorption is on the range of 20-40 kJ/mol. Physical adsorption is an exothermic process that results in decrease in free energy of the adsorption system. In chemical adsorption, the adsorbate and the adsorbent surface interact chemically and electrostatically. The heat of adsorption in this technique normally varies from 40 to 400 kJ/mol. It is also known as activated adsorption because it possesses high activation energy. The chemical adsorption is irreversible phenomena which takes place between adsorbent and adsorbate molecules due to electrostatic interaction. Chemical adsorption includes either electron transfer or sharing, or the formation of chemical bonds between molecules (Saleh *et al.*, 2022).

Unlike physical adsorption, chemisorption takes place on a specific solid surface for a given fluid and happens at temperatures substantially higher than the critical temperature.

1.4 Biosorption

Biosorption is the property of biologically originated materials to bind and concentrate biosorbate from aqueous solution even at very low concentrations. From an environmental standpoint, biosorption is potential and a viable substitute for the conventional techniques for the uptake and/recovery of toxic metals and non-metals from water. Biosorbents derived from natural or agricultural waste, have attracted a lot of attention in the last few years. Agricultural waste products such as orange peels, sugarcane bagasse, pomegranate peels, watermelon rind, banana peels, pomelo peels and so forth include cellulose, pectin, and lignin, along with hemicellulose, fat, protein, water, ash, and many other substances (Detroy & Hesseltine, 1978). Cellulose is a polysaccharide made of a linear chain of several hundred to 135000 linked D-glucose units (Brummer *et al.*, 2008). It contains hydroxyl groups. This group can form complexes with both non-metals and metals (Ghimire *et al.*, 2007). The amount and accessibility of functional groups on the biosorbent surface are crucial for the biosorption process thus, altering the surface properties can have a significant effect on the biosorbent's capacity to eliminate pollutants. The utilization of naturally occurring or locally available agricultural wastes as biosorbents for the uptake of cationic and anionic pollutant from wastewater is cost-effective and contributes to a zero-waste environment. It is an economically sound approach to utilize low-cost materials as biosorbents.

It is an excellent alternative, in terms of low production cost of biosorbents, ease of operation, high biosorption capacity, high efficiency, improved selectivity for metal ions of interest, short operation time, no generation of secondary refractory wastes, easy treatment of spent biosorbents by incineration and possibility of regeneration cycles and so forth (Reshmy *et al.*, 2022).

1.5 Biosorbents: Watermelon rinds and Banana peels

Watermelon is a member of the *Cucurbitaceae* family, which includes both seeded and seedless variations species. Its binomial name is *Citrullus lanatus* (Erhirhie & Ekene, 2013). It is huge edible fruits which have a tough green exterior and a watery reddish, yellowish, or pink juicy pulp that make it so popular (**Figure 9**). It is an important agricultural product that is used to make several food items, including fruit juices, nectars, and cocktails. The pulp of the watermelon is most advantageous

component due to the presence of anti-nutrients saponin, alkaloids, hydrogen cyanide, tannins, phytate, phenol, oxalate, and flavonoids in significant amounts (Bhattacharjee *et al.*, 2020). A natural supply of citrulline ($C_6H_{13}N_3O_3$), a non-essential amino acid, as well as carotenoids, cellulose, pectin, and protein has also been reported to exist in an agricultural waste product of watermelon (Shakoor *et al.*, 2018).

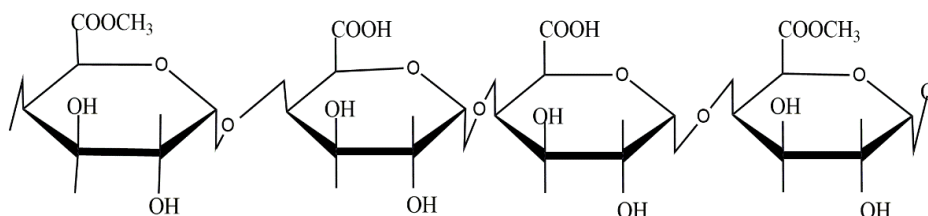


Figure 8: Chemical structure of pectin



Figure 9: Photographs of watermelon fruit and dried watermelon rinds

These compounds have aromatic rings along with heteroatoms (N, O) which are expected to be the centers for biosorption. These types of polymers possess functional groups such as $-COOH$, $-OH$, and $-(NH_2)$. **Figure 8** is the structure of pectin existed in watermelon rind (Petkowicz *et al.*, 2017).

Banana plants belong to Musaceae family. Its binomial name is *Musa paradisiaca* (Pereira & Maraschin, 2015). Banana plants are normally tall and sturdy. Commonly, they are cultivated for their fruits but to a small extent to produce fiber. The banana fruits develop from the banana heart, comprising 3-20 tiers hanging in a cluster. The hanging cluster is known as a bunch. The bunches of green bananas which when ripened turns yellow as in **Figure 10**.

It is one of the largest consumed fruits in the world and its year-round availability create a huge quantity of agro-waste problems due to useless peels. Banana peels

contain cellulose (7.6 - 9.6%), hemicellulose (6.4 - 9.4%), pectin (10 - 21%), proteins (10.2 - 12.1%) and lignin associated with hydroxyl, carboxyl, carbonyl, and amine groups (Thomas *et al.*, 2021; Emaga *et al.*, 2008). The existence of hydroxyl and methylated esterified groups of pectin cellulose in biosorbent cell wall can be appropriate for high biosorption capacity (Aryal *et al.*, 2021).



Figure 10: Photograph of banana fruits and banana peels

1.6 Biosorption mechanism

Biosorption is the process of biosorbents to rapidly bind cationic and anionic pollutants even at a low concentration from aqueous solutions through interaction of pollutants on the biosorbent surface by physical and chemical mechanism (Volesky, 2007). The functional groups associated on the surface of the biosorbents are responsible for binding. Chemisorption, physisorption, microprecipitation, and oxidation/reduction are the four basic mechanisms that make up biosorption (Veglio & Beolchini, 1997). Multiple mechanisms may occasionally operate simultaneously during biosorption due to the complexity of the process (Gadd, 2009). Ion exchange, chelation, and complexation or coordination are all components of chemisorption, whereas van der Waals forces and electrostatic interaction are components of physisorption. In chemisorption, surface functional groups are crucial for binding the biosorbate (Vijayaraghavan & Balasubramanian, 2015). Ion exchange is a reversible process occurs through electrostatic interactions between the cations in the solution and negatively charged groups in the cell walls of the biosorbent (Abdolali *et al.*, 2014). Chelation involves the development of a chelate ring structure due to the association of a ligand with cationic pollutants.

Complexation is the phenomena of the uptake of pollutants by creating a complex compound on the surface of the biosorbent with the active sites of the cell wall. Complexation involves covalent, electrostatic, or both types of bonds, and the compounds can have any charges, either neutral, negative, or positive (Srivastava and Goyal, 2010). However, during micro-precipitation, insoluble inorganic-metal/organic-metal precipitates are formed due to interactions between the biosorbate and the biosorbent surface (Naja & Volesky, 2011). After interacting with the functional groups in the biosorbent, metal ion undergoes reduction biosorption. The metal first binds to a specific location in two-step process, which serves as a nucleation point. Then the reduction occurs (Das, 2010).

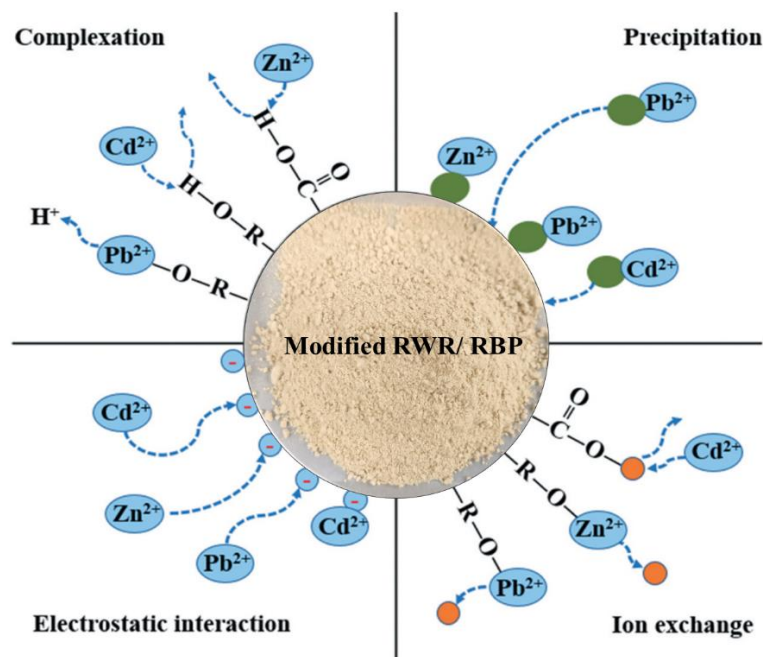


Figure 11: Biosorption mechanism (Adapted with permission from Singh *et al.*, 2020)

Metal ion characteristics (ionic size, oxidation state, molecular weight), biosorbent characteristics (porosity, surface area) and controlling parameters (pH, dosage, temperature) affect biosorption. Moreover, It is also influenced by the number of active sites, chemical state of the sites and affinity between the sites and targeted ions as a results of electrostatic interaction (Sivakumar & Lee, 2022).

1.7 Batch biosorption studies

Batch biosorption studies are used to analyze the biosorbent performance in biosorption process. This investigation is useful to know the optimum parameters to

obtain the maximum biosorption capacity of biosorbents. The analysis of these parameters can withdraw the reaction pathway and mechanism of biosorption process.

The biosorption capacity of synthesized biosorbents is studied by altering all the parameters like solution pH, dosage of biosorbents, contact times, initial concentration of ions in the solution, and so on. The effect of one parameter is analyzed by keeping other parameters constant. In the batch biosorption study, a predetermined mass of biosorbent was equilibrated with specified volume of solution containing different concentration of biosorbates in a rotatory incubator shaker for 24 h at optimum pH. The initial concentration of biosorbate and after biosorption the centrifuged residual concentration is measured. The following mass balance relationships is used in all analysis to determine the quantity of biosorbate biosorbed per one gram of biosorbent, q_e , (mg/g), and the biosorption efficiency (A %), (Vijila *et al.*, 2021)

$$q_e = \frac{(C_i - C_r)V}{m} \quad (1)$$

$$A (\%) = \frac{(C_i - C_r)}{C_i} \times 100 \quad (2)$$

where, C_i is initial concentration and C_r is residual concentration of biosorbate in the solution (mg/L), V denotes volume of biosorbate solution (in L) and m is the mass of biosorbent (g).

1.8 Factors influencing biosorption

The various factors such as solution pH, contact times, initial concentration of biosorbate ions and biosorbent dosage plays a significant role for the efficacy of biosorption process.

1.8.1 pH of solution

The pH is a fundamental parameter during biosorption experiments. The degree of ionization of surface functional groups associated with biosorbents depends on pH. The biosorption capacity is varied with pH because varying pH directly alters the surface charge density of the biosorbents and also changes the biosorbate chemistry in the solution (Wang *et al.*, 2018). Generally, the biosorption of cationic pollutants increases with increase in pH of the solution. As pH rises, there are more negatively

charged surface groups, which improves the biosorption ability of cationic pollutants. But, when pH lowered, increase in positively charged surface of biosorbents creates favorable sites for the biosorption of anionic pollutants. At highly acidic conditions, due to protonation, the overall surface charge of biosorbent becomes positive which prevent metal cations from accessing on the surface functional groups due to repulsion (Maksoud *et al.*, 2020). At highly alkaline pH, metal ion causes metal complex insolubility, permitting precipitation which create the estimation of biosorption process more difficult (Pohl, 2020). In addition, at strongly alkaline pH, the biosorption of anionic pollutants is also unfavorable due to competition of OH⁻ of solution with anionic pollutants for the same biosorption sites (Fang *et al.*, 2014).

1.8.2 Contact times

The equilibration time for the biosorption of pollutants onto the biosorbents is crucial. The biosorbate molecule can interact onto biosorbent surface through physiosorption or chemiosorption or both with lapse of time. The biosorption rate with initial contact times increases due to participation of specific functional groups and active surface sites of biosorbents (Kayranli *et al.*, 2021). The biosorption rate is a function of number of vacant biosorption sites. It is conceivable to assume that during the biosorbate biosorption process in starting phase, there is a substantial number of empty sites available, which led rise in the biosorption rate, however at equilibrium, all the vacant sites were consecutively occupied. The biosorption capacity attains equilibrium after certain interval of time. The experimental data of biosorption process at equilibration time can be computed to kinetic models to evaluate the biosorption rate and reaction pathways.

1.8.3 Initial concentration of biosorbate

The biosorption process is influenced with the initial concentration of biosorbate molecules. The starting concentration gives a significant driving force in overcoming the mass transfer hindrance between solid/liquid interface. For a fixed mass of biosorbent, the biosorption capacity increases with low initial concentration of biosorbates. The biosorption capacity of biosorbents decreases with increase in initial concentration of cationic and anionic pollutants however, the quantity of biosorbed pollutants increases per gram of the biosorbent. The decrease in biosorption capacity

is due to limited binding sites on the biosorbent surface with gradual increase in initial concentration (Ji *et al.*, 2019). To elucidate the interaction between the biosorbate molecules, biosorbent and biosorption mechanism, the experimental data of initial concentration can be applied to isotherm models.

1.8.4 Biosorbent dosages

Biosorbent dosage is one of the significant factors during biosorption process. The biosorption capacity of biosorbent increases for the limited increment in biosorbent dose. The increment in biosorption capacity is because of vacant binding sites onto the biosorbents. However, the increase in biosorbent dosages may aggregates and cover the unoccupied binding sites as a result biosorption capacity can be diminished (Verma *et al.*, 2019).

1.8.5 Effect of co-existing ions

Various co-existing ions are associated in natural/contaminated water. The existence of coexisting ions in natural/contaminated water may cause interference during biosorption for adhering on the biosorption sites. Coexisting-ions can compete for a finite number of active biosorption sites with the biosorbate, which alters the biosorption capacity of the biosorbent. The concentration of co-existing ions affects the electrostatic interaction which can cause particle aggregation. The biosorption capacity of biosorbent can either increase or decrease in existence of co-existing ions in water. (Paudyal *et al.*, 2020). The knowledge of influence of co-existing ions is fruitful to optimize the biosorption process.

1.9 Modeling of biosorption data

1.9.1 Modeling of kinetic data

The analysis of biosorption kinetics is crucial to insight the reaction pathways, biosorption rate and biosorption mechanism. Various system conditions and biosorbate biosorbent interactions affect biosorption kinetics. The biosorption mechanism relies on the physical structures and chemical property of the biosorbent and on the mass transfer process (Blazquez *et al.*, 2014). To analyze the kinetic biosorption mechanism, two kinetic models were applied and simulate the biosorption kinetics of fluoride, phosphate, As(III), Hg(II) and Pb(II) onto investigated biosorbents. The PFO

kinetics model and PSO kinetics model are the simplest models for elucidating the biosorption reactions (Ho & McKay, 1998; Lagergren, 1898).

1.9.1.1 Pseudo first order (PFO) model

Lagergren 1898, demonstrated the first order rate equation for the adsorption of oxalic acid and malonic acid onto charcoal. In his kinetic equation, Lagergren describes the adsorption of liquid-solid systems based on adsorption capacity of adsorbents in solid phase. Lagergren named first order rate equation as PFO rate equation which relates for adsorption capacity of adsorbents in adsorption process. It is valid only for the initial stage of biosorption process. The PFO is unable to predict the experimental data satisfactorily for longer times. The non-linear form of PFO is indicated as,

$$q_t = q_e(1 - e^{-k_1 t}) \quad (3)$$

The equation (3) is rearranged into linear form as

$$\log(q_e - q_t) = \log q_e - \frac{k_1}{2.303} t \quad (4)$$

where, 'q_e' and 'q_t' are the quantities of biosorbate biosorbed per unit weight of the biosorbent (mg/g) at equilibrium and at time 't'. The PFO rate constant 'k₁'(1/min) and 'q_e' can be computed from the slope and intercept of the plot log(q_e - q_t) against 't'.

1.9.1.2 Pseudo second order (PSO) kinetic model

Recent studies have shown that PSO rates are effective for the adsorption of pollutants from aqueous solutions. In contrast to PFO model, it is always effective with experimental data. PSO rate expressions are used to describe the rate limiting step may be chemisorption that comprises valency forces due to electron sharing between biosorbents and biosorbates (Ho & McKay, 1998; Blanchard *et al.*, 1984).

The non-linear form of PSO model can be rearranged as,

$$q_t = \frac{q_e^2 k_2 t}{q_e k_2 t + 1} \quad (5)$$

The equation (5) is rearranged into linearized form as,

$$\frac{t}{q_t} = \frac{1}{k_2 q_e^2} + \frac{1}{q_e} t \quad (6)$$

where 'k₂' is the PSO rate constant (g/(mg min)). A plot of 't/q_t' against 't' produces a straight line from the plot by which values of 'q_e' and 'k₂' can be evaluated using slope and intercept, respectively.

1.10 Modeling of isotherm data

Biosorption isotherm study is the relation between the equilibrium concentration of biosorbate in solution at constant temperature (C_e) and the amount of biosorbate per one gram of biosorbent q_e (mg/g). The biosorption isotherm is significant to analyze how biosorbate interacts with the biosorbents to optimize the biomaterials. Langmuir isotherm model and Freundlich isotherm model are the two most used biosorption isotherms to explain the connection of biosorbate with the biosorbent in biosorption. These isotherm parameters give information about surface properties, affinity of binding sites of biosorbents as well as biosorption mechanism.

1.10.1 Langmuir isotherm model

The Langmuir model assumes that all biosorbent sites have equal affinities, resulting in homogeneous monolayer biosorption. It indicates chemisorption on a set of well-defined localized biosorption sites having constant binding energies. There is independent surface coverage by biosorbates without interaction between biosorbed molecules in biosorbents.

The nonlinear form of the Langmuir isotherm model is represented by the following equation (Langmuir, 1918):

$$q_e = \frac{q_m b C_e}{1 + b C_e} \quad (7)$$

The Langmuir isotherm equation can be represented in its linear form as,

$$\frac{C_e}{q_e} = \frac{1}{q_{max} b} + \frac{C_e}{q_{max}} \quad (8)$$

where, 'C_e'(mg/L) and 'q_e'(mg/g) are the concentration and biosorption capability at equilibrium, 'q_m' is the maximum biosorption capability at monolayer coverage (mg/g), and 'b' is Langmuir constant related to equilibrium constant (L/mg). The variables 'q_m' and 'b', were determined from the slope and intercept of the straight-line plot of C_e/q_e against C_e.

Another important and effective parameter that characterizes Langmuir equation is R_L , a dimensionless constant separation factor, is also the indicator of the biosorption capacity can be determined from the equation as,

$$R_L = \frac{1}{1 + b.C_i} \quad (9)$$

where, 'b' stands for Langmuir equilibrium constant (L/mg) related to the affinity of binding sites and free energy of biosorption and 'C_i' denotes the initial concentration of biosorbate in the solution. The biosorption process is considered favorable when $0 < R_L < 1$ and unfavorable $R_L > 1$ (Weber & Chakravorti, 1974).

1.10.2 Freundlich isotherm model

The Freundlich isotherm model predicted that biosorbate would adhere in several layers to diverse biosorbent surfaces, with the binding sites receiving uneven amounts of energy. This isotherm implies that the biosorbent surface won't be saturated and there will be infinite surface coverage, which indicates physisorption.

The Freundlich isotherm non-linear equation is expressed as (Freundlich, 1906),

$$q_e = K_F C_e^{1/n} \quad (10)$$

Taking natural logarithm on equation (10), the linear equation is,

$$\log q_e = \log K_F + \frac{1}{n} \log C_e \quad (11)$$

where, 'C_e'(mg/L) and 'q_e'(mg/g) are the concentration and biosorption capability at equilibrium and 'K_F' is Freundlich biosorption constant (mg/g) (L/mg)^{1/n} denotes the maximum biosorption capability of biosorbent and '1/n' is a dimensionless heterogeneity of biosorbent. The biosorption process is taken more favorable when 1/n values are in the range of 0.1 to 1 (Shi, *et al.*, 2009). A plot of log q_e against log C_e should give a straight line from which '1/n' and 'K_F' can be evaluated. The slope equals to '1/n' and intercept equals to log K_F. The biosorption process is favorable when 1/n is $0 < 1/n < 1$ and unfavorable $1/n > 1$ (Ren *et al.*, 2018).

1.11 Thermodynamics studies

Biosorption is influenced with the temperature of the solution. It usually affects the stability of the metal biosorbent complexes and the ionization of the cell wall moieties

that affect the interaction between biosorbents and biosorbates. It is vital to investigate the thermodynamic parameters of the biosorption system for determining spontaneity, feasibility, and nature of the biosorption process. A Langmuir isotherm model is used to determine experimental equilibrium parameter (b) for different temperatures. Equation (12) relates the dimensionless thermodynamic equilibrium constant (k_C) with the Langmuir equilibrium parameters (b, L/mg) when the biosorption experiment is carried out in aqueous medium. The k_C can be evaluated as a dimensionless parameter multiplying 'b' by 55.5 and then 1000.

$$k_C = b \times 55.5 \times 1000 \times M_w \quad (12)$$

Where, ' M_w ' is the molecular weight of biosorbate, and 55.5 is the molar concentration of pure water (~ dividing 1000 g/L by 18 g/mol) and the term $55.5 \times 1000 \times b$ is dimensionless ((Tran *et al.*, 2016; Zhou & Zhou 2014; Milonjic, 2007).

The change in Gibbs free energy (ΔG°) associated with the biosorption process can be computed by the following equation,

$$\Delta G^\circ = -RT \ln k_C \quad (13)$$

where, ' R ' is universal gas constant (8.314 J/mol. K), ' T ' is the absolute temperature (K), and ' k_C ' is the equilibrium constant. The Gibbs free energy change (ΔG^0), enthalpy change (ΔH^0) and entropy change (ΔS^0) during biosorption at a given temperature can be analyzed from the equation as,

$$\Delta G^\circ = \Delta H^\circ - T\Delta S^\circ \quad (14)$$

Thus,

$$\ln K_C = -\frac{\Delta H^\circ}{RT} + \frac{\Delta S^\circ}{R} \quad (15)$$

The plot of $\ln K_C$ against $1/T$ according to equation (15) using the slope and intercept, ' ΔH^0 ' and ' ΔS^0 ' can be computed. The value of ' ΔG^0 ' can be calculated from equation (13) at different temperature studied. The negative values of ' ΔG^0 ' predicts the spontaneity of the biosorption process (Tran *et al.*, 2016).

1.12 Determination of distribution coefficient

Distribution coefficient (K_D), is represented as the ratio of biosorbate concentration biosorbed onto biosorbent (mg/g) to residual concentration in agitated solution in mg/L. It signifies the binding capacity of the biosorbent to trap the biosorbate. The greater value of K_D signifies the distribution of biosorbate effectively on the solid surface. It is calculated from the equation as,

$$K_D = \frac{C_i - C_r}{C_r} \times \frac{V}{M} = \frac{q_e}{C_r} \quad (16)$$

where C_i (mg/L), C_r (mg/L), V (L), M (g), and q_e (mg/g), respectively are initial concentration, residual concentration, volume of biosorbate solution, mass of biosorbent and amount of biosorbate biosorbed.

1.13 Desorption studies

Treatment by biosorption technology is economical since the exhausted biosorbent material can be regenerated. The regeneration of biosorbent is the advantageous part of the biosorption process. From the environmental point of view, reduce, recycle and reuse are the slogans to save environment. The desorption studies are performed onto loaded biosorbents using different molar concentration of suitable desorbing agents.

The desorption efficiency (% D) can be calculated from the following equation (Aryal *et al.*, 2021).

$$\% D = \frac{A_d}{A_b} \times 100 \quad (17)$$

where A_d and A_b are the total amount of biosorbate desorbed and biosorbed in mg/g, respectively.

1.14 Regeneration and reusability studies

The regeneration and reusability studies are the outstanding characteristics of biosorption process utilizing agricultural waste. The use of low-cost, easily prepared biosorbents after biosorption can be desorbed using desorbing agents. The efficiency of the biosorbents can be examined with optimum concentration of desorbing agent tested in desorption studies. The biosorption and desorption cycles for the same

investigated biosorbents can be tested for number of cycles and percentage efficiency can be evaluated.

1.15 Characterization of biosorbents

To understand the physical behavior and chemical orientation of the synthesized biosorbents, different characterization techniques were operated. The characterization methods employed in the current investigation were helpful to analyze the investigated biosorbents and their efficacy during biosorption.

1.15.1 Fourier transform infrared (FTIR) spectroscopy

FTIR spectroscopy is an effective analytical technique operated for the detection of functional groups and characterizing covalent bonding formation. It is a technique based on the determination of the interaction between an IR radiation for a sample that can be solid, liquid or gases. It measures in terms of wave number at which the sample absorbs and signalled the intensities of absorption. The frequencies are helpful for the identification of the biosorbents functional groups responsible for the absorption of radiation at different frequency ranges. It examines the different functional groups like carboxyl, amino, amide, hydroxyl, carbonyl, ether, ester, and characterizing covalent bonding formation on the surface of adsorbents. The structural changes in the adsorption process can be determined by FTIR analysis.

1.15.2 Scanning electron microscopic (FE-SEM) analysis

This type of electron microscope can scan objects with a focused beam of incredibly intense electrons to provide images of in-focus structures. The sample's electrons interact with its atoms to produce a variety of signals that reveal information about the shape and structures of the sample surface. The direction of the electron beam is linked with the detected scatter signal to produce a picture as it scans in a manner like raster. A SEM induces a variety of signals when materials are exposed to electron beams. Although all scanning electron microscopes are equipped with extra electron detectors, it is improbable that a single setup will be able to detect every possible signal. As the beam strikes a surface at different angles, the amount of extra electrons changes. No secondary electrons are released when the sample is on a smooth surface. The secondary electrons escape even more when it is on the inclined surface. In SEM experiments, a vacuum-like environment is used. Until they are examined in a SEM,

nonconducting samples are often covered with a conductive coating. In this study, SEM analysis was operated to examine the morphology of the biosorbents surface.

1.15.3 Energy dispersive X-ray (EDX) spectroscopy

EDX can detect X-rays from all the elements above atomic number 4. It gives quantitative compositional analysis in the reflection mode from solid surface together with the morphological imaging of SEM. Almost any material can yield a spectrum if it can be placed on the microscope's specimen stage. Although, the X-ray generation volume relies on the electron range in the material, the type of sample being studied should be taken into consideration when choosing an accelerating voltage. Spectrum acquisition, elemental line scans, and spatial distribution, or dot, mapping of the elements are the three generally utilized ways of analysis. EDX spectra analyze the elemental composition on the surface of biosorbents.

1.15.4 X-ray diffraction (XRD) analysis

The study of crystal structures and atomic spacing is frequently conducted using X-ray diffraction. The fundamental principle of X-ray diffraction is the constructive interference of monochromatic X-rays with a crystalline material. These X-rays are produced using a cathode ray tube filtered to produce monochromatic radiation, collimated to concentrate, and directed to the material. In situations where Bragg's law is met, the interaction of the incident rays with the sample results in constructive interference. This rule connects the diffraction angle and lattice spacing in a crystalline sample to the wavelength of electromagnetic radiation. Then, these diffracted X-rays are detected, analyzed, and counted. It was performed to analyze the crystalline property, particle size and structure of biosorbents.

1.15.5 X-ray photoelectron spectroscopic (XPS) analysis

XPS is a quantitative technique for screening the elemental composition present on the biosorbent surface. It is sensitive to elements as well as their valence states. The sample was exposed to low-energy (mono-energetic) X-rays for the purpose of surface examination. The basis for XPS analysis is the fact that every element has a distinct set of binding energy. As a result, it is possible to identify and calculate the element concentration at the surface. Due to changes in the chemical potential and polarizability of compounds, the binding energy of elements fluctuates (the chemical

shifts). These shifts lead to the identification of chemical state of the material under investigation.

1.15.6 Zetapotential analysis

Zeta potential is a common characterization technique to assess sample surfaces and is frequently used to approximate a surface charge, such as positive, negative, or neutral character. Zeta potential measurements offer broad findings concerning the nature of surface charge. The zeta potential analyzer examined the surface charge of the biosorbent. The better biosorption of cation/anion can be predicted based on the point of zero charge.

1.16 Rationale of the study

Water contamination is the major environmental problem around the globe including Nepal. Numerous conventional methods have been adopted to treat contaminated water such as membrane filtration, ion exchange, precipitation, coagulation, adsorption, etc. (Jiang *et al.*, 2021; Lau & Yong, 2021). Similarly, the use of synthetic chelating resins, activated carbon, activated alumina as adsorbents for the treatments of pollutants has drawbacks such as high operative cost, difficulties in regeneration, and hectic for post management, so it is not accessible for needy people of developing country like ours (Tang *et al.*, 2018; Kadirvelu *et al.*, 2004). Biosorption is a relatively new process that has been emerging as an effective technique in the separation of pollutants from aqueous solution. The main goal of this research is to explore the same type of functional groups onto the polymeric network of investigated biosorbents as that of synthetic chelating resins which renders quantitative separation schemes for the targeted ions. Therefore, the low-cost, year-round available agricultural waste, WR and BP are chosen and functionalized through $\text{Ca}(\text{OH})_2$ treatment followed with high valent metal loading to develop the biosorbents. To the date, no studies have been reported utilizing SWR and SBP as cation exchangers for Pb(II) and Hg(II) and metal loaded biosorbents as anion exchangers for As(III), F^- and PO_4^{3-} removal. This study can be a novel work as it utilizes locally available WR and BP waste for the biosorption of F^- , PO_4^{3-} , As(III), Pb(II), and Hg(II) from water.

1.17 Objectives

1.17.1 General objective

The general objective of the study was the exploration and characterization of low-cost biopolymer of WR and BP as ion exchangers to replace synthetic ion-exchangers and evaluation of their viability for the separation of cationic [Hg(II) & Pb(II)] and anionic [As(III), F⁻ & PO₄³⁻] pollutants from water.

1.17.2 Specific objectives

The specific objectives of the study were,

- i. Exploration of the functional moieties of WR and BP *via* saponification reaction along with loading of Zr(IV) and La(III) onto SWR and SBP to develop efficient ion exchangers.
- ii. Characterization of biosorbent prior to and after biosorption using different characterization techniques such as FE-SEM/EDX, FTIR, TGA, XRD and XPS.
- iii. Investigation of its selectivity for the separation of anionic pollutants [As(III), F⁻ & PO₄³⁻] and cationic pollutants [Hg(II) & Pb(II)] from aqueous solution using investigated ion-exchangers.
- iv. Inspection of biosorption performance using biosorption modellings.
- v. Computation of the application of investigated biosorbents for the treatment of natural water.

CHAPTER 2

LITERATURE REVIEW

A review of papers was performed to set a proper systematic procedure to meet the aim of the thesis. Different conventional techniques and procedures were employed for the separation of F^- , PO_4^{3-} , As(III), Hg(II) and Pb(II) present in the aqueous solution.

2.1 Fluoride biosorption

Al(III) and La(III) exchanged zeolite F-9 particles were studied to investigate the fluoride sorption capacity of sorbents. The experimental data was applied to different models. However, Dubinin-Radushkevitch (D-R) was fitted to model the experimental data. D-R isotherm showed that the removal of fluoride by Al(III)-exchanged zeolite carried through ion exchange mechanism while fluoride-La(III) exchanged zeolite interaction proceeded by physical adsorption. (Onyango *et al.*, 2004)

Two separation processes for adsorption of fluoride ion on natural chitosan and electro dialysis using membranes CMX-ACS was studied. Electrolysis gave good performance of fluoride removal from brackish water. Fluoride content was obtained at a high demineralization rate of 80%. However, the cost of operation and polarization problems are the limiting factors (Sahli *et al.*, 2007).

Magnesia- amended activated alumina (MAAA) was studied for the removal of fluoride. MAAA was synthesized by magnesium hydroxide impregnation followed by calcination at 450°C. The effect of pH, contact times, starting ion concentration, and dose was studied under batch mode. The impacts of co-existing ions in ground water sample were also analyzed. XRD, SEM, EDX and gas adsorption porosimetry tests were carried to screen the physiochemical characteristics of MAAA. Among various model, Sips model predicted the data well. More than 95% removal of fluoride was achieved with in 3h of contact time at neutral pH (Maliyekkal *et al.*, 2008).

The saponified orange juice residue (SOJR) loading with multivalent metal ions such as Al^{3+} , La^{3+} , Ce^{3+} , Ti^{4+} , Sn^{4+} , and V^{4+} were examined for the uptake of fluoride ion

from solution by Paudyal *et al.* (2011). The batch mode observations were conducted for different adsorbents. The maximum adsorption capacity of Al-SOJR, La-SOJR, Ti-SOJR and Sn-SOJR at pH 6, 4, 3 and 3 evaluated by the Langmuir adsorption model were 19.19, 20.33, 17.29 and 22.42 mg/g, respectively. The adsorption performance of Al-SOJR, La-SOJR, Ti-SOJR and Sn-SOJR was not interfered by co-ions such as NO_3^- , Cl^- , Ca^{2+} , and Na^+ however, HCO_3^- and SO_4^{2-} showed little interference on the adsorption capacity. The adsorbed fluoride from Al-SOJR was eluted almost 98% using 0.1M NaOH.

Defluoridation capacity (DC) of unmodified and Al(III) modified calcium hydroxyapatite was investigated. The impact of Al/Ca atomic ratio in Al-HAP, solution pH and interfering ions were examined. The results indicated that Al-HAP possessed higher DC of 32.57 mg F⁻/g than unmodified hydroxyapatite (HAP) which showed a DC of 16.38 mg F⁻/g at optimum pH 5.0. The adsorption of fluoride well described by PSO model and Langmuir isotherm model. Fluoride adsorption capacity was reduced by 10% for an initial CO_3^{2-} and PO_4^{3-} ions.

Defluoridation of water using alumina was studied to analyze the adsorption performance of synthesized adsorbents. The screening of the synthesized samples were examined by XRD, SEM, BET, and FTIR. The BET analysis showed the area of the adsorbent surface equals to 144.27 m²/g. The optimum fluoride removal was evaluated to be 8.4 mg/g at pH 4.4 followed by Langmuir isotherm. The thermodynamic parameters revealed the physical adsorption with activation energy 95.13 kJ/mol and endothermic behavior of the process. The kinetics study concluded that PSO kinetics was followed by the adsorption process. The decrease in fluoride adsorption in presence of competing ions such as bicarbonate ion, carbonate ion and sulphate ion were observed while chloride ion and nitrate ion had insignificant effect (Goswami & Purkait, 2012).

The adsorption performance of Jamun leaf ash prepared after calcination at 500°C was studied for the removal efficiency of fluoride ion by Tirkey *et al.* (2018). The study revealed that the uptake efficiency of fluoride is 77.8% with uptake capacity 4.56 mg/g within contact time of 60 min in pH = 6.5. The experimental data best suited to the Freundlich isotherm model. The kinetic adsorption data favors to the

PSO and intraparticle diffusion model. The thermodynamic variables revealed the adsorption process was evaluated to be feasible and exothermic.

According to Goswami & Kumar (2018), nanosized rice husk biochar was synthesized for the elimination of F^- from solution. TEM and EDX were operated to characterize the adsorbents. The batch adsorption tests were examined to study the potentiality of the investigated adsorbent. The equilibrium data well described by both Langmuir ($R^2 = 0.991$) and Freundlich ($R^2 = 0.995$) isotherm models. The optimum adsorption capability observed was 12.6 and 21.7 mg/g for Freundlich and Langmuir, respectively. The biosorption data better fit to the PSO kinetics in the adsorption of fluoride ion.

Zr(IV) modified activated carbon fibres (Zr-ACF) was prepared by a drop coating method for the removal of fluoride ion. The drop coating method yielded 5.5 times higher fluoride adsorption capacity than soaking method. The Zr-ACF was characterized using SEM, BET, FTIR and XPS. The batch adsorption experiments were studied, and optimum sorption was observed at pH 7. The kinetics fitted with PSO model. The biosorption isotherms agreed the Langmuir isotherm model with an optimum adsorption capability of 28.50 mg/g. The co-existing ions such as CO_3^{2-} , HCO_3^- and Cl^- had insignificant effect while SO_4^{2-} decreased the adsorption capacity by 11.5% (Pang *et al.*, 2020).

A metal organic framework (MOF-801) was synthesized impregnating zirconium onto adsorbent applying a solvothermal method and its adsorption capacity for removal of fluoride ions from water was studied by Tan *et al.* (2020). The morphology of MOF-801 was characterized by PXRD, FE-SEM, BET and XPS. The efficiency of the MOF-801 was studied in batch wise mode. The findings of the kinetic investigations suggest that PSO kinetics provided the most general description of the fluoride adsorption process. The maximal adsorption capacity was 19.42 mg/g, and the experimental data satisfied with the Langmuir isotherm model ($R^2 = 0.995$). After the fourth cycle, the synthesized MOF-801 exhibited a strong rate of reuse and a removal efficiency of 79%.

According to Siddique *et al.* (2020), $FeCl_3$ activated carbon obtained from *Citrus limetta* peels waste was synthesized for the uptake of fluoride ions from water. The

synthesized carbon materials were designated as AC-CLP₂₅₀ and AC-CLP₅₀₀ obtained by activating the selected biomass with FeCl₃ and subsequent carbonization at two different temperatures. The synthesized activated carbons were characterized by particle size distribution, point of zero charge pH_{pzc}, SEM, EDX, FTIR and XRD analysis. Batch adsorption experiments were conducted. The optimal conditions for both adsorbents were observed at pH 6.6, adsorbent dose 1.0 g/L and contact time of 240 min. Langmuir isotherm model agreed with the equilibrium data and the maximal sorption capability of AC-CLP₂₅₀ and AC-CLP₅₀₀ were found to be respectively, 4.926 and 9.709 mg/g. The adsorption process followed the PSO kinetics. Thermodynamic studies revealed feasible, spontaneous, and endothermic nature of the adsorption process. The increment in temperature from 25°C to 45°C enhanced the removal efficiency of fluoride.

2.2 Phosphate biosorption

The phosphate removal was studied from aqueous solution using blast furnace slag. A series of batch adsorption experiments was performed to optimize the pH, temperature, agitation rate and dosage. SEM, zeta potential analysis was carried to analyze the adsorbents. The phosphate removal occurred by a precipitation mechanism with a weak physical interaction. The removal of phosphate about 99% was obtained (Oguz, 2004).

The phosphate removal from wastewater using iron plate electrodes by electrocoagulation was investigated. The optimum pH for the removal of phosphate using Fe(III) electrode was in the range of 5 -7. The removal efficiency of phosphate was 61% at the end of 20 min. Low initial pH was suitable for greater efficiencies of phosphate removal or system energy consumption (Irdemez *et al.*, 2006).

The efficiency of orange waste gel loaded with zirconium was investigated for the elimination of phosphorus from water by Biswas *et al.* (2008). The adsorption behavior of phosphate onto Zr(IV)-loaded SOW gel, zirconium ferrite as well as the Zr(IV)-loaded MUROMAC XMC 3614 resin was performed on batch mode. The adsorption performance of Zr(IV)-loaded SOW gel was also examined in column mode adsorption. The interfering ions like chloride, sulphate and carbonate was also added in the batch experiments and found no interference by these ions in phosphate

adsorption. The optimal pH for the adsorption was found to be 7.0. The kinetic parameters evaluated in adsorption fitted with PSO kinetic model. The biosorption capability of Zr(IV)-loaded SOW gel agreed with Langmuir isotherm model was evaluated to be 57 mg P/g which is greater than commercial adsorbents *i.e* , zirconium ferrite (13 mg P/g) and Zr(IV)-loaded MUROMAC XMC 3614 resin (43 mg P/g). The desorption of adsorbed phosphate was successfully eluted by 0.2 M NaOH.

The removal of phosphate from an solution by adsorption onto modified wheat residue (MWS) was conducted. Investigations were also done into how flow rates and phosphate influent concentration affected column adsorption by Xu *et al.* (2009). The findings demonstrated that the PSO equation for adsorption systems matched the experimental data. The determined activation energy of 3.39 kJ/mol, indicates the physisorption process.

Nguyen *et al.*, (2015) explored the capability of Zr(IV)-loaded okara (ZLO) in the fixed bed column to remove phosphorus from aqueous solution and sewage. 0.25M Zr(IV) solution was placed onto the soybean residue, or okara. It was investigated how different variables such as flow rate, bed height, initial phosphorus concentration, pH, and adsorbent particle size affected ZLO performance. ZLO was calculated to have a utmost phosphorus adsorption capability of 16.43 mg/g. The breakthrough curve modeling showed that the Adams-Bohart and Thomas models fit the experimental data more closely than Yoon Nelson model. The successful desorption and regeneration of adsorbent was achieved with 0.2M NaOH and 0.1M HCl, respectively.

The adsorption capacity of cross-linked cerium (III)-loaded alginate bead (SA-Ca-Ce) for uptake of phosphate from aqueous solution was examined by Yang *et al.* (2016). SA-Ca-Ce had been prepared via a simple drop sphere forming method. The adsorption behaviors were studied under the batch mode with contact times, initial phosphate concentration, solution pH, temperature, and co-existing ions. The adsorbent was analyzed from SEM-EDS and FTIR. The kinetic studies agreed with PSO model. The experimental data fitted with Langmuir monolayer isotherm model with optimum adsorption capacity 41.39 mg/g at 318 K. The co-existence of anions in the adsorption of phosphate by SA-Ca-Ce had an adverse effect in the order as HCO_3^-

$> \text{SO}_4^{2-} > \text{Cl}^-$. Thermodynamic data supported spontaneous, endothermic, and entropy driven nature of phosphate adsorption onto SA-Ca-Ce.

According to He *et al.* (2017), the adsorption of phosphate using lanthanum-incorporated porous zeolite (La-Z) was performed. The La-content zeolite was characterized by zeta potential analyzer, scanning electron microscopy (SEM), XPS and ICP-OES. All batch adsorption experiments were conducted at 30°C with La-Z dosage. The equilibrium data agreed with Langmuir isotherm model and the maximal biosorption capacity was 17.2 mg P/g. Biosorption of phosphate could be well described by PSO model and the process was controlled by intra-particle diffusion. The developed La-Z adsorbent showed efficient potentiality for low level phosphate removal.

A novel nanostructured hydrated ferric oxide and hydrated zirconium oxide (nHFZO@1402) adsorbent was prepared by Zhou *et al.* (2018). The nanostructured adsorbent was characterized using TEM, SEM-EDX, FTIR, XRD and XPS. Batchwise experiments for phosphate were investigated for the adsorption capability of phosphate onto nHFZO@1402. The PSO kinetic model best fits with the kinetic data during adsorption process. The existence of coexisting ions such as chloride, nitrate, sulfate, and carbonate of different concentration did not interfere for phosphate adsorption from aqueous solution. The study showed that nHFZO@1402 served as a promising nanocomposite adsorbent for the phosphate elimination from water.

Activated sludge (WAS) based biochar impregnated with FeCl_3 for the adsorption of phosphate in the surface was studied by Yang *et al.* (2018). The biochars were modified as i) biochar decorated by co-precipitation of $\text{Fe}^{2+}/\text{Fe}^{3+}$ under N_2 atmosphere (MB₁), ii) biochar decorated by co-precipitation of $\text{Fe}^{2+}/\text{Fe}^{3+}$ under air atmosphere (MB₂) and iii) biochar decorated by impregnation with FeCl_3 under air atmosphere (MB₃). FTIR and XRD analysis were carried out on the biochars. The kinetics results showed the agreement with PSO model. The experimental results fitted well ($R^2 = 0.9$) to Weber-Morris model, suggesting the importance of intraparticle diffusion in phosphate adsorption on the modified biochars.

The adsorption performance of tea waste (TW) and the amine cross-linked tea waste (ACTW) to remove phosphate and nitrate ions from aqueous solutions was studied. The removal of nitrate and phosphate by both TW and ACTW were compared through a set of experiments that varied the adsorbent dosage, equilibration time, initial concentration of target ion and solution pH. The TW and ACTW were characterized using SEM, XRD, EDS, FTIR and XPS. The adsorption was well explained using Langmuir isotherm model. The maximal biosorption capacity ACTW for phosphate ions was 98.72 mg/g. The adsorption of phosphate on ACTW might involve electrostatic attraction as well as ion-exchange according to Qiao *et al.* (2019).

Palansooriya *et al.* (2021) fabricated Fe(III) loaded chitosan-biochar composite fibers (FBC-N and FBC-C) from paper mill sludge biochar produced under N₂ (BC-N) and CO₂ (BC-C) conditions at 600°C for adsorptive removal of phosphate from water. The morphological and physicochemical characteristics of the adsorbent was investigated using SEM/EDX, XPS, Raman spectroscopy and specific surface area measurement. The Freundlich isotherm model well described the phosphate adsorption on BC-N, while the Redlich-Peterson model best fitted the data of three other adsorbents. The solution pH 4.0 and adsorbent dosage 2 g/L were considered as the optimal conditions. The maximum adsorption capacities were 9.63, 8.56, 16.43 and 19.24 mg/g for BC-N, BC-C, FBC-N and FBC-C, respectively. The PFO kinetic model explained the phosphate adsorption on BC-C and BC-N while data of FBC-N and FBC-C followed the PSO and Elovich model, respectively.

The adsorption capacity of thermally treated seagrass residues of *Posidonia oceanica* was investigated for the phosphate removal from synthetic and real wastewater by Photiou *et al.* (2021). SEM, XRD and EDX analysis was conducted to characterize the adsorbents. The PFO kinetics better fit for the process. The adsorption capability of treated seagrass residues was evaluated to be 30.2115 mg/g based on Langmuir model; however, the equilibrium data fits satisfactorily with Freundlich isotherm model.

2.3 Arsenic biosorption

The red mud obtained as a waste product using bauxite for the adsorption of arsenic was performed. The result indicated that pH 9.5 was favorable for arsenic removal process. The As(III) adsorption followed PFO and obeys the Langmuir model. The As(III) adsorption is exothermic process (Altundogan *et al.*, 2000).

According to Ghimire *et al.* (2002), phosphorylated orange juice residue (OJR) loaded with iron (III) showed the uptake of arsenic from aqueous solution effectively. The adsorption on iron (III) loaded gel were conducted by batch wise and column studies. The utmost pH for As(III) and As(V) adsorption were determined to 10 and 3.1. The utmost adsorption capability for As(V) and As(III) was computed, respectively as 0.070 and 0.068 mg/g.

The elimination of As(III) and As(V) using Fe(II) ions after precipitation of bacterial oxidation was examined. The results showed that inorganic form of arsenic could be efficiently treated. The treatment method was based on a fixed bed upflow filtration unit. The oxidation of As(III) was found to be catalyzed by bacteria leading to As(III) removal (Katsoyiannis & Zouboulis, 2004).

Arsenate As(V) and arsenite As(III) biosorption to natural watermelon rind (WMR), xanthated watermelon rind (X-WMR) and modified WMR (CA-WMR) using citric acid in aqueous solution was investigated by Shakoor *et al.* (2018). In comparison to the citric acid modified WMR (CA-WMR), the xanthated WMR (X-WMR) demonstrated considerably higher As(V) and As(III) removal from natural water. FTIR and SEM analyses were operated on the adsorbents. By using X-WMR, the greatest removal of As(III) and As(V) was attained at pH 8.2 and 4.6, respectively. The data for As(III) and As(V) biosorption to X-WMR were best fit by the Langmuir isotherm model ($R^2 = 0.96$), and the maximal adsorption capabilities were estimated to be 4.83 and 1.5 mg/g, respectively. The PSO model on the surface of the X-WMR accurately predicted the kinetics of As(V) and As(III) ($R^2 = 0.99$). Thermodynamic studies analyzed that As(V) and As(III) was well described by the PSO model ($R^2 = 0.99$) on the surface of the X-WMR. The study concluded that As(V) and As(III) biosorption was endothermic and spontaneous. The desorption experiment suggested that 0.1M NaOH successfully desorbed As(III) and As(V).

According to He *et al.* (2019), the Zr(IV) MOFs (UiO-66 and UiO-66(NH₂)) was explored for the elimination of arsenic(As) from contaminated water. The As(III, V) uptake efficiency was examined by batch experiments. The removal capacity of UiO-66 was determined to be 205.0 and 68.21 mg/g, respectively for As(III) and As(V). FTIR and XPS studies indicated that Zr-O bonds of zirconium metal organic frameworks effectively adsorb arsenic. SEM and TEM characterized the morphology and microstructure of the adsorbents. BET surface areas were determined based on nitrogen adsorption-desorption method. The co-existing ions including CO₃²⁻, NO₃⁻, Br⁻, Cl⁻, SO₄²⁻ had no interference while H₂PO₄⁻ and HPO₄²⁻ inhibits the sorption of arsenic. The thermodynamic findings concluded that sorption of As(III, V) on UiO-66 and UiO-66(NH₂) were found to be exothermic and spontaneous.

As(III) adsorption was studied using magnetite immobilized on pinecone (MNP-PCP) and pine cone (PCP) by Pholosi *et al.* (2019). FTIR, SEM-EDX, XRD, and XPS were applied to screen the adsorbents. In batch equilibration mode, the As(III) adsorption on MNP-PCP was examined. Adsorption tests were carried out with various adsorbent doses, pH levels, and contact periods. The experimental data was suited with the PSO model and Langmuir isotherm model, and the adsorption capacities of PCP and MNP-PCP were 14.83 and 18.02 mg/g at 299 K. The influence of competing anions on the sorption were evaluated. The presence of SO₄²⁻, CO₃²⁻, NO₃⁻ and Cl⁻ had no effect while PO₄³⁻ interfered for the biosorption of As(III) on MNP-PCP. 0.1M HCl and NaOH eluted As(III) from both adsorbents. MNP-CP had better stability for five cycles of adsorption-desorption.

The potentiality of the biomass from *Bacillus thuringiensis* strain WS3 was examined for different contact time, temperature, pH, As(III) concentration and adsorbent dosages to eliminate As(III) from solution by Altowayti *et al.* (2019). The optimal pH for As(III) removal was found at pH 7.0. The highest As(III) loading capability was determined to be 10.94 mg/g. The adsorbent was characterized using Fe-SEM-EDX and FTIR. The equilibrium adsorption was simulated *via* the Langmuir isotherm model. The thermodynamic terms such as ΔG° , ΔH° , ΔS° of As(III) adsorption were calculated and found the process was endothermic and spontaneous.

The biosorption capability of almond shell (ALS) and almond shell biochar (ASB) based biomaterials for the sequestration of As(III)/As(V) from arsenic polluted

solutions was carried by Ali *et al.* (2020). The highest As(III) biosorption capability of ALS and ASB were obtained, respectively to be 4.6 and 4.86 mg/g. The isotherm modelling equilibrium data best fit to Langmuir model for both As(III) and As(V). FTIR and XPS spectroscopy analyzed the adsorption of As(III) by both adsorbents. ASB can eliminate effectively As(III) from water in comparison to ALS. The explored ALS biochar is promising adsorbent to remove As(III) present in wastewater.

2.4 Lead biosorption

Natural and pretreated clinoptilolite had been investigated for the adsorption of Pb(II) in batch mode. Toth, Sips and Redlich-Peterson isotherm equations best fitted with the experimental data. The maximum adsorption capacity of raw and pretreated clinoptilolite was evaluated to be 80.93 and 122.4 mg/g. It followed PSO kinetics (Gunay *et al.*, 2007).

Commercial Valonia tannin (VT) powder was treated with NH₃ followed by formaldehyde to obtain yellow precipitate. The precipitate was treated with acid and insoluble tannin resin was formed. The BET surface area was measured to be 11.70 m²/g. FTIR study was performed. The monolayer saturation capacity is 138.3 mg/g. It followed PSO kinetic model (Ozacar *et al.*, 2008).

According to Lu *et al.* (2009) the viability of a new chemical modified lawn grass adsorbents was studied to sequester Pb(II) ion from solution. The adsorbent was analyzed through FTIR spectra and elemental analysis. The optimal pH is in-between 5.0 -5.8. The adsorption system follows PSO kinetics. The utmost adsorption capacities computed from Langmuir-Freundlich model are 321.16 and 261.06 mg/g using 1M and 0.6M citric acid, respectively. The sorption of Pb(II) was thermodynamically spontaneous and endothermic. The desorption experiments of Pb(II) and regeneration of the column was achieved using 0.1M HCl. The breakthrough point was achieved at 100 BV by a column of 0.6 CG. The breakthrough point remains around 100 BV after 3 adsorption/desorption cycles which insinuated that grass adsorbent was regenerated and used repeatedly.

Saccharum officinarum bagasse commonly called sugarcane bagasse (SCB) was chemically modified for the removal of As(III) and As(V) ion from solution by Gupta *et al.* (2015). SEM, EDX and FTIR spectra were used to analyze the materials. For the adsorption of As(III) and As(V), the ideal equilibrium contact time, dosage rate, isotherm, and pH were investigated. The adsorption data fit the Freundlich and Langmuir isotherm models well. As(III) and As(V) were estimated to have Langmuir capacities of 28.57 and 34.48 mg/g, respectively. The thermodynamic variables revealed the process is spontaneous and endothermic. The adsorbent could be regenerated and reused for 5 cycles using 0.01M HCl.

Aryal *et al.*, (2010) studied *Staphylococcus xylosus* biomass pretreated with Fe(III) for As(III) and As(V) biosorption. Potentiometric titration and infrared spectroscopy were used to scrutinize the functional groups present on the biomass surface. The monitoring parameters for the sorption of As(III) and As(V) on biomass were examined. The maximum biosorption of As(III) (pH = 7.0) and As(V) (pH = 3.0) based on Langmuir isotherm model was evaluated to be 54.35 and 61.34 mg/g, respectively. The kinetic parameters for the biosorption of As(III) and As(V) was studied. The biosorbed As(III) and As(V) from Fe(III) loaded biomass was eluted using 0.09 M HCl. The reusability of the biomass was effective up to 3 cycles.

Investigation of saponified muskmelon peel for the uptake of Pb(II) from solution was performed by Huang & Zhu, (2013). The adsorbent was analyzed from SEM and FTIR studies. The adsorption studies were well favored by Langmuir model and PSO kinetics. The optimum adsorption capability for Pb(II) was enumerated to be 167.83 mg/g.

The removal of Pb(II) using ethylenediamine modified yeast biomass coated with magnetic chitosan (EYMC) microparticles from aqueous solution was examined by Li *et al.* (2013). Variables including initial pH, temperature, initial Pb(II) concentration, contact times and desorption studies were examined. The adsorbent was analyzed using SEM and FTIR. The concentration of Pb(II) was measured using AAS. The highest adsorption capability was recorded at pH 4.0 -6.0. The adsorption data was in harmony with Langmuir isotherm model. The utmost adsorption capacities 20°C, 30°C and 40°C, respectively enumerated from Langmuir model were 121.26, 127.37 and 134.90 mg/g. Kinetic studies indicated that PSO was appropriate for the biosorption.

The adsorption process was endothermic and spontaneous based on thermodynamics study. The adsorbed Pb(II) was effectively desorbed by 0.1M EDTA.

The pretreated *Tephrosia purpuria* leaf (TPL) powder was investigated for the uptake of Pb(II) ions from solution by Madala *et al.* (2015). The biosorbent was operated by FTIR, SEM and EDAX analysis. The ideal pH for the removal of Pb(II) was 5.4. The Langmuir isotherm gave better correlation and maximum sorption capacity which was found to 100 mg/g. The biosorption process was evaluated to be highly feasible, spontaneous, and endothermic.

Ahmad & Haseeb, (2015) studied the groundnut husk modified with Guar Gum (GG) for the uptake of Pb(II), Cu(II) and Ni(II) from solution. The adsorbent was examined by FTIR, XRD, SEM and EDX. The maximum adsorption capacity for Pb²⁺, Cu²⁺ and Ni²⁺ was found 9.76, 9.26 and 6.74 mg/g, respectively. The optimized adsorption parameters were pH = 6.0, equilibrium time = 120 min, and adsorption temperature 298K. The adsorption data follows PSO and Freundlich isotherm model. The thermodynamic results demonstrated Pb(II), Cu(II) and Ni(II) biosorption was endothermic and spontaneous.

The Pb(II) ions biosorption utilizing *goldar* residue biomass extracted from *Otostegia persica* was examined by Alavi *et al.* (2015). Investigations of contact time, pH, dose, and lead initial concentration on biosorption was performed. The maximum adsorption capacity of *goldar* residue biomass was evaluated as 18.86 mg/g at pH 5.5 based on Langmuir isotherm model. The adsorbent was characterized using ATR-FTIR. The PSO model characterized the kinetics of adsorption. The thermodynamic variables showed that the biosorption process was exothermic, decrease in randomness and spontaneous.

The biosorption process of lead (Pb) and arsenic (As) on soyabean adsorbent was reported by Gaur *et al.* (2018). The soyabean dust particles were treated with 0.5, 1.5 and 2% NaOH at 30°C. The characterization of untreated and treated adsorbent was operated conducting FT-IR, FEG-SEM, Zeta sizer and TGA. The different factors affecting adsorption process of the metal ions [Pb(II) and As(III)] such as adsorbent dose, contact time, temperature and pH was studied using wastewater. The maximal

pH for removal of As and Pb was found to be 2.0 and 4.0 ± 0.26 , respectively. The experimental data satisfied with Langmuir and Freundlich isotherm models.

Bharti & Kumar, (2018) investigated the adsorption potential of bagasse biochar biosorbent for the Pb(II) removal from wastewater of battery manufacturing industry. The biochar was obtained after pyrolysis at a temperature of $300 \pm 10^\circ\text{C}$ for 2.5 h. The optimum adsorption occurred at pH 5. The maximum removal efficiency was evaluated as 12.741 mg/g. The experimental results best fitted with Langmuir isotherm. The kinetics involved in the process was PSO. The characterization of the adsorbent biochar was done by SEM, EDX, XRD and FTIR analysis. The elution of Pb-loaded bagasse was executed using 0.1M HNO_3 .

The adsorption performance of steel making dust for Pb(II) adsorption was examined from solution. The determination of optimum pH condition adsorption isotherm, and kinetic studies were carried by Bouabidi *et al.* (2018). The maximum adsorption capacity for lead on steel dust studied from the Langmuir isotherm was 208.9 mg/g for the ladle furnace steel dust, and 39.8 mg/g for the cyclone steel dust. The adsorption kinetics study exhibited the PSO model was well fitted with lead adsorption onto steel dust.

A nanocomposite of carbon nanotubes (CNTs) covered with hydrated zirconium oxide ($\text{ZrO}(\text{OH})_2$) was created to eliminate As(III) and As(V) from drinking water by Liu *et al.* (2018). The FT-IR, XRD, SEM, and TEM were used to scrutinize the adsorbent. The highest adsorption capacities of the $\text{ZrO}(\text{OH})_2/\text{CNTs}$ nanocomposite at pH 7 were 78.2 mg/g for As(III) and 124.6 mg/g for As(V), respectively, satisfying the Langmuir model. The PSO model's fitting of the kinetic parameters for As(III) and As(V) adsorption on $\text{ZrO}(\text{OH})_2/\text{CNTs}$. Re-coating $\text{ZrO}(\text{OH})_2$ allows for the regeneration of the used $\text{ZrO}(\text{OH})_2/\text{CNTs}$. Within six cycles, the As(III) and As(V) adsorbed on the $\text{ZrO}(\text{OH})_2/\text{CNTs}$ was effective.

The capacity of *F. spiralis* waste for Pb(II) removal was successfully tested through batch experiments by Filote *et al.* (2019). The adsorbent was characterized by FTIR and pH_{pzc} . The maximal adsorption capacity evaluated based on Langmuir model was 132 ± 14 mg/g at pH 4.5 at 20°C . The kinetic data of adsorption was in parallel with PSO kinetic model. The eluent performance was analyzed using three eluents as 0.1

M EDTA, 0.1 M NaCl and 0.1M HNO₃ whereas 0.1M EDTA successfully eluted the adsorbed Pb(II).

The potentiality of a freshwater algae *Pithophora cleveana* Wittrock and *Mimusops elengi* leaves in the removal of lead by batch experiments was explored by Gaddam *et al.* (2020). The adsorbent morphology and structure were characterized by FTIR, SEM and XRD. The maximum uptake capacity of 22.96 and 14.56 mg/g was evaluated for *Pithophora cleveana* Wittrock and *Mimusops elengi*. The kinetic study concluded that the PSO kinetic model agreed with a correlation coefficient $R^2 = 0.995$. The thermodynamic study concluded that the biosorption mechanism was exothermic and spontaneous.

The modified adsorbents derived from *Cassia fistula* seeds for the uptake of Pb(II) from the aqueous solution was investigated by Hemavathy *et al.* (2021). Raw *Cassia fistula* (RCF) and three surface modified (physically treated -PMCF and chemically treated -HMCF and SMCF) adsorbent material were investigated. The adsorbent materials were characterized by FTIR and SEM analysis. The optimum pH for the adsorption was 5.0. The modelling study revealed that Freundlich isotherm and PFO kinetics fits well and the highest adsorption capability of PMCF, SMCF, RCF and HMCF was 48.66, 129.3, 13.22 and 28.28 mg/g, respectively. The thermodynamic study showed the exothermic and spontaneous nature of adsorption.

2.5 Mercury biosorption

Activated carbon (AC) heated at 293 K obtained from furfural was studied for the removal of Pb(II) ion from aqueous solution. The AC was prepared by polymerization of furfural following carbonization and activation at 800°C. Both isotherm models agreed for the process. The maximum adsorption capacity at pH 5.5 was 174 mg/g (Yardim *et al.*, 2003).

2-(3-(2-amino ethylthio)propylthio)ethanamine was used to functionalize the silica gel and ordered MCM-41. The functionalized adsorbents were characterized by XRD, ¹³C MAS, NMR spectroscopy and TGA. The optimum pH for adsorption was 4-7. Langmuir isotherm model best fit for the adsorption for both adsorbents. The maximum adsorption capacity of silica gel and MCM-41 was 159.58 and 141.4 mg/g (Puanggam & Unob, 2008).

According to Mondal *et al.* (2013), the performance of bamboo leaf powder (BLP), sodium dodecyl sulphate (SDS) modified BLP (BLPS) and Triton X-100 modified BLP (BLPT) showed endothermic and spontaneous biosorption of Hg(II). BLP was characterized by BET and FTIR analysis. The performance of the adsorbents was studied under batch experiments. The optimal pH for the adsorption was found to be 8.0. The utmost adsorption capacity was 27.11, 28.1 and 31.05 mg/g for BLP, BLPS and BLPT, respectively. BLP and BLPT followed Freundlich isotherm model and BLPS followed Langmuir isotherm model.

Pristine (CF-pristine) NaOH- treated (CF-NaOH) coconut fibers were used as a adsorbent for Hg(II) uptake from an aqueous solution reported by Johari *et al.* (2014). The coconut fiber biosorbent (CFB) was characterized by SEM and FTIR spectroscopy. The equilibrium and kinetic data of Hg(II) biosorption onto CFB, respectively followed Langmuir isotherm model and PSO kinetic model. The Hg(II) biosorption capabilities obtained for CF-pristine and CF-NaOH were 144.4 and 135.0 mg/g, respectively. The thermodynamic studies disclosed that the biosorption process was spontaneous, exothermic with increased randomness during Hg(II) biosorption.

Cellulose-based materials treated with Schiff bases for the removal of Hg(II) ions from aqueous solution was investigated by Kumari & Chauhan, (2014). FTIR, SEM, XRD, and EDAX were used to characterize the adsorbent substances. At an ideal pH of 5.0, the material's maximal adsorption capacity was calculated to be 258.75 mg/g. The equilibrium results for the adsorption of Hg(II) followed the Langmuir isotherm and PSO kinetics. The adsorption process was concluded to be endothermic and spontaneous, according to the thermodynamics data. The adsorbed Hg(II) can be eluted significantly using 0.5 N HCl. The adsorption desorption process of the material was found to be effective till 8 repeated cycles.

The uptake of Hg(II) ions from aqueous solution by means of thiol functionalized magnetic nanoparticles (TF-MNPs) was reported by Oveisi *et al.* (2017). TF-MNPs was characterized using XRD, FE-SEM, FTIR, TGA and vibrating sample magnetometer. The adsorption performance of thiol functionalized magnetic nanoparticles was evaluated in batch mode. The maximum adsorption of Hg(II) onto the adsorbent was found in the pH of 6.0. The adsorption behavior followed both Freundlich and Langmuir isotherms with a utmost adsorption capacity of 344.82

mg/g. The kinetics of adsorption agreed PSO rate equation. The Hg(II) ions were desorbed effectively from TF-MNPs using thiourea in HCl solution.

Amide functionalized cellulose from sugarcane bagasse fiber (SBF) was studied for the Hg(II) ion removal from wastewater. Different adsorbents were prepared dissolving in stearic acid (SBF-g-SA) and polyacrylamide (SBF-g-SA)-g-PAM. The characterization of the adsorbents was conducted by optical microscope (OM), scanning electron microscopy (SEM-EDS) and infrared spectrometry (FTIR). The adsorption experiments were examined in batch mode. The equilibrium data agreed with Langmuir isotherm model with utmost adsorption capacity as 178 mg/g. The kinetic data was suited more with PSO kinetic model. The adsorption process for Hg(II) on the adsorbents were found spontaneous and endothermic. The adsorbed Hg(II) was effectively desorbed using 0.2 M HCl. The regeneration and reusability of adsorbent was effective for six adsorption desorption cycles (Sun *et al.*, 2018).

Moringa oleifera gum (MOG), via acryloylation reaction to nano-polyacryloyl MOG (NPAMG) was investigated for Hg(II) removal from aqueous solution. The NPAMG was characterized using different techniques as FTIR, FE-SEM, EDX, XRD, TEM, AFM and particle size analysis. NPAMG had an utmost adsorption capacity of 840.34 mg/g evaluated by Langmuir isotherm model at optimum pH 5.6. The kinetic data agreed better with PSO model. The reusability of the adsorbents was effective up to 20 repeated cycles (Ranote *et al.*, 2018).

A functionalized graphene oxide with 3-amino-5 phenylpyrazole (F-GO) was investigated in the uptake of Hg(II) from aqueous solution. The variations of three operational variables pH, adsorbent dose, and initial metal ion concentration on Hg(II) adsorption capacity of F-GO were analyzed by central composite design. The untreated graphene oxide (GO) and functionalized graphene oxide (FGO) were characterized using FTIR, EDX, FE-SEM, XRD and TGA analysis. The maximum adsorption capacity of GO and FGO were evaluated, respectively as 179.973 and 207.861 mg/g. The adsorption behavior was best fitted with PFO kinetic models and Freundlich isotherm model. Thermodynamics studies predicted the process of adsorption was endothermic and spontaneous. The adsorbed Hg(II) was desorbed using 1M HCl solution. The adsorbent worked effectively upto 3 adsorption-desorption cycles (Alimohammady & Ghaemi, 2020).

Graphene oxide nanosheets chemically treated with chloroacetic acid and ethylene diamine for the removal of Hg(II) from aqueous solutions was studied by Awad *et al.* (2020). The improved graphene oxide (IGO) was chemically modified with chloroacetic acid and ethylene diamine to form carboxylated improved graphene oxide (IGO-COOH), aminated improved graphene oxide (Imino-IGO). The IGO, IGO-COOH, IGO-NH₂ and Imino-IGO adsorbents are fully characterized by FTIR, UV-vis, XPS, XRD, SEM, TEM, and Raman spectroscopy. Under different conditions, batch adsorption experiments were conducted to evaluate the adsorption of Hg(II) ions. The elimination of Hg(II) was investigated in relation to pH, adsorbent dosage, temperature, contact time, and starting concentration. The maximum adsorption capacity for the removal of mercury follows the order at optimum pH = 5.0; Imino-IGO (230.0) > IGO-COOH (122.0) > IGO (24.0 mg/g). The equilibrium data of adsorption showed good fits to Langmuir isotherm model. The endothermic, spontaneous, and increased entropy at the solid/solute interface during the adsorption process were shown by the thermodynamic parameters. 1M HCl eluted the adsorbed Hg(II) effectively and the adsorption-desorption was run for six cycles effectively.

Cellulose nanofibrils (CNF) extracted from rice straw were functionalized using L-methionine for biosorption of Hg(II) ions. The modified fibers were analyzed using FTIR, XRD, TEM, elemental mapping. The modified fibers demonstrated a high adsorption capacity of 131.86 mg/g for biosorption of Hg(II) ions. Langmuir isotherm model best fit with the equilibrium data. The adsorption followed PSO kinetic model. The adsorbed Hg(II) was effectively desorbed using 0.1N HCl. The regeneration and reusability of adsorbent was effective up to 7 cycles of adsorption and desorption (Bisla *et al.*, 2020).

Giraldo *et al.* (2020) modified sugarcane bagasse with thermal treatment (CSB) and chemical activation through activating agents, ZnCl₂ (SBZ) and H₃PO₄ (SBH). The modified adsorbents were utilized to sequester Hg(II) from aqueous solutions. The batch studies were performed to explore the influence of isotherm, pH, and kinetics on Hg(II) adsorption. The adsorption process was best suited with the PSO kinetics model. The maximum adsorption capacity of SBZ and CSB were evaluated to be 11.5 and 13.6 mg/g, respectively based on Langmuir isotherm model.

Ion-exchange, precipitation, electrodialysis, reverse osmosis and adsorption were in practice for the removal of F^- , PO_4^{3-} , As(III), Hg(II) and Pb(II) from aqueous solution. Ion exchange, electrodialysis and reverse osmosis are effective methods however, these methods are selective for the targeted ions, requires high operating pressure and prone to membrane fouling (Van der Bruggen, 2018). The different adsorbent materials have been used for the removal of pollutants as activated carbon, bone charcoal, zeolites, synthetic ion exchangers, saw dust, algae, weeds, red mud, lime activated alumina, and alum (Ameri *et al.*, 2020; Arumugam *et al.*, 2020; Aryal *et al.*, 2010; Beiyuan *et al.*, 2020; Mahmood *et al.*, 2018; He *et al.*, 2017; Guibal, 2004). In recent years considerable attention has been devoted to exploring different types of low-cost materials such as pomegranate peels, pomelo peels, orange peels, sugarcane bagasse and so forth for biosorption of pollutants from aqueous solution (Poudel *et al.*, 2021; Ren *et al.*, 2018; Ghimire & Inoue, 2007). The literature review showed that there has been a growing interest in the researchers to use low cost, readily available and functionalized agricultural waste as biosorbents to separate cationic and anionic pollutants present in aqueous solution.

2.5 Research gap

A thorough analysis of the literature revealed that there are many types of publications reported on the topic of removing F^- , PO_4^{3-} , As(III), Hg(II) and Pb(II) from aqueous solutions. Different conventional methods (Precipitation, ion exchange, membrane processes and reverse osmosis) have been reported to investigate the biosorption capacity of adsorbents from aqueous solution (activated carbon, zeolites, and synthetic ion exchangers)(Van der Bruggen, 2018; He *et al.*, 2017; Joo & Tansel, 2015; Zanella *et al.*, 2014; Goswami & Purkait, 2012; Fu & Wang, 2011). However, the applied conventional methods require high operational cost, problems in sludge management, not selective for the metal ions of interest and cannot remove the pollutants present in trace concentration in aqueous solution. Very few research work has been carried on raw WR and BP with/without acid- base treatments. The biosorption capacity shown by WR and BP in the literature was not convincing. Biosorbents after chemical modification through amination, saponification phosphorylation and xanthation exhibited higher biosorption capacity (Ji *et al.*, 2019; Poudyal *et al.*, 2012; Homagai *et al.*, 2010; Ghimire *et al.*, 2008). The main principle

behind it is to obtain the same types of functional group as in the plastic materials. Therefore, my research attempt is to saponify WR and BP to develop i) cation exchangers for the biosorption of Hg(II), and Pb(II) and ii) anion exchangers through M(III/IV) loading onto SWR and SBP for biosorption of F⁻, PO₄³⁻, and As(III) from aqueous solution. These low-cost biosorbents are expected to remove even a trace concentration of F⁻, PO₄³⁻, As(III), Hg(II), and Pb(II) present in aqueous solution.

CHAPTER 3

MATERIALS AND METHODS

3.1 Methodological framework

The biosorption studies were conducted in the research laboratory of the Central Department of Chemistry, Tribhuvan University, Kathmandu, Nepal, and part of this work was conducted in Water Analysis Laboratory, CSIR-Indian Institute of Toxicology Research, Lucknow, India. A detailed outline of methodological framework is displayed in **Figure 12**.

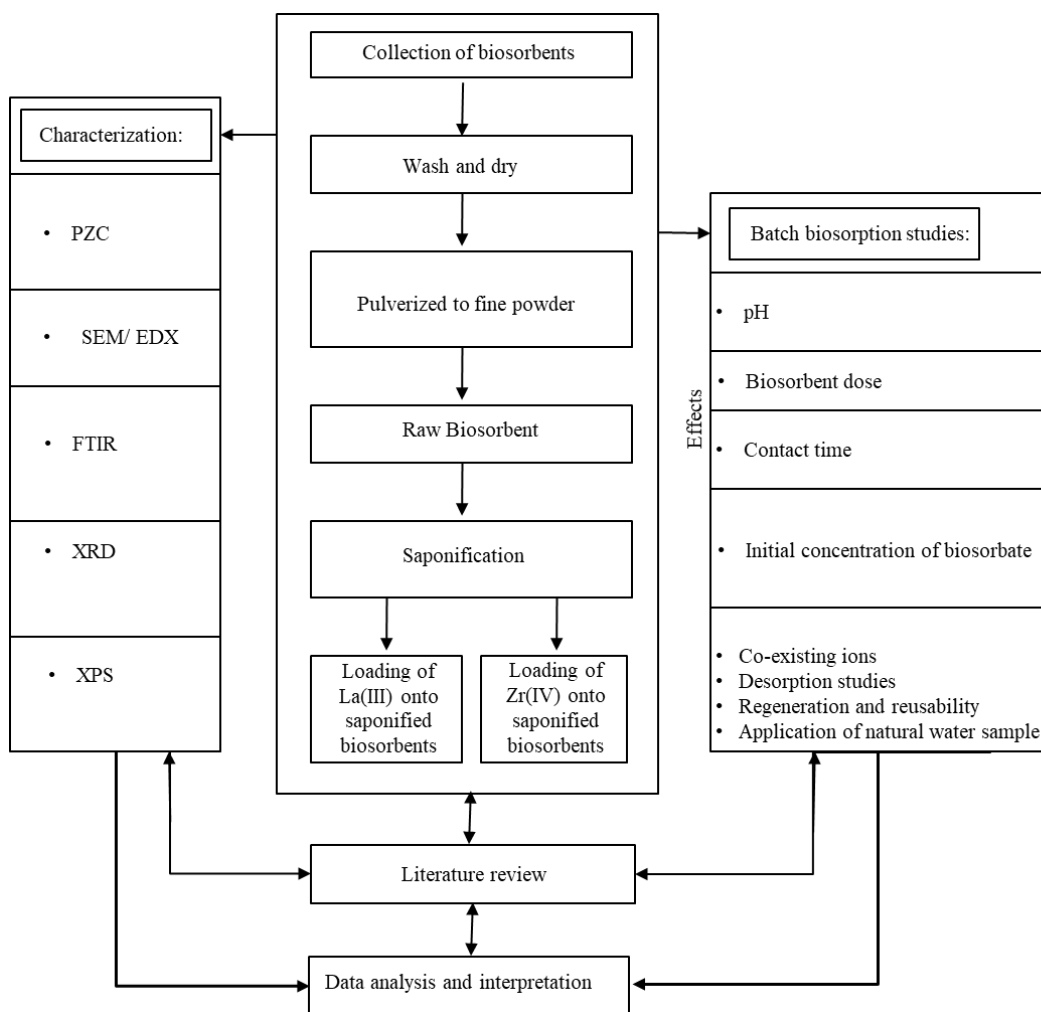


Figure 12: Methodological framework for the study

The focus of the study was to optimize the variables such as pH, biosorbent dosage, contact time, and initial concentration of tested ions onto the investigated biosorbents. The experimental procedure applied during the study for the biosorption of tested ions onto the investigated biosorbents have been discussed in this chapter.

3.2 Chemical reagents

The chemical reagents used were of analytical grades, which are listed in **Table 2**.

Table 2: List of chemicals used throughout the experimental work

Name of the chemicals	Formula	Company
Arsenic trioxide	As ₂ O ₃	AR Grade, Thermo Fisher Scientific
Buffer tablets	pH 4, 7 & 9.2	AR Grade, Qualigens Fine Chemicals, India
Calcium chloride dihydrate	CaCl ₂ .2H ₂ O	AR Grade, Thermo Fisher Scientific
Calcium hydroxide	Ca(OH) ₂	AR Grade, Sigma-Aldrich, 99.999%
Cadmium nitrate tetrahydrate	Cd(NO ₃) ₂ .4H ₂ O	AR Grade, Thermo Fisher Scientific
Copper sulphate pentahydrate	CuSO ₄ .5H ₂ O	AR Grade, Qualigens Fine Chemicals, India
Ferric chloride hexachloride	FeCl ₃ .6H ₂ O	AR Grade, Thermo Fisher Scientific
Hydrochloric acid	HCl	AR Grade, Thermo Fisher Scientific
Lanthanum chloride heptahydrate	LaCl ₃ .7H ₂ O	AR Grade, Qualigens Fine Chemicals, India
Lead acetate trihydrate	(CH ₃ COO) ₂ Pb.3H ₂ O	AR Grade, Thermo Fisher Scientific
Lead nitrate	Pb(NO ₃) ₂	AR Grade, Sigma-Aldrich, 99.999%
Mercuric chloride	HgCl ₂	AR Grade, Sigma-Aldrich, 99.999%
Magnesium chloride hexahydrate	MgCl ₂ .6H ₂ O	AR Grade, Thermo Fisher Scientific
Nickel nitrate hexahydrate	Ni(NO ₃) ₂ .6H ₂ O	AR Grade, Sigma-Aldrich, 99.999%
Potassium dihydrogen phosphate	KH ₂ PO ₄	AR Grade, Sigma-Aldrich, 99.999%
Potassium nitrate	KNO ₃	AR Grade, Thermo Fisher Scientific
Sodium fluoride	NaF	AR Grade, Sigma-Aldrich, 99.999%
Sodium chloride	NaCl	AR Grade, Thermo Fisher Scientific
Sodium sulphate	Na ₂ SO ₄	AR Grade, Thermo Fisher Scientific
Sodium hydroxide	NaOH	AR Grade, Thermo Fisher Scientific
Sodium nitrate	NaNO ₃	AR Grade, Thermo Fisher Scientific
Sodium bicarbonate	NaHCO ₃	AR Grade, Thermo Fisher Scientific
Zinc acetate dihydrate	(CH ₃ COO) ₂ Zn.2H ₂ O	AR Grade, Qualigens Fine Chemicals
Zirconium oxychloride octahydrate	ZrOCl ₂ .8H ₂ O	AR grade, Sigma-Aldrich, 99.999%

3.3 Preparation of reagents

3.3.1 Preparation of sodium fluoride solution

2.210 g of NaF was dissolved in 1000 mL of DI water to get the stock solution (1000 mg/L) of sodium fluoride. The working solutions of the required concentrations were made by successive dilutions of the stock solution.

3.3.2 Preparation of phosphate solution

1.431 g of KH_2PO_4 was dissolved in 1000 mL of DI water to make the stock solution of phosphate (1000 mg/L). The working solutions were made by dilutions of the stock solutions at the time of experiments.

3.3.3 Preparation of arsenic solution

1.320 g of As_2O_3 was dissolved in 20 mL of a 10 M NaOH, neutralized with 5M HNO_3 , and then diluted upto 1000 mL to get 1000 mg/L solution by adding the necessary amount of DI water. The stock solution was further diluted at the time of experiments to make working solution.

3.3.4 Preparation of Pb(II) solution

1.597 g of $\text{Pb}(\text{NO}_3)_2$ was dissolved in 1000 mL of DI water to make 1000 mg/L of Pb(II) stock solution.

3.3.5 Preparation of Hg(II) solution

1.353 g of HgCl_2 was dissolved in 1000 mL DI water to prepare 1000 mg/L of stock solution. The working solution of desired concentrations were prepared by diluting stock solution.

3.3.6 Preparation of HCl solution

16.5 mL of conc. HCl (37.25%) was diluted to 100 mL to give 2M HCl. Other working solutions were made by dilution methods.

3.3.7 Preparation of NaOH solution

20 g of NaOH pellets were weighed and dissolved in 100 mL distilled water to form 5M NaOH solution. Other NaOH solution (1M, 0.5 M, 0.1M, 0.05M, and 0.01M) were prepared by diluting 5 M NaOH.

3.3.8 Preparation of buffer solution

Buffer solutions of pH 4.0, 7.0, and 9.2 were made in three different 100 mL volumetric flask for the calibration of pH meter using buffer tablets.

3.3.9 Preparation of CDTA solution

57 mL glacial acetic acid, 58 g NaCl, and 4 g of 1, 2 cyclohexylene diamine tetra acetic acid (CDTA) was added in approximately 500 mL distilled water in a beaker. Then, to fix the pH in the range of 5.3 to 5.5, 6 N NaOH solution was added drop by drop keeping the beaker in cold water. Finally, the mixture was transferred in 100 mL volumetric flask and volume of CDTA solution was made upto mark using distilled water.

3.4 Instrumentation

Different instrumental analysis was carried on the investigated biosorbents before and after biosorption. The following instruments were used in the study.

Table 3: List of instruments used for the characterization of biosorbents

Name of Instruments	Company and Models
FE-SEM/EDX	JEOL JSM – 6700 F, Tokyo, Japan and Quanta FEG 450, FEI, Netherland
FTIR	IR affinity-1S SHIMADZU, Kyoto,Japan and Nicolet IS5, (Id5 ATR), Thermoscientific
XRD	Rigaku (SmartLab SE), Japan
XPS	Nexsa XPS system, ThermoFisher Scientific, UK (with an Al K α excitation source)
TGA/DSC	3+ Mettler Toledo, Switzerland
Zeta Analyzer	Malvern zetasizer NANO, Aimil Instruments Pvt. Ltd and HORIBA Scientific SZ-100
Fluoride Ion Selective Electrode	Bante 930
ICP-OES	PerkinElmer Avio 220Max, Scott/crossflow
ICP-MS	iCAP RQ, Thermoscientific

3.5 Preparation of biosorbents

3.5.1 Raw watermelon rind and banana peel powder

The watermelon rind and banana peels waste were collected from a nearby juice shop of Ratnapark, Kathmandu, Nepal. It was cut into pieces, cleaned repeatedly with DI water, and sun-dried. The dried watermelon rind pieces were then mechanically ground into a fine powder, sieved from 150-micron mesh, and dried for 24 h in an oven at 343K. The resulting dried powder was referred to as raw watermelon rind and raw banana peel and is now referred to as RWR and RBP.

3.5.2 Preparation of SWR and SBP powder

100 g of dried RWR and RBP were taken in separate 500 mL of saturated lime water with 2-3 pellets of NaOH (Ghimire & Inoue, 2007). The requisite amount of water was also added. The mixture was stirred for 24 h. After washing, the suspension was made to neutral and dried at 343K. These are referred as saponified watermelon rind (SWR) and saponified banana peel (SBP) hereafter. The synthetic route of preparation of SWR and SBP is shown in **Figure 13**.

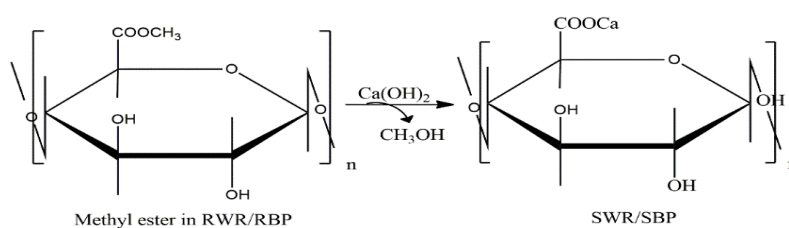


Figure 13: Reaction scheme for the saponification of RWR and RBP

3.5.3 Preparation of metal loaded watermelon rind/banana peel

500 mL of 0.1M Zr(IV) solution and 3 g of SWR/SBP were equilibrated for 24 h at pH 2.2 (Biswas *et al.*, 2008a). It was washed with distilled water several times until the pH was neutral, and then dried at 343 K. As a result, the resulting material is known as Zr(IV) loaded SWR/SBP and will hereafter abbreviated as Zr(IV)-SWR and Zr(IV)-SBP as obtained in **Figure 14**.

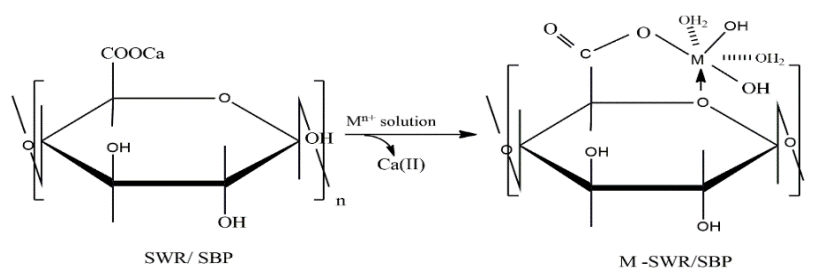


Figure 14: Reaction scheme for loading of metal onto SWR/SBP (M = Zr(IV) & La(III))

3.6 Characterization of biosorbents

The characterization of investigated biosorbents were screened through FE-SEM/EDX, FTIR, XRD, XPS, TGA/DSC and zeta potential analyzer. The surface morphology and elemental mapping were recorded by FE-SEM coupled with EDX using carbon-coated aluminum stub. The functional sites of the biosorbents were examined using FTIR in the wave number range from 4000-400 cm^{-1} . The crystallinity of biosorbents were analyzed using XRD system with built-in intelligence guidance. The thermal stability of biosorbents was studied using TGA/DSC. The thermal stability of biosorbent was measured taking 10 -15 mg of biosorbent at a heating rate of N_2 with a temperature range of 50-1000°C. The elemental composition and oxidation states onto the biosorbents were analyzed by an XPS equipped with a monochromatic Al $K\alpha$ X-ray source (1486.6 eV). The surface charge analysis of biosorbents were performed using zeta potential analyzer. The suspension of the zeta potential analysis was prepared by stirring 50 mg of the biosorbent with 25 mL of DI water for 24 h at a varying range of pH from 2-12.

3.7 Experimental procedure for batch studies

Batch biosorption experiments were performed with synthetic working solutions of F^- , PO_4^{3-} , As(III), Pb(II) and Hg(II). The suspension of biosorbent and biosorbate was equilibrated for 24h in a rotatory shaker at a speed of 190 rpm at 298K and concentration of biosorbate before and after biosorption was analyzed. The concentration of PO_4^{3-} and As(III) in the solution was analyzed using UV-Vis spectrophotometer (UV-2450 Shimadzu, Japan). The concentration of F^- in the solution was measured using fluoride ion selective electrode precision pH/Ion meter (Bante 930). The concentration of As(III), Hg(II) and Pb(II) in mg/L was measured

using ICP-OES while concentration of Hg(II) and Pb(II) in $\mu\text{g/L}$ was measured using ICP-MS.

3.7.1 Biosorption solution pH studies

The effect of pH was studied by stirring 30 mg of RWR and Zr(IV)-SWR with 20 mL of F^- ($\sim 10 \text{ mg/L}$) in separate conical flasks over the wide pH range of 2.0 -13.0. The suspension was equilibrated for 24 h and equilibrium concentration of F^- was measured. 30 mg of RBP and Zr(IV)-SBP was mixed with 20 mL of F^- ($\sim 10 \text{ mg/L}$) in separate conical flasks in the pH range of 2.0 - 13.0. The mixture was equilibrated for 24 h and equilibrium concentration was examined. 50 mg of RWR and Zr(IV)-SWR was added with 25 mL of PO_4^{3-} ($\sim 10 \text{ mg/L}$) in separate conical flasks in the pH range of 1.0-12.0. The suspension was equilibrated for 24 h and equilibrium concentration of PO_4^{3-} was measured. 25 mg of RWR and La(III)-SWR was mixed with 25 mL of As(III) solution ($\sim 10 \text{ mg/L}$) in separate conical flasks in the pH range of 2.0-13.0. The mixture was equilibrated for 24 h and residual concentration of As(III) was measured. Similarly, 10 mg of RWR, RBP, SBP, and SWR were mixed with 20 mL ($\sim 10 \text{ mg/L}$) of Hg(II)/Pb(II) in separate conical flasks adjusting the pH in the range of 1.0-7.0. The mixture was equilibrated for 24 h and residual concentration of respective ions were examined. For all experiments, the pH of the solution was adjusted adding few drops of HCl and NaOH solution.

3.7.2 Biosorption kinetic studies

The effect of contact time was studied stirring 30 mg of Zr(IV)-SWR/SBP with 20 mL of F^- ($\sim 10 \text{ mg/L}$) at varying time of 5 - 480 min. The equilibrium concentration of F^- was instantly measured. 50 mg of Zr(IV)-SWR was stirred with 25 mL of PO_4^{3-} solution ($\sim 10 \text{ mg/L}$) in the time range of 5 - 360 min and equilibrium concentration of PO_4^{3-} was measured. 25 mg of La(III)-SWR was stirred with 25 mL of As(III) solution ($\sim 10 \text{ mg/L}$) in the range of 5 - 360 min and equilibrium concentration was measured. 10 mg of SWR/SBP was equilibrated with 20 mL of Hg(II)/Pb(II) solution ($\sim 10 \text{ mg/L}$) in the range of 5 - 420 min and equilibrium concentration were measured instantly.

3.7.3 Biosorption isotherm studies

The effect of initial F^- concentration was studied by mixing 30 mg of Zr(IV)-SWR with 25 mL solution of F^- (~ 1 – 300 mg/L) at optimum pH in separate conical flasks. The suspension was equilibrated for 24 h and residual concentration of F^- was measured. 30 mg of Zr(IV)-SBP was mixed with 25 mL solution of F^- (~ 1- 300 mg/L) at optimum pH and the suspension was equilibrated for 24 h and residual concentration of F^- was measured. 50 mg of Zr(IV)-SWR was mixed with 25 mL solution of PO_4^{3-} (~ 5 – 100 mg/L) at optimum pH and the mixture was equilibrated for 24 h and residual concentration of PO_4^{3-} was measured. 25 mg of La(III)-SWR was mixed at optimum pH with 25 mL of solution of As(III) (~ 5 – 400 mg/L) and the mixture was equilibrated for 24 h and residual concentration of As(III) was measured. 10 mg of SWR and SBP was mixed with 20 mL of solution of Hg(II)/Pb(II) (~ 10 - 800 mg/L) and the mixture was equilibrated at optimum pH for 24 h and residual concentration of Hg(II)/Pb(II) was measured.

3.7.4 Biosorption biosorbent dosages studies

The effect of Zr(IV)-SBP dosages (2- 80 mg) was equilibrated for 24 h with 20 mL of F^- (~10 mg/L) at optimum pH in separate conical flasks for 24 h and the equilibrium concentration of F^- was measured. Zr(IV)- SWR of (5 - 80) mg was equilibrated with 10 mL of F^- (~10 mg/L) at optimum pH for 24 h in separate conical flasks and equilibrium concentration of F^- was measured. La(III)- SWR of (10 - 300) mg was equilibrated with 25 mL of As(III) (~10 mg/L) at optimum pH in separate conical flasks for 24 h and equilibrium concentration of As(III) was measured. Zr(IV)- SWR of (10 - 300 mg) was stirred with 25 mL of PO_4^{3-} (~10 mg/L) at optimum pH in different flasks for 24 h and equilibrium concentration was measured. SWR and SBP dosages of (5-100) mg was stirred with 20 mL of Pb(II)/Hg(II) (~15 mg/L) at optimum pH in separate conical flasks for 24 h and equilibrium concentration was measured.

3.7.5 Biosorption co-existing ions studies

The effect of co-existing ions was studied with varying concentration of (50, 150 & 200 mg/L) Cl^- , NO_3^- , and SO_4^{2-} together with PO_4^{3-} solution (~50 mg/L) in separate conical flasks at optimum pH adding 30 mg of Zr(IV)-SWR. The suspension was

stirred for 24 h and equilibrium concentration was measured. For Zr(IV)-SBP, varying concentration of (10, 50, 100, 150 & 200 mg/L) Cl^- , NO_3^- , and SO_4^{2-} synergetic effects of ($\text{Cl}^- + \text{NO}_3^- + \text{SO}_4^{2-}$) together with F^- solution (~50 mg/L) in separate conical flasks at optimum pH adding onto 30 mg of Zr(IV)-SBP. The suspension was stirred for 24 h and equilibrium concentration of F^- was measured. Different concentration of co-existing ions (10, 50, 100, 150 and 200 mg/L) of Cl^- , NO_3^- , SO_4^{2-} , and PO_4^{3-} , respectively were agitated with 25 mg of La(III)-SWR in separate conical flasks at optimum pH with 20 mL of As(III) solution (~10 mg/L) for 24 h and equilibrium concentration of As(III) was measured. 30 mg of Zr(IV)-SWR were agitated with 10, 50, 100, 150 and 200 mg/L of Cl^- , NO_3^- , SO_4^{2-} , HCO_3^- and PO_4^{3-} , respectively at optimum pH in separate conical flasks with 20 mL of F^- solution (~50 mg/L) for 24 h and equilibrium concentration of F^- was measured. 10 mg of SWR and SBP was agitated with 25 and 400 mg/L of Zn(II), Pb(II), Cd(II), Ni(II) and Cu(II), respectively at optimum pH in separate conical flasks with 20 mL of Hg(II) solution (~50 mg/L) for 24 h and equilibrium concentration of Hg(II) was measured. 10 mg of SWR and SBP was agitated with 25 and 400 mg/L of Zn(II), Hg(II), Cd(II), Ni(II) and Cu(II), respectively at optimum pH in separate conical flasks with 20 mL of Pb(II) solution (~50 mg/L) and equilibrium concentration of Pb(II) was measured.

3.7.6 Desorption studies

30 mg of F^- biosorbed Zr(IV)-SWR and Zr(IV)-SBP, respectively was put in separate conical flasks then was stirred with 10 mL of different molar concentration of NaOH (0.01- 2M) for 6 h and residual concentration of F^- was measured. 50 mg of PO_4^{3-} biosorbed Zr(IV)-SWR was stirred with 15 mL of different molar concentration of NaOH (0.01 - 5 M) in separate flasks for 6 h and residual concentration of PO_4^{3-} was measured. 50 mg of As(III) biosorbed La(III)-SWR was stirred with 15 mL of different molar concentration of NaOH (0.01 - 2 M) in separate conical flasks for 6 h and residual concentration of As(III) was measured. 30 mg of Hg(II)/Pb(II) biosorbed SWR and SBP was stirred with 10 mL of HNO_3 (0.01 - 2 M) in separate conical flasks for 6 h and residual concentration of solution was measured.

3.7.7 Regeneration and reusability studies

10 mL of 0.5 M NaOH was agitated with 50 mg of F-Zr(IV)-SWR for 10 h to regenerate Zr(IV)-SWR. It was filtered and dried in oven at 343K. The regenerated Zr(IV)-SWR was again biosorbed with F⁻. This process was repeated for 4-5 cycles and % biosorption was evaluated. 10 mL of 2 M NaOH was agitated with 50 mg of Zr(IV)-SBP@F for 10 h to regenerate Zr(IV)-SBP. It was filtered and dried in oven at 343K. The regenerated Zr(IV)-SBP was again biosorbed with F⁻. This process was repeated for 4-5 cycles and % biosorption was evaluated. 10 mL of 1 M HNO₃ was agitated with 50 mg of Hg-SWR and Pb-SWR for 10 h to regenerate SWR. It was filtered and dried in oven at 343K. The regenerated SWR was again biosorbed with Hg(II). This process was repeated for 4-5 cycles and % biosorption was evaluated. Similarly, 10 mL of 1 M HNO₃ was mixed with 50 mg of Hg-SBP and Pb-SBP for 10 h to regenerate SBP. It was filtered and dried in oven at 343K. The regenerated SBP was again biosorbed with Hg(II). This process was repeated for 4-5 cycles and % biosorption was evaluated.

3.7.8 Concentration analysis

The instruments ICP-OES and ICP-MS were calibrated by measuring the intensity of all ions of interest in ICP grade standards (AR grade, Sigma-Aldrich, 99.999%) that represents a range of concentration likely to be encountered in the unknown samples. Software was used to create a calibration graph with the measured intensity *versus* concentration of tested ions in the standard solution. The correlation coefficient of data was obtained which was closer to unity. Then, the calibrated ICP-OES and ICP-MS were used to measure the concentration of tested ions on the unknown samples in mg/L and µg/L, respectively.

3.7.9 Error function analysis

Different error functions, including Chi-square (χ^2) test, root-mean square error (RMSE), and mean absolute error (MAE), were estimated to investigate the fitting of kinetic and isotherm models, and assess the reproducibility of the biosorption process. The mathematical expression for their calculations is shown by the following equations as,

$$\chi^2 = \sum_{i=1}^N \frac{(q_{m,e} - q_{m,c})^2}{q_{m,c}} \quad (18)$$

$$\text{RMSE} = \sqrt{\left[\frac{\sum_{i=1}^N (q_{m,e} - q_{m,c})^2}{N} \right]} \quad (19)$$

$$\text{MAE} = \left(\frac{1}{N} \right) \sum_{i=1}^N |q_{m,e} - q_{m,c}| \quad (20)$$

where $q_{m,e}$ (mg/g) is the experimental biosorption capacity at equilibrium and $q_{m,c}$ (mg/g) is the theoretically calculated biosorption capacity at equilibrium. 'N' is the number of experimental data points. The lower value of error function predicts the best fits to the models. The lower values of error functions signifies that the experimental values are closer with the calculated values of the fitted models.

CHAPTER 4

RESULTS AND DISCUSSION

4.1 Chemical modification of watermelon rind and banana peels

Pectin is a weakly acidic polysaccharide, which is commonly pectic acid with some methyl esterified carboxylic acid functional groups. After $\text{Ca}(\text{OH})_2$ treatments, these methyl esters can be easily hydrolyzed converting into pectic acid salt (Ghimire & Inoue, 2007). Calcium salt of pectic acid is expected to function as weakly acidic cation exchange materials is known as saponified watermelon (SWR) and saponified banana peel (SBP). SWR and SBP has replaceable $\text{Ca}(\text{II})$ that can be substituted with cations. To develop anion exchange sites modification of SWR and SBP is necessary. The loading of $\text{La}(\text{III})$ or $\text{Zr}(\text{IV})$ onto SWR and SBP happened by the substitution of $\text{Ca}(\text{II})$ ion by cation exchange reaction as shown in **Figure 15**. It is ascribed that the carboxyl group in SWR or SBP forms a stable five membered pyranose polymeric matrices with $\text{La}(\text{III})$ and $\text{Zr}(\text{IV})$. Out of all the positive charges, 1 or 2 positive charges are neutralized with carboxylic acid functional group of watermelon/banana pectic acid but others cannot be neutralized due to steric hindrance developed on the large polymer matrix of watermelon/banana peel pectic acid. However, the remained positive charges are neutralized with hydroxyl ion of the solution. These hydroxyl ions are substituted with anionic pollutants during anion biosorption.

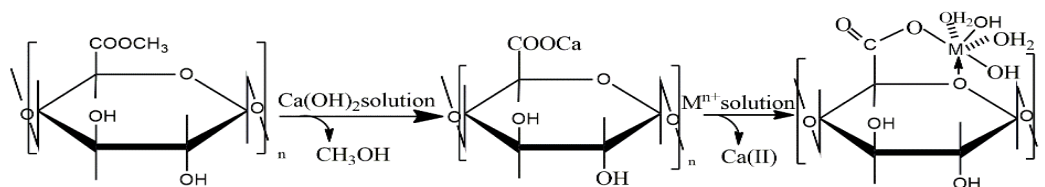


Figure 15: Reaction mechanism for the synthesis of M-SWR and M-SBP biosorbent ($M = \text{Zr}(\text{IV})$, $\text{La}(\text{III})$) (Ghimire & Inoue, 2007).

4.2 Fluoride ion biosorption

4.2.1 Characterization of biosorbents

4.2.1.1 Surface morphology of biosorbents

The Fe-SEM micrographs of RWR, SWR, Zr(IV)-SWR before and after fluoride biosorption are displayed in **Figure 16**. As observed in the images, RWR possess almost smooth surface without distinctive pores. RWR in **Figure 16 (a)** contains white patches like materials on its surface which can be nutrients, sugar, and low molecular weight organic species (Aryal *et al.*, 2022). As seen in SWR, **Figure 16 (b)** contains irregular surface with small granules. **Figure 16 (c)**, Zr(IV)-SWR and **Figure 16(d)** Zr(IV)-SBP has heterogeneous structures with uneven cavities which can be suitable for the biosorption reaction. Whereas, after biosorption, fluoride biosorbed Zr(IV)-SWR and Zr(IV)-SBP surface becomes smooth and uniform (**Figure 16 (e)** and **(f)**) in comparison to Zr(IV) SWR/SBP initially. It might be due to the fluoride anion occupancy on the surface of Zr(IV)-SWR/Zr(IV)-SBP. Jeyaseelan *et al.* (2021) also reported the consistent morphology in the fluoride ion biosorption onto amine functionalized *Shorea robusta* flower. The biosorption of fluoride ion onto Zr(IV)-SWR by EDX spectra.

4.2.1.2 EDX spectra with color mapping

The elemental mapping of SWR, Zr(IV)-SWR and F-Zr(IV)-SWR along with their spectra were displayed in **Figure 17**. The color mapping showed C (54.22%), O (40.05%), K(0.41%), Na(0.16%), Mg(0.24%), P (0.46%), Si(0.14%) and Ca(4.33%) elements present on SWR. **Figure 17 (d)** indicated the intense peak of C, O, and Ca atom. It can be attributed that Ca(II) ion on SWR surface appeared from Ca(OH)₂ during saponification reaction. SWR is expected to act as cation exchanger. **Figure 17 (e)** indicated the peaks of C (49.90%), Zr (16.37%), Cl (0.58%), Si (1.91%), and O (31.24%) at binding energies 0.27, 2.04, 2.62, 1.74, and 0.53 keV of Zr(IV)-SWR. The intense peak of Zr atom onto loaded Zr(IV)-SWR indicated the successful loading of Zr(IV) onto the polymeric matrix of SWR, which is expected to act as an anion exchanger for the biosorption of fluoride ion. The persistence of Zr peak after biosorption of fluoride ion also disseminate that Zr(IV) remains occupied on the biosorbent of Zr(IV)-SWR without leakage of Zr(IV). In **Figure 17 (f)**, the peaks of F (3.84%), Cl (0.57%) O (22.54%), Zr (14.83%) and C (58.21%) are observed in the

spectra. This is further confirmed by surface color mapping which is shown in **Figure 17 (b) and (c)**. It highlighted the loading of Zr(IV) onto SWR and biosorption of fluoride ion onto Zr(IV)-SWR occurred effectively.

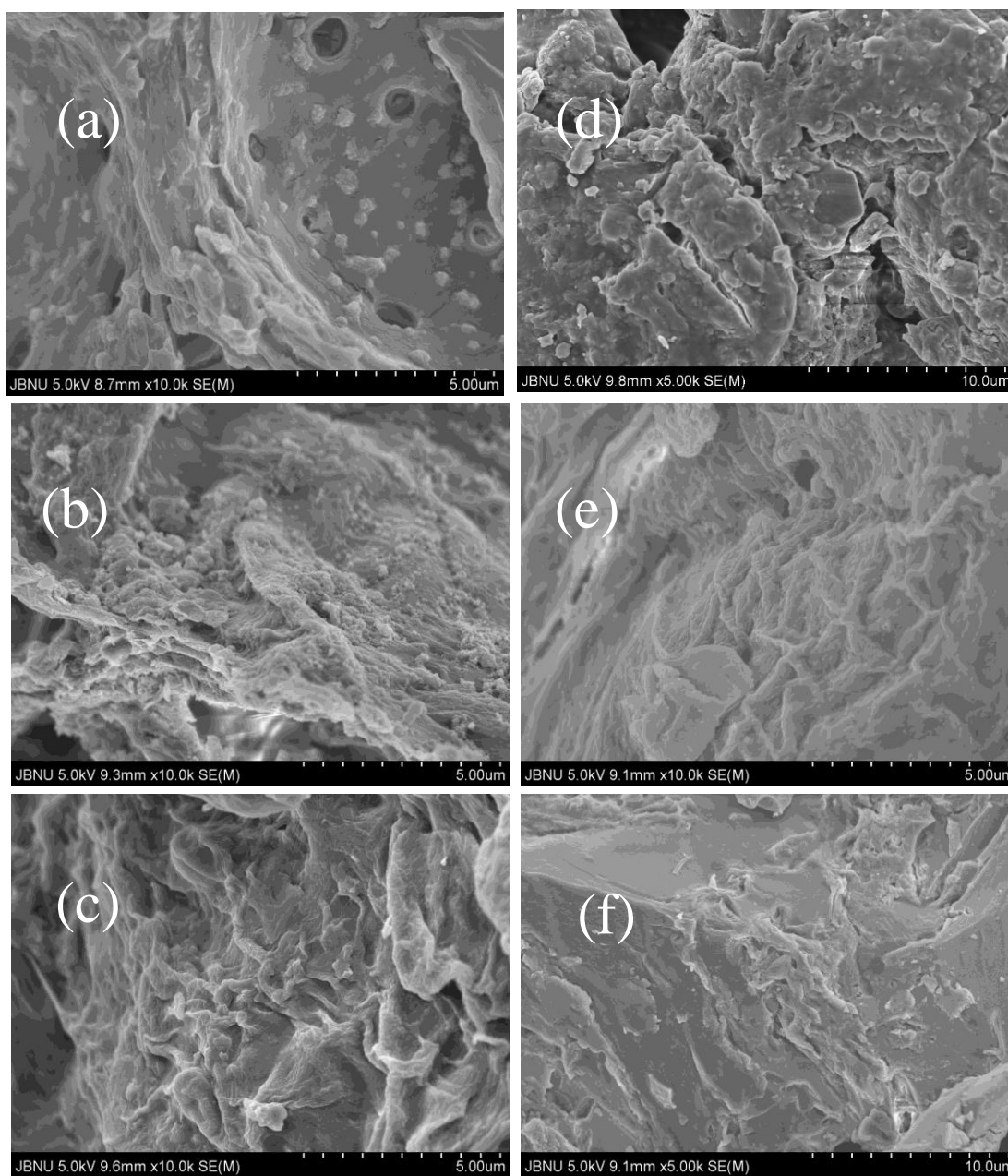


Figure 16: FE-SEM micrographs of (a) RWR (b) SWR (c) Zr(IV)-SWR (d) Zr(IV)-SBP (e) F- Zr(IV)-SWR and (f) F- Zr(IV)-SBP.

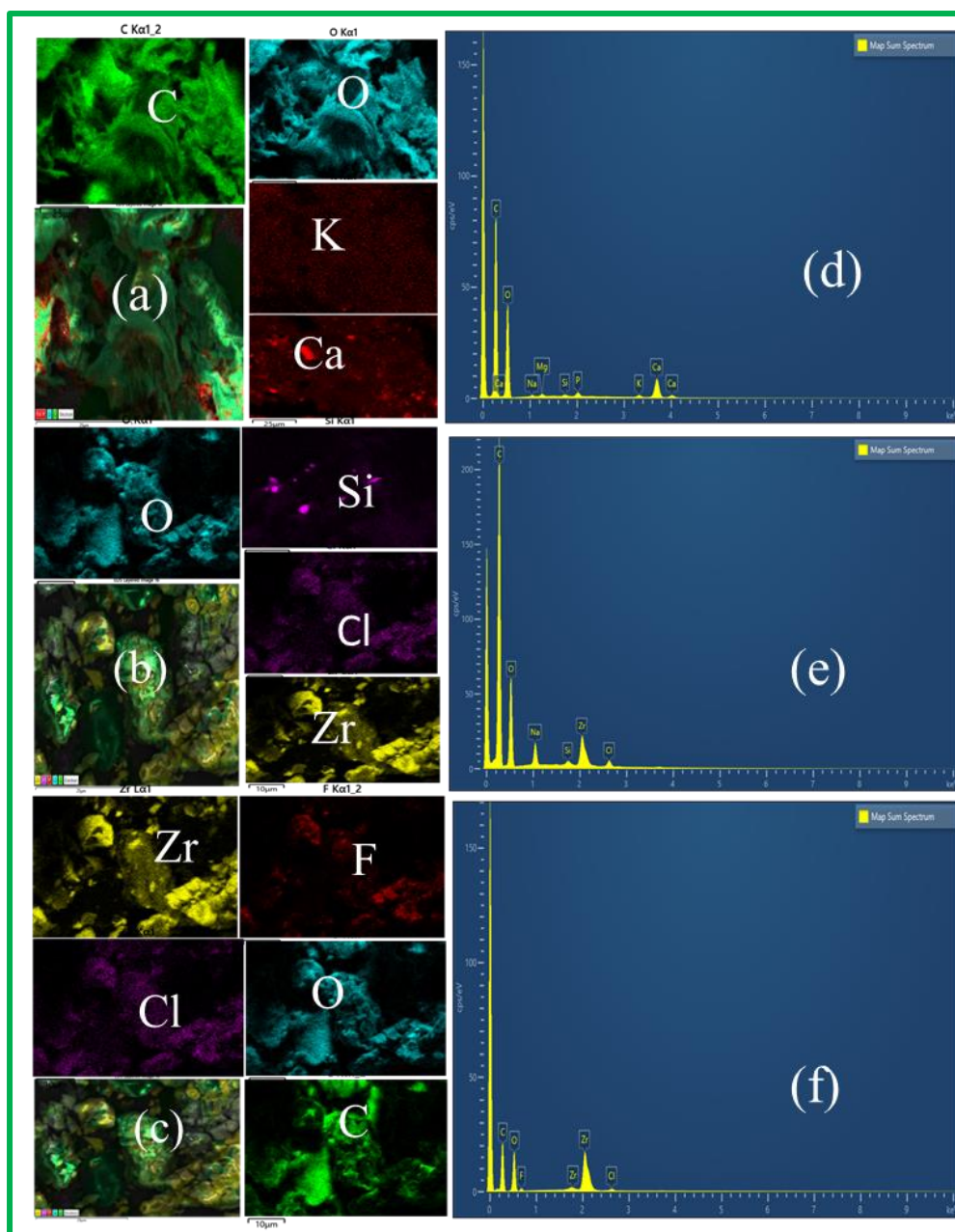


Figure 17: EDAX spectra and elemental mapping of SWR (a, d), Zr(IV)-SWR (b, e) and fluoride biosorption onto Zr(IV)-SWR (c, f).

4.2.1.3 Functional groups analysis

The FTIR spectroscopy was operated to explore the chemical changes of the functional groups of RWR, SWR and Zr(IV)-SWR as shown in **Figure 18 (a)** and RBP, SBP and Zr(IV)-SBP in **Figure 18 (b)**. The spectra of RWR shows a broad peak at around 3331 cm^{-1} and RBP at around 3340 cm^{-1} is associated with -OH stretching vibration of hydroxyl functional group present in cellulose, hemicelluloses, pectin, and lignin on the RWR or RBP surface. The peak at around 2912 cm^{-1} in RWR and

2947 cm^{-1} in RBP correspond to C-H stretching vibration of methoxyl group in cellulose, hemicellulose and in general aliphatic acids (Mondal *et al.*, 2013). This peak becomes wide after Zr(IV) loading in Zr(IV)-SWR and Zr(IV)-SBP. It might be due to coordination of hydroxyl groups and absorbed molecules of water in Zr(IV) matrices. The peak observed at around 1717 cm^{-1} in RWR and 1735 cm^{-1} in RBP is ascribed to the stretching vibration C=O and C-O of carboxylate groups (Aloulou *et al.*, 2021). After $\text{Ca}(\text{OH})_2$ treatments, this peak was vanished and two new peaks were observed at around 1534 and 1319 cm^{-1} which are the characteristics peaks of metal carboxylate (Dehghani *et al.*, 2018; Gupta *et al.*, 2015). Likewise, after Zr(IV) loading, these peaks in SWR and in SBP changed to lower frequency at around 1517 cm^{-1} and 1606 cm^{-1} that can be justifiably assessed due to the replacement of Ca(II) by Zr(IV) of greater atomic mass (Gawkowska *et al.*, 2019; De *et al.*, 2018). The peak at around 1031 cm^{-1} may be attributed due to Si-O stretching (Lopez *et al.*, 2019). The results from FTIR spectra revealed that carboxylic group is major functional group involve in chemical modification during $\text{Ca}(\text{OH})_2$ treatments and Zr(IV) loading.

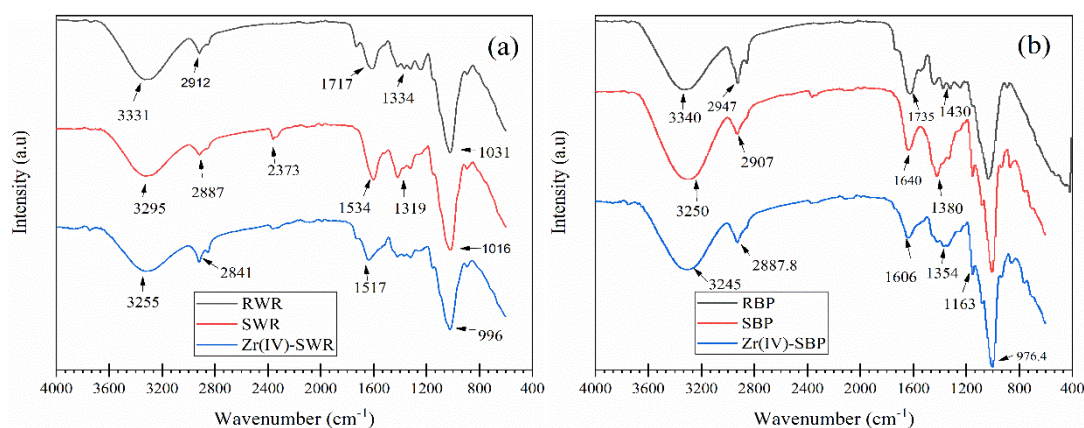


Figure 18: FTIR spectra of (a) RWR, SWR and Zr(IV)-SWR (b) RBP, SBP and Zr(IV)-SBP in the range from 4000- 400 cm^{-1}

4.2.1.4 Thermogravimetric analysis

As shown in **Figure 19**, it was found that almost 2% weight loss occurred in RWR, SWR and Zr(IV)-SWR between temperature 0 -100°C. It might be due to the loss of absorbed H_2O molecules. Additionally, 10% weight loss between 100-250°C is noticed due to hydroxy group converted into water (Zhou *et al.*, 2010). The loss could be due to the degradation of organic species as well as volatile substances. The maximum oxidation of RWR and SWR biosorbents occurred in between 750-1000°C.

However, Zr(IV)-SWR can resist high temperature due to strong polymeric matrices. Above 750°C, Zr(IV)-SWR is found stable. Hemicellulose present in the biosorbents decomposed at a considerably at lower temperature. The complete degradation of cellulose occurs at around 300°C while lignin pyrolysis occurs at around 400°C (Taib *et al.*, 2021).

4.2.1.5 XRD analysis of biosorbent

Figure 20 showed the XRD pattern of RBP and Zr(IV)-SBP. The XRD analysis of RBP showed some crystalline cellulose peaks due to crystalline structure. But Zr(IV)-SBP contains broad peaks like structures. It is attributed due to amorphous structure of Zr(IV)-SBP after Zr(IV)-loading. The amorphous structure could provide a greater specific surface area and more available active sites for biosorption (Poudel *et al.*, 2021). The distinct pattern of peaks observed on Zr(IV)-SBP indicates amorphous Zr(IV) oxide onto biosorbent matrices (Prasad *et al.*, 2014).

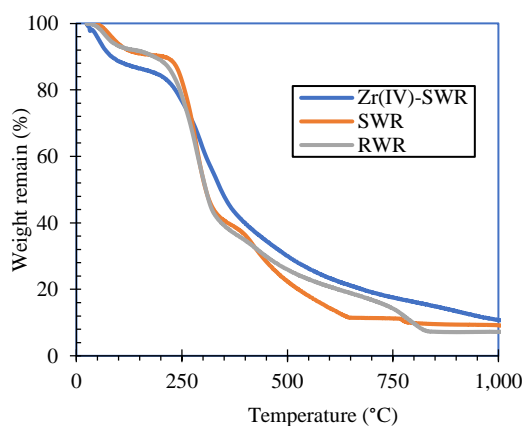


Figure 19: Thermogravimetric curves for RWR, SWR and Zr(IV)-SWR

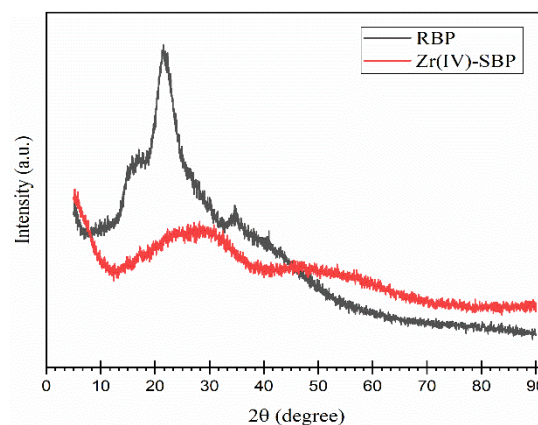


Figure 20: XRD pattern of RBP and Zr(IV)-SBP

4.2.1.6 Surface charge of Zr(IV)-loaded biosorbents

The effectiveness of biosorption process relies on the nature of ions to be biosorbed and surface charge of the biosorbent. The surface charge of Zr(IV)-SWR biosorbent was analyzed using zeta potential measurement based on point of zero charge (pH_{pzc}) of biosorbents as shown in **Figure 21**. The isoelectric point (pH_{pzc}) of Zr(IV)-SWR and Zr(IV)-SBP are evaluated to be 5.4 and 3.8, respectively. The surface charge of Zr(IV)-SWR at $pH = 5.4$ is neutral and Zr(IV)-SBP at $pH = 3.8$. At $pH < pH_{pzc}$, the

surface of biosorbents is positively charged where biosorption of negatively charged fluoride ions was expected to be favorable through columbic interaction, but at $\text{pH} > \text{pH}_{\text{pzc}}$, the biosorbents surface are negatively charged. The biosorption of fluoride ion at higher pH may be unfavorable because of competition between hydroxyl ion and fluoride ion for the same binding sites.

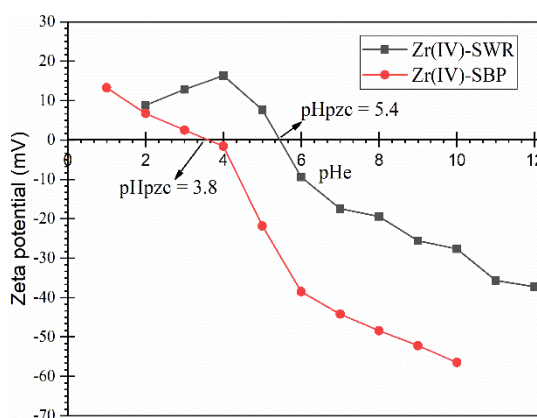


Figure 21: Zeta potential analysis at different pH of (a) Zr(IV)-SWR and (b) Zr(IV)-SBP

4.2.2 Batch biosorption studies

4.2.2.1 Effect of pH and fluoride biosorption mechanism

The effects of pH for biosorption of fluoride onto RWR and Zr(IV)-SWR is shown in Figure 22 (a) and that of RBP, Zr(IV)-SBP is shown in **Figure 22 (b)**. In figure 21(a), percentage biosorption of fluoride increased with increasing pH up to 4.03 then diminished with gradual increase in pH. At pH 2.66, the biosorption percentage of RWR and Zr(IV)-SWR reached 2.56% and 21.92%. The biosorption percentage of fluoride was 21.02% and 89.36% at pH around 4.03. Similarly, the fluoride biosorption on RBP is about 24% at optimum pH. Moreover, the biosorption of fluoride ions onto Zr(IV)-SBP reached a maximum value (94.5%) at equilibrium pH of 2.9 and gradually slowed down. The speciation of fluoride ion in aqueous solution suggested that at low pH ($\text{pH} < 2$) neutral species (HF $\text{pK}_a = 3.2$) and H_2F_2 are prevalent along with the trace of hydrogen difluoride (HF_2^-) ion. At $\text{pH} < 2$, weakly ionizable HF is produced because of union of fluoride ion with H^+ of the biosorbent surface as in reaction (a). The inadequacy of free fluoride ion leads to poor biosorption at low pH. But above $\text{pH} = 2$, the concentration of fluoride ion is

prevalent in the aqueous solution. The results showed that optimum pH for biosorption of fluoride onto Zr(IV)-SWR and Zr(IV)-SBP are 4.03 and 2.9, respectively. The hydroxyl ligands exist in coordination spheres of Zr(IV) in Zr(IV)-SWR and Zr(IV)-SBP are protonated by which positively charged surface is created as in reaction (b). This positively charge surface is favorable for the interaction of fluoride ion by columbic force of attraction with the formation of water molecules as depicted in reaction (c). Additionally, the hydroxyl ligands coordinated with Zr(IV) are easily exchanged with fluoride ion. The unique octahedral nature of the Zr(IV) center increases accessibility of the ion exchange sites, which initiates the biosorption of fluoride onto Zr(IV)-SWR and Zr(IV)-SBP through ligand exchange mechanism as in reaction (d). However, at higher pH, the hydroxyl ions along with fluoride ions competes for the same biosorption sites therefore, reduced the percentage biosorption of fluoride ion. This result is consistent with the studies reported for the biosorption of fluoride using orange waste and hydroxyapatite derived from *Limacine artica* shells (Paudyal *et al.*, 2011; Samant *et al.*, 2017).

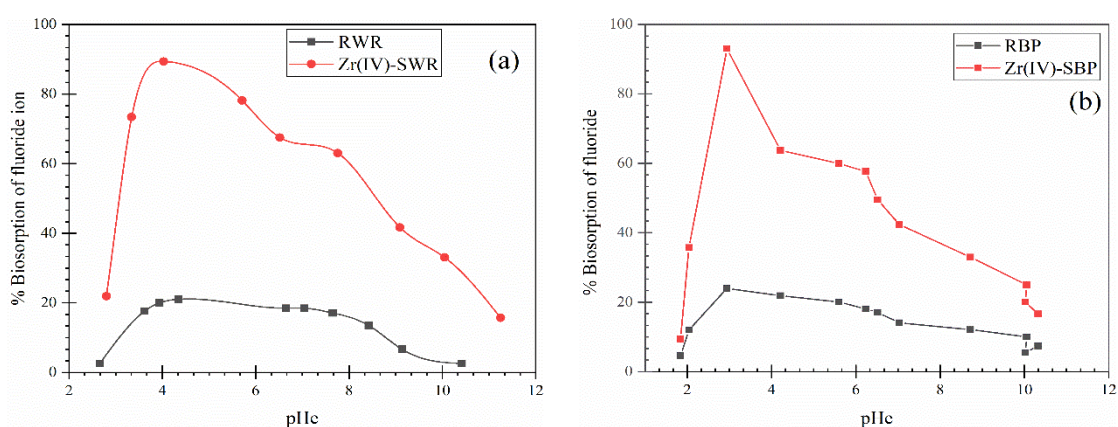
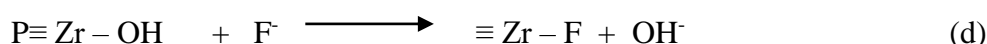
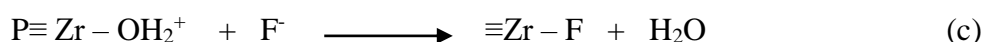
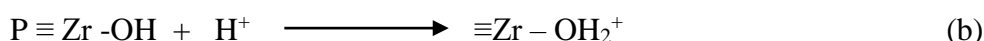


Figure 22: Effect of pH on the biosorption of fluoride onto (a) RWR and Zr(IV)-SWR and (b) RBP and Zr(IV)-RBP (Conditions: $m/v = 1.2$ g/L, $C_i = 10$ mg/L, $t = 24$ h, $T = 298$ K)

4.2.2.2 Effect of contact time

Fluoride biosorption onto RWR and RBP was found insignificant in pH studies thus, kinetics of fluoride ion biosorption was studied using Zr(IV) loaded biosorbents as depicted in **Figure 23** and **Figure 24**. It is apparent from the figure that, initially the biosorption rate increases rapidly then slowed down and attained equilibrium (plateau) at 120 min in case of Zr(IV)-SWR whereas it takes around 300 min for Zr(IV)-SBP. The results can be ascribed since Zr(IV)-SWR and Zr(IV)-SBP initially have large number of unoccupied active biosorption sites and with lapse of time, biosorption sites are gradually occupied and attained saturation after complete occupancy of fluoride ions. The kinetic data of fluoride biosorption onto Zr(IV)-SWR and Zr(IV)-SBP was further validated using kinetic modeling such as PFO and PSO models as shown in **Figure 23 (b)** and **(c)** and **Figure 24 (b)** and **(c)**, respectively.

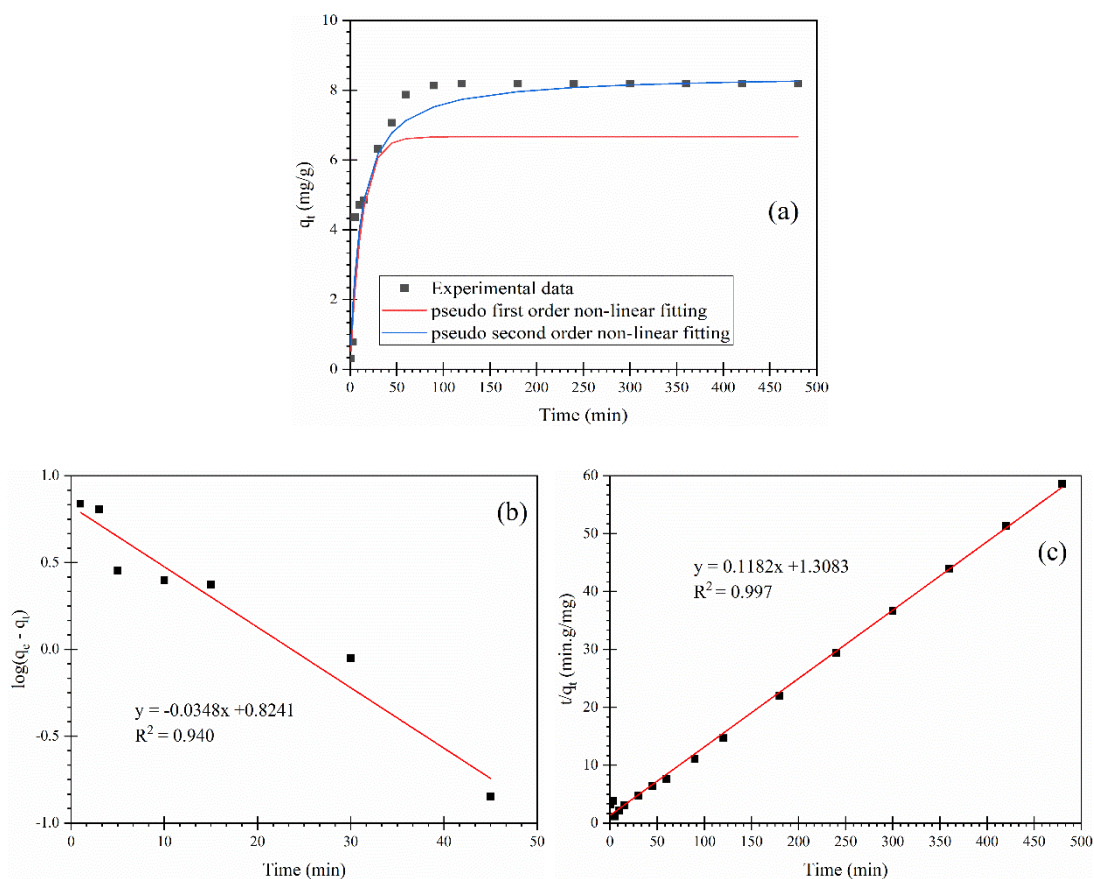


Figure 23: Biosorption kinetics of Zr(IV)-SWR (a) Non-linear plot of kinetic modelling with experimental data (b) PFO and (c) PSO model (Conditions: $m/v = 1.2$ g/L, $C_i = 10$ mg/L, pH = 4.03, $t = 24$ h, $T = 298$ K)

The evaluated values of the kinetic parameter models of Zr(IV)-SWR and Zr(IV)-SBP are represented in **Table 4**. The coefficient of determination (R^2) of PSO model is higher than PFO model for both the cases which ascertained that PSO model is more validated than PFO model. Furthermore, the calculated q_e value of PSO model in both the cases are closer to the experimental value compared to q_e , cal determined from PFO model. In addition, the experimental data in non-linear fitting agrees with PSO model as shown in Figure 23 (a) and 24 (a). Therefore, the fluoride biosorption onto Zr(IV)-SWR and Zr(IV)SBP can be described well by the PSO model thus the rate limiting step should be mainly chemisorption involving sharing or exchange of electrons between fluoride anion and biosorbent.

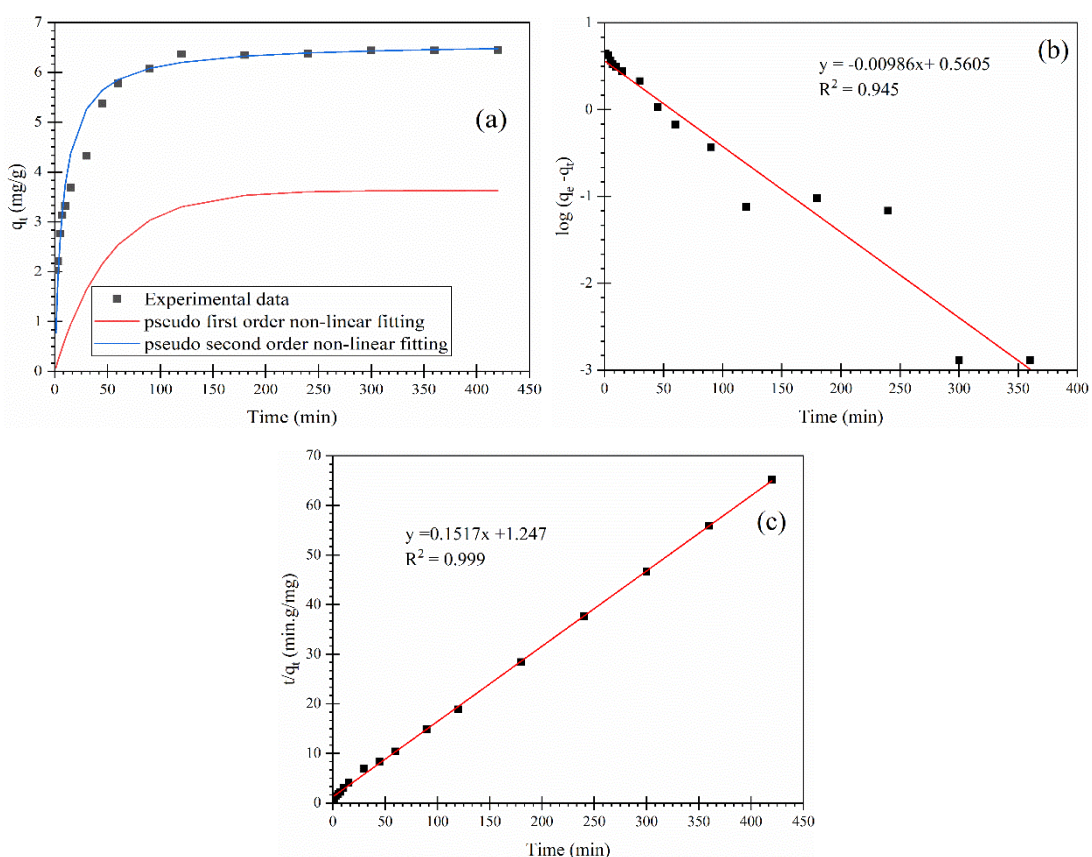


Figure 24: Biosorption of fluoride onto Zr(IV)-SBP (a) Non-linear kinetic modeling of PFO and PSO model (b) PFO and (c) PSO model (Conditions: $m/v = 1.5$ g/L, $C_i = 10$ mg/L, $pH = 2.9$, $t = 24h$, $T = 298$ K)

Table 4: Kinetic parameters for biosorption of fluoride ion onto biosorbents

Models	Parameters	Zr(IV)-SWR	Zr(IV)-SBP
PFO	k_1 (1/min)	0.0802 ± 0.02	0.02 ± 0.006
	q_e , cal (mg/g)	6.66 ± 0.43	3.63 ± 0.095
	R^2	0.94	0.94
PSO	k_2 (g/mg.min)	0.0107 ± 0.01	0.02 ± 0.011
	q_e , cal (mg/g)	8.45 ± 0.23	6.59 ± 0.15
	R^2	0.997	0.99
	q_e , exp (mg/g)	8.18 ± 0.09	6.44 ± 0.24

4.2.2.3 Biosorption isotherm of fluoride ion

Figure 25 (a) showed the effect of equilibrium concentration of fluoride on the biosorption process using Zr(IV)-SWR and Zr(IV)-SBP. It is apparent from the figure that the biosorption capacity of biosorbents increases with gradual rise in fluoride concentration and reached the equilibrium value which is marked by the plateau observed. Further the experimental data for biosorption of fluoride ion onto Zr(IV)-SWR and Zr(IV)-SBP is modeled with Langmuir biosorption isotherm and Freundlich biosorption isotherm as presented in **Figure 25** and **Figure 26 (b)** and **(c)**. The isotherm variables are listed in **Table 5**. The Langmuir plot of C_e/q_e versus C_e of Zr(IV)-SWR and Zr(IV)-SBP have very good linearity with coefficient of determination, $R^2 = 0.99$ compared with Freundlich plot. The maximum biosorption capacity of Zr(IV)-SWR and Zr(IV)-SBP according to Langmuir isotherm model are evaluated to be 28.98, 36.02 mg/g, respectively. This result is consistent with activated carbon fibers modified with zirconium and *Limacine artica* shells (Pang *et al.*, 2020; George *et al.*, 2019; Samant *et al.*, 2017). In addition, the non-linear fitting of experimental data with the modeling results of both models are compared, which agrees to non-linear modeling of Langmuir isotherm model as shown in **Figure 25 (a)** and **Figure 26 (a)**. Moreover, the dimensionless separation parameter, R_L is evaluated as displayed in **Figure 25 (d)** and **Figure 26 (d)**, which indicated that the values of R_L lies in the range of 0.658 to 0.018 for Zr(IV)-SWR and 0.01 to 0.8 for Zr(IV)-SBP which strongly suggested the favorable biosorption of fluoride ions as defined by $0 < R_L < 1$ (Xu *et al.*, 2009; Özcan *et al.*, 2009)

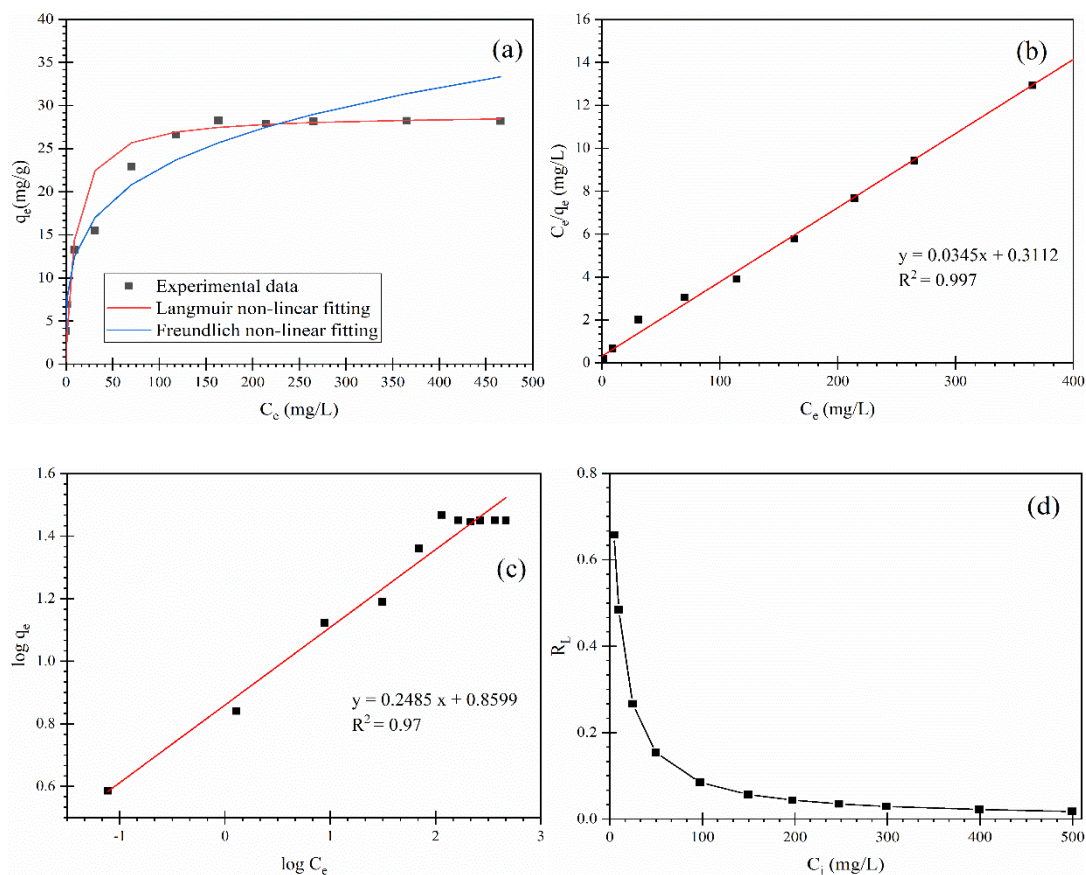


Figure 25: Biosorption isotherms of fluoride ion onto Zr(IV)-SWR (a) Non-linear modeling of Langmuir and Freundlich isotherm with experimental data (b) Langmuir isotherm model (c) Freundlich isotherm model and (d) Variation of R_L with initial concentration (Conditions: $m/v = 1.2$ g/L, $t = 24$ h, $pH = 4.03$, $T = 298$ K)

Table 5: Isotherm parameters for biosorption of fluoride ions onto biosorbents

Isotherm Models	Parameters	Zr(IV)-SWR	Zr(IV)-SBP
Langmuir	q_m exp. (mg/g)	28.18 ± 0.12	35.31 ± 2.32
	q_m cal. (mg/g)	28.98 ± 0.06	36.02 ± 1.67
	b (L/g)	0.111 ± 0.02	0.23 ± 0.08
	R^2	0.997	0.99
Freundlich	K_F (mg/g) (L/mg) $^{1/n}$	7.24 ± 0.21	4.91 ± 0.86
	$1/n$	0.25 ± 0.03	0.43 ± 0.21
	R^2	0.97	0.90

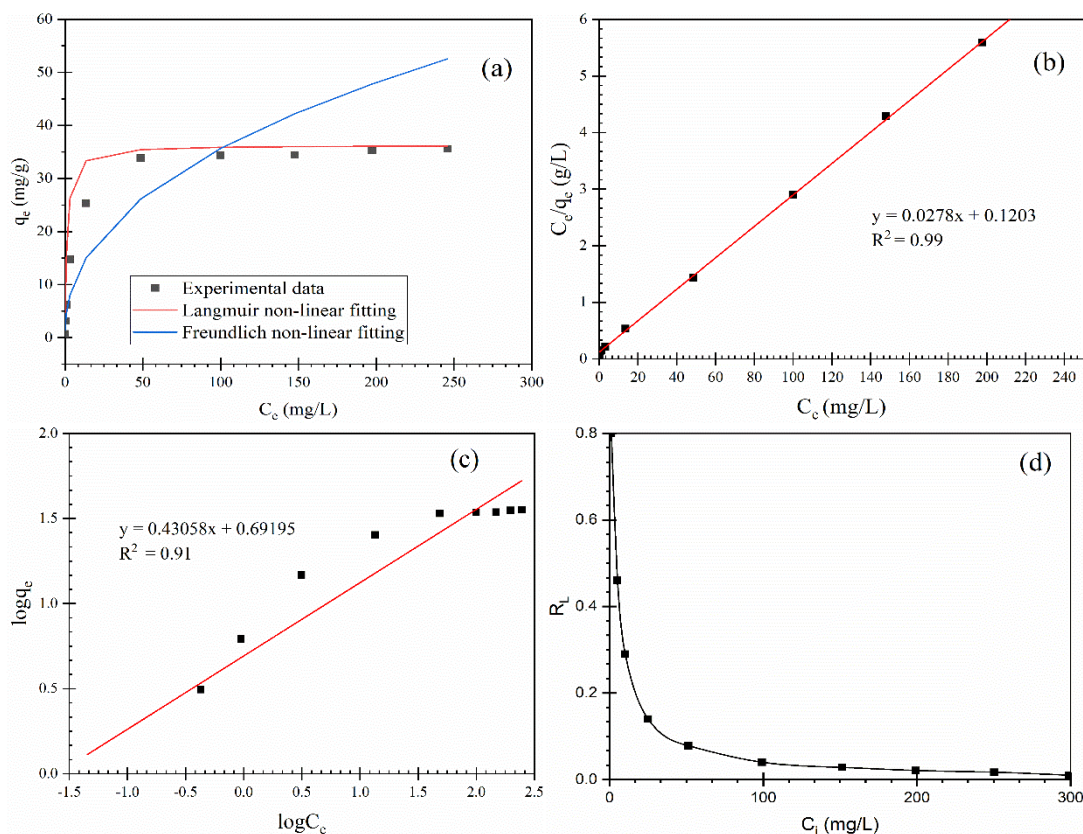


Figure 26: Biosorption isotherm studies onto Zr(IV)-SBP (a) Non-linear plot of Langmuir and Freundlich isotherm model with experimental data (b) Langmuir isotherm model and (c) Freundlich isotherm model (d) variation of R_L with initial concentration (Conditions: $m/v = 1.5$ g/L, $C_i = 10$ mg/L, $t = 24$ h, $pH = 2.9$, $T = 298$ K)

4.2.2.4 Effect of biosorbent dosage

The biosorption performance of Zr(IV)-SWR and Zr(IV)-SBP for fluoride ion at different solid-liquid ratio at its optimum pH was investigated as presented in **Figure 27**. The graphical representation showed that the residual concentration of fluoride decreases with increasing dosages of Zr(IV)-SWR and Zr(IV)-SBP. The dosages of 1.5 g/L of Zr(IV)-SWR can lowered the fluoride concentration to 1.43 mg/L and 2.5 g/L of Zr(IV)-SBP to 1.25 mg/L. The investigated biosorbents can lowered down the fluoride concentration below 1.5 mg/L in drinking water as allowable limit of fluoride as prescribed by WHO. The gradual increase of dosages avails the surface-active sites for biosorption so that biosorption can take effectively. However, at higher dosage, the binding sites of Zr(IV)-SWR and Zr(IV)-SBP becomes superfluous for the limited quantity of fluoride as a result steady biosorption takes place (Talat *et al.*, 2018; Reddy *et al.*, 2010).

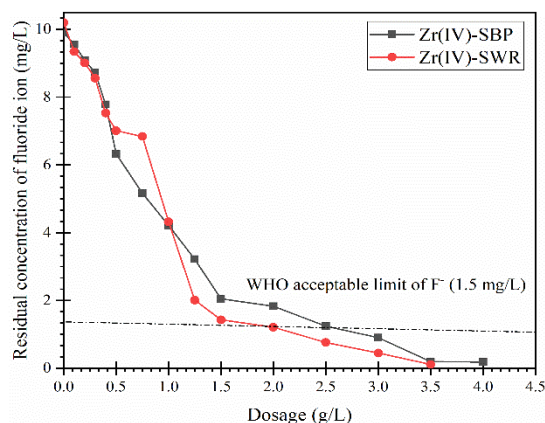


Figure 27: Effect of biosorbent dosage of Zr(IV)-SWR and Zr(IV)-SBP onto fluoride ion biosorption (Conditions: mass of Zr(IV)-SWR, Zr(IV)-SBP = 5 to 80 mg, $v = 25$ mL, $C_i = 10$ mg/L, $\text{pH} = 4.03$ and $\text{pH} = 2.9$, $t = 24$ h, $T = 298\text{K}$)

4.2.3 The error analysis

The error values determined for both the kinetic models and isotherm models were evaluated and displayed in **Table 6** and **Table 7**. The lower error function and higher R^2 values are observed for PSO kinetic and Langmuir isotherm model compared to PFO and Freundlich isotherm model. Thus, biosorption phenomenon is better described by PSO kinetic and Langmuir type monolayer biosorption.

Table 6: Error analysis on kinetic studies of fluoride ion biosorption onto biosorbents

Error function	Kinetic model (Zr(IV)-SWR)		Kinetic model (Zr(IV)-SBP)	
	PFO	PSO	PFO	PSO
χ^2	0.347 ± 0.24	0.008 ± 0.02	2.17 ± 0.46	0.0034 ± 0.002
RMSE	0.45 ± 0.12	0.081 ± 0.003	0.806 ± 0.87	0.043 ± 0.004
MAE	0.138 ± 0.131	0.024 ± 0.013	0.234 ± 0.101	0.0125 ± 0.012

Table 7: Error analysis on isotherm studies of fluoride biosorption onto biosorbents

Error function	Isotherm model (Zr(IV)-SWR)		Isotherm model (Zr(IV)-SBP)	
	Langmuir	Freundlich	Langmuir	Freundlich
χ^2	0.022 ± 0.01	2.13 ± 0.23	0.014 ± 0.004	4.22 ± 1.04
RMSE	0.24 ± 0.03	2.36 ± 1.06	0.204 ± 0.012	3.35 ± 1.11
MAE	0.072 ± 0.003	0.71 ± 0.21	0.059 ± 0.005	0.968 ± 0.96

A comparison in biosorption capacity of Zr(IV)-SWR and Zr(IV)-SBP is made with the other adsorbents found in the literature as listed in **Table 8**. The table showed that

the tested biosorbents have satisfactory biosorption capacity for fluoride ion compared to other adsorbents. In addition, it showed that materials loaded with La(III) and Zr(IV) exhibited higher biosorption capacity. It can be attributed due to the existence of hydroxyl ions in a coordination sphere of metal loaded biosorbents which can easily exchange with fluoride ion by ligand exchange reaction during biosorption (Ghimire *et al.*, 2007). Thus, Zr(IV)-SWR and Zr(IV)-SBP could be the promising biosorbent to eliminate fluoride ion present in solution.

Table 8: Comparison of defluoridation capacity of Zr(IV)-SWR and Zr(IV)-SBP with the other adsorbents

Adsorbents	pH	q _m (mg/g)	References
Zr(IV)-SWR	4.03	28.98	Current study
Zr(IV)-SBP	2.94	36.02	Current study
Al(OH) ₃ -loaded zeolite	5.5– 6.5	18.12	(Chen <i>et al.</i> , 2022)
Rice husk biosorbent	6.5	15.2	(B. Vijila <i>et al.</i> , 2021)
AC- fibers modified with Zr(IV)	5	28.50	(Pang <i>et al.</i> , 2020)
Zr(IV)-impregnated anion exchange resin	7	12.03	(Singh <i>et al.</i> , 2020)
Zr(IV)- modified tea waste	3.0 -10.0	20.56	(Mei <i>et al.</i> , 2019)
Indian sandal wood leaf powder	5-7	4.66	(Khound & Bharali, 2018)
Rice husk biochar	7	21.7	(Goswami & Kumar, 2018)
La(III)-modified pomelo peel biochar	6.5	19.86	(Wang <i>et al.</i> , 2018)
<i>Limacine artica</i> shells (HAP)	6.3	28.57	(Samant <i>et al.</i> , 2017)
Ultrafine tea powder			
UTP	3-10	10.12	(Cai <i>et al.</i> , 2016)
Zr(IV)-UTP		12.43	
Zr(IV) impregnated anion exchange resin	7	12.03	(Jha <i>et al.</i> , 2015)
Powdered Mn – Ce oxide	6	79.5	(Deng <i>et al.</i> , 2011)
Granular Mn-Ce oxide	6	45.5	(Deng <i>et al.</i> , 2011)

4.2.4 Effect of co-existing ions

The fluoride contaminated industrial water might contains co-existing ions like Cl⁻, SO₄²⁻, NO₃⁻, HCO₃⁻ and PO₄³⁻ together with fluoride ion. The effect of interfering ions Cl⁻, SO₄²⁻, NO₃⁻, HCO₃⁻ and PO₄³⁻ for the biosorption of fluoride onto Zr(IV)-SWR and Zr(IV)-SBP were examined, and result obtained are shown in the **Figure 28 (a)** and **Figure 28 (b)**.

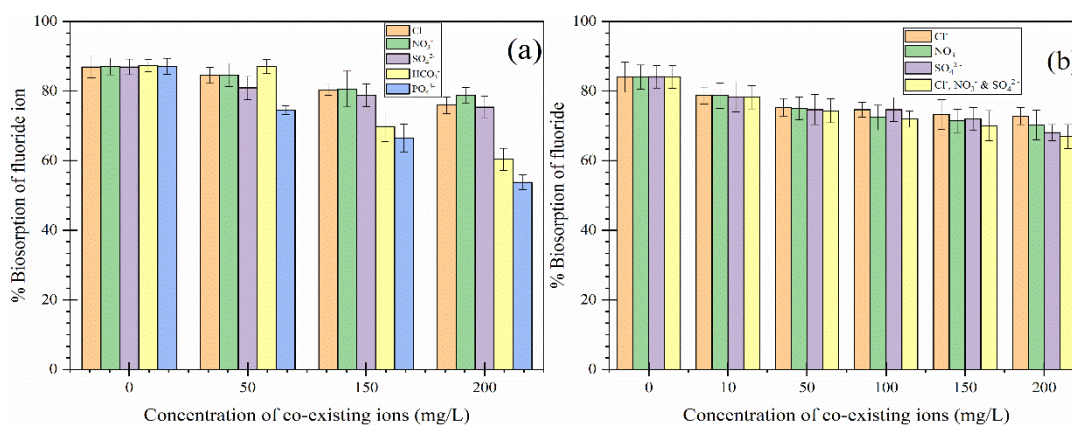


Figure 28: Effect of co-existing ions for the fluoride biosorption onto (a) Zr(IV)-SWR and (b) Zr(IV)-SBP (Conditions: $m/v = 0.6$ g/L, $C_i = 10$ mg/L, $pH = 4.03$, concentration of co-existing ions = 0 -200 mg/L)

The results showed the minimal inference caused by Cl^- and NO_3^- compared to the blank. Similarly, SO_4^{2-} exhibited mild effect in both cases. However, biosorption of fluoride decreased significantly with elevated concentration of HCO_3^- and PO_4^{3-} . The % reduction of fluoride ion using Zr(IV)-SWR is 26.9 and 33.3 % in presence of 200 mg/L of HCO_3^- and PO_4^{3-} , respectively. Moreover, the presence of multiple co-existing ions ($Cl^- + NO_3^- + SO_4^{2-}$) along with fluoride ion at higher molar concentration of co-existing ions interfere more in the biosorption of fluoride onto Zr(IV)-SBP which is caused due to combined effect of co-existing ions. The higher inhibitory effect caused by PO_4^{3-} may be conspicuous due to higher negative charges and greater affinity of phosphate with loaded Zr(IV) exist in Zr(IV)-SWR and Zr(IV)-SBP (Aryal *et al.*, 2019; Khound *et al.*, 2018).

4.2.5 Desorption studies

Since the biosorption percentage of fluoride onto Zr(IV)-SWR and Zr(IV)-SBP in strongly alkaline conditions was very poor, the desorption studies were carried with different concentration of NaOH. The desorption studies of fluoride loaded Zr(IV)-SWR and fluoride loaded Zr(IV)-SBP was analyzed with NaOH concentration varied from 0.01 to 2M and corresponding findings obtained are displayed in **Figure 29 (a)** and **(b)**. The results stated that the percentage desorption raised from 40.11 % to 95.72 % on changing NaOH concentration from 0.01M to 0.5M and gradually decreased with increased NaOH concentration in case of Zr(IV)-SWR. Similarly, in case of Zr(IV)-SBP, the desorption percentage peaked from 61.19 % to 95.6% with

rise of NaOH concentration from 0.01 - 1M and reached optimal value 98.5 % using 2 M NaOH. It is believed that the excess of Na(I) ions within the solution would neutralize the surface negative charges thus, reducing the electrostatic repulsion between fluoride and Zr(IV)-SWR or Zr(IV)-SBP surface leading to decrease in desorption with higher concentration of NaOH (Rapo & Tonk, 2021). Therefore, 0.5 M NaOH solution is the commendable choice for desorption of fluoride ion from Zr(IV)-SWR and 2 M NaOH for Zr(IV)-SBP. It can be ascribed that the hydroxide ion of NaOH solution substituted fluoride ions for desorption reaction as shown in equation (e)

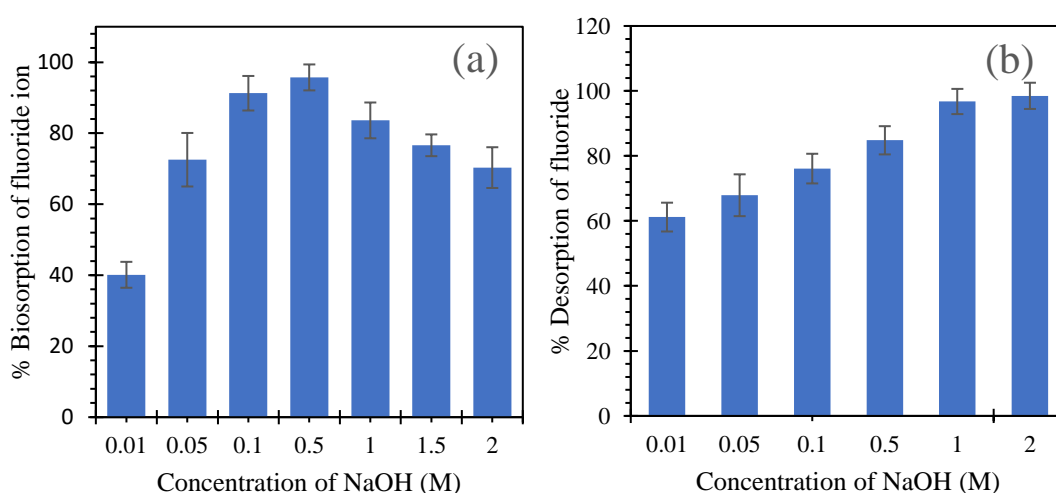
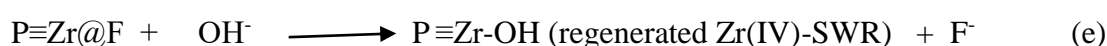


Figure 29: Desorption of fluoride from fluoride biosorbed (a) Zr(IV)-SWR and (b) Zr(IV)-SBP (Conditions: weight of biosorbed fluoride onto Zr(IV)-SWR= 30 mg, volume of NaOH = 10 mL, concentration of NaOH = 0.01 - 2 M NaOH)

4.2.6 Regeneration and reusability of biosorbents

The optimal biosorption capacity and regeneration of biosorbent saves both operational cost and time. The biosorption-desorption experiments for the regeneration and reusability of Zr(IV)-SWR and Zr(IV)-SBP were performed. For regeneration of fluoride loaded Zr(IV)-SWR and Zr(IV)-SBP, 0.5, 2M NaOH solution, respectively were used. In every cycle, the regenerated Zr(IV)-SWR and Zr(IV)-SBP were washed with DI water until neutral pH and dried. The percentage biosorption of fluoride with number of cycles were investigated as shown in **Figure 30**. It showed that percentage biosorption of fluoride decreased from 94.87 to 77.34%

in Zr(IV)-SWR whereas, in Zr(IV)-SBP decreases from 93.39 to 78% after five consecutive cycles. The decrease in biosorption might be due to some potential sites could not be completely reversed/ or some biosorption sites are destroyed during desorption process.

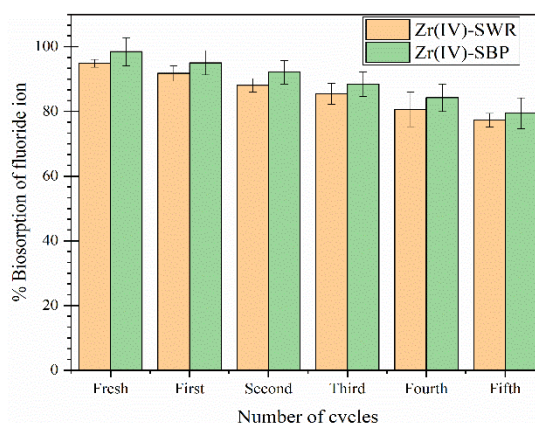


Figure 30: Variation of percentage biosorption of fluoride in 5 cycle's biosorption regeneration process of Zr(IV)-SWR and Zr(IV)-SBP.

4.3 Biosorption of phosphate onto Zr(IV)-SWR

4.3.1 Characterization of biosorbents

4.3.1.1 Surface morphology of the biosorbents

The surface morphology of biosorbent was analyzed through the scanning electron microscopy (SEM) before and after phosphate biosorption as shown in **Figure 31**. The observation showed that Zr(IV)-SWR (**Figure 31 a**) surface is irregular, uneven cavities with heterogeneity, that can give a favorable intact for phosphate anion during biosorption process. The Zr(IV)-SWR surface became homogeneous and smooth after biosorption (**Figure 31 b**). This observation attributed that phosphate ions seemed to be in the vicinity of the pores in the Zr(IV)-SWR during the biosorption process.

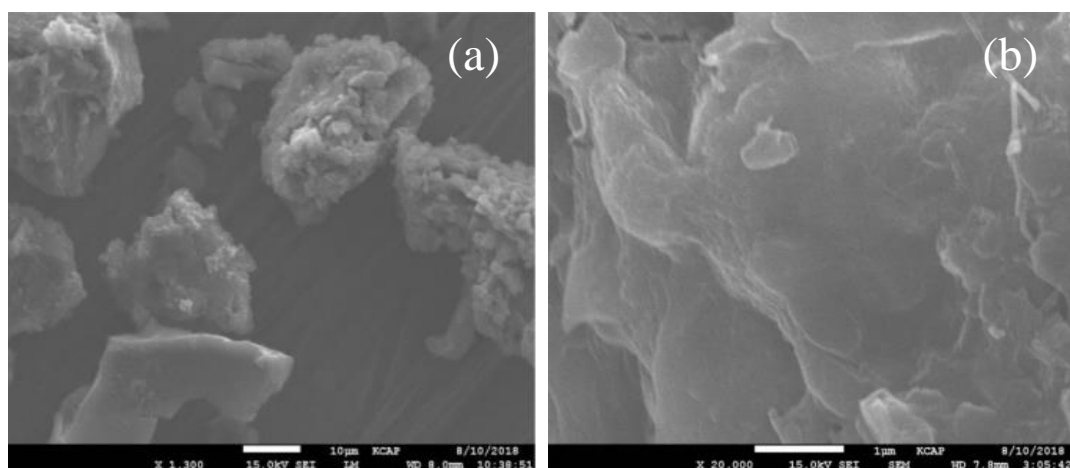


Figure 31: SEM micrographs of surface morphology of a) Zr(IV)-SWR and b) Zr(IV)-SWR after phosphate biosorption

4.3.1.2 Energy dispersive X-ray analysis (EDX)

The EDX analysis was operated on the investigated biosorbents and findings of major elements are reported in **Table 9**. It is evident that RWR comprises Ca (1.09%), K (1.21%), Si (0.26%), Fe (0.05%), Cu (0.010.%), Zn (0.004%) and other elements (97.179 %) along with C, N, P, and O. As a result of the lime treatment, calcium pectate is formed by exchanging the proton from watermelon pectic acid.

Table 9: Chemical composition of RWR, SWR and Zr(IV)-SWR

Elements	B.E. (keV)	% wt.		wt.ratio (SWR-to RWR)	%wt.in Zr(IV)-SWR	wt.ratio (Zr(IV)-SWR to SWR)
		RWR	SWR			
Ca	3.69	1.09	6.76	6.20	2.13	0.32
Zr	2.04	-	-	-	8.16	∞(new)
Si	1.73	0.37	0.27	0.73	0.07	0.26
S	2.32	0.16	0.08	0.50	0.07	0.87
Cl	2.62	0.09	0.02	0.22	1.36	68
K	3.31	1.21	0.07	0.06	-	-
Fe	6.41	0.15	0.06	0.40	0.12	2
Hf	7.89	-	-	-	0.46	∞ (new)
Cu	8.04	0.02	0.01	0.50	0.01	1
Others (C, O, P, N etc.)		97.01	92.73		87.60	
Total		100.00	100.00		100.00	

The calcium content in SWR peaked from 1.093 to 6.7%. Since the proportion of the new element Zr(IV) increased to 8.160 % and the percentage of calcium reduced from 6.75 to 2.13 % after Zr(IV) loading. The persistence of hafnium (Hf) in Zr(IV) -SWR at binding energy 7.89 keV might be due to association of hafnium impurities in the

sample of $ZrOCl_2 \cdot 8H_2O$ salt introduced during loading of Zr(IV). The findings reveals that the weight ratio (SWR to RWR) of calcium is 6.2 but (Zr(IV)-SWR to SWR) is less than unity (0.32). It is suggested the increment of calcium during $Ca(OH)_2$ treatments and release during the process of Zr(IV) loading. This outcome demonstrates that Zr(IV) is effectively loaded onto SWR through a cation exchange mechanism by replacing Ca(II) from SWR.

4.3.1.4 Surface charge of the biosorbents

Zeta potential analysis was performed to analyze the point of zero charge (pH_{pzc}) of Zr(IV)-SWR and results is shown in **Figure 32**. The pH_{pzc} of Zr(IV)-SWR is evaluated at pH 5.6 where the surface charge of Zr(IV)-SWR is chargeless. At $pH < pH_{pzc}$, Zr(IV)-SWR surface is positively charged which is favorable for phosphate anions biosorption through coulombic interaction. The hydroxyl ligands in the coordination spheres of Zr(IV)-SWR easily exchanged with phosphate anions through the ligand exchange mechanism as described in the mechanism section.

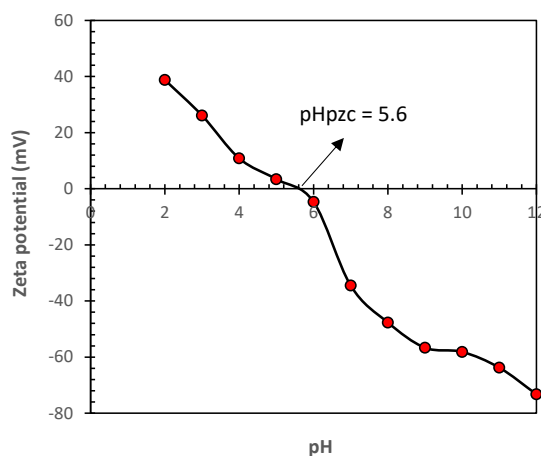


Figure 32: Zeta potential of Zr(IV)-SWR at different pH.

4.3.2 Batch biosorption studies

4.3.2.1 Effect of solution pH and phosphate biosorption mechanism

The phosphate biosorption onto Zr(IV)-SWR is remarkably influenced by the solution pH. **Figure 33** exhibited the phosphate biosorption efficiency of both RWR and Zr(IV)-loaded SWR biosorbent with pH. It was found that phosphate biosorption onto RWR is inadequate. The species distribution of the phosphate ions in the solution and the nature of the biosorbent surface determines the biosorption of phosphate ions. The

% of phosphate biosorption gradually increase from 23.21% at pH_e 1.1 to a maximum of 82.81% at pH_e 4.0, and then slowly decreased after pH_e 5.01. Therefore, pH_e 4.0 was chosen as the optimum pH. Orthophosphate can be found in a variety of ionic species depending on the pH of the aqueous solution ($pK_1=2.15$, $pK_2=7.20$, $pK_3=12.33$) (Zhang *et al.*, 2021). The phosphate removal rate is smaller at pH values lower than 2.0 since neutral H_3PO_4 is common and has poor attraction towards the binding sites (Markou *et al.*, 2016).

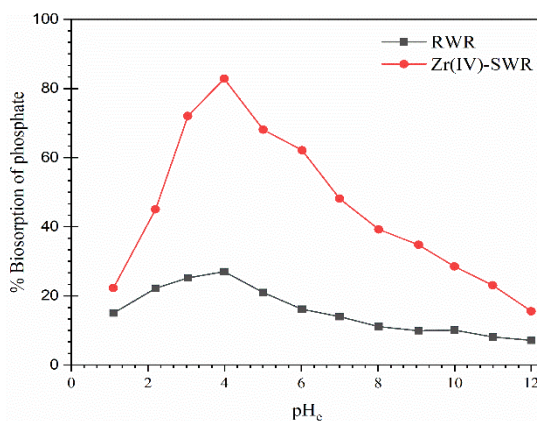


Figure 33: Effect of pH on phosphate biosorption by Zr(IV) loaded SWR (Conditions: $m/v = 1.2$ g/L, $C_i = 10$ mg/L, $t = 24$ h, $T = 298$ K)

At pH 2.1-7.2, $H_2PO_4^-$ and HPO_4^{2-} exists, where monovalent species *i.e.* $H_2PO_4^-$ is the common species, which was strongly biosorbed by ligand exchange reaction with monovalent hydroxyl ligands of Zr(IV)-SWR as shown in **Figure 34**. This results was consistent with reported work in the literature (Chakrabarti, 2018; Qiao *et al.*, 2019). At pH above 7.2, the high concentration of $[OH^-]$ in solution interferes the negatively charged phosphate species (HPO_4^{2-}) biosorption due to repulsion and competition of ions for active binding sites.

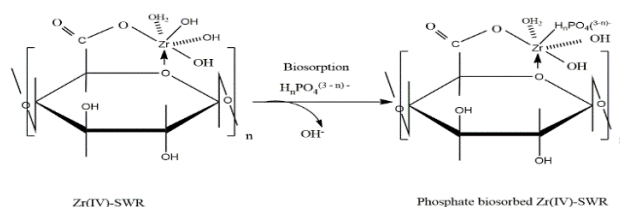


Figure 34: Phosphate biosorption mechanism in Zr(IV)-SWR (Adapted from Biswas *et al.*, 2008a)

4.3.2.2 Effect of contact time

Figure 35 illustrates the findings of a kinetic experiment that was conducted with Zr(IV)-SWR at pH 4.0. The outcome marked that the uptake of phosphate increases rapidly with contact times in the initial phase then slowed down and reached equilibration at 240 min. The findings can be logically described because during the initial phase of biosorption, there are enough vacant sites available for biosorption, which ultimately resulted in rapid uptake and the binding sites are covered with biosorbates so that finally resulted the equilibrium. The experimental data is modelled using a PFO and PSO model to find out the best fit kinetic model for the investigated biosorption system and the result obtained are depicted in **Figure 35 (b) and (c)**, respectively.

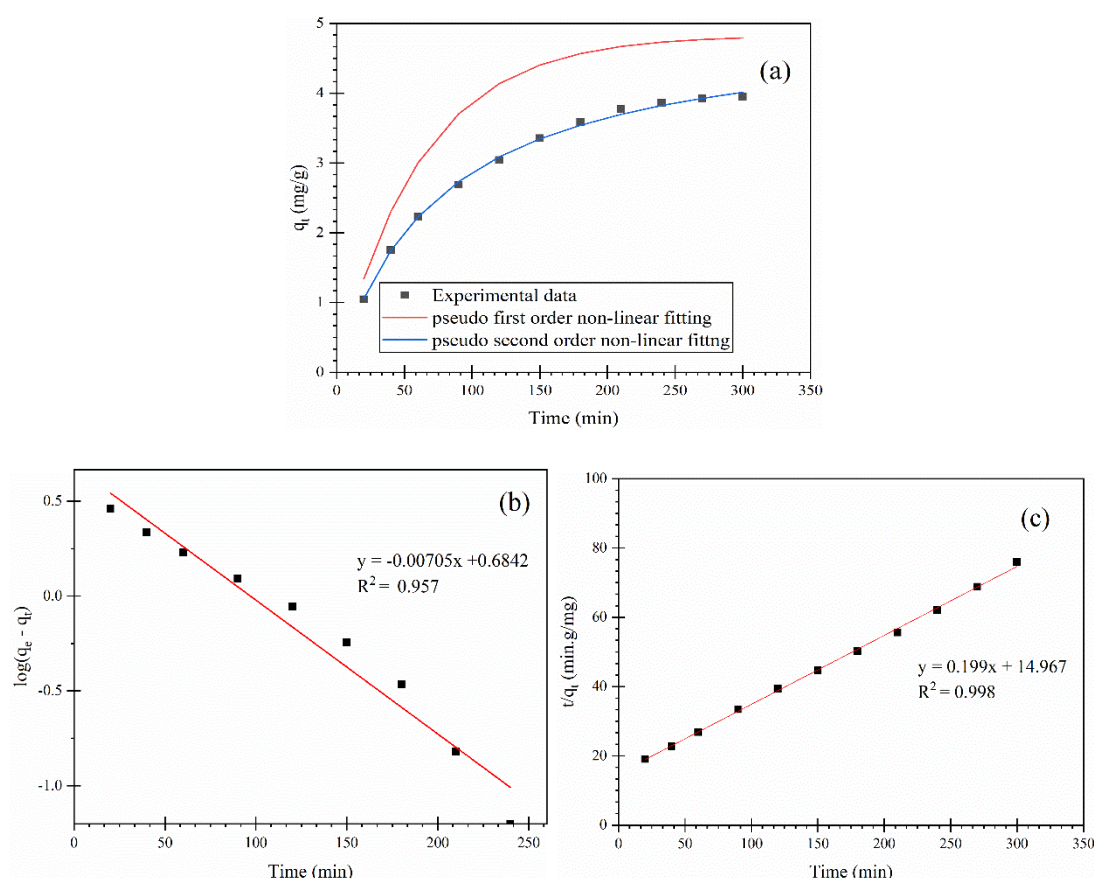


Figure 35: Phosphate biosorption onto Zr(IV)-SWR (a) Non-linear plot of PFO and PSO model with experimental data (b) PFO model and (c) PSO kinetic model (Conditions: $m/v = 1.2$ g/L, $C_i = 10$ mg/L, $t = 24$ h, $pH = 4.0$)

The outcomes of this results suggested that biosorption of phosphate onto Zr(IV)-SWR strictly follow PSO model with higher coefficient of determination values ($R^2 =$

0.998) as shown in **Table 10**. **Figure 35 (a)** is the non-linear plot of kinetic modelling that reflected the better fits of experimental data with PSO compared to PFO model. The value of q_e (5.02 mg/g) derived from the PSO model is nearer to q_e (5.03 mg/g) measured experimentally than the value obtained from the PFO model (4.83 mg/g). Thus, phosphate biosorption by Zr(IV)-SWR followed the PSO model. This kinetic model represents the chemisorption process and includes the valence forces connected to the biosorbent and biosorbate. (Paudyal *et al.*, 2020).

Table 10: Kinetics parameters for the biosorption of phosphate onto Zr(IV)-SWR.

Kinetic Models	Parameters	Values
PFO	$k_1 \times 10^{-3}$ (1/min)	16.2 ± 3.42
	$q_{e, \text{cal.}}$ (mg/g)	4.83 ± 1.32
	R^2	0.957
PSO	$k_2 \times 10^{-3}$ (g/mg min)	2.65 ± 1.03
	$q_{e, \text{cal.}}$ (mg/g)	5.02 ± 1.02
	R^2	0.998
	$q_{e, \text{exp.}}$ (mg/g)	5.03 ± 0.87

4.3.2.3 Effect of initial concentration

Figure 36 illustrates the biosorption isotherm of phosphate onto Zr(IV)-SWR. The **Figure 36 (a)** showed that at a low concentration of phosphate, the biosorption of phosphate takes place rapidly, whereas with rise of phosphate concentration, the biosorption capacity becomes slower and reached equilibrium. The results can be inferred because at low concentration the binding sites are sufficient to biosorb onto Zr(IV)-SWR surface while, as concentration of phosphate increased, the binding sites are occupied as a result it reaches a virtually constant value due to the limited number of vacant biosorption sites. The well-known Langmuir and Freundlich isotherm models were applied to examine the equilibrium data. The computed isotherm variables and coefficient of determination (R^2) are presented in **Table 11**. The outcome indicated the greater value of coefficient of determination (R^2) of Langmuir isotherm in comparison to the Freundlich isotherms. The maximum biosorption capacity (q_{max}) based on Langmuir isotherm model is computed to be 27.65 mg/g which is closer with the experimental value (23.82 mg/g) taken directly through plateau region. The non-linear plot of experimental data resembles with Langmuir non-linear fittings. Based on the results, it appeared that the Langmuir isotherm model

of phosphate biosorption is more accurate than the Freundlich isotherm model, indicating the formation of monolayers of biosorbed phosphates on the homogeneous surfaces of Zr(IV)-SWR during biosorption reaction.

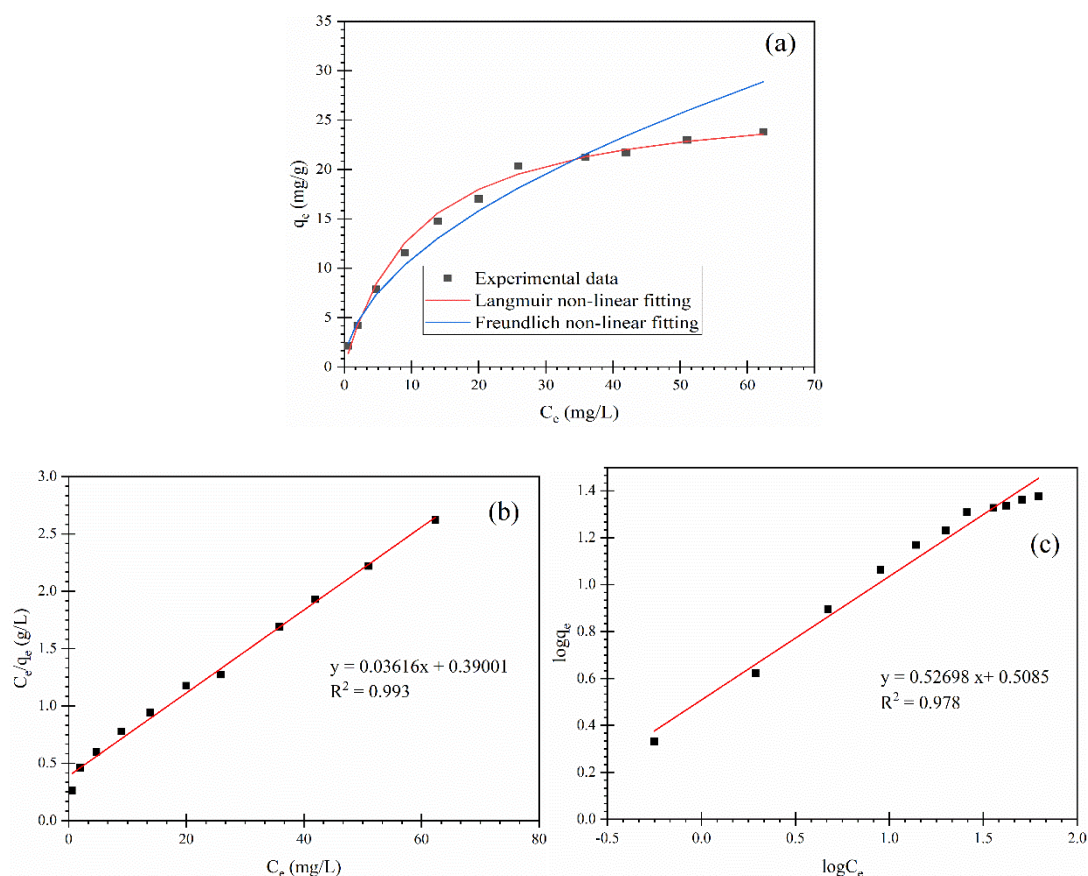


Figure 36: (a) Non-linear plot of Langmuir and Freundlich isotherm with experimental data (b) Langmuir isotherm model and (c) Freundlich isotherm for the biosorption of phosphate onto Zr(IV)-SWR (Conditions: $m/v = 1.2$ g/L, $C_i = 10$ mg/L, $t = 24$ h, $pH = 4.0$, $T = 298$ K)

Table 11: Isotherm parameters for the biosorption of phosphate onto Zr(IV)-SWR

Models	Parameters	Values
Langmuir	$q_m, \text{exp. (mg/g)}$	23.82 ± 1.32
	$q_m, \text{cal. (mg/g)}$	27.65 ± 0.91
	$b \text{ (L/g)}$	0.093 ± 0.002
	R^2	0.99
Freundlich	$K_F \text{ (mg/g)(L/mg)}^{1/n}$	3.23 ± 0.86
	$1/n$	0.53 ± 0.07
	R^2	0.97

Table 12 enlisted the maximum biosorption capacity of different biosorbents for phosphate reported in the literature together with the Zr(IV)-SWR investigated in the study. The comparative study showed that metal loaded biosorbents exhibited higher biosorption capacity than activated carbon. In addition, Zr(IV) loaded okara, Zr(IV)-loaded apple peels and commercial adsorbents exhibited comparable biosorption capacity. The biosorption capability of investigated Zr(IV)-SWR is comparatively higher than commercial adsorbents like Zr(IV)-MCM 41, Zr(IV) ferrite. Thus, Zr(IV)-SWR investigated in this study can be a promising material for the biosorption of phosphate from water.

Table 12: Comparison of biosorption capacities of Zr(IV)-SWR with other bio/adsorbents

Adsorbents	q_{\max} (mg/g)	References
Zr(IV) loaded saponified orange waste	13.94	(Biswas <i>et al.</i> , 2008)
Activated fruit juice residue	13.89	(Petkowicz <i>et al.</i> , 2017)
Ca(OH) ₂ pretreated Phragmites sp.	12.27	(Markou <i>et al.</i> , 2016)
La(III)- incorporated porous zeolite	17.2	(He <i>et al.</i> , 2017)
Zr(IV) -MCM 41	3.36	(Jutidamrongphan <i>et al.</i> , 2012)
Zr(IV) ferrite	27.73	(Jutidamrongphan <i>et al.</i> , 2012)
Fe-loaded activated carbon	2.87	(Braun <i>et al.</i> , 2019)
Fabrication of zirconium phosphate	8.06	(Zhang <i>et al.</i> , 2013)
Zr(IV)- loaded apple peels	20.35	(Mallampati & Valiyaveetil, 2013)
Modified walnut wooden shell	22.73	(Faraji <i>et al.</i> , 2020)
Modified almond wooden shell	14.71	(Faraji <i>et al.</i> , 2020)
La(III)- modified Pine needles	4.8	(Wang <i>et al.</i> , 2015)
Zr(IV)- loaded Okara	44.13	(Nguyen <i>et al.</i> , 2014)
Zr(IV)-SWR	27.65	This study

4.3.2.4 Effect of biosorbent dosage

The effect of biosorbent dosage was examined taking different masses of biosorbent keeping other parameters constant and the result is presented in **Figure 37**. The biosorption of phosphate initially increases with increasing biosorbent dosages and remains almost unchanged after addition of Zr(IV)-SWR beyond 5 g/L. It suggested that after a limited dosage of biosorbent, optimum biosorption is attained which is inferred due to accessibility of more active sites of the biosorbent. At lower dosage,

Zr(IV)-SWR have vacant sites on the surface for biosorption while increasing the biosorbent dosages the sites are occupied by phosphate. This study shows that the residual concentration of phosphate lowered to 1.334 mg/L using 5 g/L of Zr(IV)-SWR which is below the WHO/USEPA recommendation for phosphate ion in drinking water (WHO, 2004).

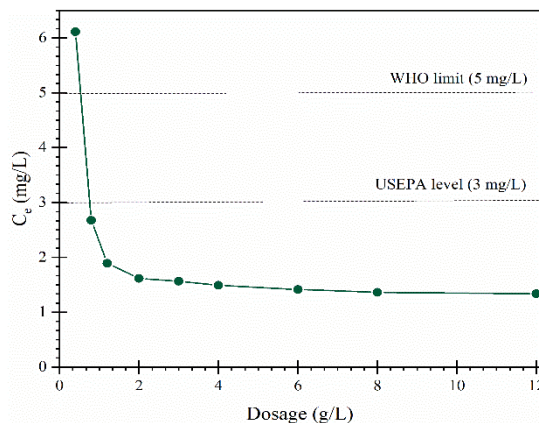


Figure 37: Effect of biosorbent dose in the biosorption of phosphate onto Zr(IV)-SWR (Conditions: $m/v = 0.4 - 12$ g/L, $C_i = 16.8$ mg/L, $v = 25$ mL, $t = 24$ h, $pH = 4.03$, $T = 289$ K)

4.3.2.5 Error function analysis

The determined error function values of kinetic models and isotherm models for phosphate biosorption capacity of Zr(IV)-SWR are shown in **Table 13**. The computed error function values for phosphate biosorption onto Zr(IV)-SWR for PSO and Langmuir isotherm models were found to be less. The higher R^2 value and lower error function values are observed for both cases during phosphate biosorption onto Zr(IV)-SWR. This implied that biosorption of phosphate on to Zr(IV)-SWR followed PSO and Langmuir isotherm model.

Table 13: Error analysis of biosorption of fluoride ion onto Zr(IV)-SWR

Error function	Kinetic model		Isotherm model	
	PFO	PSO	Langmuir	Freundlich
χ^2	0.0079 ± 0.0014	$1.99 \times 10^{-5} \pm 0.001$	0.53 ± 0.02	4.0 ± 1.3
RMSE	0.057 ± 0.022	0.01 ± 0.003	1.102 ± 0.03	3.03 ± 1.06
MAE	0.016 ± 0.101	0.00083 ± 0.0011	0.319 ± 0.003	0.87 ± 0.11

4.3.3 Effect of co-existing ions

The effect of co-existing ions on phosphate biosorption onto Zr(IV)-SWR is displayed in **Figure 38**. The figure showed that % biosorption of phosphate anion decreases with the gradual increase in concentration of interfering ions (Cl^- , NO_3^- and SO_4^{2-}). The biosorption of phosphate decreased from 85.52% to 72.08% in presence of 200 mg/L of SO_4^{2-} . It is inferred that at low concentration, Na(I) or K(I) obtained from the introduced salts in the solution may decrease the repulsion of the phosphate anions so that the biosorption of phosphate increases (Xu *et al.*, 2009). Divalent SO_4^{2-} has more interference due to high affinity of loaded Zr(IV) with SO_4^{2-} than all others (Markou *et al.*, 2016). The competitive effect of phosphate ions with co-existing ions increases with concentration for the biosorption sites which leads to decrease in biosorption percentage of phosphate.

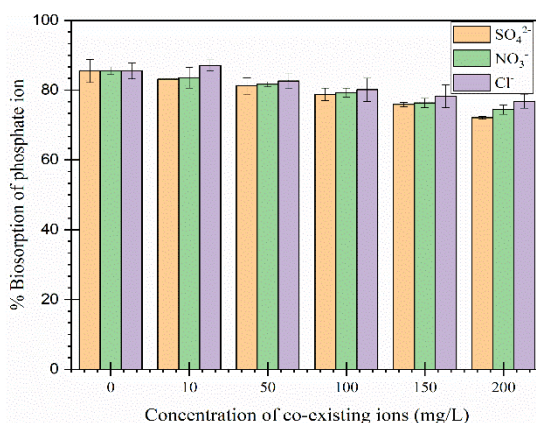


Figure 38: Effect of co-existing anions in the phosphate biosorption onto Zr(IV)-SWR (Conditions: $m/v = 1.25$ g/L, $C_i = 50$ mg/L, $\text{pH} = 4$, concentration of co-existing ions = 0 - 200 mg/L)

4.3.4 Desorption studies

Since Zr(IV)-SWR biosorbed negligible amount of phosphate at pH values higher than 10.0, thus the desorption experiment was performed using NaOH solution. The desorption of phosphate from $\text{PO}_4\text{-Zr(IV)-SWR}$ at different concentration of NaOH (0.01 to 0.3M) was examined, and outcome is displayed in **Figure 39**. The results showed that the desorption of phosphate increased from 60.03 to 94.5% with the increase in NaOH concentration from 0.01 to 0.1M, reaching its maximum value (99.65%) at concentration of 0.3M NaOH. The desorption of biosorbed phosphate inferred to take place through ligand exchange reaction with hydroxyl ion provided by NaOH solution as shown in **Figure 40** (Ghimire *et al.*, 2008).

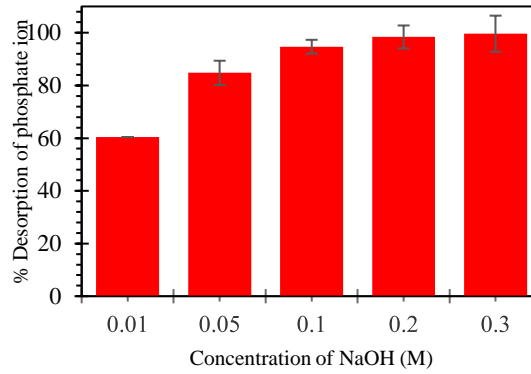


Figure 39: Desorption of phosphate from phosphate biosorbed Zr(IV)-SWR at varied molar concentration of NaOH (Conditions: weight of biosorbed phosphate on Zr(IV)-SWR = 50 mg, volume of NaOH = 15 mL, concentration of NaOH = 0.01 – 0.3 M)

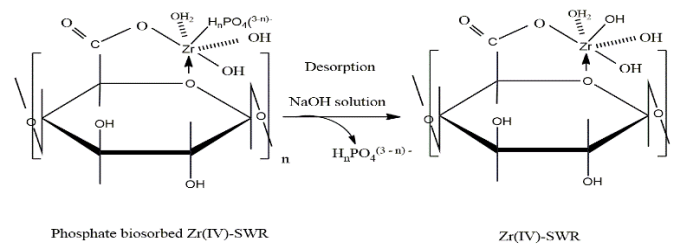


Figure 40: Plausible mechanism of phosphate desorption from biosorbed Zr(IV)-SWR (Adapted from Biswas *et al.*, 2008a)

4.4 Biosorption of As(III) onto La(III)-SWR

4.4.1 Characterization of biosorbents

4.4.1.1 FE-SEM analysis of the biosorbents

Figure 41 displayed FE-SEM images of RWR, SWR, and La(III)-SWR prior to and after As(III) biosorption. The RWR surface is homogeneous along with a few small white patches like structures (**Figure 41 a**), which might be due to presence of organic compounds of low molecular weights, sugar, and limonene. The SWR surface was found rough and has fewer hollow cavities (**Figure 41b**), which was reasonably interpreted as the result of the lixiviating of soluble organic components like sugar and limonene molecule from the watermelon rind surface during limewater treatment while La(III)-SWR (**Figure 41c**) contains hollow protuberances with unequal cavities.

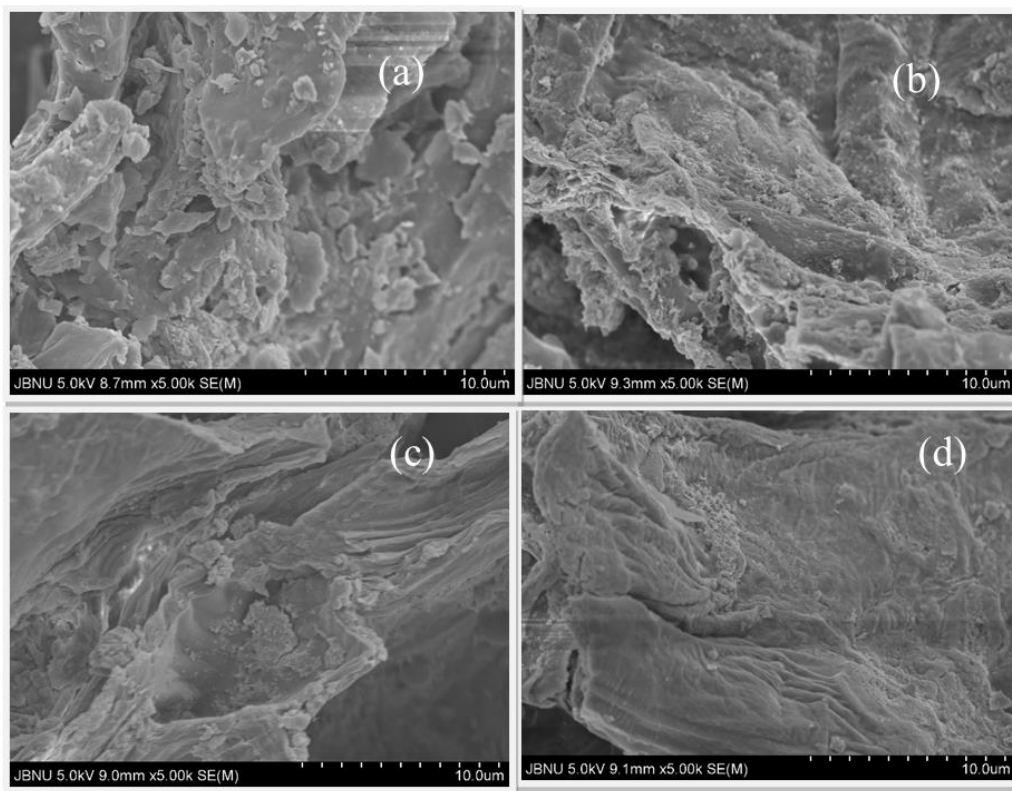


Figure 41: SEM micrographs of (a) RWR (b) SWR (c) La(III)-SWR before biosorption (d) La(III)-SWR after As(III) biosorption

After As(III) biosorption, La(III)-SWR surface became slightly uniform, smooth, and shiny appearance on the surface (**Figure 41d**). This is attributable to the As(III) anion covering La(III)-SWR surface during the biosorption process.

4.4.1.2 EDX spectra analysis with color mapping

The confirmation for the La(III) loading in SWR and As(III) biosorption onto La(III)-SWR was studied through EDX spectroscopic analysis. The elemental mapping along with an EDX spectra of SWR, La(III)-SWR and La(III)-SWR after As(III) biosorption are shown in **Figure 42**. Ca, O, and C are the most prevalent elements in SWR according to the results of the elemental mapping (**Figure 42 (a)**). The major elements such as La, C, and O are present in La(III)-SWR in **Figure 42 (b)** after La(III) loading but in As(III) loaded La(III)-SWR, the elements C, O, La, and As are identified in **Figure 42 (c)**. The EDX spectrum and elemental composition analysis of SWR (**Figure 42 (d) and Table 14**) outlined that SWR comprises 54.22%, 41.04%, and 0.41% of C, O, and K at binding energies of 0.27, 0.51, and 3.31 keV, respectively. In addition, the % weight of Ca in SWR at 3.69 and 4.12 keV is 4.33%.

The EDX spectrum of La(III)-SWR revealed a characteristic peak analogous to La element (10.67%, **Table 14**) at binding energies around 0.82, 4.71, 5.12, 5.44, 5.82, and 6.01 keV. **Figure 42 (e)**, which amply shows the proof of loading La(III) onto SWR. Additionally, the percentage of calcium diminished from 4.33% to 1.08% following the La(III) loading reaction, which is plausibly attributed to the formation of La(III) pectate by replacing the Ca(II) from the SWR with the La(III) ion. After As(III) biosorption (As-La(III)-SWR), new peak matching to arsenic element was seen at binding energy of 1.28 keV(**Figure 42 f, Table 14**) which effectively convey the tangible support for the biosorption of As(III) onto La(III)-SWR. The decrease in % weight of Ca(II) in La(III)-SWR as compared to SWR indicated loading of La(III) took place through cation exchange reaction displacing Ca(II) from SWR.

After As(III) biosorption onto La(III)-SWR, the percentage existence by weight (wt%) of oxygen accelerated from 38.07 to 44.88% along with the appearance of characteristic peak of arsenic, illuminating that the biosorption of oxo-anionic species of arsenic occurred during biosorption of As(III).

Table 14: Chemical compositions of SWR, La(III)-SWR , and arsenic biosorbed La(III)-SWR.

Elements	BE (keV)	As- La(III)-SWR	La(III)-SWR	SWR (wt%)
		(wt%)	(wt%)	
C	0.27	42.73	49.67	54.22
O	0.52	44.88	38.07	41.04
P	2.01	0.74	0.42	ND
Si	1.73	ND*	0.09	ND
K	3.31	ND*	ND*	0.41
Ca	3.69, 4.12	0.07	1.08	4.33
As	1.28	1.32	ND*	ND*
La	0.82, 4.71, 5.12, 5.44, 5.82, 6.01	10.26	10.67	ND*
Total:		100.00	100.00	100.00

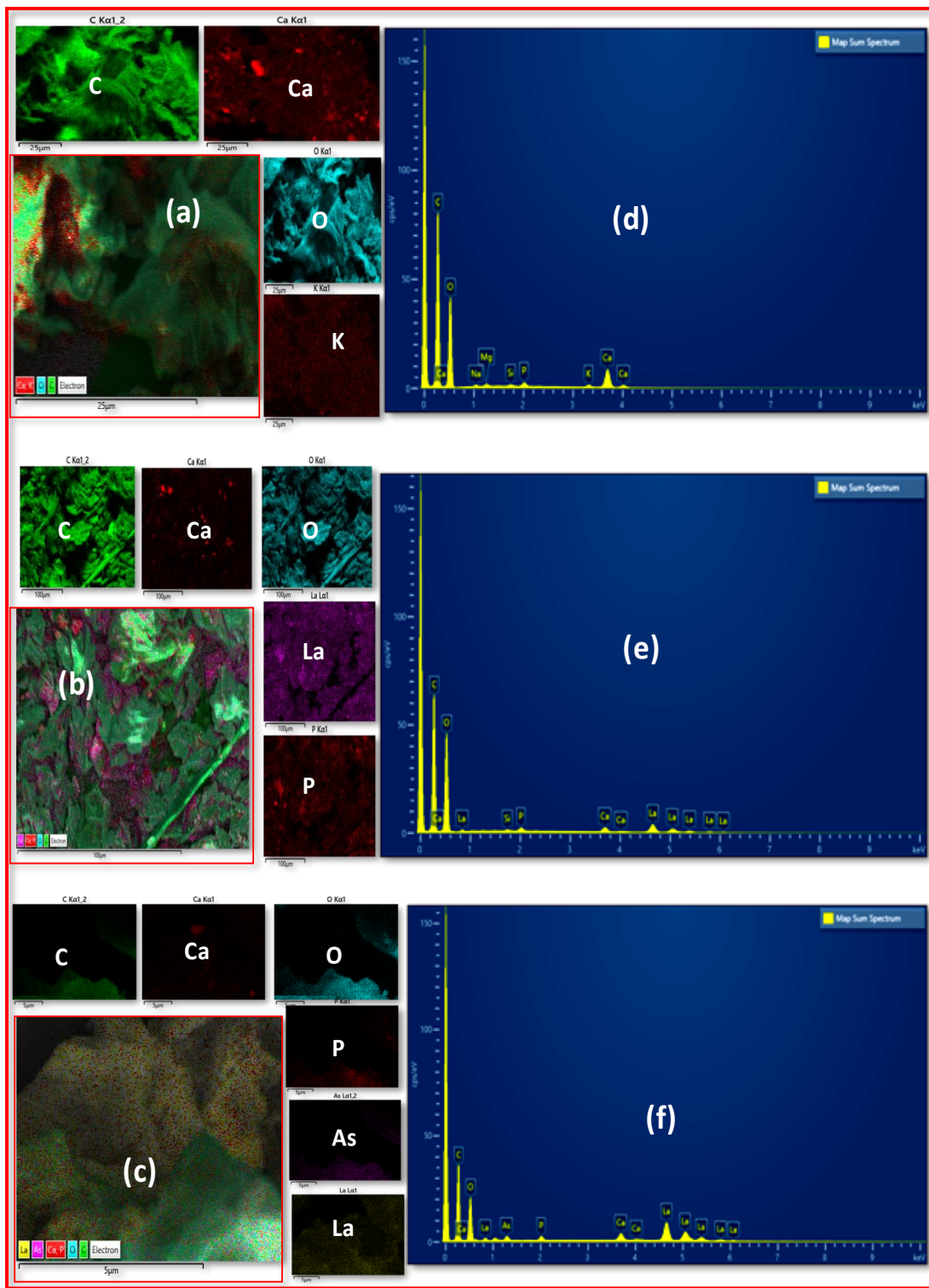


Figure 42: EDX analysis of SWR, La(III)-SWR, and As-La(III)-SWR showing respective (a), (b), and (c) elemental mapping, (d), (e), and (f) EDX spectra.

4.4.2 Functional group analysis by FTIR spectroscopy

FTIR spectra of all biosorbents (RWR, SWR, and La(III)-SWR) obtained between the range of 4000 and 400 cm^{-1} are shown in **Figure 43**. As it is reported in earlier studies, all the peels consisted mostly of cellulose, hemicellulose, proteins, carbohydrates, polyphenols, lactones, carboxylic acids, and minerals (Xu *et al.*, 2019; Sert & Tirtom, 2017). In RWR, the broad and strong band seen at around 3320 cm^{-1} is caused by the -OH vibration of the hydroxyl group present in cellulose, hemicellulose, pectin, and lignin present in the watermelon rind matrices. The narrow bands at around 2924 cm^{-1} corresponds to symmetrical and asymmetrical -CH stretching of methyl and methoxy groups in cellulose, hemicellulose, lignin and aliphatic acids (Bhatt *et al.*, 2018; Rincón *et al.*, 2021). The band associated to 1730 and 1615 cm^{-1} corresponds to -COO and -C=O stretching due to carboxylic acid or esters. Small peaks of 1412 and 1012 cm^{-1} , respectively are analogous to C-O stretching vibrations of carboxylic acids and alcohols (Qiao *et al.*, 2019). After $\text{Ca}(\text{OH})_2$ treatments, the bands observed at 1730 cm^{-1} is largely decreased in SWR to 1608 cm^{-1} that may be due to the formation of calcium carboxylate and in La(III)-SWR at around 1595 cm^{-1} because of formation of lanthanum carboxylate *via* substitution of Ca(II) by La(III) during loading La(III) in SWR. The displacement caused by high molecular weight La(III) to low molecular weight calcium, shifted carboxyl peak in La(III)-SWR towards lower frequency region. It marked the clear demonstration for metal loading and spectral shift. The primary functional group in La(III) loading is the carboxyl group, which favorably affects the biosorption sites for anionic species for biosorption of As(III) anion.

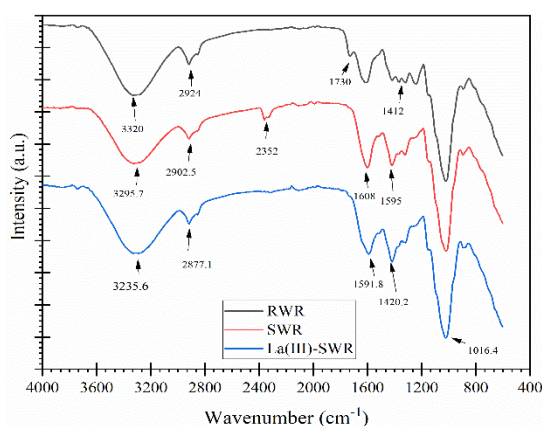


Figure 43: FTIR analysis of RWR, SWR and La(III)-SWR

4.4.3 Surface charge analysis of biosorbent

The zeta potential analysis is advantageous to find out the biosorbent's surface charge during biosorption process. The point of zero charges (pH_{pzc}) of La(III)-SWR was determined and measured values of zeta potential at different pH are illustrated in **Figure 44**. The figure showed that zeta potential values decreased with increase in pH of the solution. The value became zero at a pH of 7. The pH_{pzc} of the La(III)-SWR was estimated to be $\text{pH} = 7.0$. It refers to the Ph value where the electrical charge density on the surface of La(III)-SWR is zero. Zr(IV)-SWR has a neutral surface at pH_{pzc} , whereas at low pHs, due to $[\text{H}^+]$, the biosorbent surface becomes positively charged. But, as the pH of the solution rises, La(III)-SWR's zeta potential shifts to the negative value, which is properly attributed to an increase in the concentration of hydroxyl ions (Shi *et al.*, 2009).

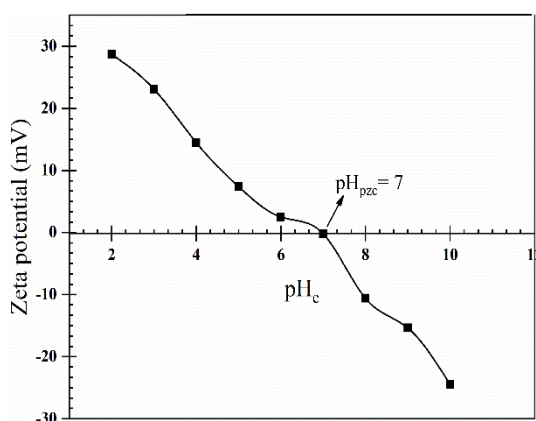


Figure 44: Plot of zeta potential *versus* pH of La(III)-SWR

4.4.1 Biosorption of As(III) in batch mode

4.4.3.1 Effect of pH and mechanism of As(III) biosorption

Figure 45 (a) displayed the biosorption of As(III) onto RWR and La(III)-SWR in the equilibrium (pH_e) range of 2.19 to 13.02. The biosorption of As(III) onto RWR shows the poor biosorption (lower than 0.5 mg/g at optimum (pH_e)) while biosorption of As(III) onto La(III)-SWR demonstrates high uptake capability. The findings showed that the amount of As(III) biosorption increased from 0.64 mg/g at pH 2.19 to 4.68 mg/g at pH 12.08 then diminishes to 2.53 mg/g at pH 13.02. Therefore, optimal pH of 12.08 is examined for other biosorption experiments. The chemistry of As(III)

varies with solution pH. As(III) is present commonly, as neutral species (H_3AsO_3) in the pH range of 2.0 to 7.0, whereas as anionic species (H_2AsO_3^-) and (HAsO_3^{2-}) at pH range of 7.0 to 12.0 but at pH > 12.0, AsO_3^{3-} is common in aqueous solution (Aryal *et al.*, 2022; Aryal *et al.*, 2010). At low pH of 2.19 to 7.03, the ligand exchange reaction between hydroxyl ligand of La(III)-SWR and neutral species of As(III) *i.e.* H_3AsO_3 is difficult as a result poor biosorption of As(III) anion takes place.

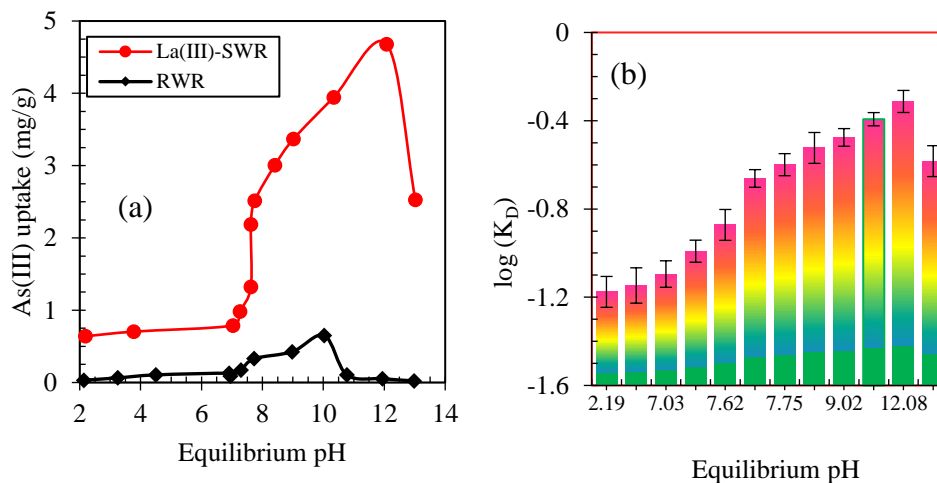


Figure 45: As(III) biosorption onto La(III)-SWR (a) Effect of pH and (b) $\log(K_D)$ versus pH_e
(Conditions: $m/v = 1 \text{ g/L}$, $T = 298\text{K}$, $C_i = 10 \text{ mg/L}$, $t = 24 \text{ h}$)

However, at pH 7.62 to 12.08, the gradual increment in biosorption of As(III) onto La(III)-SWR takes place and gradually reduced beyond pH 13.02. This observation revealed that anionic species of As(III) is biosorbed onto La(III)-SWR through ligand exchange reaction. The examined optimal pH in this study is similar with the starch stabilized ferromanganese binary oxide adsorbent (Xu *et al.*, 2019). The H_2AsO_3^- species of As(III) is common at pH 12 so the substitution of hydroxyl ions by this H_2AsO_3^- anion is more favorable leading to biosorption of As(III). At pH > 12.0, the anionic species of As(III) competes with the hydroxyl ion for the binding sites so that the reduction in As(III) biosorption took place. **Figure 45 (b)** displayed the distribution coefficient ($\log K_D$) value as a function of equilibrium pH of solution for the biosorption of As(III) onto La(III)-SWR. The findings showed that value of distribution coefficient increased from -1.17 to -0.87 with the increase of equilibrium pH from 2.19 to 7.26 and reaches a maximum value (-0.31) at 12.08. However, with further increase of equilibrium pH above 12.08, distribution coefficient again starts decreasing. At pH 12.08, the greatest value of distribution coefficient is observed. It

shows that the solid phase distribution of As(III) is in utmost at the pH during the biosorption process.

4.4.3.2 Effect of contact time

The biosorption capacity of La(III)-SWR for As(III) at different contact times is shown in **Figure 46**. It demonstrated that during the first few minutes of contact, removal of As(III) rises significantly, then becomes stable and finally reaches equilibrium at 360 min. The kinetic performance of As(III) biosorption are examined to inspect the more suited kinetic model according to equation (3) and (4) and the findings are displayed in **Figure 46 (b)** and **Figure 46 (c)**, respectively. **Table 15** includes error functions together with the evaluated PFO and PSO kinetic parameters. In contrast to the PFO model, which has an R^2 value of 0.92, the PSO model has R^2 value of 0.97, which is closer to unity. In a similar manner, the value of q_e calculated from the PSO model is closer to the q_e determined experimentally.

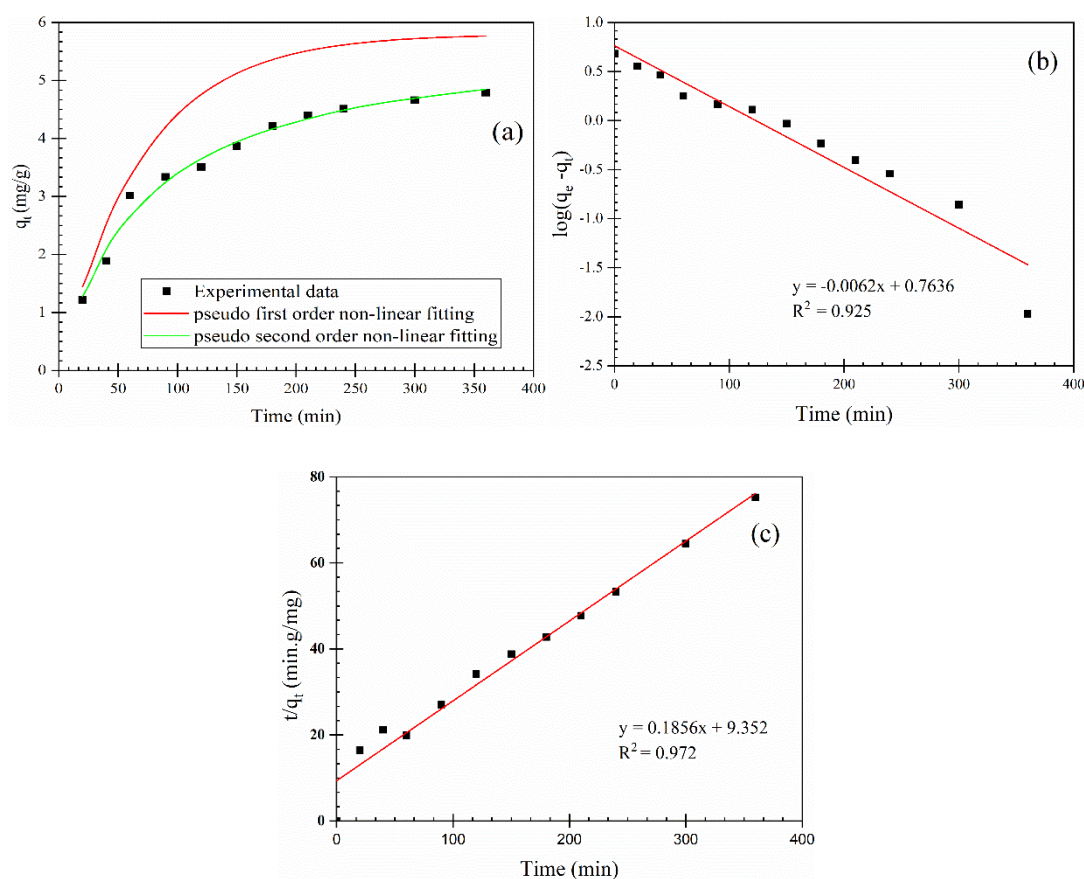


Figure 46: Biosorption kinetics of As(III) onto La(III)-SWR (a) Non-linear fitting of PFO and PSO model with experimental data (b) PFO and (c) PSO (Conditions: $m/v = 1$ g/L, $C_i = 10$ mg/L, pH 12.08, and $T = 298$ K)

For PFO, the values of χ^2 , RMSE and MAE are comparatively higher than PSO model. The experimental data, and the nonlinear fitting of the PFO and PSO kinetic models are shown together in **Figure 46 (a)**. It also shows that non-linear fitting of PSO is in the close agreement with the experimental data. Moreover, the As(III) biosorption capacity enumerated from PSO model (4.39 mg/g) is in proximity to the experimentally determined value (4.78 mg/g) compared to PFO model (5.80 mg/g). The overall findings suggested that PSO kinetics are in agreement with the As(III) biosorption onto La(III)-SWR.

Table 15: Kinetics parameters for As(III) biosorption onto La(III)-SWR

Kinetic Models	Parameters	Values
PFO	$k_1 \times 10^{-3}$ (1/min)	14.3 ± 0.43
	q_e , cal. (mg/g)	5.80 ± 0.91
	R^2	0.92
	χ^2	0.18 ± 0.36
	RMSE	3.12 ± 0.54
	MAE	0.89 ± 0.35
	PSO	$k_2 \times 10^{-3}$ (g/(mg min))
q_e , cal.(mg/g)		5.40 ± 0.13
R^2		0.97
q_e , exp. (mg/g)		4.78 ± 0.09
χ^2		0.0076 ± 0.01
RMSE		0.36 ± 0.05
MAE		0.105 ± 0.02

4.4.3.3 Biosorption isotherm studies

Figure 47 (a) demonstrated the performance of La(III)-SWR for the biosorption of As(III) at different temperatures. The graphical findings revealed that at low concentration range, increment in As(III) biosorption takes place with increase in concentration and finally achieved plateau or almost constant value at higher concentrations for all analyzed temperatures. The increase in As(III) biosorption with temperature rise is endothermic biosorption process which will be further validated from the thermodynamic study in section 4.4.4. The plateau reached at equilibrium concentrations is due to complete coverage of active binding sites of La(III)-SWR by As(III) anion. The experimental data are analyzed using the Langmuir isotherm model (equation 8) and the Freundlich isotherm model (equation 11) to determine As(III) biosorption mechanism and investigate best fit isotherm model. The isotherms

parameters are analyzed from the slope and intercept of the respective plots of **Figure 47 (c)** and **Figure 47 (d)**. The computed isotherm parameters with error functions are shown in **Table 16**. The experimental results driven by the Langmuir isotherm model has a higher coefficient of determination ($R^2 > 0.99$) in comparison to the Freundlich isotherm model. The experimental results supported the Langmuir isotherm model. At temperatures of 298 K, 303 K, and 308 K, the maximum biosorption capacity (q_m) of La(III)-SWR is calculated to be 37.73, 48.78, 62.50 mg/g, respectively. These values are also closer to the experimental value indicated by the plateau region in **Figure 47 (a)**.

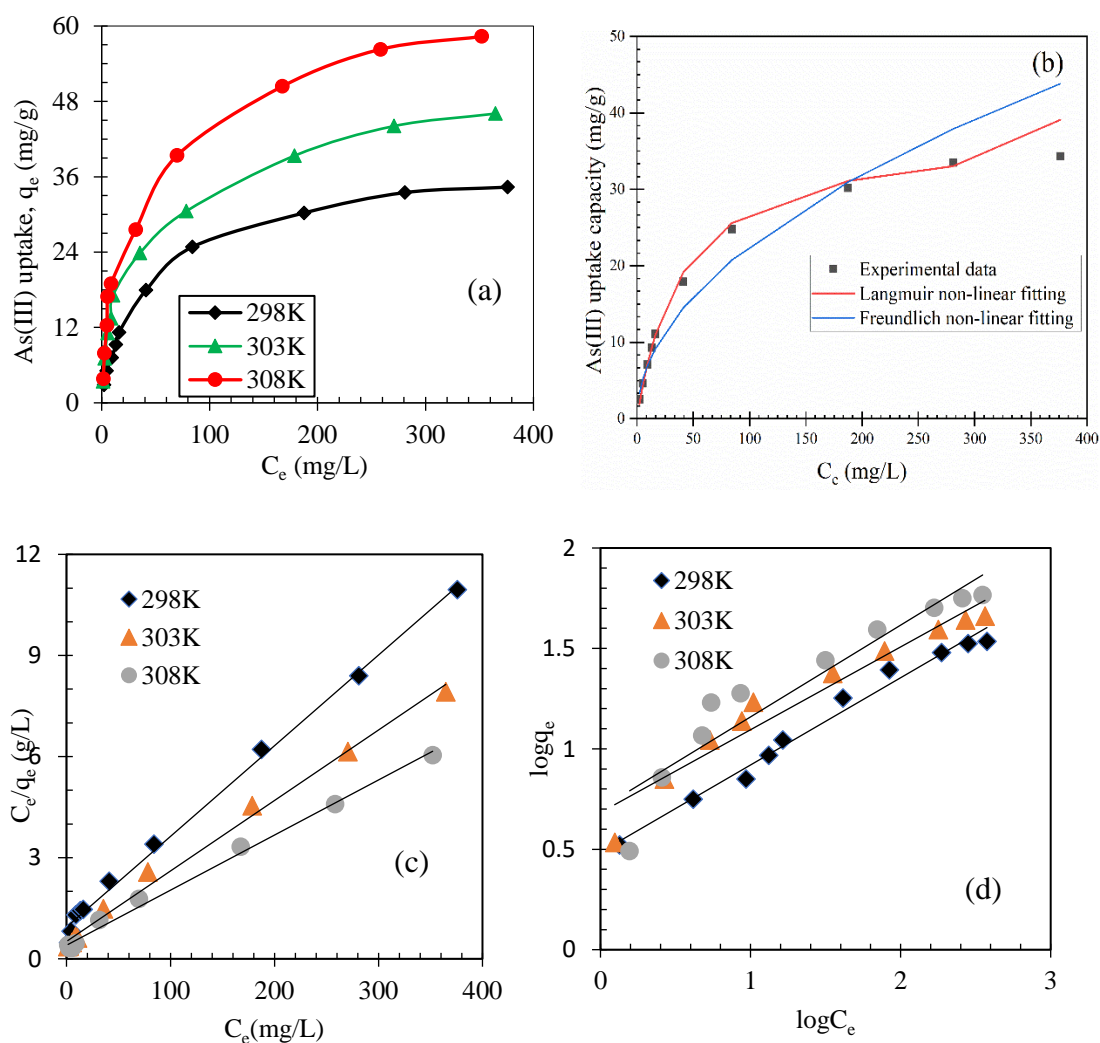


Figure 47: Isotherm of As(III) biosorption onto La(III)-SWR (a) Isotherm plot at varied temperatures (b) Non-linear modeling of Langmuir and Freundlich isotherm data with experimental data at 298K (c) Langmuir isotherm model and (d) Freundlich isotherm model (Conditions: $m/v = 1$ g/L, $\text{pH} = 12.08$, $t = 24$ h)

As(III) biosorption onto La(III)-SWR was further reassured using non-linear fitting. This also demonstrated the better support with Langmuir isotherm in comparison to Freundlich isotherm model, as outlined in **Figure 47 (b)**. The lower error function values of χ^2 , RMSE and MAE for Langmuir isotherm model determined at three different temperatures (298 K, 303K and 308 K) in comparison, indicated a greater agreement with experimental data. This finding also assists As(III) biosorption onto La(III)-SWR occurred in accordance with the Langmuir isotherm model.

The biosorption capacity of La(III)-SWR is compared with biosorbents reported in the literature as listed in **Table 17**. It showed that the biosorption capacity of powdered almond shell, *Citrus limenta* PAC-500, almond shell biochar, *Citrus limenta* PPAC-500, and *Momordica charantia* is countably less in comparison to the biosorbent which have iron (Fe), zirconium (Zr) and rare metals (Verma *et al.*, 2019; Vieira *et al.*, 2017; Pandey *et al.*, 2009). In case of La(III)-SWR, the active sites created on the matrices of La(III) in La(III)-SWR can contribute higher biosorption capability in comparison to other biosorbents summarized in **Table 17**. The biosorption capacity of La(III)-SWR is compared with metal-loaded saw dust and biocomposites (Duan *et al.*, 2017; Hao *et al.*, 2016). This comparative study revealed that La(III)-SWR can be a potential biosorbent for the removal of As(III) anion from water.

Table 16: Isotherm parameters for the biosorption of As(III) onto La(III)-SWR.

Models	Parameters	298K	303K	308K
Langmuir isotherm	$q_{exp}(mg/g)$	35.15 ± 0.12	45.28 ± 0.09	58.12 ± 0.11
	$q_m(mg/g)$	37.73 ± 0.15	48.78 ± 0.14	62.50 ± 0.17
	$b(L/mg) \times 10^3$	28.16 ± 0.03	39.88 ± 0.08	48.34 ± 0.06
	R^2	0.99	0.99	0.99
	χ^2	0.19 ± 0.05	0.27 ± 0.08	0.33 ± 0.06
	RMSE	2.96 ± 0.002	4.08 ± 0.005	6.39 ± 0.004
	MAE	0.93 ± 0.08	0.94 ± 0.05	0.91 ± 0.03
Freundlich isotherm	$K_F(mg/g)(L/mg)^{1/n}$	2.26 ± 0.87	2.76 ± 0.63	2.82 ± 0.58
	$1/n$	0.48 ± 0.26	0.68 ± 0.18	0.70 ± 0.39
	R^2	0.96	0.94	0.89
	χ^2	0.49 ± 0.47	0.53 ± 0.31	0.51 ± 0.28
	RMSE	8.41 ± 0.09	10.34 ± 0.07	9.21 ± 0.05
	MAE	2.65 ± 0.10	2.92 ± 0.15	2.87 ± 0.13

Table 17: Comparison of As(III) biosorption onto La(III)-SWR with other adsorbents

Adsorbents	q_{\max} (mg/g)	pH	References
La(III)-SWR at 308K	62.50	12.08	This study
La(III)-SWR at 303K	48.78	12.08	This study
La(III)-SWR at 298K	37.73	12.08	This study
Iron Nano Bio-composite	1.04	6.0	(Shaikh <i>et al.</i> , 2020)
Powdered almond shell (ALS)	4.6	7.2	(Shafaqat Ali <i>et al.</i> , 2020)
Pyrolyzed almond shell (ALB)	4.86	7.2	(Shafaqat Ali <i>et al.</i> , 2020)
Biochar			
Citrus limetta PAC – 500	0.72	3	(Verma <i>et al.</i> , 2019)
Citrus limetta PPAC - 500	0.53	3	(Verma <i>et al.</i> , 2019)
Bacillus thuringiensis strain WS3	10.94	7.0	(Altowayti <i>et al.</i> , 2019)
Magnetic Nanocomposite	28	2.9	(Gugushe <i>et al.</i> , 2019)
Pinecone Magnetite composite	16.8	8.0	(Ouma <i>et al.</i> , 2018)
Modified hazelnut shell	11.84	9.0	(Sert <i>et al.</i> , 2017)
Iron Coated seaweeds	4.2	7.0	(Vieira <i>et al.</i> , 2017)
Iron doped amino-functionalized sawdust	10.1	7.0	(Hao <i>et al.</i> , 2016)
ZrO ₂ coated sawdust	29	7.0	(Hao <i>et al.</i> , 2016)
La ₂ O ₃ coated sawdust	22	7.0	(Hao <i>et al.</i> , 2016)
Dried fine powdered biomass of <i>Momordica charantia</i>	0.88	9.0	(Pandey <i>et al.</i> , 2009)

4.4.4 Investigation of thermodynamic parameters

The value of Langmuir equilibrium parameter ‘b’ (L/mg) obtained from Langmuir isotherm model at different temperatures is used to determine the dimensionless thermodynamic equilibrium constant (k_c) using equation (12). The thermodynamic parameters ΔH° , ΔS° and ΔG° are evaluated from the slope and intercept of van’t Hoff plot ($\ln(k_c)$ versus $1/T$) as displayed in **Figure 48**. All the evaluated values of thermodynamic parameters are listed in **Table 18**. The values in the table showed ΔG° being negative for the temperatures studied and found more negative at higher temperatures suggesting spontaneous nature of biosorption. The positive value of ΔH° indicates the biosorption of As(III) onto La(III)-SWR is endothermic. Ouma *et al.* (2018) reported the similar observation found during arsenite biosorption onto pinecone magnetite. The positive value of ΔS° shows increased entropy. The increased entropy of the system is most likely caused through the exchange of

coordinated hydroxyl or water ligands *via* ligand exchange reaction with As(III) for the examined biosorption system (Liu *et al.*, 2015; Mahmood *et al.*, 2018).

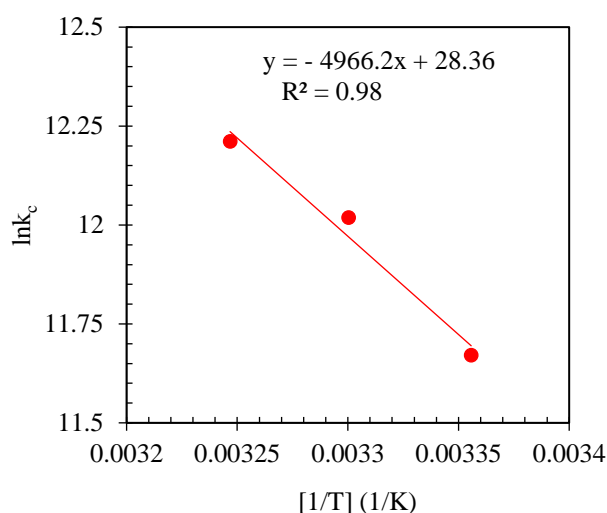


Figure 48: Van't Hoff plot of $\ln k_c$ versus reciprocal of absolute temperature.

Table 18: Thermodynamic parameters for the As(III) biosorption onto La(III)-SWR

Temp (K)	$b \times 10^3$ (L/mg)	k_c	ΔG° (kJ/mol)	ΔH° (kJ/mol)	ΔS° (J/mol K)
308	48.34	200933.83	-31.27±1.52		
303	39.88	165837.02	-30.28±2.17	40.23±0.87	235.78±3.82
298	28.16	117097.33	-28.91±1.96		

4.4.5 Effects of co-existing ions

The arsenic anions along with other co-existing ions such as PO_4^{3-} , Cl^- , SO_4^{2-} and NO_3^- anions are associated in arsenic polluted water, which may inhibit As(III) biosorption process. The interference of these anions on the biosorption of As(III) onto La(III)-SWR are presented in **Figure 49**. An insignificant effect of Cl^- is observed while NO_3^- exhibited slight effect and SO_4^{2-} exhibited countable interference for biosorption of As(III). The most effective inhibitor of biosorption of As(III) is PO_4^{3-} anion. The results revealed that the inhibitory effect shown by these ions increases with increasing concentration that can be reasonably ascertained due to the competitive effects of these ions with As(III) anions for the same binding sites (Ahmaruzzaman, 2010). The inhibitory effect of tested co-existing ion examined for the dearsenification of As(III) is in the sequence as: $\text{PO}_4^{3-} > \text{SO}_4^{2-} > \text{NO}_3^- > \text{Cl}^-$. The PO_4^{3-} and SO_4^{2-} ions have a stronger affinity for the La(III) ion (Hao *et al.*, 2016). The higher mobility of these ions during biosorption of As(III) onto La(III)-SWR causes

interference (Gizaw *et al.*, 2021). The sharp decline in biosorption of As(III) in presence of PO_4^{3-} is because of the structural and chemical resemblance of oxoanionic species of As(III) with PO_4^{3-} in aqueous medium (Biswas *et al.*, 2008; Ghimire *et al.*, 2008). This result is consistent with the tetrafluoroborate biosorption by Zr(IV)-SOJR (Paudyal *et al.*, 2012) and also with Cu(II) impregnated natural mineral tufa part (Pantić *et al.*, 2019).

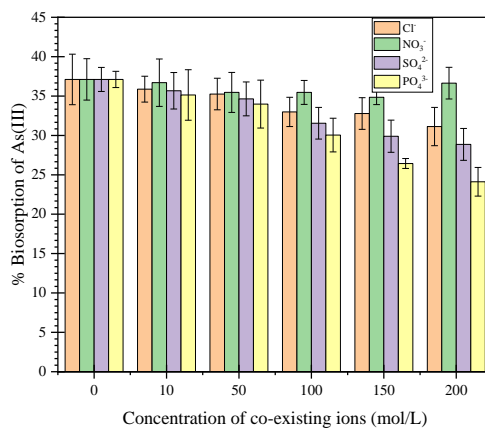


Figure 49: Effect of co-existing ions for the As(III) biosorption onto La(III)-SWR (Conditions: $m/v = 1\text{ g/L}$, $C_i = 10\text{ mg/L}$, $\text{pH} = 12.08 \pm 0.4$, $t = 24\text{ hrs}$, and $T = 298\text{K}$).

4.4.6 XPS analysis of the biosorbent

XPS survey detected the peaks of La 3d, O 1s, C 1s, and As 3d as depicted in **Figure 50 (a)**. The notable peak of the aromatic/or aliphatic carbons found in cellulose, lignin, pectin, and protein on the watermelon surface is the steep peak of C 1s observed at binding energy of 284.6 eV. The La(III)-SWR peak measurements indicated that La(III) is successfully loaded onto SWR. (**Figure 50 b**). Similar to this, As(III) anion biosorption is revealed by the existence of As 3d peaks on the XPS spectrum of As(III) biosorbed La(III)-SWR. Additionally, two characteristic peaks of As(III) and As(V) with binding energies of 44.01 and 46.2 eV, respectively, are linked to the XPS spectra of As 3d. This suggested that As(III) under the tested experimental conditions underwent partial aerial oxidation to become As(V). For La(III)-SWR, the maxima of La 3d_{5/2} and La 3d_{3/2} were found at 837.85 and 854.74 eV, respectively (**Figure 50 c**). The La 3d_{5/2} and La 3d_{3/2} binding energies changed to greater values following As(III) biosorption. Three peaks were deconvoluted from the

high-resolution XPS scan of O1s (**Figure 50 d**) and ascribed to the La - O, O - As, and O - H bonds, respectively, at energies of 531.0, 529.67, and 532.22 eV. The association of La- O bond in biosorbent surface suggested that the incorporated La(III) creates the chemical bond with active oxygen of watermelon biosorbent and formation of O –As bond in biosorption product indicated the successful biosorption of oxyanions of arsenic. This result gave clear proof of loading La(III) onto carboxylate group of watermelon pectin and profitable biosorption of oxoanionic species of arsenic onto La(III)-SWR.

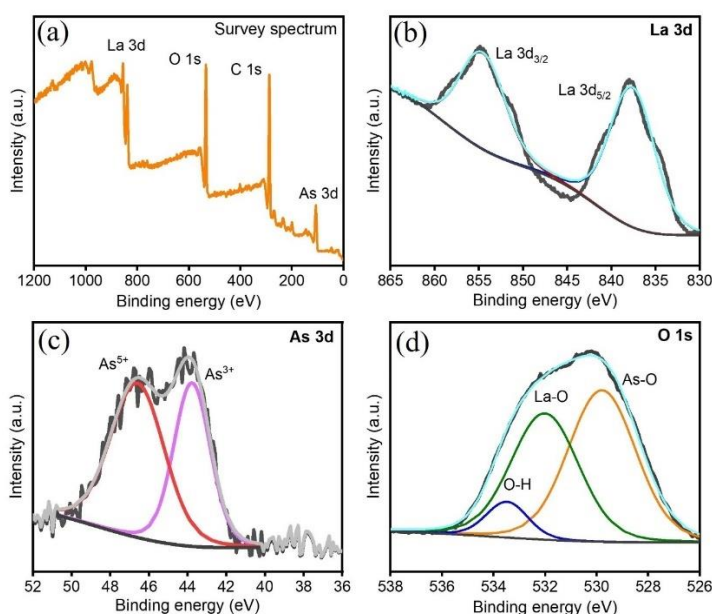


Figure 50: XPS analysis of La(III)-SWR after biosorption of As(III) (a) Survey spectrum (b) La 3d (c) As 3d (d) O 1s

4.4.7 Desorption studies

The desorption of As(III) from arsenic loaded La(III)-SWR with different NaOH concentration is illustrated in **Figure 51**. The result demonstrated that as the molar concentration of NaOH rises from 0.001 to 0.5 M, the desorption of As(III) increases from 41.11 to 71.07%, whereas the maximum desorption of 98.47 % was achieved using 2 M of NaOH. It can be ascertained with the logic that the increased concentration of hydroxyl ion enhanced ligand exchange reaction between hydroxide ion and As(III) anion so that percentage desorption increases at higher concentration of NaOH. The desorption reaction takes place as shown in **Figure 52**. Furthermore, the As(III) biosorption capacity from the regenerated La(III)-SWR is only slightly

reduced (1.28%) by NaOH treatment. There is negligible leakage of loaded La(III) that firmly supports the greater potentiality of tested La(III)-SWR in alkaline medium.

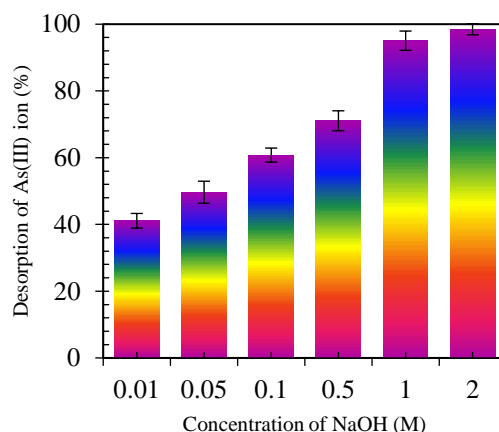


Figure 51: Desorption of As(III) from As(III) biosorbed La(III)-SWR with varied concentration of NaOH (Conditions: weight of As(III) loaded La(III)-SWR = 50 mg, volume of NaOH = 15 mL, $t = 24$ h, and $T = 298$ K)

4.4.8 Mechanism of As(III) biosorption- desorption

The La(III) incorporated onto saponified watermelon pectic acid built a stable five membered ring chelates. Therefore, La(III)-SWR becomes more rigid and stable. The loaded La(III) easily gets hydrolyzed with some water molecules and coordinated with several hydroxyl and water ligands. These hydroxyl ions and water molecules coordinated on the polymer matrices of La(III) in La(III)-SWR are easily exchanged with anionic or neutral species of As(III). The As(III) biosorption onto La(III)-SWR inferred to occurred through ligand exchange mechanism similar to orange based biosorbents (Biswas *et al.*, 2008b; Ghimire *et al.*, 2003). The regeneration of La(III)-SWR from As(III) loaded La(III)-SWR is done using alkali solution. The hydroxyl ions of alkali solution participate in ligand exchange reaction with biosorbed As(III) anion during desorption process (Aryal *et al.*, 2022). Ligand exchange mechanism of As(III) onto or from La(III)-SWR is displayed in **Figure 52**.

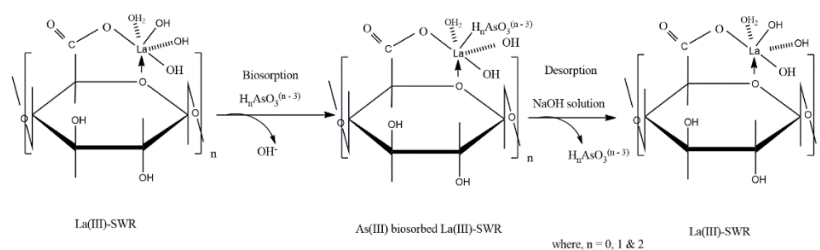


Figure 52: Inferred mechanism of As(III) biosorption-desorption onto La(III)-SWR (Ghimire *et al.*, 2003).

4.5 Biosorption of Hg(II) onto biosorbents

4.5.1 Biosorbents characterization

4.5.1.1 FE-SEM analysis on the biosorbents

FE-SEM measurements was performed to analyze the surface morphology of the shown in **Figure 53**. As seen in the image of **Figure 53 (a)** RWR has a smooth surface with a regular morphology including small white patches which may be due to ingredients like sugar, carotenoids, and low molecular weight species (Bhattacharjee *et al.*, 2020). Similarly, **Figure 53 (d)** is the image of RBP which has also even and ordered structures with smooth surfaces. After $\text{Ca}(\text{OH})_2$ treatments, the surface morphology of SWR (**Figure 53 (b)**) and SBP (**Figure 53 (e)**) are found to be rough, heterogenous with well-developed pores associated with uneven cavities. These surface structures could provide more biosorption sites. After biosorption of Hg(II) onto SWR (**Figure 53 (c)**) and SBP (**Figure 53 (f)**), the surface morphology of biosorbents is significantly changed and turned into smooth, occupied structures demonstrating that Hg(II) is successfully biosorbed onto SWR and SBP.

4.5.1.2 EDX spectra with elemental mapping

The surface chemistry of SWR and SBP was analyzed before and after Hg(II) biosorption, respectively, through EDX analysis as shown in **Figure 54**. The analysis figures out the peaks of C (63.88 %), O (24.73%), Ca (19.59 %), Mg (0.39 %), Si (0.26%) and P (1.08%) in SWR (**Figure 54 (a)**) at binding energies around 0.28, 0.53, 3.70, 1.25, 1.74, and 2.01 keV, respectively. Similarly, SBP (**Figure 55 (a)**) constitutes peaks of C (74.74 %), O (22.30 %), Ca (13.94 %), and Mg (0.11%) on its surface. The significant percentage of Ca atom on both biosorbents is due to $\text{Ca}(\text{OH})_2$ treatments. The calcium atom with sharp peak in EDX spectra suggested that calcium

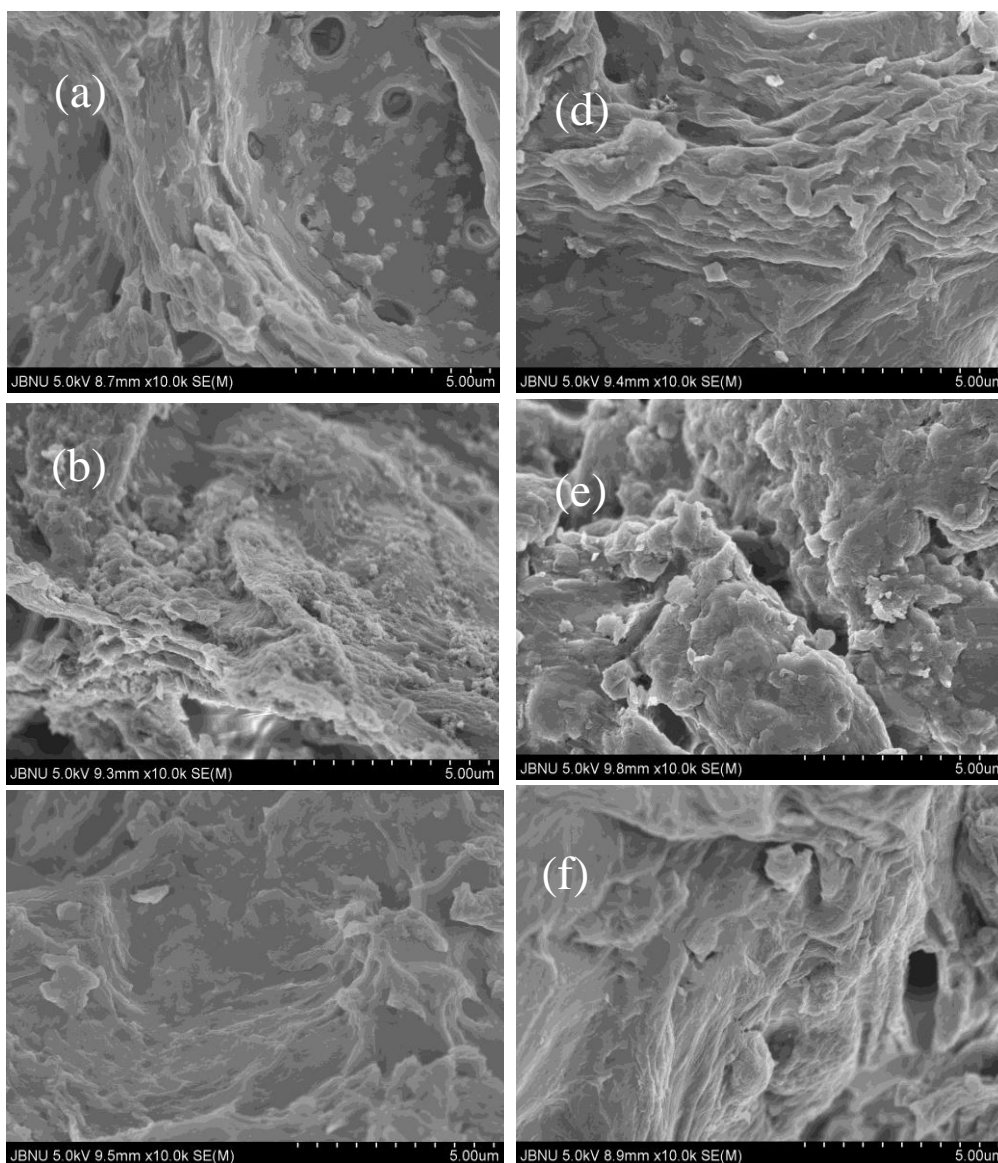


Figure 53: FE- SEM micrographs of (a) RWR (b) SWR and (c) Hg(II) biosorbed SWR (d) RBP (e) SBP and (f) Hg(II) biosorbed SBP

atom formed calcium pectate. After biosorption of Hg(II) onto SWR, it (**Figure 54 (b)**) contains major elements such as C (43.18%), O (43.98%), and Hg (11.42%) and SBP after biosorption (**Figure 55 (b)**) contains C (50.24 %), O (39.31%), and Hg (9.47%). The peaks associated to Hg(II) appeared in both Hg(II) biosorbed SWR and SBP around binding energy 2.19 eV while the peaks of Ca(II) are atypical due to substitution caused by Hg(II) through cation exchange reaction. In addition, the elemental distribution found in color mapping of SWR (**Figure 54 (c)**) and SBP (**Figure 55 (c)**) before and after biosorption of Hg(II) (**Figure 54 (d)**) and **Figure**

55(d)) are the solid evidence of existing elements. These results anticipated that biosorption of Hg(II) can take place in SWR and SBP.

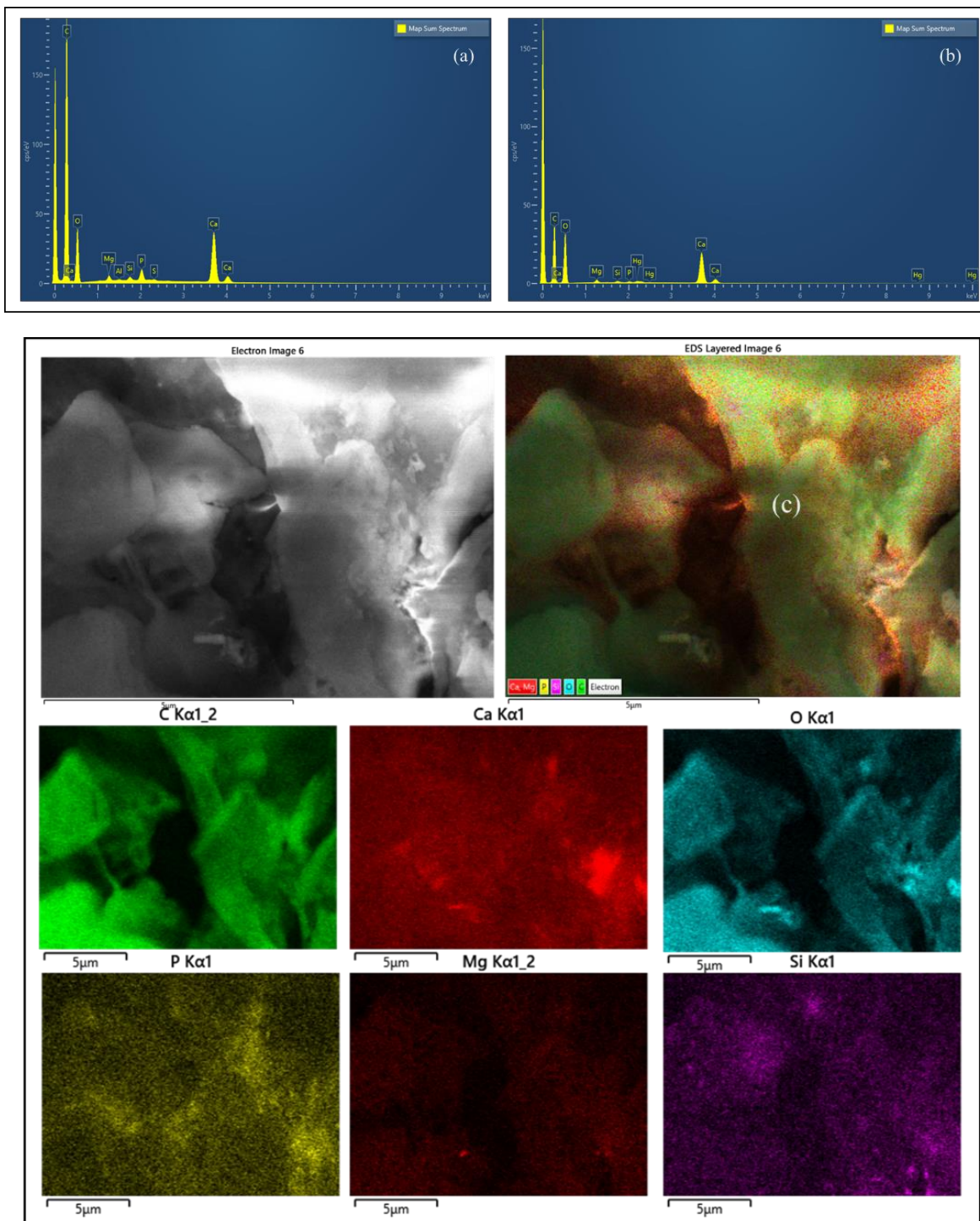


Figure 54: EDX spectra (a) SWR (b) after Hg(II) biosorption (c) EDX electron image layered images, and EDX color mapping images of all elements of SWR

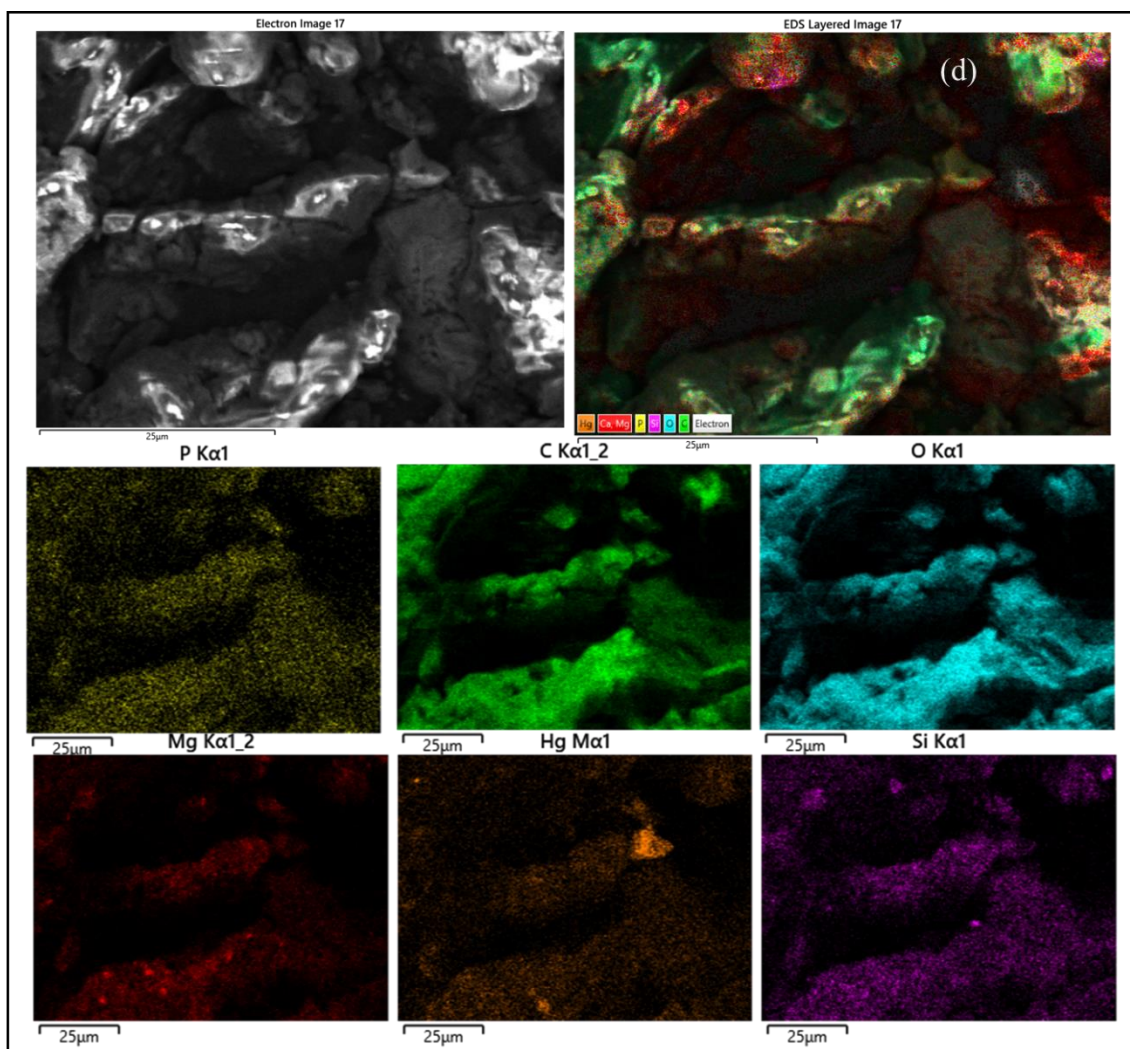


Figure 54: (d) EDX electron image, layered images, and EDX color mapping images of all elements of SWR after Hg(II) biosorption

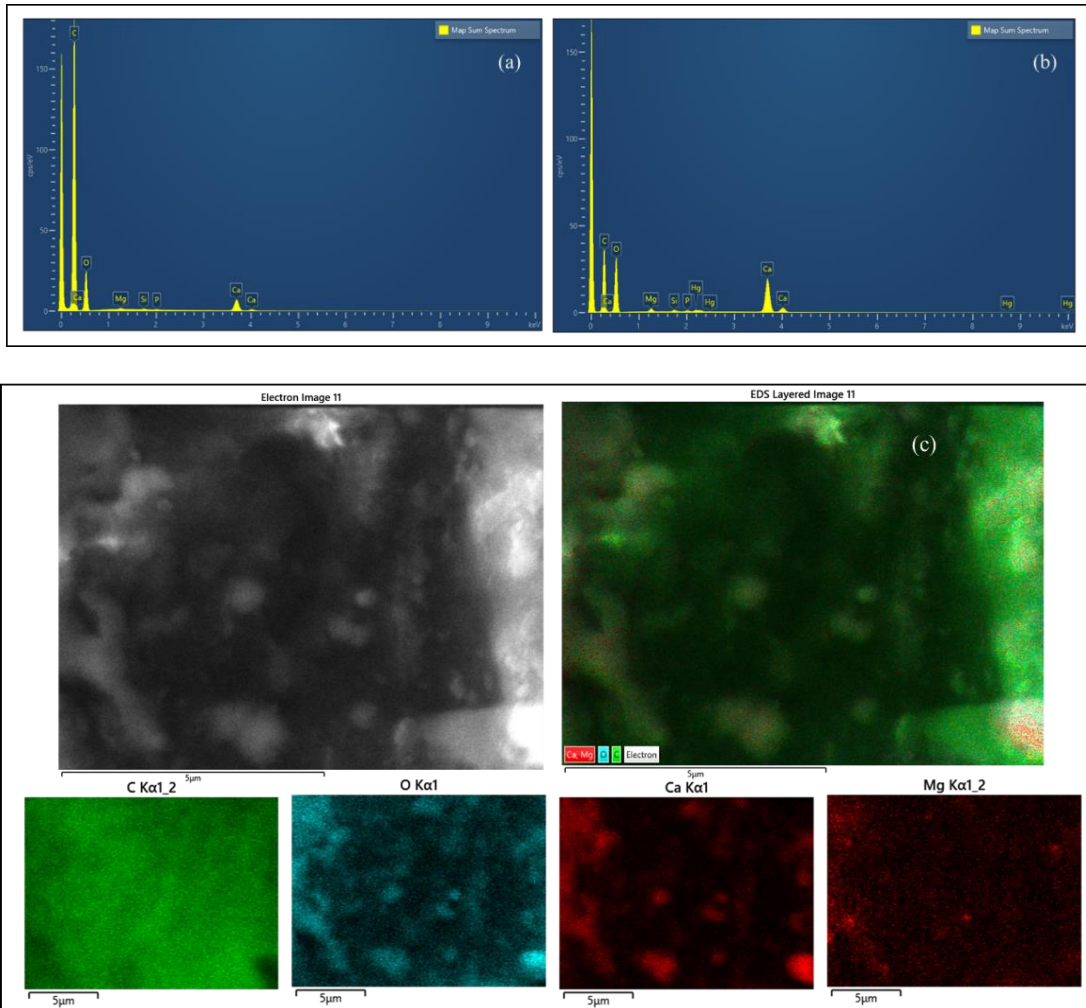


Figure 55: EDX spectra of (a) SBP (b) Hg(II) biosorbed SBP (c) EDX electron image, layered images and EDX color mapping images of all overlapping elements of SBP

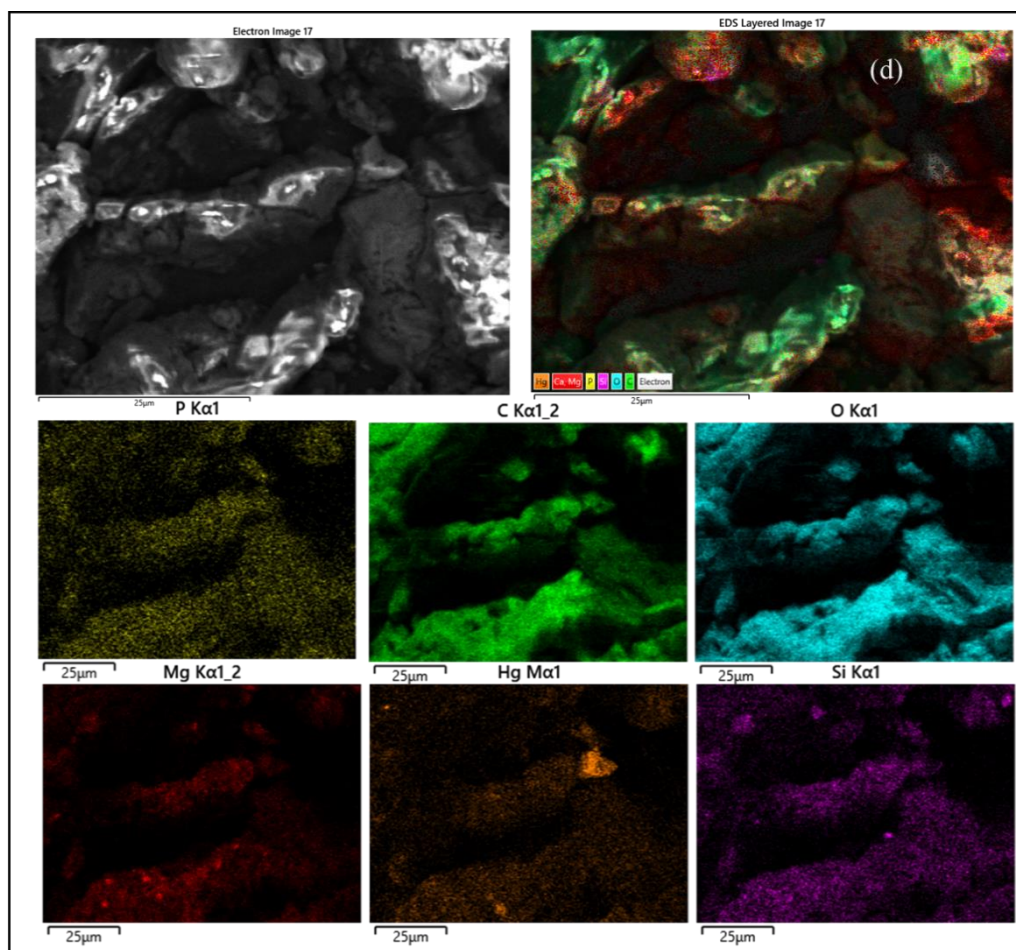


Figure 55: (d) EDX electron image, layered images and EDX color mapping images of all overlapping elements Hg(II) biosorbed SBP.

4.5.1.3 FTIR analysis

The FTIR spectra of RWR, SWR and Hg(II) biosorbed SWR are shown in **Figure 56 (a)** and RBP, SBP and Hg(II) biosorbed SBP are displayed in **Figure 56 (b)**. In the spectra of RWR and RBP, the broad peak at around 3316 cm^{-1} in SWR and 3305 cm^{-1} in SBP is stretching vibration of -OH groups of alcohol, carboxylic acid present in cellulose, hemicelluloses, pectin, and lignin and the adsorbed water molecules (Rachini *et al.*, 2009). The smaller peak at around 2928 cm^{-1} in SWR and 2947 cm^{-1} in SBP is associated to vibrations of -CH and -CH₂ groups (Adhikari *et al.*, 2017). Two characteristics stretching peaks of carboxylates groups are observed at around 1702 cm^{-1} in SWR and 1736 cm^{-1} and 1606 cm^{-1} . These absorption peaks revealed carboxyl group of RWR is a characteristic functional group of pectic acid (Aryal *et al.*, 2022). The peaks observed at 1242.26 and 1098.4 cm^{-1} associated with -C-O-

bond of alcoholic, phenolic and carboxyl group present in RWR and RBP (Tavares *et al.*, 2017). After $\text{Ca}(\text{OH})_2$ treatment, the peak around 3280 cm^{-1} became broad and peaks of 1702 cm^{-1} almost disappeared and new peaks at around 1571 , 1375 cm^{-1} in SWR and 1596 and 1399 cm^{-1} in SBP are appeared indicating the presence of O-Ca bond of calcium pectate. The intensity of peaks decreases and shifted to lower frequency region after $\text{Ca}(\text{OH})_2$ treatments indicates the changes of functional groups during lime water treatment (Paudyal *et al.*, 2012). The modified SWR is expected to be a promising biosorbent for biosorption of $\text{Hg}(\text{II})$ ions. In the $\text{Hg}(\text{II})$ biosorbed SWR, the peak at 991 cm^{-1} become shifted to lower frequency region due to biosorption of $\text{Hg}(\text{II})$. After $\text{Hg}(\text{II})$ biosorption, new peaks observed at 1360 and 991 cm^{-1} due to Hg-O bonds observed in $\text{Hg}(\text{II})$ biosorbed SWR (Oveisi *et al.*, 2017). This conclusion is consistent with other studies found in literature (Dias *et al.*, 2021; Fayazi, 2020; Huang *et al.*, 2019; Ge *et al.*, 2013).

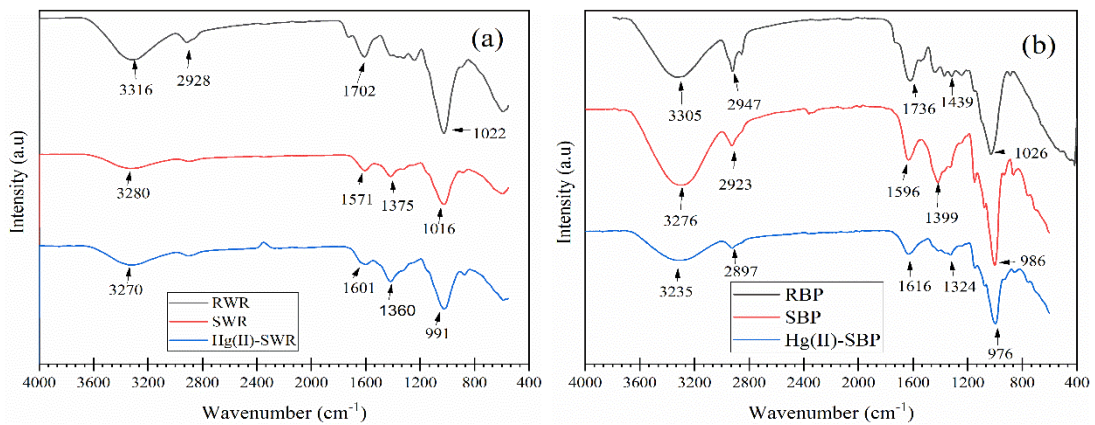


Figure 56: FTIR spectra of (a) RWR, SWR, $\text{Hg}(\text{II})$ biosorbed SWR and (b) RBP, SBP, $\text{Hg}(\text{II})$ biosorbed SBP

4.5.1.4 Surface charge of biosorbents

The zeta potential of SWR and SBP was measured at different pH and displayed in **Figure 57**. The point of zero charge (pH_{pzc}) of SWR and SBP are found at 2.88 and 3.33. At this pH, the surface charge of SWR and SBP biosorbent is found neutral. As pH of the solution increases, zeta potential values of both SWR and SBP becomes more negative indicating the surface charge of SWR and SBP becomes negatively charged (Lee & Choi, 2021). At $\text{pH} < \text{pH}_{\text{pzc}}$, the surface of SWR and SBP is protonated so that SWR and SBP surface become positive that causes poor

biosorption for Hg(II) and Pb(II) ion. However, at $\text{pH} > \text{pH}_{\text{pzc}}$, the negatively charged surface of SWR and SBP can biosorb Hg(II) and Pb (II) effectively.

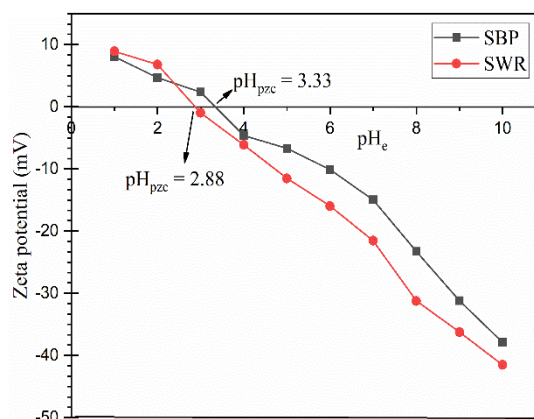


Figure 57: Zeta potential at different pH showing pH_{pzc} of SWR and SBP.

4.5.2 Batch studies

4.5.2.1 Effect of pH

The pH of solution influences the biosorption of Hg(II) onto RWR and SWR as shown in **Figure 58 (a)** and **Figure 58 (b)**. The biosorption of Hg(II) onto RWR at equilibrium pH 2.05 is found to be 2.33 % while at equilibrium pH 5.94 it is increased to 19.54%. Similarly, the biosorption of Hg(II) onto SWR at pH 2.05 is 18.32% and percentage removal gradually increases and reached 86.92% at equilibrium pH 5.94. Similarly, in **Figure 58 (b)** at equilibrium pH 2.61 biosorption onto RBP and SBP are observed to be 4.88% and 17.51%, respectively. Further, at pH 5.92, RBP and SBP biosorbs 23.13% and 91.8%, respectively. The results showed that the biosorption of Hg(II) is pH dependent. At low pH, the surface functional sites of biosorbents are protonated as a result biosorption of Hg(II) is unfavorable due to electrostatic repulsions (Fayazi *et al.*, 2020; Baheti *et al.*, 2013). As pH increases, induced negative charge on the biosorbent surface increases by deprotonation which is favorable for cation biosorption (Song *et al.*, 2011). The optimum pH for biosorption of Hg(II) onto SWR and SBP is determined to be 5.94. The speciation diagram of mercury species showed the existence of Hg(II) in the form of Hg(OH)₂ at this pH, which is expected to be biosorbed onto SWR and SBP during biosorption (Ugrina *et al.*, 2020). The biosorption of Hg(II) onto SWR and SBP is shown in the elementary reaction (a). The reported studies also showed that the optimum pH for Hg(II)

biosorption using activated carbons were found in the range of 5 - 6 (Guo *et al.*, 2017; Kadirvelu *et al.*, 2004).

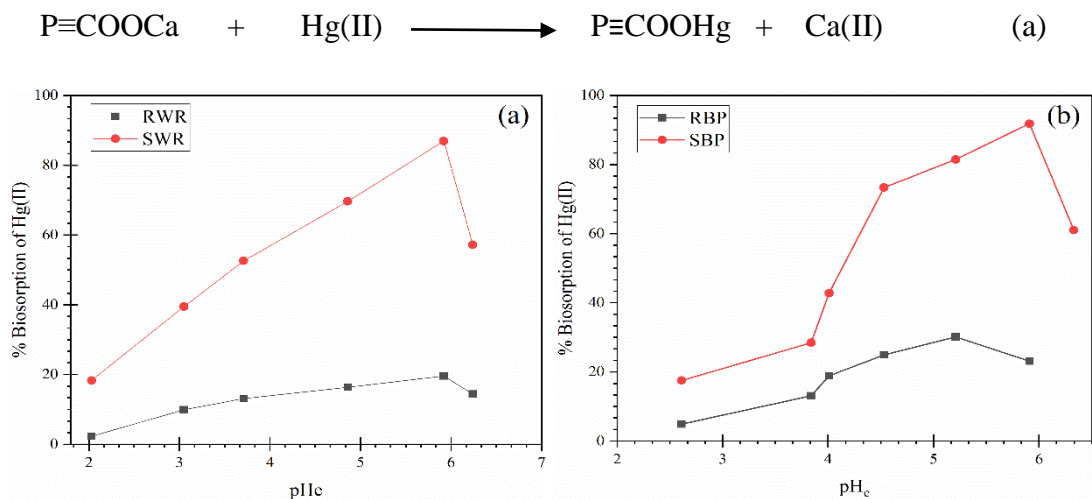


Figure 58: Effect of pH in the biosorption of Hg(II) onto (a) RWR, SWR and (b) RBP, SBP (Conditions: $m/v = 0.5 \text{ g/L}$, $C_i = 10 \text{ mg/L}$, $t = 24\text{h}$, $T = 298 \text{ K}$)

4.5.2.2 Effect of contact time

The kinetic study for the biosorption of Hg(II) onto SWR and SBP were carried out at optimum pH 5.94 and the result is depicted in **Figure 59 (a)** and **Figure 60 (a)**. The results indicated that the biosorption capacity of Hg(II) onto SWR and SBP is rapid for the first 120 min. After 120 min, the biosorption capacity of SWR and SBP attained equilibrium which is indicated by the formation of plateau over the time. It can be described that the biosorption of Hg(II) increases initially due to the existence of large number of unoccupied binding sites. With lapse of time, most of the unoccupied binding sites are occupied by Hg(II) and finally leads to constancy after the biosorption. To validate the experimental data, the data are fitted to the PFO and PSO kinetic models according to equation (4) and (6) and graphs are depicted in **Figure 59 (b) & (c)** and **60 (b) & (c)**. The rate constants and other parameters obtained from the graphs of Hg(II) biosorption onto SWR and SBP are given in **Table 19**. The PSO model best fitted the experimental data with a coefficient of distribution ($R^2 = 0.999$) as compared to the PFO model ($R^2 = 0.958$). Moreover, the value of q_e calculated (16.815 mg/g) from PSO model is closer to experimental values (16.586 mg/g). A similar trend is observed in case of SBP. The experimental data on non-linear kinetic modeling is also in agreement with PSO kinetic modeling shown in **Figure 59 (a)** for SWR and **Figure 60 (a)** for SBP. Therefore, the biosorption of

Hg(II) onto SWR and SBP follows PSO model, implying the biosorption of Hg(II) is driven by chemisorption.

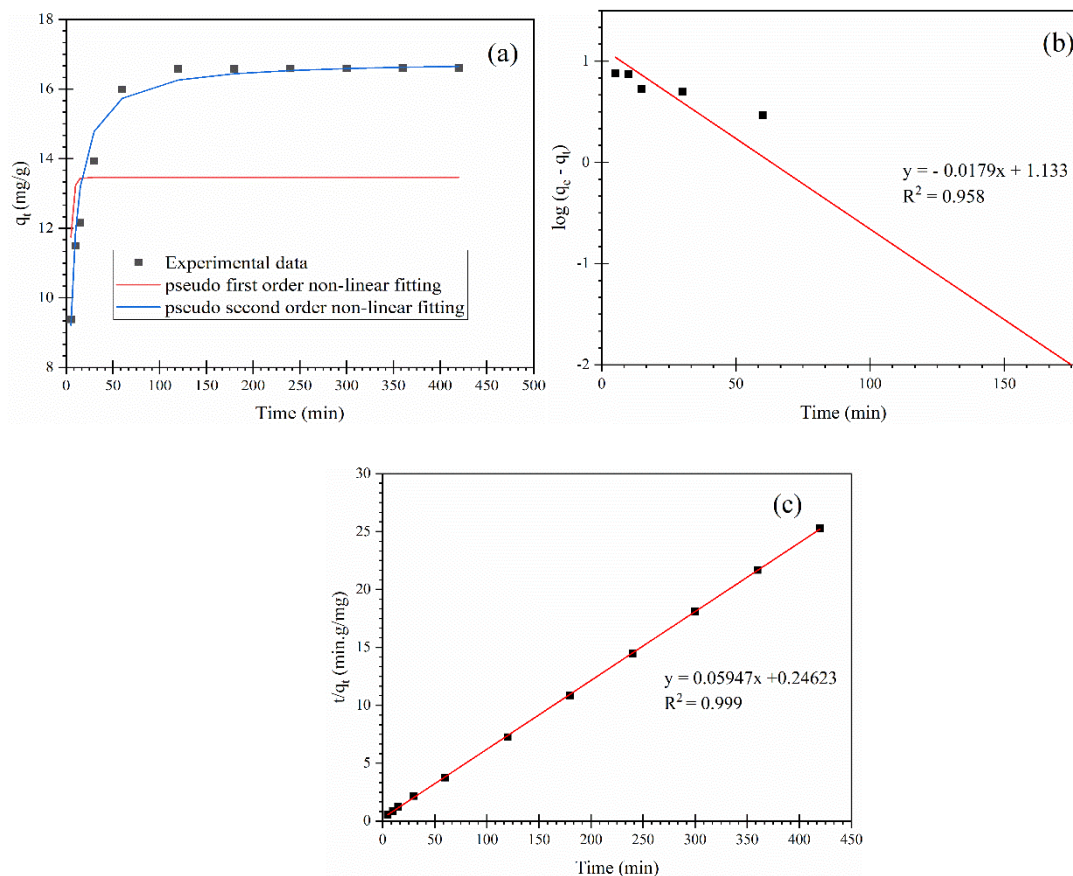


Figure 59: Biosorption of Hg(II) onto SWR (a) Non-linear plot of PFO and PSO fittings with experimental data (b) PFO and (c) PSO model (Conditions: $m/v = 0.5$ g/L, $pH = 5.94$, $C_i = 10$ mg/L, $t = 24$ h, $T = 298$ K)

Table 19: Kinetic parameters for biosorption of Hg(II) onto SWR and SBP biosorbents

Kinetic Models	Parameters	SWR	SBP
PFO	k_1 (1/min)	0.412 ± 0.321	0.042 ± 0.024
	q_e, cal (mg/g)	13.46 ± 1.23	13.47 ± 2.24
	R^2	0.958	0.958
PSO	k_2 (g/mg.min)	0.0144 ± 0.012	0.007 ± 0.06
	q_e, cal (mg/g)	16.815 ± 2.04	17.40 ± 1.24
	R^2	0.999	0.999
	q_e, exp (mg/g)	16.586 ± 0.456	16.59 ± 2.21

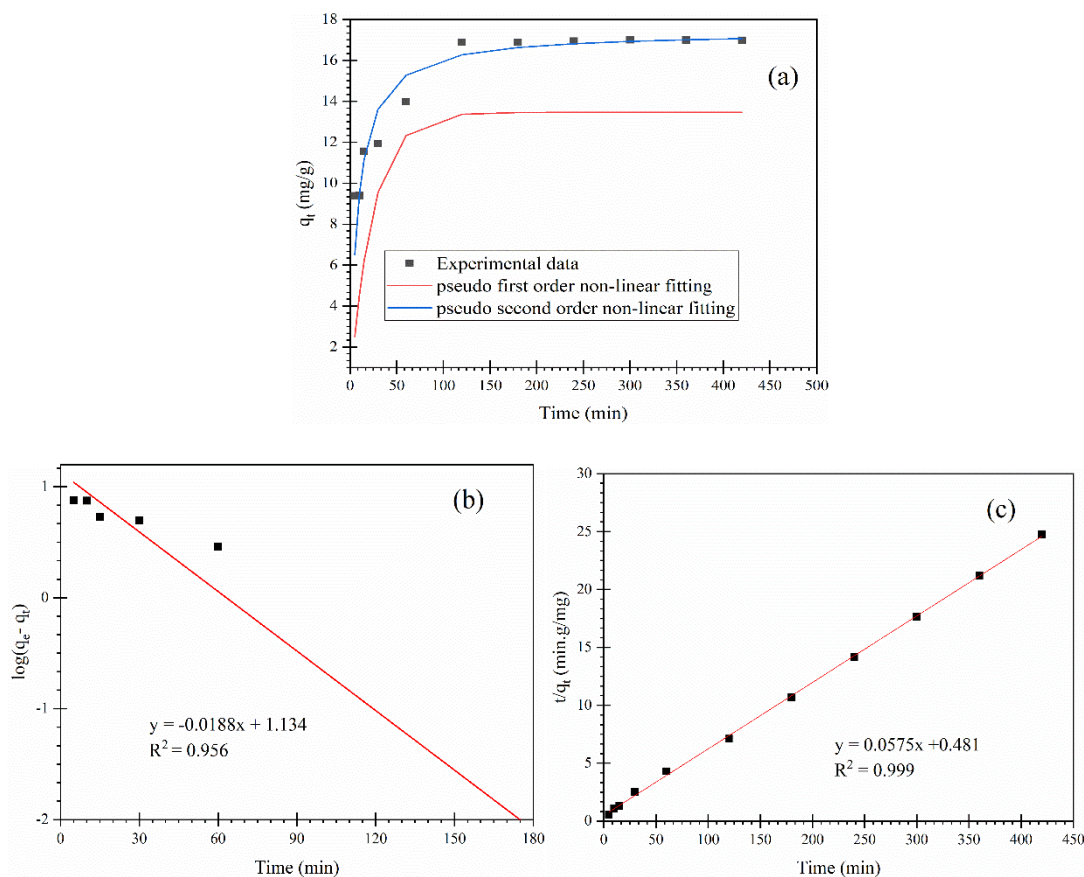


Figure 60: Biosorption kinetic study of Hg(II) onto SBP (a) Non-linear kinetic modeling of PFO and PSO with experimental data (b) PFO model and (c) PSO model (Conditions: $m/v = 0.5$ g/L, $C_i = 10$ mg/L, $pH = 5.92$, $t = 24$ h, $T = 298$ K)

4.5.2.3 Effect of initial concentration

The biosorption isotherm of Hg(II) onto SWR and SBP are presented in **Figure 61** and **Figure 62**. The results revealed that the biosorption capacity of SWR and SBP increased rapidly as the Hg(II) concentration increases and reached at a saturation point. The high biosorption rate in the beginning might be due to vacant biosorption sites onto the biosorbent. The biosorption capacity reached a plateau at a high concentration region, indicating that no more binding sites are available for further biosorption. To elucidate the Hg(II) biosorption performance, the experimental data are analyzed using Langmuir and Freundlich isotherm models according to equation 8 and 11. The evaluated values of Langmuir and Freundlich isotherm parameters, as well as R^2 value, are mentioned in **Table 20** together with R^2 values. The results showed that the equilibrium data assessed by the Langmuir isotherm model give a better R^2 than the Freundlich isotherm model for both the biosorbents. As a result, the

Langmuir isotherm model may be better describing the biosorption of Hg(II) onto SWR and SBP. It set forth that the biosorption of Hg(II) onto the SWR and SBP surface, occurred by the formation of monolayer. The q_m of SWR and SBP for Hg(II) biosorption calculated using Langmuir model is 97.18 and 61.31mg/g. In addition, the biosorption capacity of Hg(II) biosorption determined from experimental data is compared with data calculated from non-linear fittings of Langmuir and Freundlich models to assure the best fit model. It connotes that the biosorption of Hg(II) onto both SWR and SBP followed Langmuir isotherm model.

The $1/n$ value of Freundlich isotherm model for both the cases lies between 0 to 1 suggesting the favorable biosorption of Hg(II) onto SWR and SBP. When the value of $1/n = 1$ imply biosorption is reversible, $1/n > 1$ set out unfavorable biosorption, and $0 < 1/n < 1$ suggests the process is favorable (Guo *et al.*, 2017; Yao *et al.*, 2010).

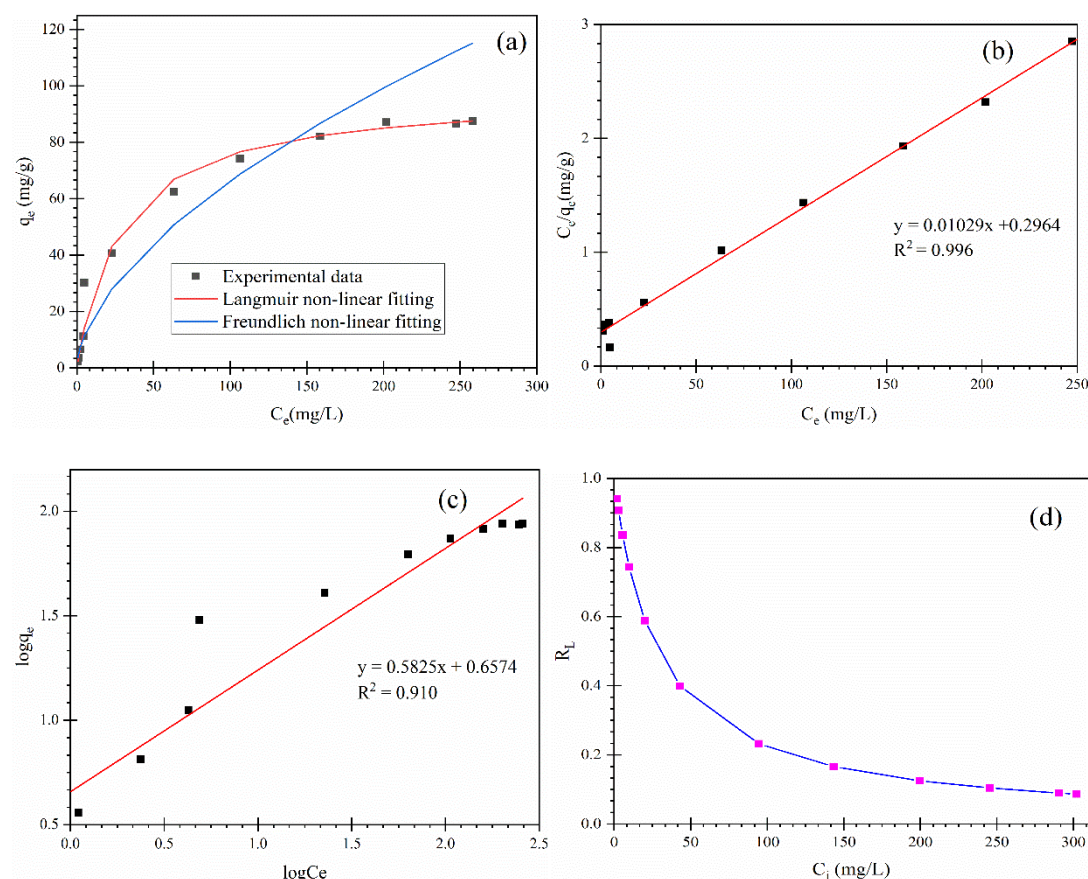
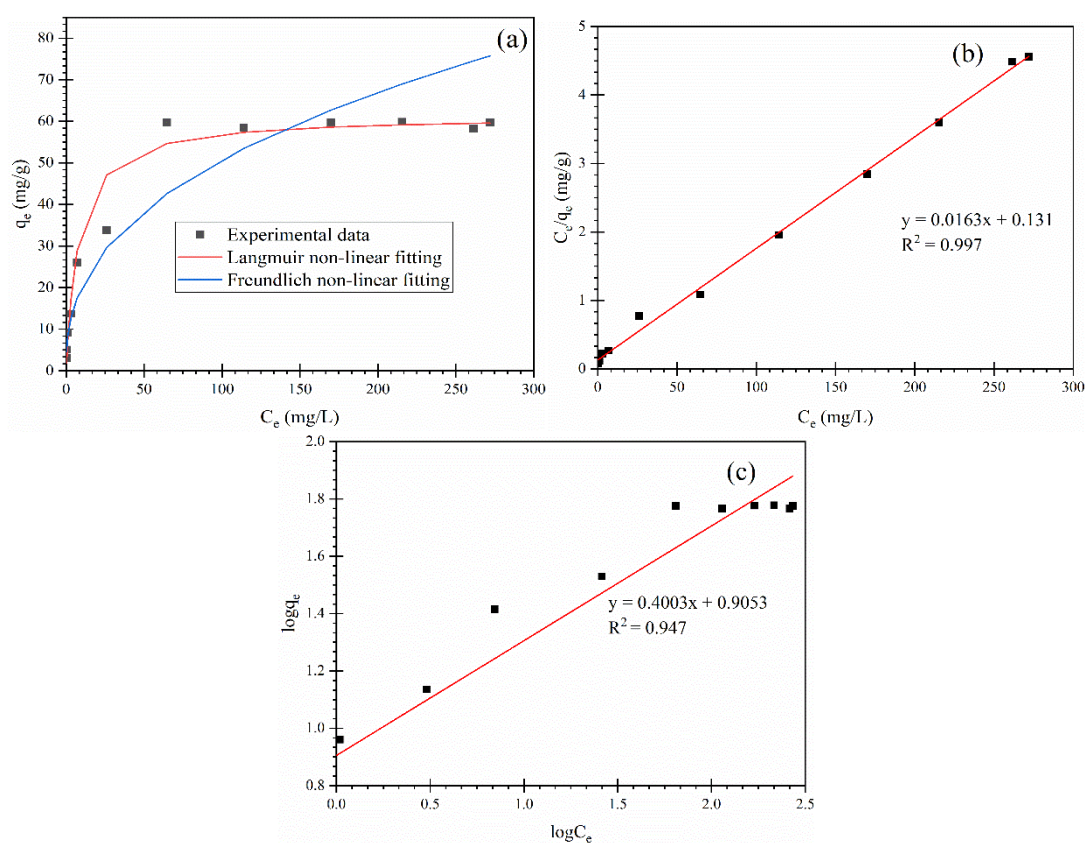


Figure 61: Biosorption isotherm studies onto SWR (a) Non-linear plot of Langmuir and Freundlich isotherm model with experimental data (b) Langmuir isotherm model (c) Freundlich isotherm model and (d) Variation of R_L with initial concentration (Conditions: $m/v = 0.5$ g/L, $C_i = 10$ mg/L, $pH = 5.94$, $t = 24h$, $T = 298$ K)

Table 20: Biosorption isotherm parameters of Hg(II) onto SWR and SBP

Models	Parameters	SWR	SBP
Langmuir	$q_{m, \text{exp}}$ (mg/g)	87.49 ± 0.21	59.76 ± 4.02
	$q_{m, \text{cal}}$ (mg/g)	97.18 ± 0.43	61.31 ± 2.46
	b (L/mg)	0.035 ± 0.012	0.127 ± 0.07
	R^2	0.996	0.997
Freundlich	$K_F(\text{mg/g}) (\text{L/mg})^{1/n}$	4.544 ± 1.031	8.04 ± 2.03
	$1/n$	0.582 ± 0.213	0.400 ± 0.061
	R^2	0.910	0.947

**Figure 62:** Biosorption isotherm of SBP on Hg(II) biosorption (a) Non-linear Langmuir and Freundlich isotherm fittings with experimental data (b) Langmuir isotherm and (c) Freundlich isotherm model (Conditions: $m/v = 0.5$ g/L, $C_i = 10$ mg/L, pH = 5.92, $t = 24$ h, $T = 298$ K)

The biosorption capacity of investigated SWR and SBP is compared with the adsorbents already studied which are listed in **Table 21**. It showed that *Pleurotus eryngii* fungal biomass, exhausted coffee waste, unmodified bamboo leaf powder (BLP) exhibited low biosorption capacity whereas the chemically modified biosorbents such as rice husk using KOH (Liu *et al.*, 2020), gold functionalized Fe_3O_4

magnetic nanoparticles (Maia *et al.*, 2018), PANi/PVAc composite (Samani & Toghraie, 2020), thiol functionalized spent grain (Chai *et al.*, 2010) exhibited higher biosorption capacity. The biosorption capacity of SWR found in the study is higher than the commercial adsorbent i.e., *P. chrysosporium* loaded cryogel and most of others (Çetin *et al.*, 2016). Therefore, this tested SWR and SBP investigated in the study are expected to be potential material for the biosorption of Hg(II) ions from aqueous solution.

4.5.2.4 Effect of biosorbent dosage

The biosorption of Hg(II) onto SWR and SBP is studied with different biosorbent dosages from 0.25 to 5 g/L at optimum pH as shown in **Figure 63**. The figure indicated the gradual decrease in equilibrium concentration of Hg(II) ions in the initial phases and slowed down and remained almost constant with increasing SWR and SBP dosages. This observation can be attributed because with increase in biosorbent dosage, Hg(II) ions can reside in the excess binding sites of SWR and SBP. The equilibrium concentration of Hg(II) gradually lowered and is found to be 3.84 µg/L with SWR dosage of 1.5 g/L. Similarly, 2 g/L of SBP lowered equilibrium concentration of Hg(II) ion from water to 5.94 µg/L. The decrease in Hg(II) concentration in residual solution with increase in the biosorbent dose is due to increase in the number of biosorption sites. However, the biosorption capacity remains constant at higher dosages (Aryal *et al.*, 2019; Al Rmalli *et al.*, 2008). This study revealed that 1.5 g/L of SWR dosage can remove 74.01% and 2 g/L of SBP dosage can remove 59.81 % Hg(II).

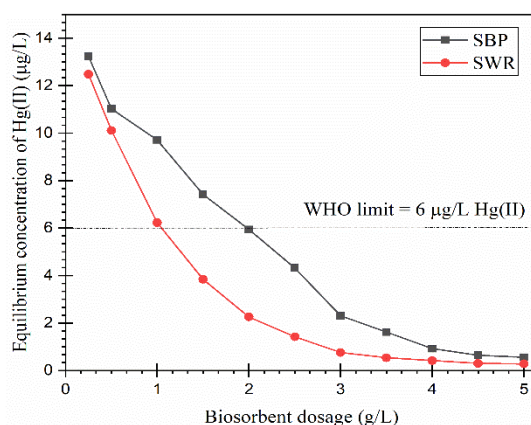


Figure 63: Effect of SWR and SBP dosage on biosorption of Hg(II) (Conditions: $m/v = 0.25 - 5$ g/L, $C_i = 14.78$ µg/L, $pH = 5.94$, $t = 24$ h, $T = 298$ K)

The permissible limit of Hg(II) in drinking water set by WHO is 6 µg/L (WHO, 2014). These biosorbents can bring Hg(II) below the acceptable limit of Hg(II) in drinking water. Therefore, SWR investigated in this research work can be a potential biosorbent to treat trace concentration of Hg(II) ion from water.

Table 21: Comparison of Hg(II) removal capacities of SWR and SBP with other adsorbents

Adsorbents	q _{max} (mg/g)	pH	References
SWR	97.18	5.94	This study
SBP	61.31	5.92	This study
Sulphur coated magnetic carbon nanotubes	62.11	4.5	(Fayazi, 2020)
Rice husk using KOH	55.87	5	(Liu <i>et al.</i> , 2020)
PANi/PVAc composite	76.92	6	(Samani & Toghraie, 2020)
Gold functionalized Fe ₃ O ₄ magnetic nanoparticles	79.59	9	(Maia <i>et al.</i> , 2018)
Exhausted coffee waste	31.75	7	(Alvarez <i>et al.</i> , 2018)
P. chrysosporium loaded cryogel	88	6	(Çetin <i>et al.</i> , 2016)
Pleurotus eryngii fungal biomass	34.01	7	(Amin <i>et al.</i> , 2016)
Sugarcane bagasse	35.71	4	(Khoramzadeh <i>et al.</i> , 2013)
Unmodified bamboo leaf powder (BLP)	27.11	8	(Mondal <i>et al.</i> , 2013)
Triton X-100 (BLPT)	28.10	8	(Mondal <i>et al.</i> , 2013)
Sodium dodecyl sulphate (BLPS)	31.05	8	(Mondal <i>et al.</i> , 2013)
Jute nanofiber	85.5	6	(Baheti <i>et al.</i> , 2013)
Malt spent rootlets (MSR)	50	5	(Anagnostopoulos <i>et al.</i> , 2012)
Thiol- functionalized spent grain	221.73	2	(Chai <i>et al.</i> , 2010)
Activated carbon from sago waste	55.6	5	(Kadirvelu <i>et al.</i> , 2004)

4.5.3 Error Analysis

The most used error functions such as χ^2 , RMSE and MAE were applied to analyze the most fitting model. These error functions are determined based on experimental and calculated values of both kinetic and isotherms (**Table 22** and **23**). The low error functions of PSO and Langmuir isotherm model better satisfied the biosorption of Hg(II) onto SWR and SBP.

Table 22: Error function determination for kinetics studies for the biosorption of Hg(II)

Error function	Kinetic model (SWR)		Kinetic model (SBP)	
	PFO	PSO	PFO	PSO
χ^2	0.721 ± 0.210	0.003 ± 0.001	0.723 ± 0.112	0.037 ± 0.021
RMSE	0.942 ± 0.312	0.068 ± 0.011	0.9 ± 0.2	0.232 ± 0.045
MAE	0.265 ± 0.107	0.019 ± 0.004	0.283 ± 0.043	0.073 ± 0.011

Table 23: Error function determination for isotherm studies for the biosorption of Hg(II)

Error function	Isotherm model (SWR)		Isotherm model (SBP)	
	Langmuir	Freundlich	Langmuir	Freundlich
χ^2	0.97 ± 0.21	2.77 ± 1.13	0.044 ± 0.023	2.71 ± 1.41
RMSE	2.02 ± 1.01	4.21 ± 2.01	0.44 ± 0.11	6.28 ± 3.21
MAE	0.88 ± 0.23	3.41 ± 1.63	0.129 ± 0.054	1.82 ± 0.92

4.5.4 Effect of co-existing ions

The mercury contaminated water can contain different co-existing ions like Zn(II), Ni(II), Cu(II), Cd(II), and Pb(II). The effect on the biosorption of Hg(II) in presence of different concentration of co-existing ions like Zn(II), Ni(II), Cu(II), Cd(II), and Pb(II) onto SWR and SBP was investigated with varying concentrations as shown in **Figure 64**. It is observed that the biosorption percentage of SWR for Hg(II) using 25 mg/L of co-existing Zn(II), Pb(II), Cd(II), Ni(II), and Cu(II), respectively are 80.07, 69.70, 71.15, 84.52 and 80.09 %. Similarly, with further increase in concentration of co-existing ions to 400 mg/L, the biosorption of Hg(II) onto SWR decreased to 65.37, 32.46, 37.48, 63.35 and 51.21%, respectively (**Figure 64 (a)**). Similar observation is found for SBP (**Figure 64 (b)**). The biosorption of Hg(II) with blank is found to be 85.93% whereas at 400 mg/L percentage biosorption diminished to 65.37, 63.35, 51.21, 47.50, and 42.49% with Zn(II), Ni(II), Cu(II), Cd(II) and Pb(II), respectively using SBP biosorbent. The observation showed that percentage biosorption of Hg(II) decreased significantly in presence of co-existing ions, Cu(II), Pb(II) and Cd(II) which is because of the fact that these metal ions have similar ionic radius, masses, and electronegativity (Shi *et al.*, 2009). These similarities between the metal ions enhance their competition for the same active sites onto SWR and SBP surfaces and

consequently reduced the Hg(II) biosorption (Figueira *et al.*, 2022). Therefore, biosorption of Hg(II) largely influenced at higher concentration of co-existing ions.

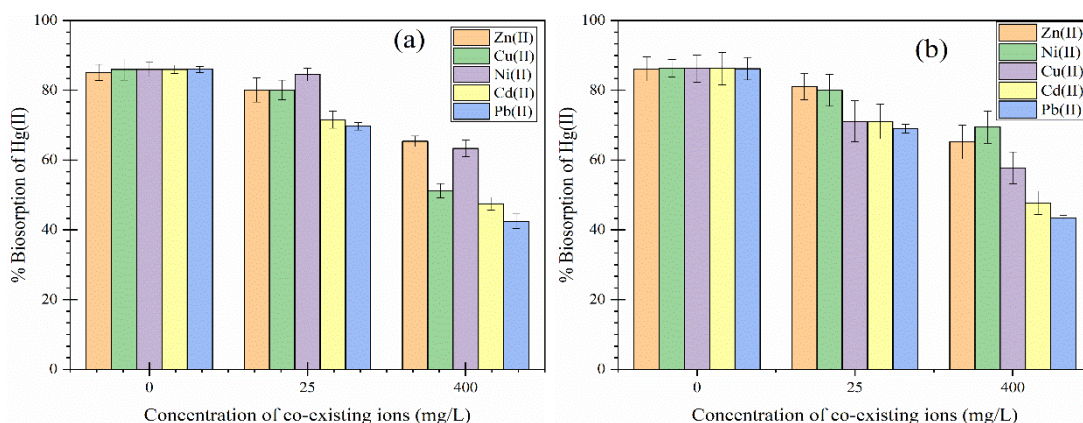


Figure 64: Effect on biosorption of Hg(II) with co-existing ions (a) SWR and (b) SBP (Conditions: $m/v = 1$ g/L, $C_i = 10$ mg/L, $pH = 5.94$, co-existing ions concentration = 0 – 400 mg/L, $t = 24$ h, $T = 298$ K)

4.5.5 Desorption studies

Since poor biosorption of Hg(II) was observed onto SWR and SBP at low pH, thus desorption study was carried out with varying concentration of HNO_3 (0.01- 2 M) and the results are displayed in **Figure 65**. The results showed that percentage desorption of Hg(II) loaded SWR increased from 48.21% to 95.69% on increasing the concentration of HNO_3 from 0.01 to 1 M. Further, as concentration of HNO_3 increases, desorption percentage gradually decreased. Similar trends are observed in the Hg(II) biosorption onto SBP. 1 M HNO_3 is optimized for the effective desorption of biosorbed Hg(II) on both SWR and SBP biosorbents. Under acidic conditions, proton exists in acid solution displaced Hg(II) ions through cation exchange process thereby enhanced the desorption of Hg(II) ions. The elementary reaction for Hg(II) desorption is shown in reaction (b),



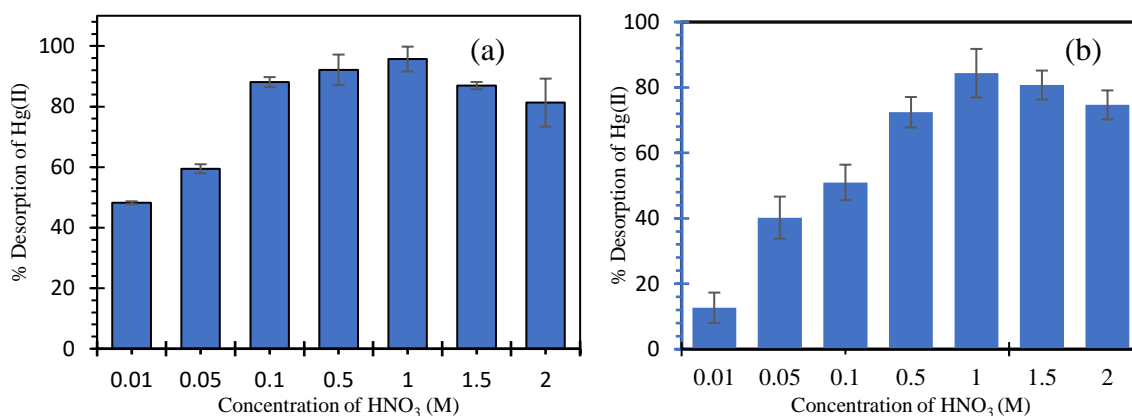


Figure 65: Desorption of Hg(II) from Hg(II) biosorbed (a)SWR and (b) SBP (Conditions: m/v = 3 g/L, concentration of HNO₃ = 0.01 – 2M)

4.5.6 Regeneration and reusability of biosorbent

The regeneration and reusability of biosorbent is a unique feature of biosorption process. The biosorption-desorption studies of Hg(II) onto investigated SWR and SBP was performed upto five cycles as shown in **Figure 66**. The biosorption of Hg(II) onto fresh SWR is found to be 89.42% and that of SBP is 84.87% . Moreover, after fifth cycle, the percentage biosorption of Hg(II) onto SWR and SBP is 71.68% and 64.87%, respectively.

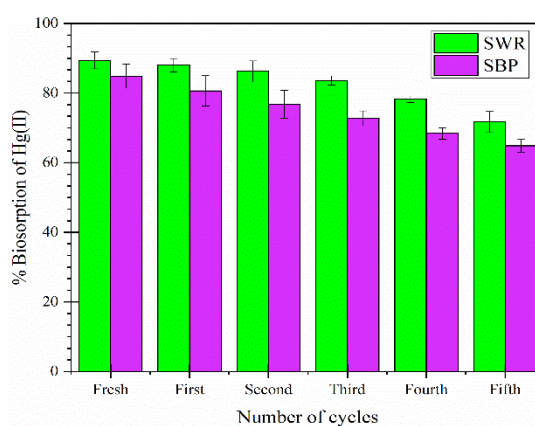


Figure 66: Variation of biosorption capacity in successive biosorption-desorption cycles of Hg(II) biosorption onto SWR, SBP (Conditions: volume of HNO₃ = 20 mL, concentration of HNO₃ = 1M, biosorption pH = 5.94, concentration of Hg(II) = 100 mg/L)

The percentage decrease of Hg(II) biosorption onto SWR and SBP in comparison to fresh, after repeated five cycles is 17.74% and 20%. However, the efficiency of

investigated biosorbents is higher as reported in the literature (Poudel, *et al.*, 2021). SWR and SBP are considered as a promising biosorbent for the biosorption of Hg(II) ion. Further, the loaded Hg(II) ions from Hg-SWR and Hg-SBP is desorbed using 1 M HNO₃ in desorption-biosorption experiments. These results signified that SWR and SBP can have the potential of Hg(II) biosorption and regeneration significantly.

4.6 Biosorption of Pb(II) onto biosorbents

4.6.1 Biosorbents characterization

4.6.1.1 Surface morphology of the biosorbents

Scanning electron microscopy was used to screen the surface morphology of SWR and SBP before and after Pb(II) biosorption as shown in **Figure 67**. SWR (**Figure 67 (a)**) and SBP (**Figure 67 (c)**) have irregular and heterogenous surface morphology with a well-developed porous structure.

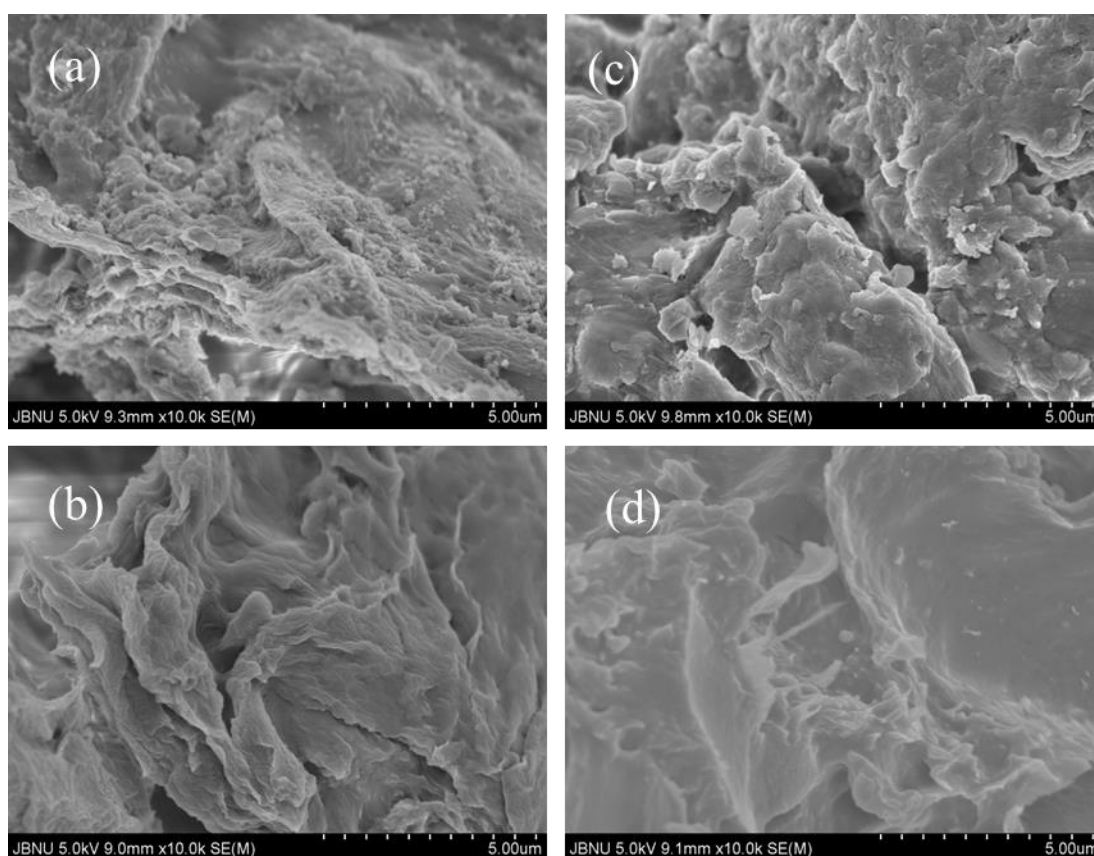


Figure 67: SEM images of (a) SWR (b) Pb(II) biosorbed SWR (c) SBP and (d) Pb(II) biosorbed SBP.

This morphology can be appropriate for the biosorption of Pb(II) ions. After Pb(II) biosorption as seen in **Figure 67 (b)** in case of SWR and **Figure 67(d)** in case of SBP,

the surface of Pb(II) loaded SWR and SBP turned into homogeneous and smooth morphology. The homogeneity and smoothness of SWR and SBP surface clearly evidenced that biosorption of Pb(II) onto SWR and SBP take place. A similar observation was also found on biosorption of fluoride onto Zr(IV)-loaded SBP (Aryal *et al.*, 2021).

4.6.1.2 EDX spectra with elemental mapping

EDX analysis was carried out prior to and after biosorption of Pb(II) as shown in **Figure 68** (SWR) and **Figure 69** (SBP). The elemental peaks along with percentage of SWR (**Figure 68 (a)**) analyzed through EDX are, Ca (5.44%), C (54.22), O (40.05 %), Mg (0.24 %) and Si (0.05%) and SBP (**Figure 69 (a)**) with Ca (6.02 %), C (71.51%), O (22.30 %), Mg (0.11 %) and Si (0.06 %) at binding energies of 3.68, 0.27, 0.52, 1.26 and 1.74 keV, respectively. The Ca(II) content in both biosorbents are available in significant amount because of saponification reaction. The Ca(II) present in the SWR and SBP as Ca(II) pectate can be substituted by Pb(II) during biosorption of Pb(II) ion (Ghimire *et al.*, 2008). After Pb(II) biosorption, the peak of Pb(II) is appeared on both Pb(II) loaded SWR (3.46 % of Pb(II) (**Figure 68 (b)**) and SBP (5.04 % of Pb(II) (**Figure 69 (b)**) with binding energy 2.34 keV, whereas Ca(II) content is almost vanished. The loading of Pb(II) occurred onto SWR and SBP through cation exchange reaction. Furthermore, layered images and color mapping images of SWR shown in **Figure 68 (c)** and **Figure 68 (d)**) and SBP in **Figure 69 (c)** and **Figure 69 (d)** supports the elemental distribution before and after Pb(II) loading. These results showed that biosorption of Pb(II) can take place on the investigated biosorbents.

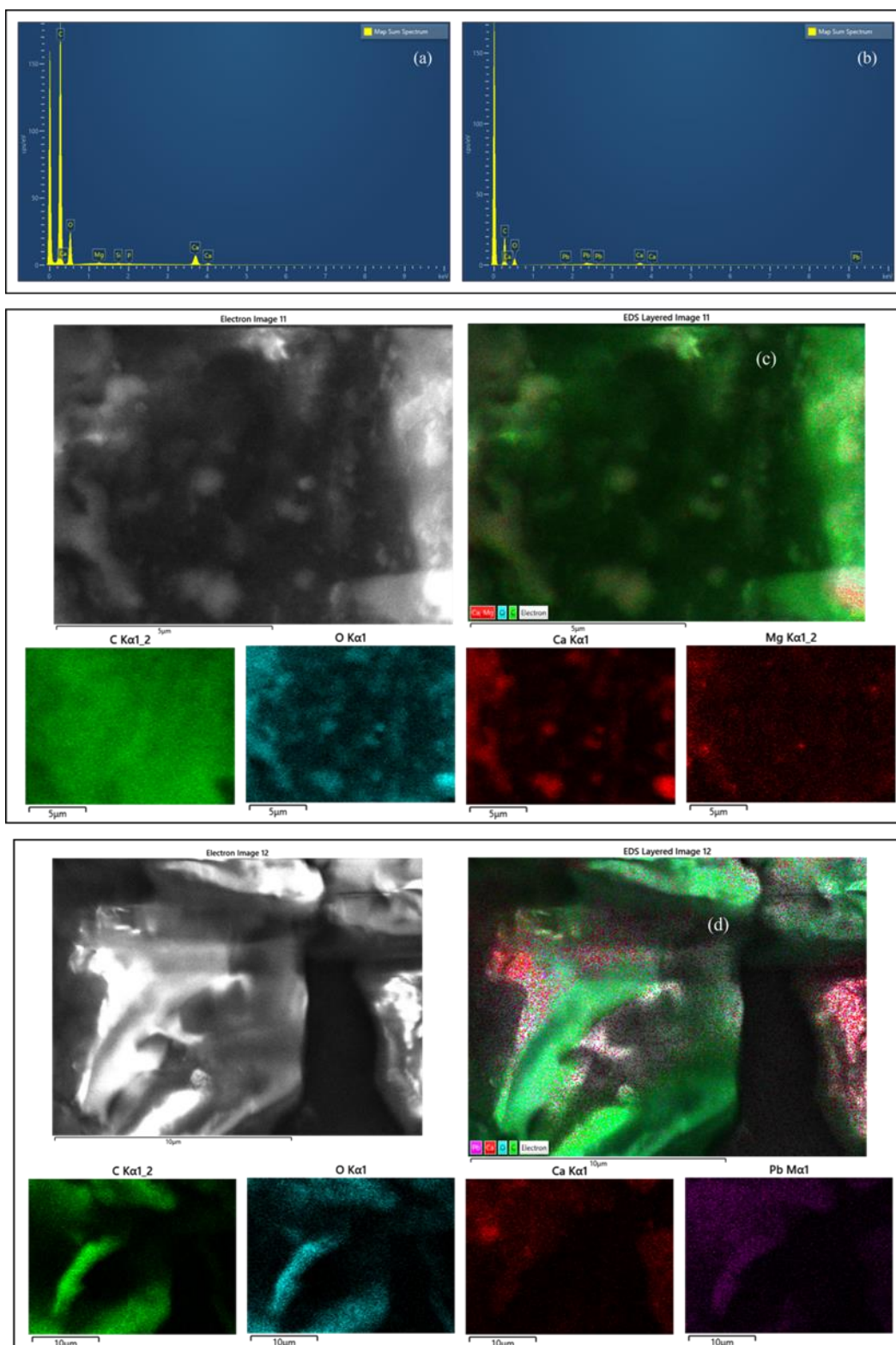


Figure 68: EDX spectra of (a) SWR (b) Pb(II) biosorption (c) EDX electron image, layered images and EDX color mapping images of all overlapping elements of SWR (d) Pb(II) loaded SWR

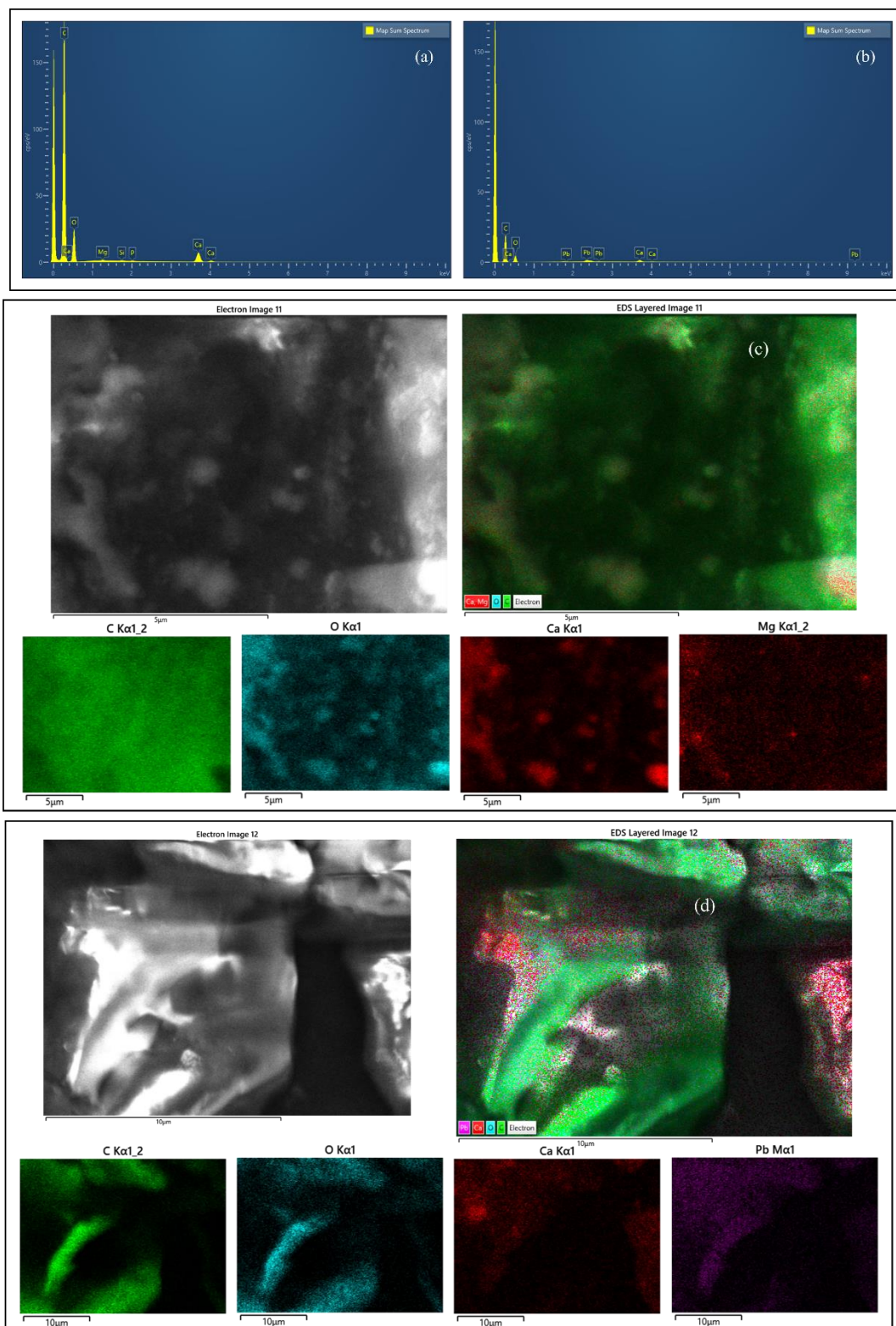


Figure 69: EDX spectra of (a) SBP (b) Pb(II) biosorption; EDX electron image, layered images and EDX color mapping images of all overlapping elements of (c) SBP and (d) after Pb(II) loaded SBP

4.6.1.3 FTIR spectroscopy analysis

The characteristics peaks of functional groups of RWR, SWR, Pb(II)-SWR and RBP, SBP, Pb(II)-SBP analyzed using FTIR spectroscopy are presented in **Figure 70 (a)** and **Figure 70 (b)**. The broad peaks around 3325.84 and 3305.6 cm^{-1} of RWR and RBP is associated with -OH stretching vibration of the hydroxyl groups present in cellulose, hemicelluloses, pectin, lignin and adsorbed water on the biosorbents (Hong *et al.*, 2022). The smaller peak around 2914.62 in RWR and 2917 cm^{-1} in RBP is associated with -CH and -CH₂ stretching vibrations (Hong *et al.*, 2022; Zou *et al.*, 2019). The characteristics peaks around 1728 in RWR and 1736 cm^{-1} in RBP are observed of C=O and -COO groups (Xing *et al.*, 2018; Fan *et al.*, 2013). The peaks observed around 1242.26 and 1098.4 cm^{-1} is due to -C-O- bond found in alcoholic, phenolic and carboxyl group present in the pyranose ring of RWR and RBP (Yang *et al.*, 2022).

After Ca(OH)₂ treatment, the peak associated with -COO group around 1728 and 1736 cm^{-1} disappeared and new peaks around 1416.81 and 1396 cm^{-1} is appeared in SWR and SBP, indicating the presence of O-Ca bond of calcium pectate. The minor alterations in the peak intensity after Ca(OH)₂ treatments suggests the modification of functional groups in SWR and SBP. After Pb(II) biosorption, the peaks slightly shifted to 1319 and 1295 cm^{-1} due to the formation of lead pectate (Xing *et al.*, 2018). It is anticipated that Pb(II) is loaded onto SWR and SBP due to cation exchange reaction with Ca(II).

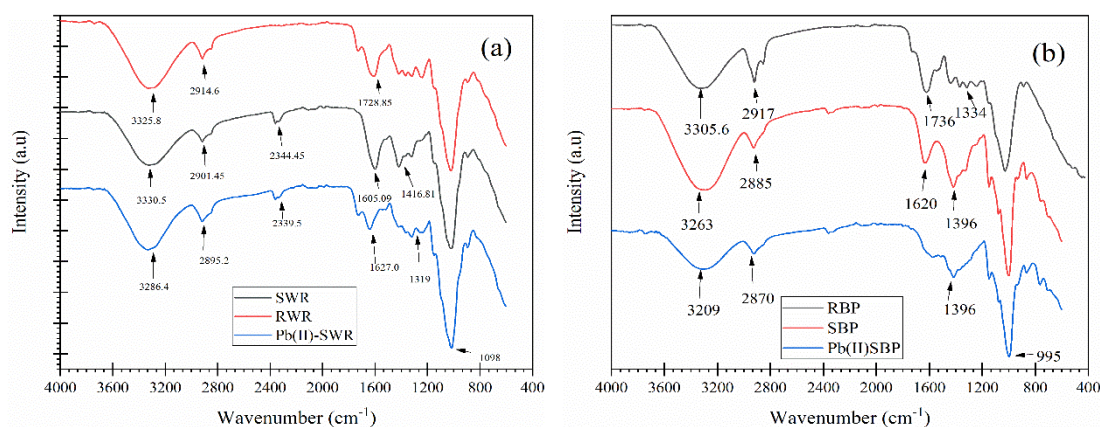


Figure 70: FTIR spectra of (a) RWR, SWR, Pb(II) biosorbed SWR and (b) RBP, SBP and Pb(II) biosorbed SBP

4.6.2 Batch wise biosorption studies

4.6.2.1 Effect of solution pH and biosorption mechanism

The biosorption of Hg(II) onto RWR, SWR and RBP, SBP was studied at different equilibrium pH and results are shown in **Figure 71 (a)** and **71 (b)**. The Pb(II) biosorption onto RWR at pH 2.18 is 11.85% and increases to 31.27% at pH 5.27. Similarly, Pb(II) biosorption onto RBP at pH 2.18 is 6.39% which increases to 33.96% at pH 5.27. The percentage biosorption of Pb(II) onto SWR at pH 2.18 is 23.87% which progressively increases to 94.65% at pH 5.27. The Pb(II) biosorption onto SBP at pH 2.18 is 18.33% which increases to 94.19% at pH 5.27. At pH 6.42, a slight decline in biosorption of Pb(II) is observed because of Pb(OH)₂ precipitate in alkaline medium (Gao *et al.*, 2021; Ma *et al.*, 2021). The optimal pH for the biosorption of Pb(II) onto SWR and SBP is determined to be 5.27. The lead speciation diagram also showed that at pH < 6.0, lead exists predominantly in the form of Pb(II) ions. Therefore, Pb(II) biosorption onto SWR and SBP might take place at optimal pH from the predominant Pb(II) species present in water.

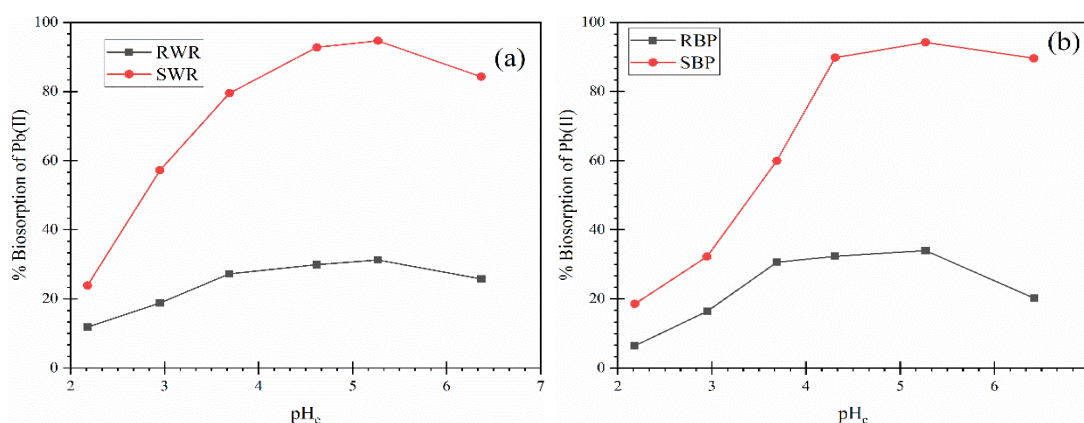


Figure 71: Effect of solution pH for biosorption of Pb(II) onto SWR and SBP (Conditions: $m/v = 0.5$ g/L, $C_i = 10$ mg/L, $t = 24$ h, $T = 298$ K)

4.6.2.2 Effect of contact time

The kinetic studies of Pb(II) biosorption onto SWR and SBP was displayed in **Figure 72** and **Figure 73**. The results showed that biosorption of Pb(II) onto both biosorbents increases rapidly in early stage and slowed down and achieved equilibrium (plateau) in 180 min for SWR and 240 min for SBP. A further increase in equilibration times has minor effect on the biosorption of Pb(II) ions. Initially, the rapid increase in biosorption can be ascribed due to vacant binding sites onto the biosorbents (Sun *et al.*, 2018). However, in the midway, due to partial saturation of binding sites of

biosorbents slow biosorption takes place (Ranote *et al.*, 2018). Furthermore, the kinetic data for biosorption of Pb(II) onto SWR are analyzed with PFO model and PSO model as shown in **Figure 72 (b) & (c)** and SBP in **Figure 73 (b) & (c)**. The kinetic parameters together with coefficient of determination (R^2) of Pb(II) biosorption onto biosorbents are listed in **Table 24**. The coefficient of determination (R^2) of PSO kinetics for both biosorbents is found higher than PFO kinetics. In addition, the values of biosorption capacity (q_e) calculated from the PSO plots is very close with experimental value (q_e) which suggests that the biosorption of Pb(II) on both biosorbents follows PSO kinetics suggesting that the biosorption is driven by chemisorption. The experimental data on non-linear fitting also satisfy with PSO kinetic modeling of SWR shown in **Figure 72(a)** and SBP shown in **Figure 73 (a)**. This suggests that Pb(II) biosorption onto SWR and SBP follows PSO kinetics.

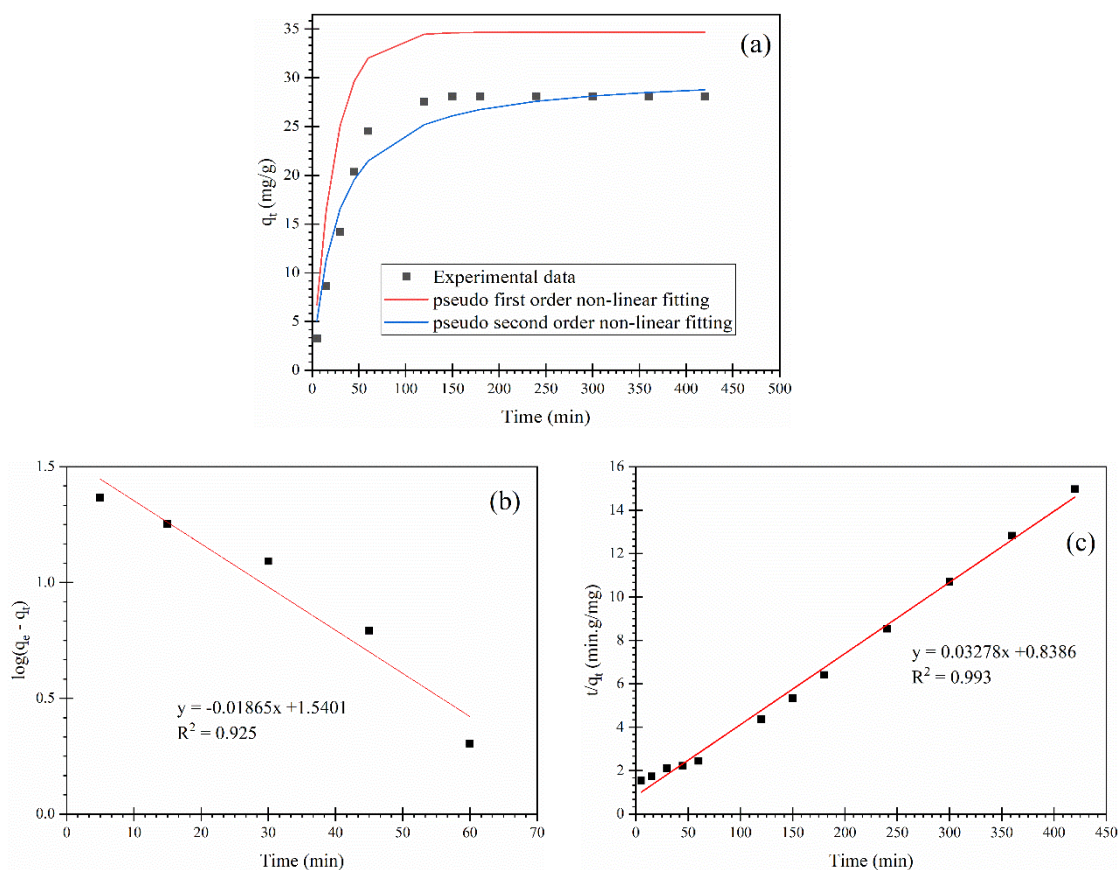
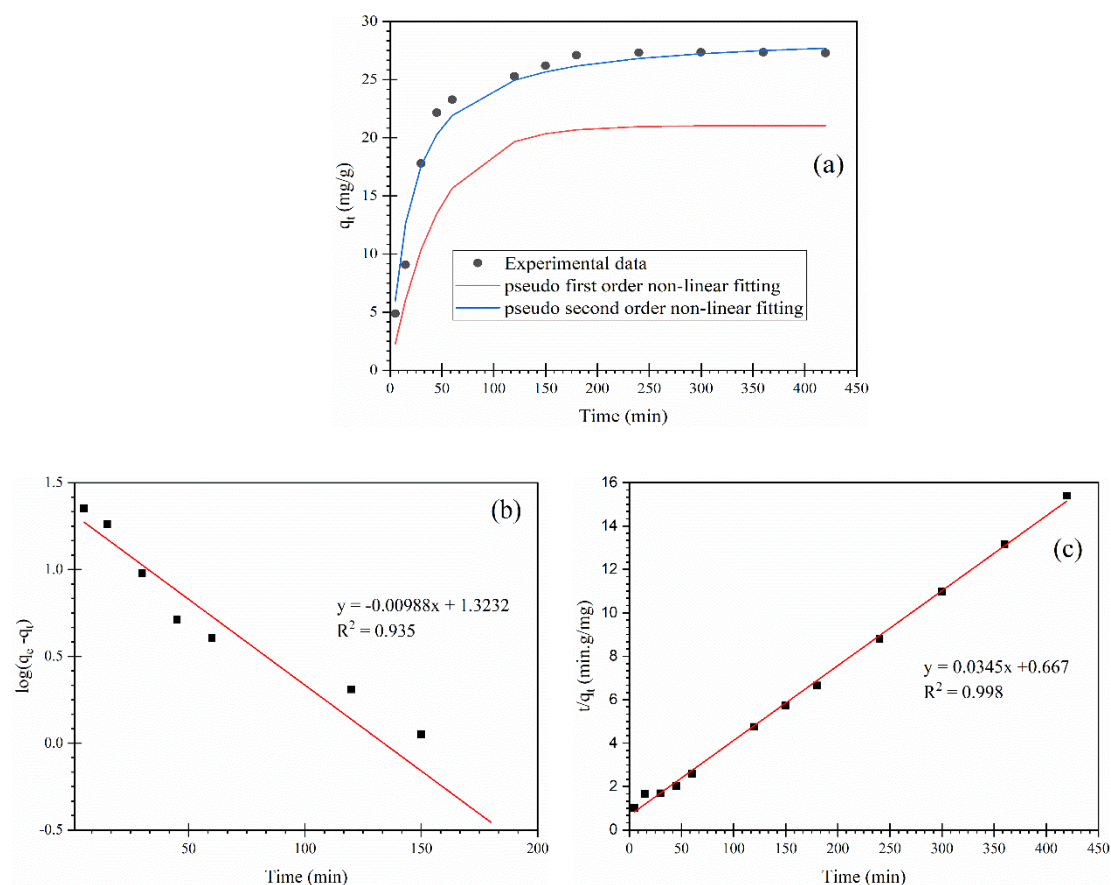


Figure 72: Biosorption kinetics of Pb(II) onto SWR (a) Non-linear plot of PFO and PSO model with experimental data (b) PFO model and (c) PSO model (Conditions: $m/v = 0.5$ g/L, $C_i = 10$ mg/L, $pH = 5.27$, $T = 298$ K, $t = 24$ h)

Table 24: Kinetic parameters for the Pb(II) biosorption onto biosorbents

Models	Parameters	SWR	SBP
PFO	k_1 (1/min)	0.043 ± 0.12	0.0227 ± 0.046
	q_e , cal (mg/g)	34.67 ± 0.23	21.04 ± 1.006
	R^2	0.925	0.935
PSO	k_2 (g/mg min)	0.0013 ± 0.002	0.005 ± 0.001
	q_e cal (mg/g)	30.50 ± 0.21	28.98 ± 2.32
	R^2	0.993	0.998
	q_e , exp (mg/g)	28.08 ± 1.04	27.34 ± 3.04

**Figure 73:** Biosorption of Pb(II) onto SBP (a) Non-linear fitting of kinetics models with experimental data (b) PFO and (c) PSO model (Conditions: $m/v = 0.5$ g/L, $C_i = 10$ mg/L, $pH = 5.27$, $t = 24h$, $T = 298K$)

4.6.2.3 Biosorption isotherm of Pb(II) ion

Figure 74 and **Figure 75** showed the biosorption isotherm of Pb(II) onto SWR and SBP, respectively. The biosorption capacity of both biosorbents increased rapidly in the beginning at low concentration and attain plateau at higher concentration. The results can be ascribed due to availability of more binding sites at the beginning. At higher concentration, the binding sites are occupied with Pb(II) that results no further

biosorption. Langmuir and Freundlich isotherm model are used to analyze the biosorption data to find out the best fit model for the investigated systems. The results of Pb(II) biosorption onto SWR is presented in **Figure 74 (b) and (c)** and SBP in **Figure 75 (b) and (c)**.

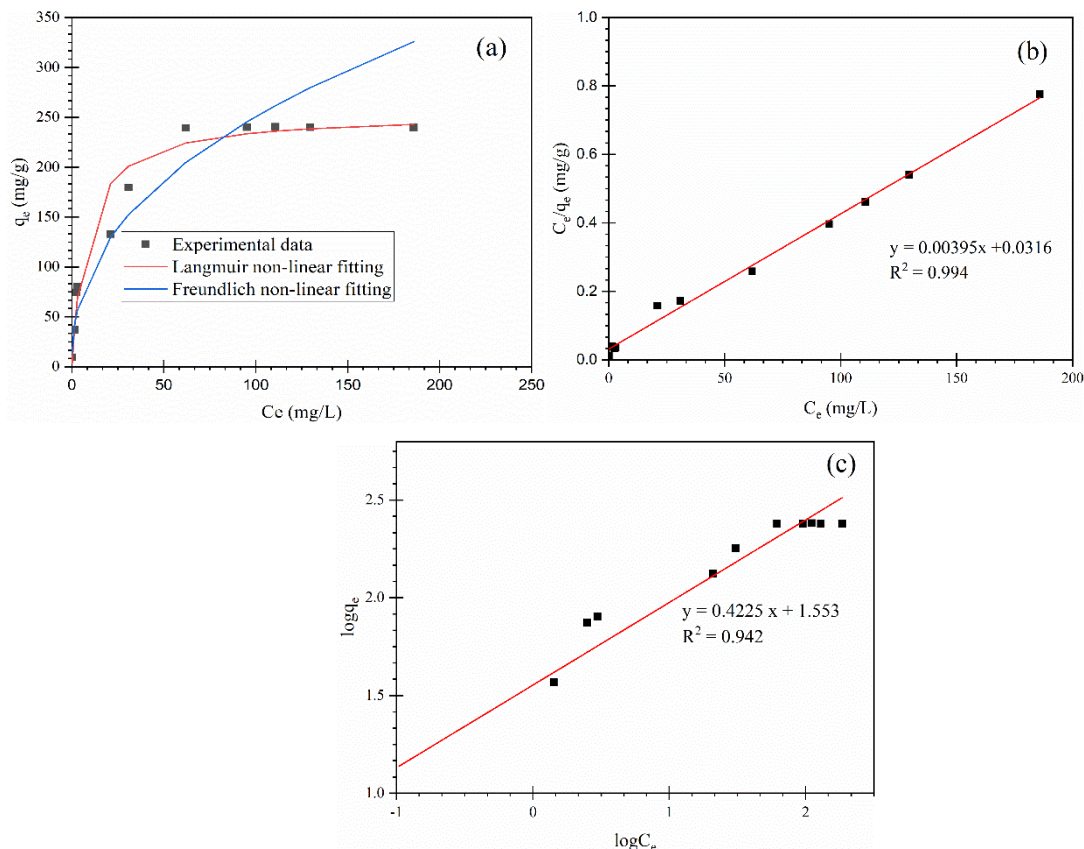


Figure 74: Biosorption of Pb(II) onto SWR (a) Non-linear plot of Langmuir and Freundlich modeling with experimental data (b) Langmuir and (c) Freundlich isotherm model (Conditions: $m/v = 0.5$ g/L, $C_i = 10$ mg/L, $pH = 5.27 \pm 0.5$, $t = 24$ h, $T = 298$ K)

The calculated Langmuir and Freundlich isotherm constants together with correlation coefficients (R^2) of SWR and SBP are presented in **Table 25**. Based on R^2 values, Langmuir isotherm described better the biosorption of Pb(II) onto both biosorbents. The maximum monolayer biosorption capacities of SWR and SBP are evaluated to be 253.16 and 230.94 mg/g, respectively. The non-linear fitting of Langmuir isotherm modeling resembles with the experimental data as shown in **Figure 74 (a)** and **Figure 75 (a)**. Moreover, to analyze the appropriateness of Pb(II) biosorption onto investigated biosorbents, the value of dimensionless parameter ' R_L ' is calculated. The R_L values with examined initial concentration of Pb(II) biosorption onto SWR is presented in **Figure 75 (d)**. The R_L values are found to vary within range 0.84 - 0.078

for SWR and 0.62 - 0.03 for SBP, respectively. Therefore, Pb(II) biosorption onto SWR and SBP come up with the favorable biosorption process assigned by $0 < R_L < 1$ (Qu *et al.*, 2022; Bharti & Kumar, 2018; Lu *et al.*, 2009).

Table 25: Biosorption isotherm parameters of Pb(II) biosorption onto biosorbents

Models	Parameters	SWR	SBP
Langmuir	q_m (mg/g)	253.16 ± 0.96	230.94 ± 2.31
	b (L/mg)	0.125 ± 0.004	0.0383 ± 0.014
	R^2	0.994	0.988
Freundlich	$K_F(\text{mg/g})(\text{L/mg})^{1/n}$	35.73 ± 2.01	13.536 ± 3.334
	$1/n$	0.423 ± 0.076	0.5642 ± 0.046
	R^2	0.942	0.954

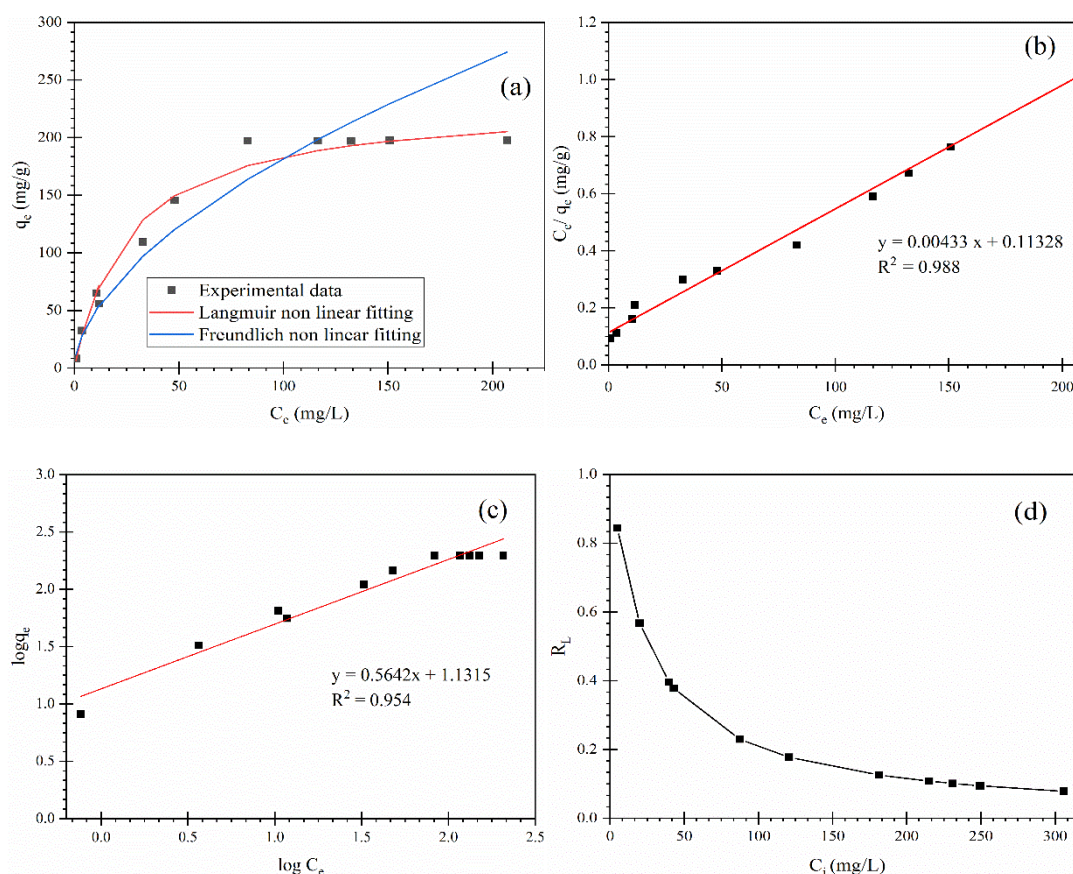


Figure 75: Biosorption isotherm of Pb(II) onto SBP (a) Nonlinear isotherm plot of Langmuir and Freundlich modelling with experimental data (b) Langmuir isotherm model (c) Freundlich isotherm model and (d) Variation of R_L with initial concentration (Conditions: $m/v = 0.5$ g/L, $C_i = 10$ mg/L, $\text{pH} = 5.27$, $t = 24$ h, $T = 298\text{K}$)

Table 26 shows the comparison of potentiality of investigated SWR and SBP with other biosorbents/adsorbents reported in the literature. It showed that the biosorption

capacity of modified chitosan with o-hydroxyphenyl thiourea (Yang *et al.*, 2022), Fe/Co metal organic nanosheets (Hong *et al.*, 2022), thiol functionalized multiwalled carbon nanotubes (Qu *et al.*, 2022), Fe₃O₄@TATS@ATA (Alqadami *et al.*, 2020), *Fucus spiralis* bio refinery waste (Filote *et al.*, 2019) exhibited higher Pb(II) biosorption whereas unmodified *Azadirachta indica* leaves and Algae biomass exhibited low biosorption capacity. The higher Pb(II) biosorption onto functionalized adsorbents is ascribed due to large number of enhanced binding sites (Poudyal *et al.*, 2013). Thus, investigated SWR and SBP in this study also exhibits higher biosorption capacities. The locally available, and easily prepared SWR and SBP can be efficient material for the removal of Pb(II) ions from aqueous solution.

Table 26 Comparative study of Pb(II) biosorption onto investigated biosorbents with other adsorbents

Adsorbents	q _{max} (mg/g)	pH	References
SWR	253.16	5.27	Present study
SBP	230.94	5.27	Present study
Fe/Co metal organic nanosheets	220.48	7.0	(Hong <i>et al.</i> , 2022)
o-hydroxyphenyl thiourea modified Chitosan (OTCS)	208.33	7.0	(Yang <i>et al.</i> , 2022)
Thiol functionalized multiwalled carbon nanotubes (MWCNT-SH)	144.9	5.0	(Qu <i>et al.</i> , 2022)
Straw-derived biochar	124.5	5.5	(Wang <i>et al.</i> , 2021)
<i>Azadirachta indica</i> leaves	39.7	7.0	(Elkhaleefa <i>et al.</i> , 2021)
Fe ₃ O ₄ @TATS@ATA	205.2	5.7	(Alqadami <i>et al.</i> , 2020)
Amino/thiol bifunctionalized magnetic nanoadsorbent	110.13	5.0	(Ji <i>et al.</i> , 2019)
<i>Fucus spiralis</i> bio refinery waste	132	4.5	(Filote <i>et al.</i> , 2019)
Algae biomass	42.9	6.0	(Mousavi <i>et al.</i> , 2019)
Polyacrylonitrile/magnetite nanofibers	156.25	6.0	(Malik <i>et al.</i> , 2018)
Moringa oleifera	209.54	5.0	(Reddy <i>et al.</i> , 2010)

4.6.2.4 Effect of biosorbent dosages

The extent of Pb(II) biosorption onto SWR was investigated by varying dosages. The result is sketched in **Figure 76**. It is observed that when SWR dosage increased from 0.25 g/L to 6.5 g/L the biosorption percentage increased from 45.74% to 99.47%. However, beyond 6.5 g/L there is no significant change in percentage biosorption.

The increase in biosorption at higher SWR dosage can be inferred due to the increase in active binding sites for Pb(II) biosorption (Elfeghe *et al.*, 2022). The SWR dosage of 1.5 g/L can successfully reduce the Pb(II) concentration below 10 $\mu\text{g/L}$ from the solution. The permissible limit of Pb(II) in drinking water as prescribed by WHO is 10 $\mu\text{g/L}$ (WHO, 2004). Thus, it can be suggested that SWR can be a promising biosorbent to treat trace concentration of Pb(II) ions present in water.

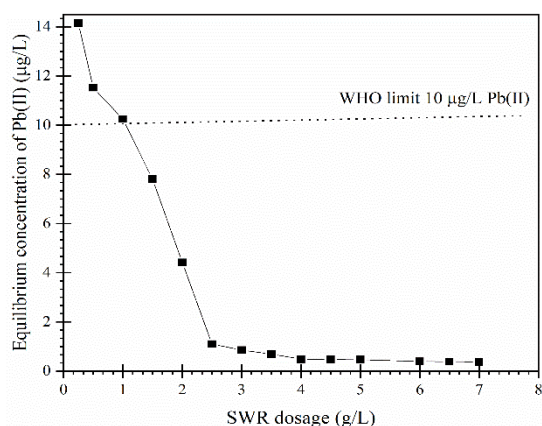


Figure 76: Effect of SWR dosage in the biosorption of Pb(II) ions (Conditions: $m/v = 0.5 - 7 \text{ g/L}$, $C_i = 18.2 \mu\text{g/L}$, $\text{pH} = 5.27$, $T = 298 \text{ K}$, $t = 24 \text{ h}$)

4.6.3 Error Analysis

The determined error function values for the biosorption of Pb(II) onto SWR and SBP for kinetic models and isotherm models are summarized in **Table 27** and **28**. It is apparent from the table that Pb(II) biosorption onto SWR and SBP exhibited a better suit to the PSO and Langmuir isotherm model with the lower determined error functions. These values are also in parallel with higher R^2 values of models. Therefore, Pb(II) biosorption onto SWR and SBP agree with PSO model and Langmuir isotherm model.

Table 27: Error analysis for kinetic studies of biosorption of Pb(II) onto biosorbents

Error function	Kinetic model (SWR)		Kinetic model (SBP)	
	PFO	PSO	PFO	PSO
χ^2	1.25 ± 0.13	0.19 ± 0.02	1.88 ± 0.54	0.092 ± 0.031
RMSE	3.61 ± 0.32	0.48 ± 0.11	1.89 ± 0.32	0.494 ± 0.121
MAE	0.54 ± 0.12	0.20 ± 0.22	0.572 ± 0.06	0.150 ± 0.026

Table 28: Error analysis for isotherm studies of biosorption of Pb(II) onto biosorbents

Error function	Isotherm model (SWR)		Isotherm model (SBP)	
	Langmuir	Freundlich	Langmuir	Freundlich
χ^2	0.68 ± 0.12	3.82 ± 0.97	4.81 ± 1.21	8.39 ± 2.31
RMSE	3.8 ± 0.03	5.72 ± 1.04	1.04 ± 0.05	3.26 ± 0.87
MAE	1.09 ± 0.08	7.59 ± 2.04	3.03 ± 0.86	4.003 ± 1.98

4.6.4 Effect of co-existing ions

Commonly, industrial wastewater contains co-existing ions such as Cu(II), Ni(II), Zn(II), Hg(II), and Cd(II) (Bansal *et al.*, 2022). The biosorption efficiency of SWR and SBP for the biosorption of Pb(II) is analyzed in presence of Cu(II), Ni(II), Zn(II), Hg(II), and Cd(II). The results are presented in **Figure 77**. The percentage biosorption of Pb(II) onto SWR and SBP without co-existing ions (blank) is 93.21% and 92.51% , respectively. However, with progressive increase in concentration of co-existing ions to 400 mg/L of Cu(II), Ni(II), Zn(II), Hg(II), and Cd(II), the percentage biosorption of Pb(II) onto SWR decreases to 64.15, 58.12, 57.56, 51.07 and 53.74 % , respectively as shown in **Figure 77 (a)**.

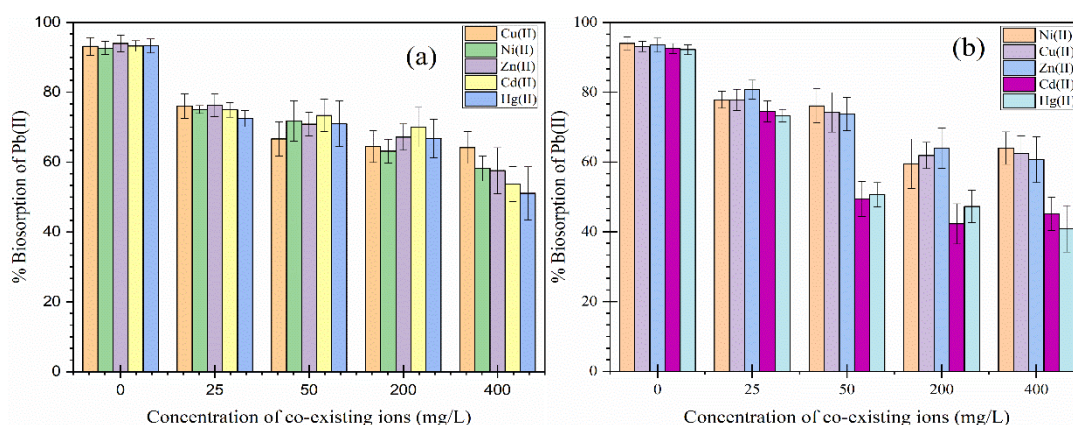


Figure 77: Effect of co-existing ions on biosorption of Pb(II) onto (a) SWR and (b) SBP (Conditions: $m/v = 0.5$ g/L, $C_i = 50$ mg/L, $pH = 5.27$, concentration of co-existing ions = 0 – 400 mg/L, $T = 298$ K)

Similar trends are also continued in SBP. The percentage decrease in Pb(II) biosorption in presence of 400 mg/L of co-existing ions of Cd(II) and Hg(II) is found 45.20 and 40.85% and Zn(II), Cu(II) and Ni(II) inhibits to 60.68, 62.43 and 63.98% as shown in **Figure 77 (b)**. The result showed that the increment in concentration of

co-existing ions significantly diminish the biosorption of Pb(II). Hg(II) and Cd(II) markedly inhibits the biosorption of Pb(II). Bansal *et al.* (2022) also reported the similar observation in sequestration of heavy metal ions using processed agricultural biomass. The significant interference caused at higher concentration of co-existing ions can be attributed due to competing effect for the same biosorption sites during the Pb(II) biosorption (Fan *et al.*, 2013; Shi *et al.*, 2009).

4.6.5 Mechanism of biosorption of Hg(II) and Pb(II)

The pectic acid of RWR and RBP converts into Ca(II) pectate after Ca(OH)₂ treatments (Ghimire *et al.*, 2007; Inoue *et al.*, 2017). The biosorption of Hg(II) and Pb(II) takes place onto SWR and SBP surface through cation exchange mechanism as shown in **Figure 78**. In alkaline conditions, Hg(II) and Pb(II) can form Hg(II) and Pb(II) hydroxide precipitate. Therefore, biosorption study for cations at higher pH can be difficult (Dias *et al.*, 2021).

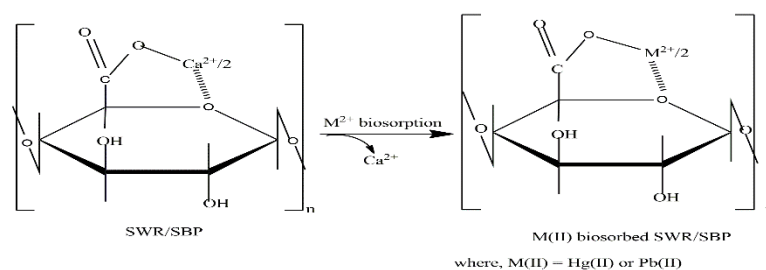


Figure 78: Biosorption mechanism of M(II) onto monomeric unit of SWR and SBP (Ghimire *et al.*, 2007)

4.6.6 Desorption studies

Since biosorption of Pb(II) onto SWR and SBP in strongly acidic condition is insignificant, HNO₃ is used as a desorbing agent to desorb biosorbed Pb(II) from SWR and SBP. The desorption test was carried out for both biosorbents with different concentration of HNO₃ ranging from 0.01–2M as displayed in **Figure 79**. The desorption percentage of Pb(II) increases from 19.26 % to 97.12 % from Pb(II)-SWR with the increase in concentration of HNO₃ (0.01 to 1M). A similar observation is found in desorption of Pb(II)-SBP using different molar concentration of HNO₃. The biosorption percentage Pb(II) desorbed from Pb(II)-SBP increases from 21.71 to 97.7% using (0.01-1M) HNO₃. After then, the desorption efficiency slightly lowered with increase in concentration of HNO₃. It might be due to partial damage on the

polymeric structure of SWR and SBP caused by higher concentration of acidic solution (Yang *et al.*, 2022). Thus, 1M solution of HNO₃ is found appropriate for the regeneration of the SWR and SBP biosorbent. The H⁺ ions released from HNO₃ solution might replace the biosorbed Pb(II) from SWR and SBP. The desorption of Pb(II) from Pb(II)-SWR and Pb(II)-SBP is believed to take place by cation exchange mechanism (Zanella, *et al.*, 2014).

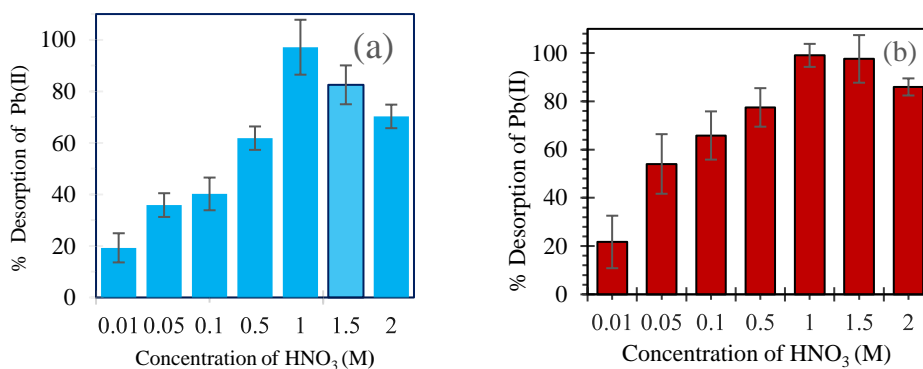


Figure 79: Desorption of Pb(II) using HNO₃ (a) biosorbed SWR and (b) biosorbed SBP (Conditions: m/v = 3 g/L, concentration of HNO₃ = 0.01 – 2 M)

To analyze the reusability of the SWR and SBP, it is subjected to four-five consecutive series of biosorption-desorption cycles as depicted in **Figure 80**. The results demonstrated that the biosorption efficiency of fresh SWR and SBP are found to be 97.22 % and 97.04%. However, after fifth cycle the biosorption efficiency of Pb(II) from Pb(II)- SBP is 80.04% and 75.21% from Pb(II)-SWR. The biosorption efficiency of SBP at fifth cycle is decreased by 17 % at fifth cycle and SWR by 22.01% in comparison with fresh SBP and SWR. The gradual decrease in biosorption efficiency of SWR and SBP during recycle might be due to partial fulfillment of binding sites and partial damage of the biosorbents (Martin-Lara *et al.*, 2012). Thus, investigated SWR and SBP could be the potential biosorbents for Pb(II) removal from aqueous solution.

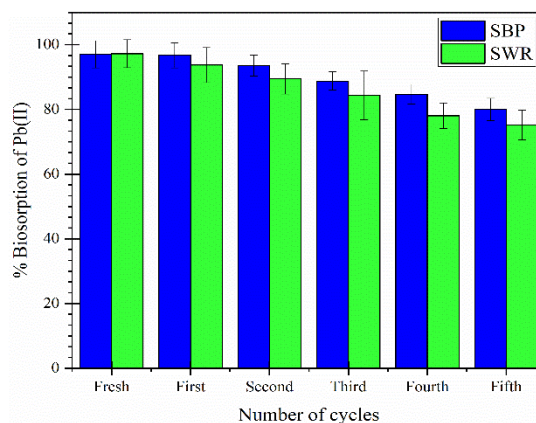


Figure 80: Variation of the % biosorption of Pb(II) in four- five cycle's biosorption-regeneration process of SWR and SBP.

4.7 Application of investigated biosorbents for the treatment of natural water sample

4.7.1 Application of investigated SBP for the treatment of Pb(II) polluted textile wastewater

The water samples were collected on the month of February from Rooma Industrial area, Kanpur, Uttar Pradesh, India. It was collected in polyethylene bottles from the center of flow. The physiochemical parameters like pH, turbidity, alkalinity, and conductivity were analysed onsite. The sample bottles were stored in ice bags and transported to the laboratory after samples preservation as per APHA (American Public Health Association) guidelines. Until further analysis, the sample bottles were stored in a refrigerator at 4°C in the laboratory. The other parameters and the biosorption performance of SBP was examined using Pb(II) contaminated water. The various parameters of this wastewater are as, pH = 8.31, total hardness = 155000 mg/L, Cl^- = 1297.18 mg/L, F^- = 0.86 mg/L, NO_3^- = 29.35 mg/L, PO_4^{3-} = 0.8 mg/L, SO_4^{2-} = 179.16 mg/L whereas Pb(II) concentration is 52.4 µg/L which is higher than WHO standard (10µg/L). **Figure 81** showed the residual concentration of Pb(II) in textile wastewater as a function of SBP dosage ranging from 0.5 to 6 g/L. The results showed the significant decrease in Pb(II) concentration with increase in SBP dosage. The concentration of Pb(II) in the residual solution is lowered to 4.02 µg/L on treatment with 3 g/L of SBP, where the acceptable limit of Pb(II) in drinking water is 10 µg/L recommended by WHO. This result showed that the investigated SBP could

be an essential biosorbent for the removal of trace amount of Pb(II) from textile water.

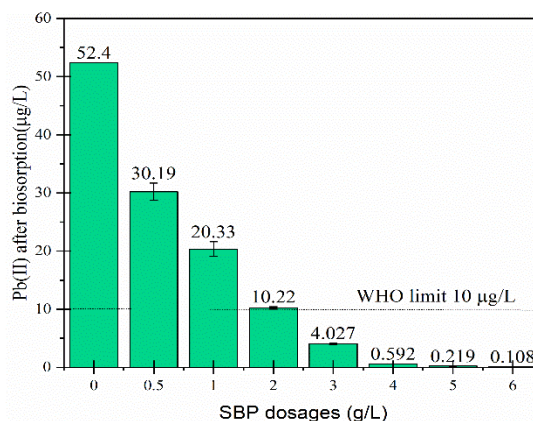


Figure 81: Application of investigated SBP for the removal of Pb(II) from polluted textile water (Conditions: Pb(II) concentration = 52.4 µg/L, volume of water = 10 mL, native pH of textile water = 8.31, t=24 h and T = 298K)

4.7.2 Application of La(III)-SWR for the dearsenification of contaminated groundwater

To assess the viability of La(III)-SWR for the biosorption of arsenic, its biosorption behavior was examined using groundwater contaminated with arsenic. The water sample was collected from the handpumps of water levels of 40 – 100 ft depth on the month of falgun (premonsoon) from the Mahuwa village of Manari V. D. C. of Nawalparasi district, Lumbini Province, Nepal. Polyethylene bottles washed with DI water and dried in oven were used to collect water samples. The physiochemical parameters like pH, turbidity, alkalinity, and conductivity were analysed onsite with the portable device. The water samples were collected in bottles adding preservatives (2% HNO₃) and transported to the laboratory kept in ice-bags for further analysis. The water sample parameters were examined as: pH (7.1), total hardness (387 mg/L), Cl⁻ (224 mg/L), F⁻ (0.32 mg/L), total dissolved solid (457 mg/L), SO₄²⁻ (14.7 mg/L), PO₄³⁻ (1.3 mg/L), and Fe (0.57 mg/L), all of which are within the range of drinking water quality while concentration of arsenic (86.8 µg/L) exceeds 8.68 folds greater than WHO acceptable limit (10 µg/L). **Figure 82** displays the equilibrium arsenic concentration in the arsenic contaminated groundwater with dosages of La(III)-SWR ranging from 0.5 to 5 g/L. The finding showed that the equilibrium concentration of arsenic was reduced significantly with the increment in biosorbent dosage and La(III)-

SWR dose of 0.5 g/L reduced arsenic below the Nepalese standard (50 $\mu\text{g/L}$) while 1.5 g/L of La(III)-SWR lowered the concentration of arsenic below the WHO and USEPA standard (WHO, 2014). These findings strongly imply that La(III)-SWR could be used as a possible biosorbent to remove the trace amounts of arsenic found in arsenic-polluted water.

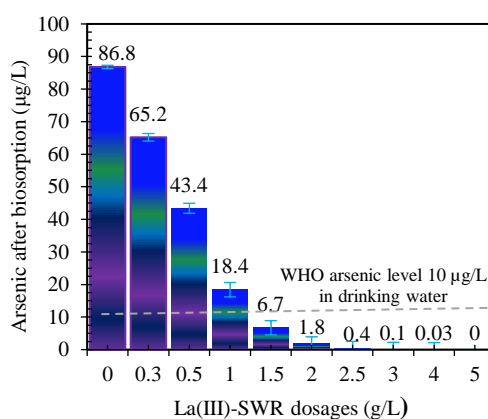


Figure 82: Application of La(III)-SWR for the dearsenification of contaminated groundwater (Conditions: $C_i = 86.8 \mu\text{g/L}$, $v = 10 \text{ mL}$, native pH of ground water = 7.1, $t = 24 \text{ h}$, $T = 298\text{K}$)

CHAPTER 5

CONCLUSION AND RECOMMENDATION

5.1 Conclusion

In the present study, RWR and RBP were saponified to develop cation exchangers. Furthermore, the anion exchangers were developed from SWR and SBP after loading with high valent metal ions such as Zr(IV) and La(III). These ion exchangers were used for biosorption of As(III), F⁻ and PO₄³⁻. The SWR and SBP were used for biosorption of Pb(II) and Hg(II). Characterization of investigated biosorbents were performed using FE-SEM/EDX, FTIR, XRD, TGA, XPS and Zeta potential measurements. FE-SEM study showed the porous and rough morphology of SWR, Zr(IV)-SWR, La(III)-SWR and SBP in comparison with RWR and RBP. However, after biosorption, the surface became smooth that insights the biosorption of tested ions. FTIR spectra showed the surface functional groups of biosorbents. The carboxyl group is found to be modified in the biosorbents synthesis. There is a shifting of the absorption peaks of the COOH group to lower frequency with a change in intensity of the peaks due to the biosorption. EDX analysis indicated the occupancy of Ca(II) onto SWR and SBP. The appearance of Zr(IV) peaks on the loaded SWR and fluoride peaks after biosorption implied the successful biosorption of fluoride onto Zr(IV)-SWR. In addition, the prominent peaks of Ca(II) onto SWR and SBP gets almost vanished after biosorption of Pb(II) and Hg(II) suggesting exchange of Ca(II) with Pb(II) and Hg(II) occurred during biosorption. The XRD analysis of Zr(IV)-SBP revealed the amorphous structure that could provide more active binding sites for the tested ions. TGA analysis indicated the high thermal stability of Zr(IV)-SWR then RWR. The p*H*_{pzc} of Zr(IV)-SWR, La(III)-SWR, Zr(IV)SBP, SWR and SBP are observed to be 5.46, 7.0, 3.8, 2.88 and 3.33, respectively. Batch biosorption experiments were conducted for the biosorption of F⁻, PO₄³⁻, As(III) onto the metal loaded biosorbents and Pb(II), and Hg(II) onto SWR, and SBP. The optimum pH for biosorption of fluoride, phosphate As(III), Hg(II) and Pb(II), respectively are evaluated to be 2.9, 4.03, 4.0, 12.08, 5.9, and 5.27. Based on the higher coefficient of determination (R²) and lower error function values, PSO model and Langmuir isotherm model described better the biosorption of investigated biosorbents. The

maximum monolayer biosorption capacities of Zr(IV)-SWR, Zr(IV)-SBP, La(III)-SWR, SWR and SBP are evaluated to be 28.98 mg F⁻/g and 27.65 mg PO₄³⁻/g, 36.02 mg F⁻/g, 37.73 mg As(III)/g, 97.18 mg Hg(II)/g, 253.16 mg Pb(II)/g, 61.31mg Hg(II)/g, 230.94 mg Pb(II)/g, respectively. Thermodynamics parameters for the biosorption of As(III) using La(III)-SWR indicated the endothermic and spontaneous nature of biosorption process. XPS analysis gave the strong support of loading La(III) onto the polymeric structure and effective biosorption of oxoanionic species of arsenic. The biosorption capacity of investigated biosorbents at higher concentration of HCO₃⁻ and PO₄³⁻ remarkably influenced the biosorption of tested anions. Similarly, higher concentration of Cu(II), Hg(II) and Pb(II) inhibited the biosorption capacity of SWR and SBP for the tested ions. NaOH solution can effectively desorbed anionic species of F⁻, PO₄³⁻ and As(III) whereas HNO₃ solution is effective for Hg(II) and Pb(II). The regeneration and reusability studies showed that the biosorption capacity of investigated biosorbents were found effective upto five consecutive cycles. Application of La(III)-SWR and SBP to actual contaminated water showed that these biosorbents successfully lowered the arsenic and lead concentration down to the WHO standard.

Finally, the research studies suggest that the low cost investigated biosorbents could be an effective alternative material for the separation of trace concentration of cationic and anionic pollutants from aqueous solutions.

5.2 Recommendations

The relevant suggestions and recommendations from this study for practical use in the future are as follows.

- The additional modification method of the surface functional groups of BP and WR can be a fruitful area of investigation.
- More investigations on the behaviour of biosorbents in real industrial effluents and make more efforts to bring biosorption process in continuous mode to pilot or industrial scale.

Limitations of the study

The biosorption process in this study could be promising method for removal of

cationic and anionic pollutants. However, it comprises few limitations.

- The present outcome of this should be tested with continuous mode that is applicable in Real water column studies.
- Since the material is of biomaterial, it cannot be used for several cycles as in case of synthetic chelating materials.

CHAPTER 6

SUMMARY

Nowdays, cationic and anionic pollutants are the emerging environmental issues due to unplanned urbanization, a self-centered way of life, and haphazard use of resources. Researchers are seriously worried in the aspects of solid waste management and deterioration of water quality. The contamination of heavy metals and metalloids degrade the quality of surface water and ground water. Because of their acute toxicity, heavy metals (like As, Pb, and Hg) and excessive usage of non-metals (P and F) pose substantial risks to living beings and the environment. Therefore, observing the seriousness of the pollutants, the present research has been carried out for the removal of these pollutants. The main aim of the study is to utilize locally available watermelon rind (WR) & banana peel (BP) waste to develop low-cost ion exchangers which might be an alternative substitute to non-degradable synthetic ion-exchangers for the effective separation of cationic (As, Pb, and Hg) and anionic pollutants (P and F) from water. A preliminary study and extensive literature review targeted that the utilization of low cost, pectin-rich WR and BP *via* saponification, can be an eco-friendly, effective precursor for the exploration of suitable ion-exchangers to remove cationic pollutants and metal loaded saponified product for anionic pollutants from water. The current research work has been summarized as,

Chapter 1 includes the brief introduction related to water sources, heavy metal pollutants, and remedial techniques. All living beings need water to survive, but less than 0.3% of fresh water is present in rivers, lakes, and the atmosphere and even less (0.003 %) can be present in biological sources. The natural and anthropogenic activities directly or indirectly release cationic and anionic pollutants into water resources, causes adverse effect in human health, water resources and eco-system. Heavy metals are non-degradable, and they accumulate in living tissues, causing various diseases and disorders. In this regard, the attraction of biosorption over costly conventional treatment technologies, utilizing low-cost ion-exchangers obtained from watermelon rind and banana peels waste as a replacement for commercial ion exchangers has been attempted.

The extensive literature review for the separation of As(III), F⁻, PO₄³⁻, Hg(II) and Pb(II) was done in Chapter 2. This chapter screened the effectiveness and potentiality of commercial activated carbon, alumina, rice husk biochar, metal organic framework, modified chitosan biochar and so forth for the removal of cationic and anionic pollutants. Nevertheless, due to high cost and the energy demands for the physical and chemical activation, commonly adopted to produce low-cost biosorbents from locally available biopolymers, many researchers have reported the feasibility of using low cost biosorbents for the removal of pollutants from aqueous solution. Additionally, the adopted procedure employed in the prior studies using watermelon rind and banana peels has been analyzed broadly and clearly. The clear-cut research gap for the study and targeted plan to achieve the research goal has been elaborated.

After literature review and finding the research gap, the the general methodological framework for biosorbent synthesis, biosorption procedure and charecterization techniques adopted in this study are included in Chapter 3. The experimental conditions and methodological framework are practiced from the insights of literature review. Watermelon rind and banana peels waste are chosen as the raw biosorbents. These investigated biosorbents are synthesized *via* saponification to develop natural cation exchangers. Furthermore, the saponified biosorbents are loaded with high valent metal ions (M (III/IV)) to develop anion exchangers. The biosorption performance of SWR and SBP with and without metal loading was studied for the removal of pollutants (F⁻, PO₄³⁻ As(III), Hg(II) and Pb(II)) from aqueous solution under Batch experiments. To inspect the structural changes in the investigated biosorbents, the biosorbents were characterized before and after biosorption, using FE-SEM/EDX, XRD, TGA, FTIR and XPS.

Chapter 4 includes the results and discussion of biosorption performance of anion exchangers metal loadd-SWR and metal loaded-SBP and cation exchangers (SWR, SBP) for the removal of F⁻, PO₄³⁻ As(III), Hg(II) and Pb(II)) from aqueous solution. The metal loaded biosorbents associated with hydroxyl groups in its coordination spheres can biosorb anionic pollutants (F⁻, PO₄³⁻, As(III)) through ligand exchange mechanism. The saponified biosorbentsbiosorb the cationic pollutants (Hg(II) and Pb(II)) through cation exchange mechanism. FE-SEM studies showed the surface

morphology of investigated biosorbents prior to biosorption is found to be rough, irregular with distinct pores but after biosorption the surface morphology turned into smooth and uniform structures. FTIR studies showed carboxyl group is the main functional group in the investigated biosorbents. The disappearance or shifting of absorption peaks to lower frequency with change in intensity is observed which indicates the substitution of cations or anions. EDX analysis indicated C, O, and Ca(II) are the major elements present in SWR and SBP. After metal loading, the peaks of Ca(II) vanished and new peaks of loaded metal ions are appeared. The EDX spectra analysis after biosorption showed the successful loading of pollutants. The XRD studies showed the amorphous structure of the biosorbents which could provide a greater surface area and more available active sites for biosorption. TGA analysis showed the stability of the Zr(IV)-SWR biosorbents. XPS analysis onto La(III)-SWR demonstrates the loading of La(III) onto polymeric structure of SWR and effective biosorption of oxoanionic species of As(III) onto La(III)-SWR. The optimum pH for the biosorption of F^- , PO_4^{3-} and As(III) onto metal loaded SWR and SBP takes place at 2.9, 4.03, 4.0, 12.08. Similarly, optimum pH for biosorption of Hg(II) and Pb(II) takes place at 5.9 and 5.27. The kinetic and isotherm studies showed that the biosorption behaviour of investigated biosorbents followed PSO model and Langmuir isotherm models. The maximum monolayer biosorption capacities of Zr(IV)-SWR, Zr(IV)-SBP, La(III)-SWR, SWR and SBP are evaluated to be 28.98 mg F^- /g and 27.65 mg PO_4^{3-} /g, 36.02 mg F^- /g, 37.73 mg As(III)/g, 97.18 mg Hg(II)/g, 253.16 mg Pb(II)/g, 61.31mg Hg(II)/g, 230.94 mg Pb(II)/g, respectively. The regeneration and reusability studies showed the effectiveness of investigated biosorbents above four-five cycles. La(III)-SWR and SBP showed the excellent performance of removing pollutants present in real water system below the contaminant level as recommended by WHO.

Chapter 5 includes the conclusion of the study and recommendations for further study. It can be concluded by the results that the investigated metal loaded biosorbents acts as effective anion exchangers for separation of anionic pollutants and cation exchangers (SWR and SBP) to separate cationic pollutants present in aqueous solution. These investigated biosorbents can effectively reduce trace

concentration of pollutants present in aqueous solution. Thus, developed natural ion exchangers can be a better substitute of expensive synthetic ion-exchangers.

REFERENCES

- Abdolali, A., Guo, W. S., Ngo, H. H., Chen, S. S., Nguyen, N. C., & Tung, K. L. (2014). Typical Lignocellulosic Wastes and By-products for Biosorption Process in Water and Wastewater Treatment: A Critical Review. *Bioresource Technology*, **160**: 57-66.
- Abujazar, M. S. S., Karaağaç, S. U., Amr, S. S. A., Alazaiza, M. Y., & Bashir, M. J. (2022). Recent Advancement in the Application of Hybrid Coagulants in Coagulation-Flocculation of Wastewater: A Review. *Journal of Cleaner Production*, **345**: 131133.
- Adhikari, D. L., Aryal, R. L., Bhattarai, S., Gautam, S. K., & Poudel, B. R. (2017). Removal of Cr(VI) from Aqueous Solution Using Chemically-Modified Sweet Lime (*Citrus limetta*) Peels as Adsorbent. *Journal of Nepal Chemical Society*, **36**: 82-95.
- Ahmad, R., & Haseeb, S. (2015). Absorptive Removal of Pb(II), Cu(II) and Ni(II) from the Aqueous Solution by Using Groundnut Husk Modified with Guar Gum (GG): Kinetic and Thermodynamic Studies. *Groundwater for Sustainable Development*, **1**(1-2): 41-49.
- Ahmaruzzaman, M. (2011). Industrial Wastes as Low-Cost Potential Adsorbents for the Treatment of Wastewater Laden with Heavy Metals. *Advances in Colloid and Interface Science*, **166**(1-2): 36-59.
- Ahmaruzzaman, M. (2010). A Review on the Utilization of Fly Ash. *Progress in Energy and Combustion Science*, **36**(3): 327-363.
- Ajmal, Z., Muhmood, A., Usman, M., Kizito, S., Lu, J., Dong, R., & Wu, S. (2018). Phosphate Removal from Aqueous Solution Using Iron Oxides: Adsorption, Desorption and Regeneration Characteristics. *Journal of Colloid and Interface Science*, **528**: 145-155.

- Akhtar, N., Syakir Ishak, M. I., Bhawani, S. A., & Umar, K. (2021). Various Natural and Anthropogenic Factors Responsible for Water Quality Degradation: A Review. *Water*, **13**(19): 2660.
- Al Rmalli, S. W., Dahmani, A. A., Abuein, M. M., & Gleza, A. A. (2008). Biosorption of Mercury from Aqueous Solutions by Powdered Leaves of Castor Tree (*Ricinus communis L.*). *Journal of Hazardous Materials*, **152**(3): 955-959.
- Alavi, S., Zilouei, H., & Asadinezhad, A. (2015). *Otostegia Persica* Biomass as a New Biosorbent for the Removal of Lead from Aqueous Solutions. *International Journal of Environmental Science and Technology*, **12**(2): 489-498.
- Algieri, C., Chakraborty, S., & Candamano, S. (2021). A Way to Membrane-based Environmental Remediation for Heavy Metal Removal. *Environments*, **8**(6): 52.
- Ali, H., & Khan, E. (2018). Bioaccumulation of Non-Essential Hazardous Heavy Metals and Metalloids in Freshwater Fish. Risk to Human Health. *Environmental Chemistry Letters*, **16**(3): 903-917.
- Ali, S., Rizwan, M., Shakoob, M. B., Jilani, A., & Anjum, R. (2020). High Sorption Efficiency for As(III) and As(V) from Aqueous Solutions Using Novel Almond Shell Biochar. *Chemosphere*, **243**: 125330.
- Alimohammady, M., & Ghaemi, M. (2020). Adsorptive Removal of Hg(II) from Aqueous Solutions Using Amino Phenyl-Pyrazole-Functionalized Graphene Oxide. *Carbon Letters*, **30**(5): 493-508.
- Alka, S., Shahir, S., Ibrahim, N., Ndejiko, M. J., Vo, D. V. N., & Abd Manan, F. (2021). Arsenic Removal Technologies and Future Trends: A Mini Review. *Journal of Cleaner Production*, **278**: 123805.
- Alqadami, A. A., Naushad, M., Alothman, Z. A., Alsuhybani, M., & Algamdi, M. (2020). Excellent Adsorptive Performance of a New Nanocomposite for

- Removal of Toxic Pb(II) from Aqueous Environment: Adsorption Mechanism and Modeling Analysis. *Journal of Hazardous Materials*, **389**: 121896.
- Altowayti, W. A. H., Algaifi, H. A., Bakar, S. A., & Shahir, S. (2019). The Adsorptive Removal of As(III) Using Biomass of Arsenic Resistant *Bacillus thuringiensis* Strain WS3: Characteristics and Modelling Studies. *Ecotoxicology Environment and Safety*, **172**: 176-185.
- Altundoğan, H. S., Altundoğan, S., Tümen, F., & Bildik, M. (2000). Arsenic Removal from Aqueous Solutions by Adsorption on Red Mud. *Waste Management*, **20**(8): 761-767.
- Alvarez, N. M. M., Pastrana, J. M., Lagos, Y., & Lozada, J. J. (2018). Evaluation of Mercury Hg(II) Adsorption Capacity Using Exhausted Coffee Waste. *Sustainable Chemistry and Pharmacy*, **10**: 60-70.
- Ameri, A., Tamjidi, S., Dehghankhalili, F., Farhadi, A., & Saati, M. A. (2020). Application of Algae as Low Cost and Effective Bio-adsorbent for Removal of Heavy Metals from Wastewater: A Review Study. *Environmental Technology Reviews*, **9**(1): 85-110.
- Amin, F., Talpur, F. N., Balouch, A., Chandio, Z. A., Surhio, M. A., & Afridi, H. I. (2016). Biosorption of Mercury (II) from Aqueous Solution by Fungal Biomass (*Pleurotus eryngii*): Isotherm, Kinetic, and Thermodynamic Studies. *Environmental Progress and Sustainable Energy*, **35**(5): 1274-1282.
- Anagnostopoulos, V. A., Manariotis, I. D., Karapanagioti, H. K., & Chrysikopoulos, C. V. (2012). Removal of Mercury from Aqueous Solutions by Malt Spent Rootlets. *Chemical Engineering Journal*, **213**: 135-141.
- Arumugam, N., Chelliapan, S., Thirugnana, S. T., & Jasni, A. B. (2020). Optimisation of Heavy Metals Uptake from Leachate Using Red Seaweed (*Gracilaria changii*). *Journal of Environmental Treatment Techniques*, **8**(3): 1089-1092.

- Aryal, M., Ziagova, M., & Liakopoulou-Kyriakides, M. (2010). Study on Arsenic Biosorption Using Fe(III)-treated Biomass of *Staphylococcus xylosum*. *Chemical Engineering Journal*, **162**(1): 178-185.
- Aryal, R. L., Bhurtel, K. P., Poudel, B. R., Pokhrel, M. R., Paudyal, H., & Ghimire, K. N. (2022). Sequestration of Phosphate from Water onto Modified Watermelon Waste Loaded with Zr(IV). *Separation Science and Technology*, **57**(1): 70-82.
- Aryal, R. L., Poudel, B. R., Gautam, S. K., Paudyal, H., Ghimire, K. N., & Pokhrel, M. R. (2019). Removal of Fluoride from Aqueous Solution Using Biomass-Based Adsorbents: A Review. *Journal of Nepal Chemical Society*, **40**: 44-51.
- Aryal, R. L., Poudel, B. R., Pokhrel, M. R., Paudyal, H., & Ghimire, K. N. (2021). Effectiveness of Zr(IV)-Loaded Banana Peels Biomass for the Uptake of Fluoride Anion from Water. *Journal of Institute of Science and Technology*, **26**(2): 67-78.
- Aryal, R. L., Thapa, A., Poudel, B. R., Pokhrel, M. R., Dahal, B., Paudyal, H., & Ghimire, K. N. (2022). Effective Biosorption of Arsenic from Water Using La(III) Loaded Carboxyl Functionalized Watermelon Rind. *Arabian Journal of Chemistry*, **15**(3): 103674.
- Awad, F. S., Abouzied, K. M., Abou El-Maaty, W. M., El-Wakil, A. M., & El-Shall, M. S. (2020). Effective Removal of Mercury(II) from Aqueous Solutions by Chemically Modified Graphene Oxide Nanosheets. *Arabian Journal of Chemistry*, **13**(1): 2659-2670.
- Awual, M. R. (2016). Assessing of Lead(II) Capturing from Contaminated Wastewater Using Ligand Doped Conjugate Adsorbent. *Chemical Engineering Journal*, **289**: 65-73.
- Azizul-Rahman, M. F. H., Mohd Suhaimi, A. A., & Othman, N. (2013). Biosorption of Pb(II) and Zn(II) in Synthetic Waste Water by Watermelon Rind (*Citrullus lanatus*). *Applied Mechanics and Materials*, **465**: 906-910.

- Baheti, V., Padil, V. V. T., Militky, J., Cernik, M., & Mishra, R. (2013). Removal of Mercury from Aqueous Environment by Jute Nanofiber. *Journal of Fiber Bioengineering and Informatics*, **6**(2): 175-184.
- Bansal, M., Garg, R., Garg, V. K., Garg, R., & Singh, D. (2022). Sequestration of Heavy Metal ions from Multi-Metal Simulated Wastewater Systems Using Processed Agricultural Biomass. *Chemosphere*, **296**: 133966.
- Barragan, J. A., Ponce de León, C., Alemán Castro, J. R., Peregrina-Lucano, A., Gómez-Zamudio, F., & Larios-Durán, E. R. (2020). Copper and Antimony Recovery from Electronic Waste by Hydrometallurgical and Electrochemical Techniques. *ACS Omega*, **5**(21): 12355-12363.
- Basu, A., Saha, D., Saha, R., Ghosh, T., & Saha, B. (2014). A Review on Sources, Toxicity and Remediation Technologies for Removing Arsenic from Drinking Water. *Research on Chemical Intermediates*, **40**(2): 447-485.
- Beiyan, J., Awad, Y. M., Beckers, F., Wang, J., Tsang, D. C., Ok, Y. S., Wang, S. L., Wang, H., & Rinklebe, J. (2020). (Im) mobilization and Speciation of Lead Under Dynamic Redox Conditions in a Contaminated Soil Amended with Pine Sawdust Biochar. *Environment International*, **135**: 105376.
- Bharti, S. K., & Kumar, N. (2018). Kinetic Study of Pb(II) Removal from Battery Manufacturing Wastewater Using Bagasse Biochar as Biosorbent. *Applied Water Science*, **8**(4): 1-13.
- Bhatt, P. R., Aryal, R. L., Poudel, B. R., Bhattarai, S., & Gautam, S. K. (2018). Adsorptive Removal of Cr(VI) from Aqueous Solution onto Charred Sugarcane Bagasse. *Journal of Nepal Chemical Society*, **39**: 62-69.
- Bhattacharjee, C., Dutta, S., & Saxena, V. K. (2020). A Review on Biosorptive Removal of Dyes and Heavy Metals from Wastewater Using Watermelon Rind as Biosorbent. *Environmental Advances*, **2**: 100007.
- Bisla, V., Rattan, G., Singhal, S., & Kaushik, A. (2020). Green and Novel Adsorbent from Rice Straw Extracted Cellulose for Efficient Adsorption of Hg(II) ions in

an Aqueous Medium. *International Journal of Biological Macromolecules*, **161**: 194-203.

- Biswal, B. K., Jadhav, U. U., Madhaiyan, M., Ji, L., Yang, E. H., & Cao, B. (2018). Biological Leaching and Chemical Precipitation Methods for Recovery of Co and Li from Spent Lithium-ion Batteries. *ACS Sustainable Chemistry and Engineering*, **6**(9): 12343-12352.
- Biswas, B. K., Inoue, K., Ghimire, K. N., Harada, H., Ohto, K., & Kawakita, H. (2008a). Removal and Recovery of Phosphorus from Water by Means of Adsorption onto Orange Waste gel Loaded with Zirconium. *Bioresource Technology*, **99**(18): 8685-8690.
- Biswas, B. K., Inoue, K., Ghimire, K. N., Kawakita, H., Ohto, K., & Harada, H. (2008b). Effective Removal of Arsenic with Lanthanum (III)- and Cerium (III)-Loaded Orange Waste Gels. *Separation Science and Technology*, **43**(8): 2144-2165.
- Biswas, B. K., Inoue, K., Ghimire, K. N., Ohta, S., Harada, H., Ohto, K., & Kawakita, H. (2007). The Adsorption of Phosphate from an Aquatic Environment Using Metal-Loaded Orange Waste. *Journal of Colloid and Interface Science*, **312**(2): 214-223.
- Blanchard, G., Maunaye, M., & Martin, G. (1984). Removal of Heavy Metals from Waters by Means of Natural Zeolites. *Water Research*, **18**(12): 1501-1507.
- Blazquez, G., Calero, M., Ronda, A., Tenorio, G., & Martín Lara, M. A. (2014). Study of Kinetics in the Biosorption of Lead onto Native and Chemically Treated Olive Stone. *Journal of Industrial and Engineering Chemistry*, **20**(5): 2754-2760.
- Boskabady, M., Marefati, N., Farkhondeh, T., Shakeri, F., Farshbaf, A., & Boskabady, M. H. (2018). The Effect of Environmental Lead Exposure on Human Health and the Contribution of Inflammatory Mechanisms, A Review. *Environment International*, **120**: 404-420.

- Bouabidi, Z. B., El Naas, M. H., Cortes, D., & McKay, G. (2018). Steel-making Dust as a Potential Adsorbent for the Removal of Pb(II) from an Aqueous Solution. *Chemical Engineering Journal*, **334**: 837-844.
- Braun, J. C., Borba, C. E., Godinho, M., Perondi, D., Schontag, J. M., & Wenzel, B. M. (2019). Phosphorus Adsorption in Fe(III)-Loaded Activated Carbon: Two-Site Monolayer Equilibrium Model and Phenomenological Kinetic Description. *Chemical Engineering Journal*, **361**: 751-763.
- Brummer, Y., Jones, S., Tosh, S. M., & Wood, P. J. (2008). Extraction and Physicochemical Characterization of Rye β -glucan and Effects of Barium on Polysaccharide Molecular weight. *Cereal Chemistry*, **85**(2): 174-181.
- Cai, H., Xu, L., Chen, G., Peng, C., Ke, F., Liu, Z., Li, D., Zhang, Z., & Wan, X. (2016). Removal of Fluoride from Drinking Water Using Modified Ultrafine Tea Powder Processed Using a Ball-Mill. *Applied Surface Science*, **375**: 74-84.
- Cai, L., Sun, J., Cui, L., Jiang, Y., & Huang, Z. (2020). Stabilization of Heavy Metals in Piggery Wastewater Sludge Through Coagulation-Hydrothermal Reaction–Pyrolysis Process and Sludge Biochar for Tylosin Removal. *Journal of Cleaner Production*, **260**: 121165.
- Çetin, K., Türkmen, D., Qureshi, T., Sağlam, N., & Denizli, A. (2016). Phanerochaete Chrysosporium Loaded Cryogel Column for Biosorption of Hg(II) ions from Aqueous Solutions. *Hacettepe Journal of Biology and Chemistry*, **44**(1): 77-86.
- Chakrabarti, S. (2018). Eutrophication-A Global Aquatic Environmental Problem: A Review. *Research Reviews: Journal of Ecology and Environmental Sciences*, **6**: 1-6.
- Chai, L., Wang, Q., Li, Q., Yang, Z., & Wang, Y. (2010). Enhanced Removal of Hg(II) from Acidic Aqueous Solution Using Thiol-Functionalized Biomass. *Water Science and Technology*, **62**(9): 2157-2166.

- Chalkidis, A., Jampaiah, D., Hartley, P. G., Sabri, Y. M., & Bhargava, S. K. (2020). Mercury in Natural Gas Streams: A Review of Materials and Processes for Abatement and Remediation. *Journal of Hazardous Materials*, **382**: 121036.
- Chen, R. F., Liu, T., Rong, H. W., Zhong, H. T., & Wei, C. H. (2021). Effect of Organic Substances on Nutrients Recovery by Struvite Electrochemical Precipitation from Synthetic Anaerobically Treated Swine Wastewater. *Membranes*, **11**(8): 594.
- Chen, J., Yang, R., Zhang, Z., & Wu, D. (2022). Removal of Fluoride from Water Using Aluminum Hydroxide-Loaded Zeolite Synthesized from Coal Fly Ash. *Journal of Hazardous Materials*, **421**: 126817.
- Crini, G., Lichtfouse, E., Wilson, L. D., & Morin-Crini, N. (2019). Conventional and Non-conventional Adsorbents for Wastewater Treatment. *Environmental Chemistry Letters*, **17**(1): 195-213.
- Das, N. (2010). Recovery of Precious Metals Through Biosorption. A Review. *Hydrometallurgy*, **103**(1-4): 180-189.
- Deng, S., Liu, H., Zhou, W., Huang, J., & Yu, G. (2011). Mn–Ce Oxide as a High-Capacity Adsorbent for Fluoride Removal from Water. *Journal of Hazardous Materials*, **186**(2-3): 1360-1366.
- Deng, Y., Nordstrom, D. K., & Blaine McCleskey, R. (2011). Fluoride Geochemistry of Thermal Waters in Yellowstone National Park: I. Aqueous Fluoride Speciation. *Geochimica et Cosmochimica Acta*, **75**(16): 4476-4489.
- Desai, A. V., Manna, B., Karmakar, A., Sahu, A., & Ghosh, S. K. (2016). A Water-stable Cationic Metal-Organic Framework as a Dual Adsorbent of Oxoanion Pollutants. *Angewandte Chemie*, **128**(27): 7942-7946.
- Detroy, R., & Hesseltine, C. (1978). Availability and Utilization of Agricultural and Agro Industrial Wastes. *Process Biochemistry*, **13**(9): 2-31.

- Dey, S., Haripavan, N., Basha, S., & Babu, G. (2021). Removal of Ammonia and Nitrates from Contaminated Water by Using Solid Waste Bio-adsorbents. *Current Research in Chemical Biology*, **1**: 100005.
- Dias, M., Pinto, J., Henriques, B., Figueira, P., Fabre, E., Tavares, D., Vale, C., & Pereira, E. (2021). Nutshells as Efficient Biosorbents to Remove Cadmium, Lead, and Mercury from Contaminated Solutions. *International Journal of Environmental Research and Public Health*, **18**(4): 1580.
- Du, T. M., Yang, H. S., & Niu, X. F. (2021). Phosphorus-Containing Compounds Regulate Mineralization. *Materials Today Chemistry*, **22**: 100579.
- Duan, X., Zhang, C., Srinivasakannan, C., & Wang, X. (2017). Waste Walnut Shell Valorization to Iron Loaded Biochar and Its Application to Arsenic Removal. *Resource-Efficient Technologies*, **3**(1): 29-36.
- Elfeghe, S., Sheng, Q., Mamudu, A., James, L. A., & Zhang, Y. (2022). Recovery of Pb(II) ions From Aqueous Solutions Using G-26 and MTS9570 Resins with Sulfonic/Phosphonic Functional Groups. *Minerals*, **12**(10): 1312.
- Elkhaleefa, A., Ali, I. H., Brima, E. I., Shigidi, I., Elhag, A. B., & Karama, B. (2021). Evaluation of the Adsorption Efficiency on the Removal of Lead(II) ions from Aqueous Solutions Using *Azadirachta indica* Leaves as an Adsorbent. *Processes*, **9**(3): 559.
- Emaga, T. H., Robert, C., Ronkart, S. N., Wathélet, B., & Paquot, M. (2008). Dietary Fibre Components and Pectin Chemical Features of Peels During Ripening in Banana and Plantain Varieties. *Bioresource Technology*, **99**(10): 4346-4354.
- Erhirhie, E. O., & Ekene, N. E. (2013). Medicinal Values on *Citrullus lanatus* (watermelon): Pharmacological Review. *International Journal of Research in Pharmaceutical and Biomedical Sciences*, **4**(4): 1305-1312.
- Fabre, E., Lopes, C. B., Vale, C., Pereira, E., & Silva, C. M. (2020). Valuation of Banana Peels as an Effective Biosorbent for Mercury Removal Under Low

- Environmental Concentrations. *Science of The Total Environment*, **709**: 135883.
- Fan, L., Luo, C., Sun, M., Li, X., & Qiu, H. (2013). Highly Selective Adsorption of Pb(II) by Water-Dispersible Magnetic Chitosan/Graphene Oxide Composites. *Colloids and Surfaces B: Biointerfaces*, **103**: 523-529.
- Fang, Q., Chen, B., Lin, Y., & Guan, Y. (2014). Aromatic and Hydrophobic Surfaces of Wood-Derived Biochar Enhance Perchlorate Adsorption via Hydrogen Bonding to Oxygen-Containing Organic Groups. *Environmental Science and Technology*, **48**(1): 279-288.
- Faraji, B., Zarabi, M., & Kolahchi, Z. (2020). Phosphorus Removal from Aqueous Solution Using Modified Walnut and Almond Wooden Shell and Recycling as Soil Amendment. *Environmental Monitoring and Assessment*, **192**(6): 1-16.
- Fatima, F., Du, H., & Kommalapati, R. R. (2021). Treatment of Poultry Slaughterhouse Wastewater with Membrane Technologies: A Review. *Water*, **13**(14): 1905.
- Fayazi, M. (2020). Removal of Hg(II) from Wastewater Using a New and Effective Composite: Sulfur-Coated Magnetic Carbon Nanotubes. *Environmental Science and Pollution Research*, **27**(11): 12270-12279.
- Figueira, P., Henriques, B., Teixeira, F., Afonso, N., Pinto, J., Tavares, D., Vale, C., & Pereira, E. (2022). Potentialities of Agro-Based Wastes to Remove Cd, Hg, Pb, and As from Contaminated Waters. *Water, Air, and Soil Pollution*, **233**(3): 1-17.
- Filote, C., Volf, I., Santos, S. C., & Botelho, C. M. (2019). Bioadsorptive Removal of Pb(II) from Aqueous Solution by the Biorefinery Waste of *Fucus spiralis*. *Science of the Total Environment*, **648**: 1201-1209.
- Freundlich, H. (1906). Over the Adsorption in Solution. *The Journal of Physical Chemistry A*, **57**(385471): 1100-1107.

- Fu, F., & Wang, Q. (2011). Removal of Heavy Metal ions from Wastewaters: A Review. *Journal of Environmental Management*, **92**(3): 407-418.
- Gadd, G. M. (2009). Biosorption: Critical Review of Scientific Rationale, Environmental Importance and Significance for Pollution Treatment. *Journal of Chemical Technology and Biotechnology: International Research in Process, Environmental and Clean Technology*, **84**(1): 13-28.
- Gaddam, K., Sivananaintha Perumal, M., & Ravindiran, G. (2020). Removal of Lead Metal ion Using Biowaste of *Pithophora Cleveana Wittrock* and *Mimusops elengi*. *Energy Sources, Part A: Recovery, Utilization, and Environmental Effects*, 1-19.
- Gao, L., Li, Z., Yi, W., Li, Y., Zhang, P., Zhang, A., & Wang, L. (2021). Impacts of Pyrolysis Temperature on Lead Adsorption by Cotton Stalk-Derived Biochar and Related Mechanisms. *Journal of Environmental Chemical Engineering*, **9**(4): 105602.
- Gaur, N., Kukreja, A., Yadav, M., & Tiwari, A. (2018). Adsorptive Removal of Lead and Arsenic from Aqueous Solution Using Soya bean as a Novel Biosorbent: Equilibrium Isotherm and Thermal Stability Studies. *Applied Water Science*, **8**(4): 1-12.
- Gawkowska, D., Cieśla, J., Zdunek, A., & Cybulska, J. (2019). Cross-Linking of Diluted Alkali-Soluble Pectin from Apple (*Malus domestica* fruit) in Different Acid-Base Conditions. *Food Hydrocolloids*, **92**: 285-292.
- Ge, L., Lu, J., Yang, R. F., & Liu, Y. J. (2013). Properties of Heat Treatment Alkaline Pulping Black Liquor with Aluminum chloride. *Advanced Materials Research*, **610**: 2220-2223.
- Gizaw, A., Zewge, F., Kumar, A., Mekonnen, A., & Tesfaye, M. (2021). A Comprehensive Review on Nitrate and Phosphate Removal and Recovery from Aqueous Solutions by Adsorption. *AQUA-Water Infrastructure, Ecosystems and Society*, **70**(7): 921-947.

- Ghimire, K. N., Inoue, K., Ohto, K., & Hayashida, T. (2008). Adsorption Study of Metal ions onto Crosslinked Seaweed *Laminaria japonica*. *Bioresource Technology*, **99**(1): 32-37.
- Ghimire, K. N., Inoue, J. I., Inoue, K., Kawakita, H., & Ohto, K. (2008). Adsorptive Separation of Metal ions onto Phosphorylated Orange Waste. *Separation Science and Technology*, **43**(2): 362-375.
- Ghimire, K., & Inoue, K. (2007). Optimization of Saponification Process for Orange and Apple Wastes. *Journal of Nepal Chemical Society*, **22**: 41-46.
- Ghimire, K. N., Inoue, K., Yamaguchi, H., Makino, K., & Miyajima, T. (2003). Adsorptive Separation of Arsenate and Arsenite Anions from Aqueous Medium by Using Orange Waste. *Water Research*, **37**(20): 4945-4953.
- Ghimire, K. N., Inoue, K., Makino, K., & Miyajima, T. (2002). Adsorptive Removal of Arsenic Using Orange Juice Residue. *Separation Science and Technology*, **37**(12): 2785-2799.
- Giraldo, S., Robles, I., Ramirez, A., Flórez, E., & Acelas, N. (2020). Mercury Removal from Wastewater Using Agroindustrial Waste Adsorbents. *SN Applied Sciences*, **2**(6): 1-17.
- Golzadeh, N., Barst, B. D., Basu, N., Baker, J. M., Auger, J. C., & Mc Kinney, M. A. (2020). Evaluating the Concentrations of Total Mercury, Methylmercury, and Selenium: Mercury Molar Ratios in Traditional Foods of the Bigstone Cree in Alberta, Canada. *Chemosphere*, **250**: 126285.
- Goswami, A., & Purkait, M. K. (2012). The Defluoridation of Water by Acidic Alumina. *Chemical Engineering Research and Design*, **90**(12): 2316-2324.
- Goswami, R., & Kumar, M. (2018). Removal of Fluoride from Aqueous Solution Using Nanoscale Rice Husk Biochar. *Groundwater for Sustainable Development*, **7**: 446-451.
- Gugushe, A. S., Nqombolo, A., & Nomngongo, P. N. (2019). Application of Response Surface Methodology and Desirability Function in the Optimization

- of Adsorptive Remediation of Arsenic from Acid Mine Drainage Using Magnetic Nanocomposite: Equilibrium Studies and Application to Real Samples. *Molecules*, **24**(9): 1792.
- Guibal, E. (2004). Interactions of Metal ions with Chitosan-Based Sorbents: A Review. *Separation and Purification Technology*, **38**(1): 43-74.
- Guimarães, T., Paquini, L. D., Ferraz, B. R. L., Profeti, L. P. R., & Profeti, D. (2020). Efficient Removal of Cu(II) and Cr(III) Contaminants from Aqueous Solutions Using Marble Waste Powder. *Journal of Environmental Chemical Engineering*, **8**(4): 103972.
- Günay, A., Arslankaya, E., & Tosun, I. (2007). Lead Removal from Aqueous Solution by Natural and Pretreated Clinoptilolite: Adsorption Equilibrium and Kinetics. *Journal of Hazardous Materials*, **146**(1-2): 362-371.
- Guo, Y., Wang, Z., Zhou, X., & Bai, R. (2017). Removal of Hg(II) from Aqueous Solution with Three Commercial Raw Activated Carbons. *Research on Chemical Intermediates*, **43**(4): 2273-2297.
- Gupta, A., Vidyarthi, S., & Sankararamakrishnan, N. (2015). Concurrent Removal of As(III) and As(V) Using Green Low Cost Functionalized Biosorbent—*Saccharum officinarum* bagasse. *Journal of Environmental Chemical Engineering*, **3**(1): 113-121.
- Han, J., Kiss, L., Mei, H., Remete, A. M., Ponikvar-Svet, M., Sedgwick, D. M., Roman, R., Fustero, S., Moriwaki, H., & Soloshonok, V. A. (2021). Chemical Aspects of Human and Environmental Overload with Fluorine. *Chemical Reviews*, **121**(8): 4678-4742.
- Hao, L., Zheng, T., Jiang, J., Zhang, G., & Wang, P. (2016). Removal of As(III) and As(V) from Water Using Iron Doped Amino Functionalized Sawdust: Characterization, Adsorptive Performance and UF Membrane Separation. *Chemical Engineering Journal*, **292**: 163-173.

- He, M., Xu, Z., Hou, D., Gao, B., Cao, X., Ok, Y. S., Rinklebe, J., Bolan, N. S., & Tsang, D. C. (2022). Waste-Derived Biochar for Water Pollution Control and Sustainable Development. *Nature Reviews Earth and Environment*, **3**: 444-460.
- He, X., Deng, F., Shen, T., Yang, L., Chen, D., Luo, J., Luo, X., Min, X., & Wang, F. (2019). Exceptional Adsorption of Arsenic by Zirconium Metal-Organic Frameworks: Engineering Exploration and Mechanism Insight. *Journal of Colloid and Interface Science*, **539**: 223-234.
- He, Y., Lin, H., Dong, Y., & Wang, L. (2017). Preferable Adsorption of Phosphate Using Lanthanum-Incorporated Porous Zeolite: Characteristics and Mechanism. *Applied Surface Science*, **426**: 995-1004.
- Hemavathy, R., Saravanan, A., Kumar, P. S., Vo, D.-V. N., Karishma, S., & Jeevanantham, S. (2021). Adsorptive Removal of Pb(II) ions onto Surface Modified Adsorbents Derived from *Cassia fistula* seeds: Optimization and modelling study. *Chemosphere*, **283**: 131276.
- Hinrichsen, D., & Tacio, H. (2002). The Coming Freshwater Crisis is Already Here. *The linkages between population and water. Washington, DC: Woodrow Wilson International Center for Scholars*, 1-26.
- Ho, Y. S., & McKay, G. (1998). Sorption of Dye from Aqueous Solution by Peat. *Chemical Engineering Journal*, **70**(2): 115-124.
- Ho, Y., & McKay, G. (1998). Kinetic Model for Pb(II) Sorption onto Peat. *Adsorption Science and Technology*, **16**(4): 243-255.
- Homagai, P. L., Ghimire, K. N., & Inoue, K. (2010). Adsorption Behavior of Heavy Metals onto Chemically Modified Sugarcane Bagasse. *Bioresource Technology*, **101**(6), 2067-2069.
- Hong, J., Kang, L., Shi, X., Wei, R., Mai, X., Pan, D., Naik, N., & Guo, Z. (2022). Highly Efficient Removal of Trace Pb(II) from Wastewater by 1, 4-

- Dicarboxybenzene Modified Fe/Co Metal Organic Nanosheets. *Journal of Materials Science and Technology*, **98**: 212-218.
- Hu, X., Zhu, F., Kong, L., & Peng, X. (2021). A Novel Precipitant for the Selective Removal of Fluoride ion from Strongly Acidic Wastewater: Synthesis, Efficiency, and Mechanism. *Journal of Hazardous Materials*, **403**: 124039.
- Huang, K., & Zhu, H. (2013). Removal of Pb(II) from Aqueous Solution by Adsorption on Chemically Modified Muskmelon Peel. *Environmental Science and Pollution Research*, **20**(7): 4424-4434.
- Huang, S., Liang, Q., Geng, J., Luo, H., & Wei, Q. (2019). Sulfurized Biochar Prepared by Simplified Technic with Superior Adsorption Property Towards Aqueous Hg(II) and Adsorption Mechanisms. *Materials Chemistry and Physics*, **238**: 121919.
- Inoue, K., Parajuli, D., Ghimire, K. N., Biswas, B. K., Kawakita, H., Oshima, T., & Ohto, K. (2017). Biosorbents for Removing Hazardous Metals and Metalloids. *Materials*, **10**(8): 857.
- İrdemez, Ş., Demircioğlu, N., & Yildiz, Y. Ş. (2006). The Effects of pH on Phosphate Removal from Wastewater by Electrocoagulation with Iron Plate Electrodes. *Journal of Hazardous Materials*, **137**(2): 1231-1235.
- Jaishankar, M., Tseten, T., Anbalagan, N., Mathew, B. B., & Beeregowda, K. N. (2014). Toxicity, Mechanism and Health Effects of Some Heavy Metals. *Interdisciplinary Toxicology*, **7**(2): 60.
- Jeyaseelan, A., Naushad, M., Ahamad, T., & Viswanathan, N. (2021). Design and Development of Amine Functionalized Iron Based Metal Organic Frameworks for Selective Fluoride Removal from Water Environment. *Journal of Environmental Chemical Engineering*, **9**(1): 104563.
- Jha, R., Jha, U., Dey, R., Mishra, S., & Swain, S. (2015). Fluoride Sorption by Zr(IV) Loaded Carboxylated Orange peel. *Desalination and Water Treatment*, **53**(8): 2144-2157.

- Ji, J., Chen, G., & Zhao, J. (2019). Preparation and Characterization of Amino/Thiol Bifunctionalized Magnetic Nanoadsorbent and Its Application in Rapid Removal of Pb(II) from Aqueous System. *Journal of Hazardous Materials*, **368**: 255-263.
- Jiang, S., Sun, H., Wang, H., Ladewig, B. P., & Yao, Z. (2021). A Comprehensive Review on the Synthesis and Applications of Ion Exchange Membranes. *Chemosphere*, **282**: 130817.
- Johari, K., Saman, N., Song, S., Heng, J., & Mat, H. (2014). Study of Hg (II) Removal from Aqueous Solution Using Lignocellulosic Coconut Fiber Biosorbents: Equilibrium and Kinetic Evaluation. *Chemical Engineering Communications*, **201**(9): 1198-1220.
- Joo, S. H., & Tansel, B. (2015). Novel Technologies for Reverse Osmosis Concentrate Treatment: A Review. *Journal of Environmental Management*, **150**: 322-335.
- Joseph, L., Jun, B.-M., Flora, J. R., Park, C. M., & Yoon, Y. (2019). Removal of Heavy Metals from Water Sources in the Developing World Using Low-Cost Materials: A Review. *Chemosphere*, **229**: 142-159.
- Jutidamrongphan, W., Park, K., Dockko, S., Choi, J., & Lee, S. (2012). High Removal of Phosphate from Wastewater Using Silica Sulfate. *Environmental Chemistry Letters*, **10**(1): 21-28.
- Kadirvelu, K., Kavipriya, M., Karthika, C., Vennilamani, N., & Pattabhi, S. (2004). Mercury (II) Adsorption by Activated Carbon Made from Sago Waste. *Carbon*, **42**(4): 745-752.
- Katsoyiannis, I. A., & Zouboulis, A. I. (2004). Application of Biological Processes for the Removal of Arsenic from Groundwaters. *Water Research*, **38**(1): 17-26.
- Kayranli, B., Gok, O., Yilmaz, T., Gok, G., Celebi, H., Seckin, I. Y., & Kalat, D. (2021). Zinc Removal Mechanisms with Recycled Lignocellulose: From Fruit

- Residual to Biosorbent then Soil Conditioner. *Water, Air, and Soil Pollution*, **232**(8): 1-15.
- Khoramzadeh, E., Nasernejad, B., & Halladj, R. (2013). Mercury Biosorption from Aqueous Solutions by Sugarcane bagasse. *Journal of the Taiwan Institute of Chemical Engineers*, **44**(2): 266-269.
- Khound, N. J., & Bharali, R. K. (2018). Biosorption of Fluoride from Aqueous Medium by Indian Sandalwood (*Santalum album*) Leaf Powder. *Journal of Environmental Chemical Engineering*, **6**(2): 1726-1735.
- Kumarathilaka, P., Seneweera, S., Meharg, A., & Bundschuh, J. (2018). Arsenic Speciation Dynamics in Paddy Rice Soil-Water Environment: Sources, Physico-chemical, and Biological Factors- A Review. *Water Research*, **140**: 403-414.
- Kumari, S., & Chauhan, G. S. (2014). New Cellulose–Lysine Schiff Base based Sensor Adsorbent for Mercury ions. *ACS Applied Materials and Interfaces*, **6**(8): 5908-5917.
- Lagergren, S. K. (1898). About The Theory of So-Called Adsorption of Soluble Substances. *Sven. Vetenskapsakad. Handlingar*, **24**: 1-39.
- Langmuir, I. (1918). The Adsorption of Gases on Plane Surfaces of Glass, Mica and Platinum. *Journal of the American Chemical Society*, **40**(9): 1361-1403.
- Lau, S. K., & Yong, W. F. (2021). Recent Progress of Zwitterionic Materials as Antifouling Membranes for Ultrafiltration, Nanofiltration, and Reverse Osmosis. *ACS Applied Polymer Materials*, **3**(9): 4390-4412.
- Lee, S. Y., & Choi, H. J. (2021). Efficient Adsorption of Methylene Blue from Aqueous Solution by Sulfuric Acid Activated Watermelon Rind (*Citrullus lanatus*). *Applied Chemistry for Engineering*, **32**(3): 348-356.
- Lewoyehu, M. (2021). Comprehensive Review on Synthesis and Application of Activated Carbon from Agricultural Residues for the Remediation of

Venomous Pollutants in Wastewater. *Journal of Analytical and Applied Pyrolysis*, **159**: 105279.

Li, T. T., Liu, Y. G., Peng, Q. Q., Hu, X. J., Liao, T., Wang, H., & Lu, M. (2013). Removal of Pb(II) from Aqueous Solution with Ethylenediamine-Modified Yeast Biomass Coated with Magnetic Chitosan Microparticles: Kinetic and Equilibrium Modeling. *Chemical Engineering Journal*, **214**: 189-197.

Liang, Y. M., Jun, M., & Liu, W. (2007). Enhanced Removal of Pb(II) and Cd(II) from Water in Alum Coagulation by Ferrate(VI) Pretreatment. *Water Environment Research*, **79**(12): 2420-2426.

Liu, C. H., Chuang, Y. H., Chen, T. Y., Tian, Y., Li, H., Wang, M. K., & Zhang, W. (2015). Mechanism of Arsenic Adsorption on Magnetite Nanoparticles from Water: Thermodynamic and Spectroscopic Studies. *Environmental Science and Technology*, **49**(13): 7726-7734.

Liu, D., Deng, S., Maimaiti, A., Wang, B., Huang, J., Wang, Y., & Yu, G. (2018). As(III) and As (V) Adsorption on Nanocomposite of Hydrated Zirconium Oxide Coated Carbon Nanotubes. *Journal of Colloid and Interface Science*, **511**: 277-284.

Liu, H., Wang, J. G., You, Z., Wei, C., Kang, F., & Wei, B. (2021). Rechargeable Aqueous Zinc-ion Batteries: Mechanism, Design Strategies and Future Perspectives. *Materials Today*, **42**: 73-98.

Liu, Z., Sun, Y., Xu, X., Qu, J., & Qu, B. (2020). Adsorption of Hg(II) in an Aqueous Solution by Activated Carbon Prepared from Rice Husk Using KOH Activation. *ACS Omega*, **5**(45): 29231-29242.

López, R., Antelo, J., Fiol, S., & Macías-García, F. (2019). Phosphate Adsorption on an Industrial Residue and Subsequent Use as an Amendment for Phosphorous Deficient Soils. *Journal of Cleaner Production*, **230**: 844-853.

Loucks, D. P. (2000). Sustainable Water Resources Management. *Water International*, **25**(1): 3-10.

- Lu, D., Cao, Q., Cao, X., & Luo, F. (2009). Removal of Pb(II) Using the Modified Lawny Grass: Mechanism, Kinetics, Equilibrium and Thermodynamic Studies. *Journal of Hazardous Materials*, **166**(1): 239-247.
- Ma, Z., Xue, R., Li, J. S., Zhao, Y., Xue, Q., Chen, Z., Wang, Q., & Poon, C. S. (2021). Use of Thermally Modified Waste Concrete Powder for Removal of Pb(II) from Wastewater: Effects and Mechanism. *Environmental Pollution*, **277**: 116776.
- Madala, S., Mudumala, V. N. R., Vudagandla, S., & Abburi, K. (2015). Modified Leaf Biomass for Pb(II) Removal from Aqueous Solution: Application of Response Surface Methodology. *Ecological Engineering*, **83**: 218-226.
- Mahmood, T., Aslam, M., Naeem, A., Siddique, T., & Din, S. U. (2018). Adsorption of As(III) from Aqueous Solution onto Iron Impregnated Used Tea activated carbon: Equilibrium, Kinetic and Thermodynamic Study. *Journal of the Chilean Chemical Society*, **63**(1): 3855-3866.
- Maia, L. F. O., Santos, M. S., Andrade, T. G., de Carvalho Hott, R., da Silva Faria, M. C., Oliveira, L. C. A., Pereira, M. C., & Rodrigues, J. L. (2018). Removal of Hg(II) from Contaminated Water by Gold-Functionalised Fe₃O₄ Magnetic Nanoparticles. *Environmental Technology*, **41**(8): 959-970.
- Maksoud, M. A., Elgarahy, A. M., Farrell, C., Ala'a, H., Rooney, D. W., & Osman, A. I. (2020). Insight on Water Remediation Application Using Magnetic Nanomaterials and Biosorbents. *Coordination Chemistry Reviews*, **403**: 213096.
- Malik, H., Qureshi, U. A., Muqeet, M., Mahar, R. B., Ahmed, F., & Khatri, Z. (2018). Removal of Lead from Aqueous Solution Using Polyacrylonitrile/magnetite Nanofibers. *Environmental Science and Pollution Research*, **25**(4): 3557-3564.
- Maliyekkal, S. M., Shukla, S., Philip, L., & Nambi, I. M. (2008). Enhanced Fluoride Removal from Drinking Water by Magnesia-amended Activated Alumina Granules. *Chemical Engineering Journal*, **140**(1-3): 183-192.

- Mallampati, R., & Valiyaveettil, S. (2013). Apple Peels. A Versatile Biomass for Water Purification? *ACS Applied Materials and Interfaces*, **5**(10): 4443-4449.
- Manna, A., Naskar, N., Sen, K., & Banerjee, K. (2022). A Review on Adsorption Mediated Phosphate Removal and Recovery by Biomatrices. *Journal of the Indian Chemical Society*, **99**(10): 100682.
- Markou, G., Mitrogiannis, D., Muylaert, K., Çelekli, A., & Bozkurt, H. (2016). Biosorption and Retention of Orthophosphate onto Ca(OH)₂-Pretreated Biomass of Phragmites sp. *Journal of Environmental Sciences*, **45**: 49-59.
- Martín-Lara, M. A., Blázquez, G., Ronda, A., Rodríguez, I. L., & Calero, M. (2012). Multiple Biosorption–Desorption Cycles in a Fixed-Bed Column for Pb(II) Removal by Acid-Treated Olive Stone. *Journal of Industrial and Engineering Chemistry*, **18**(3): 1006-1012.
- Milonjić, S. K. (2007). A Consideration of the Correct Calculation of Thermodynamic Parameters of Adsorption. *Journal of the Serbian Chemical Society*, **72**(12): 1363-1367.
- Min, S. H. (2004). *Development of Surface Modified Wood Filter Media for Removing Toxic Metal Ions*. The University of Wisconsin, Madison Proquest Dissertations Publishing, 3143132.
- Mohan, D., & Pittman Jr, C. U. (2007). Arsenic Removal from Water/Wastewater Using Adsorbents- A Critical Review. *Journal of Hazardous Materials*, **142**(1-2): 1-53.
- Mondal, D. K., Nandi, B. K., & Purkait, M. (2013). Removal of Hg(II) from Aqueous Solution Using Bamboo Leaf Powder: Equilibrium, Thermodynamic and Kinetic Studies. *Journal of Environmental Chemical Engineering*, **1**(4): 891-898.
- Mousavi, S. A., Almasi, A., Navazeshkha, F., & Falahi, F. (2019). Biosorption of Lead from Aqueous Solutions by Algae Biomass: Optimization and Modeling. *Desalination and Water Treatment*, **148**: 229-237.

- Mudau, F., Motsa, M., Hassard, F., & de Kock, L. A. (2022). Resin-Loaded Heterogeneous Polyether Sulfone Ion Exchange Membranes for Saline Groundwater Treatment. *Membranes*, **12**(8): 736.
- Naja, G., & Volesky, B. (2011). The Mechanism of Metal Cation and Anion Biosorption. In *Microbial Biosorption of Metals*, 19-58.
- National Drinking Water Quality Standards and Directives (NDWQS), Nepal (2005). *Nepal Gazette* (B. S. 2062); Government of Nepal/Ministry of Physical Planning: Kathmandu, Nepal.
- Navarathna, C., Alchouron, J., Liyanage, A., Herath, A., Wathudura, P., Nawalage, S., Rodrigo, P., Gunatilake, S., Mohan, D., & Pittman Jr, C. (2020). Recent Developments in Aqueous As(III) Remediation Using Biomass-based Adsorbents. *Contaminants in Our Water: Identification and Remediation Methods*, **1352**: 197-251.
- Nguyen, T., Ngo, H., Guo, W., Pham, T., Li, F., Nguyen, T., & Bui, X. (2015). Adsorption of Phosphate from Aqueous Solutions and Sewage Using Zirconium loaded okara (ZLO): Fixed-bed Column Study. *Science of the Total Environment*, **523**: 40-49.
- Nguyen, T., Ngo, H., Guo, W., Zhou, J., Wang, J., Liang, H., & Li, G. (2014). Phosphorus Elimination from Aqueous Solution Using ‘Zirconium Loaded Okara’ as a Biosorbent. *Bioresource Technology*, **170**: 30-37.
- Nie, Y., Hu, C., & Kong, C. (2012). Enhanced Fluoride Adsorption Using Al(III) Modified Calcium Hydroxyapatite. *Journal of Hazardous Materials*, **233**: 194-199.
- Nikolenko, M. V., Vasylenko, K. V., Myrhorodska, V. D., Kostyniuk, A., & Likozar, B. (2020). Synthesis of Calcium Orthophosphates by Chemical Precipitation in Aqueous Solutions: The Effect of the Acidity, Ca/P Molar Ratio, and Temperature on the Phase Composition and Solubility of Precipitates. *Processes*, **8**(9): 1009.

- Nivetha, A., Sakthivel, C., & Prabha, I. (2021). Heavy Metal Contamination in Groundwater and Impact on Plant and Human. *In Spatial Modeling and Assessment of Environmental Contaminants*, 233-246.
- Nizam, S., Virk, H. S., & Sen, I. S. (2022). High Levels of Fluoride in Groundwater from Northern Parts of Indo-Gangetic Plains Reveals Detrimental Fluorosis Health Risks. *Environmental Advances*, **8**: 100200.
- Obotey Ezugbe, E., & Rathilal, S. (2020). Membrane Technologies in Wastewater Treatment: A Review. *Membranes*, **10**(5): 89.
- Oguz, E. (2004). Removal of Phosphate from Aqueous Solution with Blast Furnace Slag. *Journal of Hazardous Materials*, **114**(1-3): 131-137.
- Onyango, M. S., Kojima, Y., Aoyi, O., Bernardo, E. C., & Matsuda, H. (2004). Adsorption Equilibrium Modeling and Solution Chemistry Dependence of Fluoride Removal from Water by Trivalent-Cation-Exchanged Zeolite F-9. *Journal of Colloid and Interface Science*, **279**(2): 341-350.
- Özacar, M., Şengil, İ. A., & Türkmenler, H. (2008). Equilibrium and Kinetic Data, and Adsorption Mechanism for Adsorption of Lead onto Valonia Tannin Resin. *Chemical Engineering Journal*, **143**(1-3): 32-42.
- Ouma, I. L. A., Naidoo, E. B., & Ofomaja, A. E. (2018). Thermodynamic, Kinetic and Spectroscopic Investigation of Arsenite Adsorption Mechanism on Pine Cone-Magnetite Composite. *Journal of Environmental Chemical Engineering*, **6**(4): 5409-5419.
- Oveisi, F., Nikazar, M., Razzaghi, M. H., Mirrahimi, M. A. S., & Jafarzadeh, M. T. (2017). Effective Removal of Mercury from Aqueous Solution Using Thiol-Functionalized Magnetic Nanoparticles. *Environmental Nanotechnology, Monitoring and Management*, **7**: 130-138.
- Özcan, A. S., Tunali, S., Akar, T., & Özcan, A. (2009). Biosorption of Pb(II) ions onto Waste Biomass of *Phaseolus vulgaris L.*: Estimation of the Equilibrium, Kinetic and Thermodynamic Parameters. *Desalination*, **244**(1-3): 188-198.

- Ozsvath, D. L. (2006). Fluoride Concentrations in a Crystalline Bedrock Aquifer Marathon County, Wisconsin. *Environmental Geology*, **50**(1): 132-138.
- Palansooriya, K. N., Kim, S., Igalavithana, A. D., Hashimoto, Y., Choi, Y. E., Mukhopadhyay, R., Sarkar, B., & Ok, Y. S. (2021). Fe(III)- Loaded Chitosan-Biochar Composite Fibers for the Removal of Phosphate from Water. *Journal of Hazardous Materials*, **415**: 125464.
- Pandey, L. M. (2021). Surface Engineering of Nano-Sorbents for the Removal of Heavy Metals: Interfacial Aspects. *Journal of Environmental Chemical Engineering*, **9**(1): 104586.
- Pandey, P. K., Choubey, S., Verma, Y., Pandey, M., & Chandrashekhar, K. (2009). Biosorptive Removal of Arsenic from Drinking Water. *Bioresource Technology*, **100**(2): 634-637.
- Pang, T., Aye Chan, T. S., Jande, Y. A. C., & Shen, J. (2020). Removal of Fluoride from Water Using Activated Carbon Fibres Modified with Zirconium by a Drop-Coating Method. *Chemosphere*, **255**: 126950.
- Pangeni, B., Paudyal, H., Inoue, K., Kawakita, H., Ohto, K., Harada, H., Biswas, B. K., & Alam, S. (2012). Optimization of an Adsorption Process for Tetrafluoroborate Removal by Zr(IV)-Loaded Orange Waste Gel from Aqueous Solution. *Environmental Technology*, **33**(8): 845-850.
- Pantić, K., Bajić, Z. J., Veličković, Z. S., Nešić, J. Z., Đolić, M. B., Tomić, N. Z., & Marinković, A. D. (2019). Arsenic Removal by Copper-Impregnated Natural Mineral Tufa Part II: A Kinetics and Column Adsorption Study. *Environmental Science and Pollution Research*, **26**(23): 24143-24161.
- Paudyal, H., Ohto, K., Kawakita, H., & Inoue, K. (2020). Recovery of Fluoride from Water through Adsorption Using Orange-Waste Gel, Followed by Desorption Using Saturated Lime Water. *Journal of Material Cycles and Waste Management*, **22**(5): 1484-1491.

- Paudyal, H., Pangeni, B., Ghimire, K. N., Inoue, K., Ohto, K., Kawakita, H., & Alam, S. (2012). Adsorption Behavior of Orange Waste Gel for Some Rare Earth ions and its Application to the Removal of Fluoride from Water. *Chemical Engineering Journal*, **195**: 289-296.
- Paudyal, H., Pangeni, B., Inoue, K., Kawakita, H., Ohto, K., Ghimire, K. N., & Alam, S. (2013). Preparation of Novel Alginate based Anion Exchanger from *Ulva japonica* and its Application for the Removal of Trace Concentrations of Fluoride from Water. *Bioresource Technology*, **148**: 221-227.
- Paudyal, H., Pangeni, B., Inoue, K., Kawakita, H., Ohto, K., Harada, H., & Alam, S. (2011). Adsorptive Removal of Fluoride from Aqueous Solution Using Orange Waste Loaded with Multi-valent Metal ions. *Journal of Hazardous Materials*, **192**(2): 676-682.
- Pereira, A., & Maraschin, M. (2015). Banana (*Musa spp*) from Peel to Pulp: Ethnopharmacology, Source of Bioactive Compounds and its Relevance for Human Health. *Journal of Ethnopharmacology*, **160**: 149-163.
- Peters, N. E., & Meybeck, M. (2000). Water Quality Degradation Effects on Freshwater Availability: Impacts of Human Activities. *Water International*, **25**(2): 185-193.
- Petkowicz, C., Vriesmann, L., & Williams, P. (2017). Pectins from Food Waste: Extraction, Characterization and Properties of Watermelon Rind Pectin. *Food Hydrocolloids*, **65**: 57-67.
- Pholosi, A., Naidoo, E. B., & Ofomaja, A. E. (2019). Enhanced As(III) Adsorption from Aqueous Solution by Magnetic Pine Cone Biomass. *Materials Chemistry and Physics*, **222**: 20-30.
- Photiou, P., Koutsokeras, L., Constantinides, G., Koutinas, M., & Vyrides, I. (2021). Phosphate Removal from Synthetic and Real Wastewater Using Thermally Treated Seagrass Residues of *Posidonia oceanica*. *Journal of Cleaner Production*, **278**: 123294.

- Pirrone, N., Cinnirella, S., Feng, X., Finkelman, R. B., Friedli, H. R., Leaner, J., Mason, R., Mukherjee, A. B., Stracher, G. B., Streets, D. G., & Telmer, K. (2010). Global Mercury Emissions to the Atmosphere from Anthropogenic and Natural Sources. *Atmospheric Chemistry and Physics*, **10**(13): 5951-5964.
- Pohl, A. (2020). Removal of Heavy Metal ions from Water and Wastewaters by Sulfur-Containing Precipitation Agents. *Water, Air, and Soil Pollution*, **231**(10): 1-17.
- Poudel, B. R., Aryal, R. L., Bhattarai, S., Koirala, A. R., Gautam, S. K., Ghimire, K. N., Pant, B., Park, M., Paudyal, H., & Pokhrel, M. R. (2020). Agro-waste Derived Biomass Impregnated with TiO₂ as a Potential Adsorbent for Removal of As(III) from Water. *Catalysts*, **10**(10): 1125.
- Poudel, B. R., Aryal, R. L., Gautam, S. K., Ghimire, K. N., Paudyal, H., & Pokhrel, M. R. (2021). Effective Remediation of Arsenate from Contaminated Water by Zirconium Modified Pomegranate Peel as an Anion Exchanger. *Journal of Environmental Chemical Engineering*, **9**(6): 106552.
- Poza-Pascual, A., Serna-Muñoz, C., Pérez-Silva, A., Martínez-Beneyto, Y., Cabello, I., & Ortiz-Ruiz, A. J. (2021). Effects of Fluoride and Calcium Phosphate-based Varnishes in Children at High Risk of Tooth Decay: A Randomized Clinical Trial. *International Journal of Environmental Research and Public Health*, **18**(19): 10049.
- Prasad, K. S., Amin, Y., & Selvaraj, K. (2014). Defluoridation Using Biomimetically Synthesized Nano Zirconium Chitosan Composite: Kinetic and Equilibrium Studies. *Journal of Hazardous Materials*, **276**: 232-240.
- Puanggam, M., & Unob, F. (2008). Preparation and Use of Chemically Modified MCM-41 and Silica Gel as Selective Adsorbents for Hg(II) ions. *Journal of Hazardous Materials*, **154**(1-3): 578-587.
- Qiao, H., Mei, L., Chen, G., Liu, H., Peng, C., Ke, F., Hou, R., Wan, X., & Cai, H. (2019). Adsorption of Nitrate and Phosphate from Aqueous Solution Using Amine Cross-Linked Tea Wastes. *Applied Surface Science*, **483**: 114-122.

- Qu, G., Zhou, J., Liang, S., Li, Y., Ning, P., Pan, K., Ji, W., & Tang, H. (2022). Thiol-Functionalized Multi-Walled Carbon Nanotubes for Effective Removal of Pb(II) from Aqueous Solutions. *Materials Chemistry and Physics*, **278**: 125688.
- Rachini, A., Le Troedec, M., Peyratout, C., & Smith, A. (2009). Comparison of the Thermal Degradation of Natural, Alkali-treated and Silane-treated Hemp Fibers Under Air and an Inert Atmosphere. *Journal of Applied Polymer Science*, **112**(1): 226-234.
- Rahman, Z., & Singh, V. P. (2019). The Relative Impact of Toxic Heavy Metals (THMs)(Arsenic (As), Cadmium (Cd), Chromium (Cr)(VI), Mercury (Hg), and Lead (Pb)) on the Total Environment: An Overview. *Environmental Monitoring and Assessment*, **191**(7): 1-21.
- Rai, R., Karki, D. R., Bhattarai, K. P., Pahari, B., Shrestha, N., Adhikari, S., Gautam, S. K., & Poudel, B. R. (2021). Recent Advances in Biomass-based Waste Materials for the Removal of Cr(VI) from Wastewater: A Review. *Amrit Research Journal*, **2**(01): 37-50.
- Ranote, S., Ram, B., Kumar, D., Chauhan, G. S., & Joshi, V. (2018). Functionalization of *Moringa oleifera* Gum for Use as Hg(II) ions Adsorbent. *Journal of Environmental Chemical Engineering*, **6**(2): 1805-1813.
- Rápó, E., & Tonk, S. (2021). Factors Affecting Synthetic Dye Adsorption; Desorption Studies: A Review of Results from the Last Five Years (2017–2021). *Molecules*, **26**(17): 5419.
- Razzak, S. A., Farooque, M. O., Alsheikh, Z., Alsheikhmohamad, L., Alkuroud, D., Alfayez, A., Hossain, S. Z., & Hossain, M. M. (2022). A Comprehensive Review on Conventional and Biological-Driven Heavy Metals Removal from Industrial Wastewater. *Environmental Advances*, **7**: 100168.
- Reddy, D. H. K., Harinath, Y., Sessaiah, K., & Reddy, A. (2010). Biosorption of Pb(II) from Aqueous Solutions Using Chemically Modified *Moringa oleifera* Tree Leaves. *Chemical Engineering Journal*, **162**(2): 626-634.

- Ren, Y., Cui, C., & Wang, P. (2018). Pomelo Peel Modified with Citrate as a Sustainable Adsorbent for Removal of Methylene Blue from Aqueous Solution. *Molecules*, **23**(6): 1342.
- Reshmy, R., Philip, E., Madhavan, A., Pugazhendhi, A., Sindhu, R., Sirohi, R., Awasthi, M. K., Pandey, A., & Binod, P. (2022). Nanocellulose as Green Material for Remediation of Hazardous Heavy Metal Contaminants. *Journal of Hazardous Materials*, **424**: 127516.
- Richards, S., Rao, L., Connelly, S., Raj, A., Raveendran, L., Shirin, S., Jamwal, P., & Helliwell, R. (2021). Sustainable Water Resources through Harvesting Rainwater and the Effectiveness of a Low-Cost Water Treatment. *Journal of Environmental Management*, **286**: 112223.
- Rincón, E., Espinosa, E., García-Domínguez, M. T., Balu, A., Vilaplana, F., Serrano, L., & Jiménez-Quero, A. (2021). Bioactive Pectic Polysaccharides from Bay Tree Pruning Waste: Sequential Subcritical Water Extraction and Application in Active Food Packaging. *Carbohydrate Polymers*, **272**: 118477.
- Sahli, M. M., Annouar, S., Tahaikt, M., Mountadar, M., Soufiane, A., & Elmidaoui, A. (2007). Fluoride Removal for Underground Brackish Water by Adsorption on the Natural Chitosan and by Electrodialysis. *Desalination*, **212**(1-3): 37-45.
- Sakamoto, M., Itai, T., Marumoto, K., Marumoto, M., Kodamatani, H., Tomiyasu, T., Nagasaka, H., Mori, K., Poulain, A. J., & Domingo, J. L. (2020). Mercury Speciation in Preserved Historical Sludge: Potential Risk from Sludge Contained within Reclaimed Land of Minamata Bay, Japan. *Environmental Research*, **180**: 108668.
- Saleh, T. A., Mustaqeem, M., & Khaled, M. (2022). Water Treatment Technologies in Removing Heavy Metal ions from Wastewater: A Review. *Environmental Nanotechnology, Monitoring and Management*, **17**: 100617.
- Samal, A. C., Bhattacharya, P., Biswas, P., Maity, J. P., Bundschuh, J., & Santra, S. C. (2021). Variety-Specific Arsenic Accumulation in 44 Different Rice Cultivars (*O. sativa L.*) and Human Health Risks Due to Co-exposure of

Arsenic-Contaminated Rice and Drinking Water. *Journal of Hazardous Materials*, **407**: 124804.

Samani, M. R., & Toghraie, D. (2020). Using of Polyaniline–Polyvinyl Acetate Composite to Remove Mercury from Aqueous Media. *International Journal of Environmental Research*, **14**(3): 303-310.

Samant, A., Nayak, B., & Misra, P. K. (2017). Kinetics and Mechanistic Interpretation of Fluoride Removal by Nanocrystalline Hydroxyapatite Derived from *Limacine artica* shells. *Journal of Environmental Chemical Engineering*, **5**(6): 5429-5438.

Shamsudin, M. S., & Ismail, S. (2019). Thin Adsorbent Coating for Contaminant of Emerging Concern (CEC) Removal. In *AIP Conference Proceedings*, **2124**: 020044.

Segura, J. J., Elbourne, A., Wanless, E. J., Warr, G. G., Voitchovsky, K., & Atkin, R. (2013). Adsorbed and Near Surface Structure of Ionic Liquids at a Solid Interface. *Physical Chemistry Chemical Physics*, **15**(9): 3320-3328.

Sert, S., Çelik, A., & Tirtom, V. N. (2017). Removal of As(III) ions from Aqueous Solutions by Modified Hazelnut Shell. *Desalination and Water Treatment*, **75**: 115-123.

Shaikh, W. A., Alam, M. A., Alam, M. O., Chakraborty, S., Owens, G., Bhattacharya, T., & Mondal, N. K. (2020). Enhanced Aqueous Phase Arsenic Removal by a Biochar based Iron Nanocomposite. *Environmental Technology and Innovation*, **19**: 100168.

Shakoor, M. B., Niazi, N. K., Bibi, I., Shahid, M., Sharif, F., Bashir, S., Shaheen, S. M., Wang, H., Tsang, D. C., & Ok, Y. S. (2018). Arsenic Removal by Natural and Chemically Modified Watermelon Rind in Aqueous Solutions and Groundwater. *Science of the Total Environment*, **645**: 1444-1455.

Shen, L. C., Nguyen, X. T., & Hankins, N. P. (2015). Removal of Heavy Metal ions from Dilute Aqueous Solutions by Polymer–Surfactant Aggregates: A Novel

- Effluent Treatment Process. *Separation and Purification Technology*, **152**: 101-107.
- Shi, T., Jia, S., Chen, Y., Wen, Y., Du, C., Guo, H., & Wang, Z. (2009). Adsorption of Pb(II), Cr(III), Cu(II), Cd(II) and Ni(II) onto a Vanadium Mine Tailing from Aqueous Solution. *Journal of Hazardous Materials*, **169**(1-3): 838-846.
- Siddique, A., Nayak, A. K., & Singh, J. (2020). Synthesis of FeCl₃-Activated Carbon Derived from Waste *Citrus limetta* Peels for Removal of Fluoride: An Eco-Friendly Approach for the Treatment of Groundwater and Bio-waste Collectively. *Groundwater for Sustainable Development*, **10**: 100339.
- Simon, G., Huang, H., Penner-Hahn, J. E., Kesler, S. E., & Kao, L. S. (1999). Oxidation State of Gold and Arsenic in Gold-bearing Arsenian pyrite. *American Mineralogist*, **84**(7-8): 1071-1079.
- Singh, S., Kumar, V., Datta, S., Dhanjal, D. S., Sharma, K., Samuel, J., & Singh, J. (2020). Current Advancement and Future Prospect of Biosorbents for Bioremediation. *Science of the Total Environment*, **709**: 135895.
- Singh, S., German, M., Chaudhari, S., & Sengupta, A. K. (2020). Fluoride Removal from Groundwater Using Zirconium Impregnated Anion Exchange Resin. *Journal of Environmental Management*, **263**: 110415.
- Sinha, S., Yoon, Y., Amy, G., & Yoon, J. (2004). Determining the Effectiveness of Conventional and Alternative Coagulants through Effective Characterization Schemes. *Chemosphere*, **57**(9): 1115-1122.
- Sivakumar, R., & Lee, N. Y. (2022). Adsorptive Removal of Organic Pollutant Methylene Blue Using Polysaccharide-based Composite Hydrogels. *Chemosphere*, **286**: 131890.
- Song, B. Y., Eom, Y., & Lee, T. G. (2011). Removal and Recovery of Mercury from Aqueous Solution Using Magnetic Silica Nanocomposites. *Applied Surface Science*, **257**(10): 4754-4759.

- Spyropoulou, A., Lazarou, Y. G., & Laspidou, C. (2018). Mercury Speciation in the Water Distribution System of Skiathos Island, Greece. *Multidisciplinary Digital Publishing Institute Proceedings*, **2**(11): 668.
- Srivastava, S., & Goyal, P. (2010). *Novel Biomaterials: Decontamination of Toxic Metals from Wastewater*. Springer Science & Business Media.
- Srivastava, S., & Flora, S. (2020). Fluoride in Drinking Water and Skeletal Fluorosis: A Review of the Global Impact. *Current Environmental Health Reports*, **7**(2): 140-146.
- Sun, N., Wen, X., & Yan, C. (2018). Adsorption of Mercury ions from Wastewater Aqueous Solution by Amide Functionalized Cellulose from Sugarcane bagasse. *International Journal of Biological Macromolecules*, **108**: 1199-1206.
- Sun, Y., Zhou, S., Pan, S. Y., Zhu, S., Yu, Y., & Zheng, H. (2020). Performance Evaluation and Optimization of Flocculation Process for Removing Heavy Metal. *Chemical Engineering Journal*, **385**: 123911.
- Taib, N. I., Rosli, N. A., Saharrudin, N. I., Rozi, N. M., Kasdiehram, N. A. A., & Nazri, N. A. (2021). Kinetic, Equilibrium, and Thermodynamic Studies of Untreated Watermelon Peels for Removal of Cu(II) from Aqueous Solution. *Desalination and Water Treatment*, **227**: 289-299.
- Tan, T. L., Krusnamurthy, P. A. P., Nakajima, H., & Rashid, S. A. (2020). Adsorptive, Kinetics and Regeneration Studies of Fluoride Removal from Water Using Zirconium-based Metal Organic Frameworks. *RSC Advances*, **10**(32): 18740-18752.
- Tang, N., Niu, C. G., Li, X. T., Liang, C., Guo, H., Lin, L. S., Zheng, C. W., & Zeng, G. M. (2018). Efficient Removal of Cd(II) and Pb(II) from Aqueous Solution with Amino- and Thiol-Functionalized Activated Carbon: Isotherm and Kinetics Modeling. *Science of the Total Environment*, **635**: 1331-1344.

- Tavares, F. O., Pinto, L. A. D. M., Bassetti, F. D. J., Vieira, M. F., Bergamasco, R., & Vieira, A. M. S. (2017). Environmentally Friendly Biosorbents (husks, pods and seeds) from *Moringa oleifera* for Pb(II) Removal from Contaminated Water. *Environmental Technology*, **38**(24): 3145-3155.
- Tetteh, E. K., Rathilal, S., Chetty, M., Armah, E. K., & Asante-Sackey, D. (2019). Treatment of Water and Wastewater for Reuse and Energy Generation-Emerging Technologies. *Water and Wastewater Treatment*, 53-80.
- Thomas, B., Shilpa, E., & Alexander, L. (2021). Role of Functional Groups and Morphology on the pH-dependent Adsorption of a Cationic Dye Using Banana Peel, Orange Peel, and Neem Leaf Bio-adsorbents. *Emergent Materials*, **4**(5): 1479-1487.
- Tirkey, P., Bhattacharya, T., & Chakraborty, S. (2018). Optimization of Fluoride Removal from Aqueous Solution Using Jamun (*Syzygium cumini*) Leaf Ash. *Process Safety and Environmental Protection*, **115**: 125-138.
- Tiwari, A. K., & Pal, D. B. (2022). Nutrients Contamination and Eutrophication in the River Ecosystem. *In Ecological Significance of River Ecosystems*, 203-216.
- Tran, H. N., You, S.-J., & Chao, H.-P. (2016). Thermodynamic Parameters of Cadmium Adsorption onto Orange Peel Calculated from Various Methods: A Comparison Study. *Journal of Environmental Chemical Engineering*, **4**(3): 2671-2682.
- Ugrina, M., Čeru, T., Nuić, I., & Trgo, M. (2020). Comparative Study of Hg(II) Removal from Aqueous Solutions onto Natural and Iron-Modified Clinoptilolite Rich Zeolite. *Processes*, **8**(11): 1523.
- Vaish, B., Sharma, B., Singh, P., & Singh, R. P. (2020). E-waste and Their Implications on the Environment and Human Health. In *E-waste Recycling and Management*, 219-232 Springer.

- Van der Bruggen, B. (2018). Ion-exchange Membrane Systems- Electrodialysis and Other Electromembrane Processes. *In Fundamental Modelling of Membrane Systems*, 251-300.
- Veglio, F., & Beolchini, F. (1997). Removal of Metals by Biosorption: A Review. *Hydrometallurgy*, **44**(3): 301-316.
- Verma, L., Siddique, M. A., Singh, J., & Bharagava, R. N. (2019). As(III) and As(V) Removal by Using Iron Impregnated Biosorbents Derived from Waste Biomass of *Citrus limmeta* (Peel and Pulp) from the Aqueous Solution and Groundwater. *Journal of Environmental Management*, **250**: 109452.
- Vieira, B. R. C., Pintor, A. M. A., Boaventura, R. A. R., Botelho, C. M. S., & Santos, S. C. R. (2017). Arsenic Removal from Water Using Iron-Coated Seaweeds. *Journal of Environmental Management*, **192**: 224-233.
- Vijayaraghavan, K., & Balasubramanian, R. (2015). Is Biosorption Suitable for Decontamination of Metal-Bearing Wastewaters? A Critical Review on the State-of-the-art of Biosorption Processes and Future Directions. *Journal of Environmental Management*, **160**: 283-296.
- Vijila, B., Gladis, E. E., Jose, J. M. A., Sharmila, T., & Joseph, J. (2021). Removal of Fluoride with Rice Husk Derived Adsorbent from Agro Waste Materials. *Materials Today: Proceedings*, **45**: 2125-2129.
- Volesky, B. (2007). Biosorption and Me. *Water Research*, **41**(18): 4017-4029.
- Wang, J., Chen, N., Feng, C., & Li, M. (2018). Performance and Mechanism of Fluoride Adsorption from Groundwater by Lanthanum-Modified Pomelo Peel Biochar. *Environmental Science and Pollution Research*, **25**(16): 15326-15335.
- Wang, M., Li, Y., Zhao, D., Zhuang, L., Yang, G., & Gong, Y. (2020). Immobilization of Mercury by Iron Sulfide Nanoparticles alters Mercury Speciation and Microbial Methylation in Contaminated Groundwater. *Chemical Engineering Journal*, **381**: 122664.

- Wang, X., Liu, Z., Liu, J., Huo, M., Huo, H., & Yang, W. (2015). Removing Phosphorus from Aqueous Solutions Using Lanthanum Modified Pine Needles. *PLoS One*, **10**(12): 0142700.
- Wang, Z., Xu, J., Yellezuome, D., & Liu, R. (2021). Effects of Cotton Straw-derived Biochar Under Different Pyrolysis Conditions on Pb(II) Adsorption Properties in Aqueous Solutions. *Journal of Analytical and Applied Pyrolysis*, **157**: 105214.
- Ward, M. H., Jones, R. R., Brender, J. D., De Kok, T. M., Weyer, P. J., Nolan, B. T., Villanueva, C. M., & Van Breda, S. G. (2018). Drinking Water Nitrate and Human Health: An Updated Review. *International Journal of Environmental Research and Public Health*, **15**(7): 1557.
- Wattanakornsiri, A., Pasada, S., Kornram, S., Satchawan, S., Kheangkhun, N., & Phuengphai, P. (2022). Removal of Pb(II) from Aqueous Solution Using Fibroin from Cocoon Waste as a Potential Biosorbent. *Science and Technology Asia*, **27**: 84-97.
- Weber, T. W., & Chakravorti, R. K. (1974). Pore and Solid Diffusion Models for Fixed-Bed Adsorbers. *AIChE Journal*, **20**(2): 228-238.
- Wimalawansa, S. J. (2020). Molecular and Cellular Toxicity of Fluoride in Mystery, Tubulointerstitial Chronic Kidney Disease: A Systematic Review. *Reviews in Environmental Science and Bio/Technology*, **19**(1): 117-147.
- Wood, S. A., Tait, C. D., & Janecky, D. R. (2002). A Raman Spectroscopic Study of Arsenite and Thioarsenite Species in Aqueous Solution at 25°C. *Geochemical Transactions*, **3**(4): 31-39.
- World Health Organization. (2022). *Guidelines for Drinking-Water Quality: Fourth Edition Incorporating the First and Second Addenda*. Geneva. Licence: CC BY-NC-SA 3.0 IGO.
- World Health Organization. (2014). WHO (1993). *Trace Elements in Human Nutrition and Health*.

- World Health Organization, & WHO. (2004). *Guidelines for Drinking-water Quality* (Vol. 1). World Health Organization.
- World Health Organization. (2003). *Lead in Drinking-water: Background Document for Development of WHO Guidelines for Drinking-water Quality* (No. WHO/SDE/WSH/03.04/09). World Health Organization.
- Xing, P., Wang, C., Ma, B., & Chen, Y. (2018). Removal of Pb(II) from Aqueous Solution Using a New Zeolite-type Adsorbent: Potassium Ore Leaching Residue. *Journal of Environmental Chemical Engineering*, **6**(6): 7138-7143.
- Xu, F., Chen, H., Dai, Y., Wu, S., & Tang, X. (2019). Arsenic Adsorption and Removal by a New Starch Stabilized Ferromanganese Binary Oxide in Water. *Journal of Environmental Management*, **245**: 160-167.
- Xu, X., Gao, B., Wang, W., Yue, Q., Wang, Y., & Ni, S. (2009). Adsorption of Phosphate from Aqueous Solutions onto Modified Wheat Residue: Characteristics, Kinetic and Column Studies. *Colloids and Surfaces B: Biointerfaces*, **70**(1): 46-52.
- Yang, H., Zhou, Q., Luo, W., Yan, C., & Zhou, C. (2016). The Preparation of a Cross-linked Cerium (III)-Loaded Alginate Bead Adsorbent for the Removal of Phosphate from Wastewater. *Desalination and Water Treatment*, **57**(39): 18354-18365.
- Yang, Q., Wang, X., Luo, W., Sun, J., Xu, Q., Chen, F., Zhao, J., Wang, S., Yao, F., & Wang, D. (2018). Effectiveness and Mechanisms of Phosphate Adsorption on Iron-Modified Biochars Derived from Waste Activated Sludge. *Bioresource Technology*, **247**: 537-544.
- Yang, X., Chen, L., Ren, D., Wang, S., & Ren, Z. (2022). Adsorption of Pb(II) from Water by Treatment with an o-hydroxyphenyl Thiourea-Modified Chitosan. *International Journal of Biological Macromolecules*, **220**: 280-290.

- Yao, Z. Y., Qi, J. H., & Wang, L. H. (2010). Equilibrium, Kinetic and Thermodynamic Studies on the Biosorption of Cu(II) onto Chestnut Shell. *Journal of Hazardous Materials*, **174**(1-3): 137-143.
- Yardim, M. F., Budinova, T., Ekinici, E., Petrov, N., Razvigorova, M., & Minkova, V. (2003). Removal of Hg(II) from Aqueous Solution by Activated Carbon obtained from Furfural. *Chemosphere*, **52**(5): 835-841.
- Zainuddin, N. A., Mamat, T. A. R., Maarof, H. I., Puasa, S. W., & Yatim, S. R. M. (2019). Removal of Ni(II), Zn(II) and Cu(II) from Plating Process Industrial Raw Effluent via Hydroxide Precipitation versus Sulphide Precipitation. IOP Conference Series: *Materials Science and Engineering*, **551**: 012122
- Zamora-Ledezma, C., Negrete-Bolagay, D., Figueroa, F., Zamora-Ledezma, E., Ni, M., Alexis, F., & Guerrero, V. H. (2021). Heavy Metal Water Pollution: A Fresh Look About Hazards, Novel and Conventional Remediation Methods. *Environmental Technology and Innovation*, **22**: 101504.
- Zanella, O., Tessaro, I. C., & Féris, L. A. (2014). Desorption-and Decomposition-based Techniques for the Regeneration of Activated Carbon. *Chemical Engineering and Technology*, **37**(9): 1447-1459.
- Zhang, H., Ke, S., Xia, M., Bi, X., Shao, J., Zhang, S., & Chen, H. (2021). Effects of Phosphorous Precursors and Speciation on Reducing Bioavailability of Heavy Metal in Paddy Soil by Engineered Biochars. *Environmental Pollution*, **285**: 117459.
- Zhang, Q., Du, Q., Jiao, T., Pan, B., Zhang, Z., Sun, Q., Wang, S., Wang, T., & Gao, F. (2013). Selective Removal of Phosphate in Waters Using a Novel of Cation Adsorbent: Zirconium Phosphate (ZrP) Behavior and Mechanism. *Chemical Engineering Journal*, **221**: 315-321.
- Zheng, J., Li, Y., Xu, D., Zhao, R., Liu, Y., Li, G., Gao, Q., Zhang, X., Volodine, A., & Van der Bruggen, B. (2022). Facile Fabrication of a Positively Charged Nanofiltration Membrane for Heavy Metal and Dye Removal. *Separation and Purification Technology*, **282**: 120155.

- Zhou, K., Wu, B., Su, L., Xin, W., & Chai, X. (2018). Enhanced Phosphate Removal Using Nanostructured Hydrated Ferric-Zirconium Binary Oxide Confined in a Polymeric Anion Exchanger. *Chemical Engineering Journal*, **345**: 640-647.
- Zhou, L., Liu, Y., Liu, S., Yin, Y., Zeng, G., Tan, X., Hu, X., Hu, X., Jiang, L., & Ding, Y. (2016). Investigation of the Adsorption-Reduction Mechanisms of Hexavalent Chromium by Ramie Biochars of Different Pyrolytic Temperatures. *Bioresource Technology*, **218**: 351-359.
- Zhou, X., & Zhou, X. (2014). The Unit Problem in the Thermodynamic Calculation of Adsorption Using the Langmuir Equation. *Chemical Engineering Communications*, **201**(11): 1459-1467.
- Zou, C., Jiang, W., Liang, J., Sun, X., & Guan, Y. (2019). Removal of Pb(II) from Aqueous Solutions by Adsorption on Magnetic Bentonite. *Environmental Science and Pollution Research*, **26**(2): 1315-1322.
- Zhou, L., Gao, C., & Xu, W. (2010). Magnetic Dendritic Materials for Highly Efficient Adsorption of Dyes and Drugs. *ACS Applied Materials and Interfaces*, **2**(5): 1483-1491.

APPENDIX

Scientific Publications

Aryal, R. L., Thapa, A., Poudel, B. R., Pokhrel, M. R., Dahal, B., Paudyal, H., & Ghimire, K. N. (2022). Effective biosorption of arsenic from water using La(III) loaded carboxyl functionalized watermelon rind. *Arabian Journal of Chemistry*, 103674. <https://doi.org/10.1016/j.arabjc.2021.103674>

Aryal, R. L., Bhurtel, K. P., Poudel, B. R., Pokhrel, M. R., Paudyal, H., & Ghimire, K. N. (2022). Sequestration of phosphate from water onto modified watermelon waste loaded with Zr (IV). *Separation Science and Technology*, 57(1), 70-82 <https://doi.org/10.1080/01496395.2021.1884878>

Aryal, R. L., Poudel, B. R., Pokhrel, M. R., Paudyal, H., & Ghimire, K. N. (2021). Effectiveness of Zr (IV)-Loaded Banana Peels Biomass for the Uptake of Fluoride Anion from Water. *Journal of Institute of Science and Technology*, 26(2), 67-78. <https://doi.org/10.3126/jist.v26i2.41436>

Participation of National and International Conferences

8th Asian Conference on Colloid & Interface Science (ACCIS 2019) organized by the Asian Society of Colloid and Surface Science (ASCASS) held in Pulchowk Campus, Institute of Engineering, Tribhuvan University, Lalitpur, Kathmandu, Nepal.

POLYCHAR 2019 (Polymers for Sustainable Global Development) May 19 – 23, 2019 in Kathmandu, Nepal

International Winter School on Frontiers in Materials Science hosted at Jawaharlal Nehru Centre for Advanced Scientific Research, Bengaluru, India on December 3 – 7, 2018

International Chemical Congress -2018 " Chemistry for Sustainable Development" March 8-10, Sauraha, Chitwan, Nepal organized by Nepal Chemical Society in association with Department of Chemistry, Birendra M. Campus, Bharatpur, Tribhuvan University.



Tribhuvan University
Institute of Science and Technology
Dean's Office

SEMESTER EXAMINATION 2075

Name of Student: Ram Lochan Aryal

Exam Roll No.: 100030

Level: Ph.D.

Ph.D. Enrolment No.: 53/074

Department: Central Dept. of Chemistry

T.U. Regd. No.: 18539-92

Semester: I

Grade Sheet

Code No.	Course Title	Cr. Hrs.	Grade Point	Grade
PHS 911	Philosophy of Science	3	3.3	B+
RM 912	Research Methodology	3	3.7	A-
Sem 913	Seminar	3	4	A

SGPA: 3.7

Verified By: *Jdy*

Date: *oct. 9, 2018*



Veragen
Asst. Dean

Institute of Science & Technology
Dean's Office
Kirtipur 2045



Tribhuvan University
Institute of Science and Technology
Dean's Office

SEMESTER EXAMINATION-2075

Name of Student: Ram Lochan Aryal **Exam Roll No.:** 200029
Level: Ph.D. **Ph.D. Enrolment No.:** 53/074
Department: Central Dept. of Chemistry **T.U. Regd. No.:** 18539-92
Semester: 2

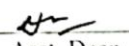
Grade Sheet

Code No.	Course Title	Cr. Hrs.	Grade Point	Grade
CHE 951	Advanced Research Methodology	3	4	A
CHE 954	Separation Science and Environmental Chemistry	3	4	A
CHE 952	Seminar	3	4	A

SGPA: 4.00

Verified By: 

Date: - ... *Sept* ... 16, 2019


Asst. Dean

**The 8th Asian Conference on Colloid
& Interface Science (ACCIS 2019)**

Sept. 24-27, Kathmandu, Nepal



Certificate of Participation

This is to certify that

Ram Lochan Aryal

has participated and contributed **Poster Presentation** in

The 8th Asian Conference on Colloid & Interface Science (ACCIS 2019) organized by the **Asian Society for Colloid and Surface Science (ASCASS)** held in Pulchowk Campus, Institute of Engineering, Tribhuvan University, Lalitpur, Kathmandu, Nepal.

A handwritten signature in black ink, appearing to read 'Lok K. Shrestha', written over a horizontal dashed line.

Dr. Lok Kumar Shrestha
Chairperson (ACCIS 2019)

A handwritten signature in black ink, appearing to read 'Toyoko Imae', written over a horizontal dashed line.

Prof. Dr. Toyoko Imae
President (ASCASS)

September 27, 2019



School of Advanced Materials (SAMat)
International Centre for Materials Science
and the Sheikh Saqr Laboratory
Jawaharlal Nehru Centre for Advanced Scientific Research

This is to certify that

Ram Lochan Aryal

Tribhuvan University, NEPAL

has participated in the

International Winter School 2018
on
Frontiers in Materials Science

Directors

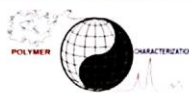
Prof. C.N.R. Rao & Prof. A. K. Cheetham

Prof. S. M. Shivaprasad
Convener

Prof. Umesh V. Waghmare
Convener



POLY-CHAR 2019



Certificate of Participation

This is to certify that

Prof. / Dr. / Mr. / Ms. **Ram Lochan Aryal**

has participated as an **oral** presenter on
Modification of Sugarcane Bagasse as a Natural
Functional Bio-polymer for the Adsorptive Removal of
Phosphate from Aqueous Solution in the

POLY-CHAR 2019

(Polymers for Sustainable Global Development)

May 19-23, 2019 in Kathmandu, Nepal.

Jean M. Saiter
POLY-CHAR President

Rameshwar Adhikari
POLY-CHAR 2019 Chair